

REPORT DOCUMENTATION PAGE

Form Approved
OMB No. 0704-0188

Public reporting burden for this collection of information is estimated to average 1 hour per response, including the time for reviewing instructions, searching existing data sources, gathering and maintaining the data needed, and completing and reviewing the collection of information. Send comments regarding this burden estimate or any other aspect of this collection of information, including suggestions for reducing this burden, to Washington Headquarters Services, Directorate for Information Operations and Reports, 1215 Jefferson Davis Highway, Suite 1204, Arlington, VA 22202-4302, and to the Office of Management and Budget, Paperwork Reduction Project (0704-0188), Washington, DC 20503.

1. AGENCY USE ONLY (Leave blank)		2. REPORT DATE Nov. 30, 2005		3. REPORT TYPE AND DATES COVERED Technical 01/04/99 to 11/30/05	
4. TITLE AND SUBTITLE: Structure of Three-Dimensional Separated Flow on Symmetric Bumps				4. FUNDING NUMBERS N00014-99-1-0228 N00014-01-1-0421	
5. AUTHORS Gwibo Byun and Roger L. Simpson					
6. PERFORMING ORGANIZATION NAME(S) AND ADDRESS(ES) Department of Aerospace and Ocean Engineering Virginia Polytechnic Institute and State University Blacksburg, Virginia 24061-0203				7. PERFORMING ORGANIZATION REPORT NUMBER VPI-AOE-297	
8. SPONSORING/MONITORING AGENCY NAME(S) AND ADDRESS(ES) Office of Naval Research, 800 N. Quincy Street Arlington, Virginia 22217				10. SPONSORING/MONITORING AGENCY REPORT NUMBER	
11. SUPPLEMENTARY NOTES					
12a. DISTRIBUTION/AVAILABILITY STATEMENT Unlimited				12b. DISTRIBUTION CODE Approved for Public Release	
13. ABSTRACT (Maximum 200 words) Surface mean pressures, oil flow visualization, and 3-velocity-component laser-Doppler velocimeter measurements are presented for a turbulent boundary layer (TBL) of momentum thickness Reynolds number, $Re_{\theta} \approx 7300$ and TBL thickness $\delta = 39\text{mm}$ over 2 axisymmetric bump cases of the same shape (Bump#3) but with heights of $H = \delta$ and 2δ and one symmetric bump (Bump#1) of $H = 2\delta$. LDV data were obtained at one plane $x/H = 3.26$ for each case. Vortical separations on the leeside merge into large stream-wise mean vortices downstream for the 2 Bump#3 cases. The near-wall flow ($y^+ < 90$) is dominated by the wall. For the axisymmetric cases, the vortices in the outer region produce large turbulence levels near the centerline and appear to have low frequency motions that contribute to turbulent diffusion. For Bump#1 there are sharper separation lines and lower turbulence intensities in the vortical downstream flow. Fine-spatial-resolution LDV measurements were also obtained on half of the leeside of the axisymmetric bump ($H/\delta = 2$). Three-dimensional (3-D) separations occur on the leeside with one saddle separation on the centerline that is connected by a separation line to one focus separation on each side of the centerline. Downstream of the saddle point the mean backflow converges to the focal separation points in a thin region confined within about 0.15δ from the local bump surface. The mean backflow zone is supplied by the intermittent large eddies as well as by the near surface flow from the side of the bump. The separated flow has a higher turbulent kinetic energy and shows bimodal histograms in local U and W , which appear to be due to highly unsteady turbulent motions. By the mode-averaged analysis of bimodal histograms, highly unsteady flow structures are estimated and unsteady 3-D separations seem to be occurring over a wide region on the bump leeside. The process of these separations has very complex dynamics having a large intermittent attached and detached flow region which is varying in time. These bimodal features with highly correlated u_L and w_L fluctuating motions are the major source of large Reynolds stresses u_L^2 , w_L^2 and $-uw_L$. Because of the variation of the mean flow angle in the separation zones, the turbulent flow from different directions is non-correlated, resulting in lower shearing stresses. Farther from the wall, large stream-wise vortices form from flow around the sides of the bump.					
14. SUBJECT TERMS laser-Doppler velocimetry, three-dimensional separation, turbulent separation				15. NUMBER OF PAGES 289	
				16. PRICE CODE	
17. SECURITY CLASSIFICATION OF REPORT UNCLASSIFIED	18. SECURITY CLASSIFICATION OF THIS PAGE UNCLASSIFIED	19. SECURITY CLASSIFICATION OF ABSTRACT UNCLASSIFIED	20. LIMITATION OF ABSTRACT UNLIMITED		

Abstract

Structure of Three-Dimensional Separated Flow on Symmetric Bumps

Gwibo Byun

Surface mean pressures, oil flow visualization, and 3-velocity-component laser-Doppler velocimeter measurements are presented for a turbulent boundary layer of momentum thickness Reynolds number, $Re_\theta \approx 7300$ and of thickness δ over 2 circular based axisymmetric bumps of height $H = \delta$ and 2δ and one rectangular based symmetric bump of $H = 2\delta$. LDV data were obtained at one plane $x/H \geq 3.26$ for each case. Complex vortical separations occur on the leeside and merge into large stream-wise mean vortices downstream for the 2 axisymmetric cases. The near-wall flow ($y^+ < 90$) is dominated by the wall. For the axisymmetric cases, the vortices in the outer region produce large turbulence levels near the centerline and appear to have low frequency motions that contribute to turbulent diffusion. For the case with a narrower span-wise shape, there are sharper separation lines and lower turbulence intensities in the vortical downstream flow.

Fine-spatial-resolution LDV measurements were also obtained on half of the leeside of an axisymmetric bump ($H/\delta = 2$) in a turbulent boundary layer. Three-dimensional (3-D) separations occur on the leeside with one saddle separation on the centerline that is connected by a separation line to one focus separation on each side of the centerline. Downstream of the saddle point the mean backflow converges to the focal separation points in a thin region confined within about 0.15δ from the local bump surface. The mean backflow zone is supplied by the intermittent large eddies as well as by the near surface flow from the side of the bump. The separated flow has a higher turbulent kinetic energy and shows bimodal histograms in local U and W , which appear to be due to highly unsteady turbulent motions. By the mode-averaged analysis of bimodal histograms, highly unsteady flow structures are estimated and unsteady 3-D separations seem to be occurring over a wide region

on the bump leeside. The process of these separations has very complex dynamics having a large intermittent attached and detached flow region which is varying in time. These bimodal features with highly correlated u_L and w_L fluctuating motions are the major source of large Reynolds stresses $\overline{u_L^2}$, $\overline{w_L^2}$ and $-\overline{u_L w_L}$. Because of the variation of the mean flow angle in the separation zones, the turbulent flow from different directions is non-correlated, resulting in lower shearing stresses. Farther from the wall, large stream-wise vortices form from flow around the sides of the bump.

Table of Contents

Abstract	ii
Acknowledgements	iv
Table of Contents.....	v
Nomenclature	viii
List of Figures	xii
List of Tables.....	xxi
1 Introduction	1
1.1 Research Motivation	1
1.2 Literature Review.....	3
1.3 Outline of Dissertation.....	8
2 Apparatus and Instrumentation.....	9
2.1 Boundary Layer Wind Tunnel	9
2.2 The Bumps.....	10
2.2.1 Bump#3 (Large and Small)	10
2.2.2 Bump#1	11
2.3 The Coordinate Systems	11
2.4 Laser Doppler Velocimeter (LDV) System	12
2.4.1 Optical table equipment.....	12
2.4.2 Probe head.....	13

2.4.3 Data acquisition and reduction	16
2.4.4 Seeding system	18
2.5 Rotating turret for the measurements around large bump#3	19
3 Surface Static Pressure Measurements and Oilflow Visualization.....	29
3.1 Surface Static Pressure Coefficient and Vorticity Flux.....	29
3.2 Surface Oilflow Visualization.....	32
3.3 Discussion of Oilflow Visualization and Surface Static Pressure Distribution.....	32
4 Wake Plane LDV Measurements	45
4.1 Undisturbed 2-DTBL Measurements.....	45
4.1.1 Velocity Gradient Broadening.....	47
4.2 Wake Plane LDV Measurements	48
4.2.1 Skin Friction Velocity	48
4.2.2 Mean Velocity	49
4.2.3 Reynolds Stresses	52
4.2.4 1/S Parameter and Correlation Coefficient, R_{uv}	55
4.2.5 Turbulent Kinetic Energy and its Diffusion Velocity Vector.....	56
4.2.6 Townsend's Structural Parameter, $A1$	58
4.2.7 Flow Angle, Flow Gradient Angle and Shear Stress Angle	58
4.2.8 Anisotropy factor, N	60
4.2.9 Mixing Length and Eddy Viscosity.....	61
4.2.10 Span-wise Velocity Spectra.....	63
4.3 Estimation of Dissipation Rate	63
4.4 Summary of Flow Structures of Each Bump at Wake Plane.....	68
5 LDV Measurements near Large Bump#3 Surface	128
5.1 Mean Flow Symmetry.....	129

5.2 Mean Velocities and Separations	129
5.2.1 Across the Center Plane.....	129
5.2.2 On the Leaside of the Bump.....	131
5.2.3 Three-Dimensional Mean Streamlines	132
5.3 Reynolds Stresses and Correlation Parameters	133
5.3.1 Reynolds Stresses.....	133
5.3.2 The Correlation Coefficients related to Reynolds Stresses	137
5.4 Turbulent Kinetic Energy and its Transport Velocity Vectors.....	138
5.5 Structural Parameters A1, B and B2	140
5.6 Flow Angle, Flow Gradient Angle and Shear Stress Angle.....	141
5.7 Bimodal Histogram.....	142
5.7.1 Forward and Backward Modes.....	143
5.7.2 Combination of Forward and Backward Modes.....	145
5.7.3 Time Dependence of Bimodal Histograms.....	146
5.8 Skewness and Flatness Factors	147
5.9 Summary of the Flow Structure of Large Bump#3 Leaside.....	149
6 Large Bump#3 CFD Calculations	209
6.1 Introduction.....	209
6.2 Prof. Menon Group	210
6.3 Prof. Leschziner Group	211
6.4 Prof. Davidson Group	213
6.5 Summary	214
7 Conclusions.....	226
References.....	229
Appendix A Uncertainties of LDV Measurements.....	237

A.1 Standard Uncertainty Analysis.....	237
A.1.1 Cross Angle Measurement.....	238
A.1.2 Laser Wavelength.....	238
A.1.3 Fringe Spacing Gradient due to Misalignment	238
A.1.4 Signal Processor Resolution	239
A.2 Uncertainty Estimation using Measured Quantities	241
Appendix B Contour Plots of Reynolds Stresses at the Wake Plane	244
Appendix C Inertial Subrange Curve Fit at the Wake Plane Centerline.....	251
Appendix D Combination of Forward and Backward Modes on the Leaside.....	255

Nomenclature

Roman

A1	Structural parameter, $\sqrt{(-\overline{uv})^2 + (-\overline{vw})^2} / (\overline{u^2} + \overline{v^2} + \overline{w^2})$
B	Triple products ratio, $\overline{v^3} / (\overline{u^2 v} + \overline{v^3} + \overline{vw^2})$
B2	Triple products ratio, $\overline{v^3} / \sqrt{(\overline{uv^2})^2 + (\overline{v^2 w})^2}$
C	Kolmogorov constant in Eq.(4.20)
C ₁ , C ₂	Coefficients for curve fit of skin friction velocity
C _p	Pressure coefficient, $\frac{P_{local,static} - P_{ref,static}}{P_{ref,total} - P_{ref,static}}$
f	Frequency [1/s]
f _s	Sampling frequency [1/s]
F	Flatness, $\overline{u_i^4} / (\overline{u_i^2})^2$
FA	Flow Angle, $\tan^{-1}(\overline{W}/\overline{U})$
FGA	Flow Gradient Angle, $\tan^{-1}\left(\frac{\partial \overline{W} / \partial y}{\partial \overline{U} / \partial y}\right)$
G _{uu}	One-dimensional stream-wise energy spectrum defined by Eq.(4.16) [m ² /s]
G _{ww}	One-dimensional span-wise energy spectrum defined by Eq(4.15) [m ² /s]
$\vec{i}, \vec{j}, \vec{k}$	Unit vectors in the x, y, z direction, respectively
H	Bump height
\mathcal{H}	Total helicity in y-z plane, $\iint h dy dz$ [m ³ /s ²]
h	Helicity density, $\overline{U}\omega_i$ [m/s ²]
L _ε	Dissipation lengthscale, $TKE^{3/2} / \varepsilon$ [m]

L_{11}	Longitudinal integral lengthscale defined by Eq.(4.22) [m]
L_m	Mixing length defined by Eq.(4.12) [m]
N	Anisotropy factor, ν_{Tz} / ν_{Tx}
	Number of samples
$P_{ref,static}$	Static pressure of the undisturbed free-stream
$P_{ref,total}$	Stagnation pressure of the undisturbed free-stream
$\overline{q^2}$	Two times turbulent kinetic energy [m^2/s^2]
r	Local radius of large bump#3
R_C	Correlation coefficient of the curve fit
R_{uv}	Correlation coefficient of Reynolds shear stress, $-\overline{uv}/(\overline{u'^2}\overline{v'^2})^{1/2}$
Re_H	Reynolds number based on bump height, $U_{ref} H / \nu$
Re_θ	Momentum thickness Reynolds number, $U_{ref} \theta / \nu$
S	Skewness, $\overline{u_i^3} / (\overline{u_i^2})^{3/2}$
$1/S$	Reynolds stresses ratio, $\sqrt{(-\overline{uv})^2 + (-\overline{vw})^2} / \overline{v^2}$
SSA	Shear Stress Angle, $\tan^{-1}(-\overline{vw}/-\overline{uv})$
TKE	Turbulent Kinetic Energy defined by Eq.(4.5) [m^2/s^2]
t	Time [s]
U, V, W	Instantaneous velocities in the x, y, z directions, respectively [m/s]
$\overline{U}, \overline{V}, \overline{W}$	Mean velocities in the x, y, z directions, respectively [m/s]
U_{ref}	Reference free-stream velocity [m/s]
u, v, w	Velocity fluctuations in the x, y, z directions, respectively [m/s]
u', v', w'	Standard deviation of velocity fluctuations in the x, y, z directions, respectively [m/s]
$\overline{u^2}, \overline{v^2}, \overline{w^2}$	Reynolds kinematic normal stresses [m^2/s^2]
$-\overline{uv}, -\overline{uw}, -\overline{vw}$	Reynolds kinematic shear stresses [m^2/s^2]
u_τ	Skin friction velocity, $\sqrt{\tau_w / \rho}$ [m/s]

U^+, V^+, W^+	Non-dimensional mean velocities normalized by u_τ
\vec{V}	Mean velocity vector [m/s]
\vec{V}_q	Normalized diffusion velocity vector defined by Eq.(4.6),
x	Stream-wise direction in tunnel coordinates
y	Vertical direction in tunnel coordinates
z	Span-wise direction in tunnel coordinates
x_l	Radial direction tangent to large bump#3 surface in local right-hand coordinates
y_l	Vertical direction normal to large bump#3 surface in local right-hand coordinates
z_l	Circumferential direction tangent to large bump#3 surface in local right-hand coordinates
y_{shift}	Wall location refinement
y^+	Non-dimensional distance from the wall, $y u_\tau / \nu$
y_{l0}^+	Non-dimensional distance from large bump#3 surface normalized by 2-DTBL $u_{\tau 0}$

Greek

δ	Boundary layer thickness defined as the distance from the wall to where the local velocity is 99% of U_{ref}
	Uncertainty
ε	Dissipation rate defined by Eq.(4.17) [m^2/s^3]
γ_P	Intermittency, the time fraction of forward flow
γ_N	Intermittency, the time fraction of backward flow
η	Kolmogorov lengthscale, $(\nu^3 / \varepsilon)^{1/4}$ [m]
κ_l	1-D Stream-wise wavenumber defined by Eq.(4.18) [m^{-1}]
Γ	Circulation in y-z plane, $\oint_C \vec{V} \cdot d\vec{s}$ [m^2/s]

ν	Kinematic viscosity [m^2/s]
ν_{Tx}	Eddy viscosity in stream-wise direction defined by Eq.(4.13) [m^2/s]
ν_{Tz}	Eddy viscosity in span-wise direction defined by Eq.(4.14) [m^2/s]
θ	Momentum thickness [m], Pitch angle [$^\circ$]
τ	Local shear stress magnitude [N/m^2]
τ_E	Integral time scale [s]
τ_w	Local wall shear stress magnitude [N/m^2]
ω_x	Stream-wise vorticity, $\partial \bar{W} / \partial y - \partial \bar{V} / \partial z$ [s^{-1}]
ψ	Yaw angle [$^\circ$]

Subscript

L	Denotes quantities in local coordinate system
LR	Denotes quantities in rotated local coordinate system in which there is only bimodal histogram in U_L
0	Denotes quantities normalized by 2-DTBL u_τ

Abbreviations

2-DTBL	Two-Dimensional Turbulent Boundary Layers
3-DTBL	Three-Dimensional Turbulent Boundary Layers
CFD	Computational Fluid Dynamics
DNS	Direct Numerical Simulation
JPDF	Joint Probability Density Function
LDV	Laser Doppler Velocimeter
LES	Large-Eddy Simulation
PDF	Probability Density Function
RANS	Reynolds-Averaged Navier-Stokes

List of Figures

Figure 2.1 Side view schematic of the wind tunnel test section for bump measurements.....	20
Figure 2.2 Axisymmetric shapes of bump#3 and the stream-wise shape of bump#1.....	21
Figure 2.3 3D shapes of bumps.	21
Figure 2.4 Schematic of bumps in the wind tunnel.	22
Figure 2.5 Optical table equipments.....	23
Figure 2.6 Schematic diagrams of “Short” (right) and “Long” (left) LDV configurations.	23
Figure 2.7 Photo of “Short” LDV probe.....	24
Figure 2.8 Photo of “MiniLDV” probe (scale in inches).....	24
Figure 2.9 Schematic of “MiniLDV” probe (unit : mm).	25
Figure 2.10 Optical components in the blue transmission unit.....	25
Figure 2.11 Signal processing unit. Dostek board for the wake plane measurement and Labview 3D DAQ with external trigger for the leeside measurement.....	26
Figure 2.12 DOP seeder.	26
Figure 2.13 Rotating turret for large bump#3 leeside measurements.	27
Figure 2.14 Rotating turret with LDV probes.	27
Figure 2.15 Photo of measuring large bump#3 leeside.	28
Figure 3.1 Surface pressure coefficient of the bumps (Byun et al., 2004).....	35
Figure 3.2 Surface pressure gradient of large bump#3.....	37
Figure 3.3 Surface pressure gradient of small bump#3.	38
Figure 3.4 Magnitude of surface pressure gradient of bump#1.	39
Figure 3.5 Vector plot of non-dimensional vorticity flux of large bump#3.....	40
Figure 3.6 Vector plot of non-dimensional vorticity flux of small bump#3.....	41

Figure 3.7 Oilflow visualization results for large bump#3 (Simpson et al., 2002).....	42
Figure 3.8 Oilflow visualization results for small bump#3 (Byun et al., 2004).	43
Figure 3.9 Oilflow visualization results for bump#1 (Byun et al., 2004).	44
Figure 4.1 Comparison of 2-DTBL data with miniLDV, short LDV data and DNS results.	71
Figure 4.2 Effect of velocity gradient broadening.	73
Figure 4.3 $ u_t /U_{ref}$ vs. z/H for 3 different bumps.	74
Figure 4.4 Large bump#3 Mean velocity \bar{U} at wake plane, $x/H=3.63$	75
Figure 4.5 Small bump#3 Mean velocity \bar{U} at wake plane, $x/H=3.26$	76
Figure 4.6 Bump#1 Mean velocity \bar{U} at wake plane, $x/H=3.46$	77
Figure 4.7 Large bump#3 Mean velocity \bar{W} at wake plane, $x/H=3.63$	78
Figure 4.8 Small bump#3 Mean velocity \bar{W} at wake plane, $x/H=3.26$	79
Figure 4.9 Bump#1 Mean velocity \bar{W} at wake plane, $x/H=3.46$	80
Figure 4.10 Mean velocity pattern. \bar{U} contour and \bar{V} , \bar{W} vectors.	81
Figure 4.11 Contour of normalized stream-wise vorticity, $\omega_x H/U_{ref}$	83
Figure 4.12 Contour of normalized helicity density, hH/U_{ref}^2	84
Figure 4.13 Reynolds stress $\overline{u^2}$ at wake planes.	85
Figure 4.14 Reynolds stress $\overline{v^2}$ at wake planes.	87
Figure 4.15 Reynolds stress $\overline{w^2}$ at wake planes.	89
Figure 4.16 Reynolds stress $-\overline{uv}$ at wake planes.	91
Figure 4.17 Reynolds stress $-\overline{vw}$ at wake planes.	93
Figure 4.18 Reynolds stress $-\overline{uw}$ at wake planes.	95
Figure 4.19 Magnitude of Reynolds shear stresses at wake planes.	97

Figure 4.20 Parameter $1/S = \sqrt{(-\overline{uv})^2 + (-\overline{vw})^2} / \overline{v^2}$ at wake planes.....	99
Figure 4.21 Correlation coefficient $R_{uv} = -\overline{uv} / u'v'$ at wake planes.	101
Figure 4.22 Turbulent kinetic energy at wake planes.	103
Figure 4.23 Contours of turbulent kinetic energy and its transport velocity vectors.	105
Figure 4.24 Parameter $AI = \sqrt{(-\overline{uv})^2 + (-\overline{vw})^2} / 2TKE$ at wake planes.	106
Figure 4.25 Flow angle (FA) at wake planes.	108
Figure 4.26 Flow gradient angle (FGA) at wake planes.	110
Figure 4.27 Shear stress angle (SSA) at wake planes.	112
Figure 4.28 Anisotropy constant, N at wake planes.	114
Figure 4.29 Mixing length (L_m) at wake planes.	116
Figure 4.30 Stream-wise eddy viscosity (ν_{Tx}) at wake planes.	118
Figure 4.31 Span-wise eddy viscosity (ν_{Tz}) at wake planes.	120
Figure 4.32 Normalized w spectra of each bump at the centerline.	122
Figure 4.33 Integration of $G_{uu}(\kappa_1)$ at large bump#3 wake plane, $y/H = 0.065$, $z/H = 0$	123
Figure 4.34 Curve fitting of $G_{uu}(\kappa_1)$ at the wake plane centerline of large bump#3.	123
Figure 4.35 Normalized dissipation rate at the centerline of wake plane.	125
Figure 4.36 Normalized macro lengthscales at the centerline of wake plane.	125
Figure 4.37 Illustration of flow structures at measured wake plane for bumps #3.	126
Figure 4.38 Illustration of flow structures at measured wake plane, $x/H = 3.46$ for bump#1.	127
Figure 5.1 Mean symmetric flow around large bump#3 at $r/H=1.112$ and $y_1=4$ mm.	152
Figure 5.2 Normalized $\overline{U}\vec{i} + \overline{V}\vec{j}$ vectors in the center plane.	154
Figure 5.3 $\overline{U_L}$ in local coordinates along the centerline.	155

Figure 5.4 Intermittency of U_L in local coordinates along the centerline.....	156
Figure 5.5 Law of mean backflow $\overline{U_L}$ in local coordinates along the centerline.	157
Figure 5.6 Near wall flow field.	158
Figure 5.7 Normalized $\overline{U_L} + \overline{W_L}$ vectors locally tangent to surface.	159
Figure 5.8 Intermittency of U_L in local coordinates along r/H	160
Figure 5.9 Intermittency of W_L in local coordinates along r/H	161
Figure 5.10 Law of mean backflow $\overline{U_L}$ in local coordinates along $r/H = 1.386$	162
Figure 5.11 Some 3-D streamlines using \overline{U} , \overline{V} and \overline{W} from various $y_{1,0}$ starting points.	163
Figure 5.12 Normalized $\overline{u_L^2}$ in local coordinates.	164
Figure 5.13 Contours of normalized $\overline{u^2}$ in tunnel coordinates.	165
Figure 5.14 Normalized $\overline{v_L^2}$ in local coordinates.....	166
Figure 5.15 Contours of normalized $\overline{v^2}$ in tunnel coordinates.....	167
Figure 5.16 Normalized $\overline{w_L^2}$ in local coordinates.....	168
Figure 5.17 Contours of normalized $\overline{w^2}$ in tunnel coordinates.....	169
Figure 5.18 Normalized $-\overline{uv_L}$ in local coordinates.	170
Figure 5.19 Contours of normalized $-\overline{uv}$ in tunnel coordinates.	171
Figure 5.20 Normalized $-\overline{vw_L}$ in local coordinates.	172
Figure 5.21 Contours of normalized $-\overline{vw}$ in tunnel coordinates.....	173
Figure 5.22 Normalized $-\overline{uw_L}$ in local coordinates.	174
Figure 5.23 Contours of normalized $-\overline{uw}$ in tunnel coordinates.	175

Figure 5.24 The ratio of $-\overline{vw_L}$ to $-\overline{uw_L}$ in local coordinates.....	176
Figure 5.25 The magnitude of Reynolds shear stresses in local coordinates.....	177
Figure 5.26 1/S parameter in local coordinates.....	178
Figure 5.27 R_{uv} in local shear stress coordinates.....	179
Figure 5.28 TKE contour and its normalized transport vectors $V_{qu}\vec{i} + V_{qn}\vec{j}$ in the center plane.....	180
Figure 5.29 TKE contours and its normalized transport vectors $V_{qu}\vec{i}_L + V_{qn}\vec{k}_L$ locally tangent to surface at different y_{L0}^+	181
Figure 5.30 Normalized TKE in local coordinates.....	182
Figure 5.31 Turbulence Intensity contours at different y_{L0}^+	183
Figure 5.32 A1 parameter in local coordinates.....	184
Figure 5.33 B parameter in local coordinates.....	185
Figure 5.34 B2 parameter in local coordinates.....	186
Figure 5.35 FA, FGA and SSA in local coordinates along $r/H = 1.179$	187
Figure 5.36 FA, FGA and SSA in local coordinates along $r/H = 1.386$	188
Figure 5.37 FA, FGA and SSA in local coordinates along $r/H = 1.615$	189
Figure 5.38 Bimodal histograms of U_L and W_L in local coordinates.....	190
Figure 5.39 Joint probability density function of U_L and W_L along the centerline in local coordinates.....	191
Figure 5.40 Joint probability density function of U_L and W_L in local coordinates.....	192
Figure 5.41 Coherency functions at $r/H = 1.386$, $\psi = 30^\circ$, $y_{L0}^+ = 261$	193
Figure 5.42 Least square fit of bimodal PDF.....	194
Figure 5.43 The forward mode at $y_{L0}^+ = 11$	195
Figure 5.44 The backward mode at $y_{L0}^+ = 11$	196
Figure 5.45 The combination of forward and backward modes at $y_{L0}^+ = 11$ for $\gamma_{N,U_L} = 0.8$	197

Figure 5.46 The combination of forward and backward modes at $y_{1,0}^+ = 11$ for $\gamma_{N,U_L} = 0.6$	198
Figure 5.47 The combination of forward and backward modes at $y_{1,0}^+ = 11$ for $\gamma_{N,U_L} = 0.5$	199
Figure 5.48 The combination of forward and backward modes at $y_{1,0}^+ = 11$ for $\gamma_{N,U_L} = 0.4$	200
Figure 5.49 The combination of forward and backward modes at $y_{1,0}^+ = 11$ for $\gamma_{N,U_L} = 0.2$	201
Figure 5.50 Time dependence of bimodal U_L and W_L at $r/H = 1.386$, $\psi = 30^\circ$ and $y_{1,0}^+ = 261$ in local coordinates.....	202
Figure 5.51 Time dependence of bimodal U_{LR} at $r/H = 1.386$, $\psi = 30^\circ$ and $y_{1,0}^+ = 261$ in locally rotated coordinates.....	203
Figure 5.52 Skewness and flatness factor of U_L upstream from separation along the centerline in local coordinates.....	204
Figure 5.53 Skewness and flatness factor of U_L downstream from separation along the centerline in local coordinates.....	205
Figure 5.54 Skewness and flatness factor of U_L along $r/H = 1.386$ in local coordinates.	206
Figure 5.55 Skewness and flatness factor of W_L along $r/H = 1.386$ in local coordinates.	207
Figure 5.56 Illustration of flow structures on leeside of bump.....	208
Figure 6.1 Computational domain for Patel et al. (2003) LES.....	218
Figure 6.2 C_p on bump surface from Patel et al. (2003) LES.....	218
Figure 6.3 Mean streamline patterns at $y^+ = 8.63$ over the bump surface from Patel et al. (2003) LES.....	219
Figure 6.4 Skin friction velocity at $x/H=3.63$ from Patel et al. (2003) LES.....	219
Figure 6.5 \overline{U}^+ at $x/H=3.63$ from Patel et al. (2003) LES.....	220
Figure 6.6 \overline{W}^+ at $x/H=3.63$ from Patel et al. (2003) LES.....	220
Figure 6.7 \overline{uv}^+ at $x/H=3.63$ from Patel et al. (2003) LES.....	221
Figure 6.8 Secondary flow vectors at $x/H=3.63$ from Menon et al. (2004) LES.....	221

Figure 6.9 Two-layer zonal model of Tessicini et al. (2005).....	222
Figure 6.10 Mean velocity vectors across the center plane from Tessicini et al. (2005).....	222
Figure 6.11 Streamline patterns of the closest wall plane from Tessicini et al. (2005).....	222
Figure 6.12 Computational domain for Davidson's Hybrid LES-RANS (2005).....	223
Figure 6.13 U/U_{in} at $x/H=3.63$ from Davidson's Hybrid LES-RANS (2005).....	223
Figure 6.14 W/U_{in} at $x/H=3.63$ from Davidson's Hybrid LES-RANS (2005).....	223
Figure 6.15 Secondary flow vectors at $x/H=3.63$ from Davidson's Hybrid LES-RANS (2005).....	224
Figure 6.16 Vector fields in the center plane from Davidson's Hybrid LES-RANS (2005).....	224
Figure 6.17 The direction of the flow at the wall from Davidson's Hybrid LES-RANS(2005).....	224
Figure 6.18 TKE/U_{in}^2 at $x/H=3.63$ from Davidson's Hybrid LES-RANS (2005).....	225
Figure 6.19 C_p along the centerline from Davidson's Hybrid LES-RANS (2005).....	225
Figure B.1 Contour of normalized $\overline{u^2}$ at wake planes.....	245
Figure B.2 Contour of normalized $\overline{v^2}$ at wake planes.....	246
Figure B.3 Contour of normalized $\overline{w^2}$ at wake planes.....	247
Figure B.4 Contour of normalized \overline{uv} at wake planes.....	248
Figure B.5 Contour of normalized \overline{uw} at wake planes.....	249
Figure B.6 Contour of normalized \overline{vw} at wake planes.....	250
Figure C.1 Curve fitting of $G_{uu}(\kappa_1)$ at the wake plane centerline of large bump#3, $x/H = 3.63$	252
Figure C.2 Curve fitting of $G_{uu}(\kappa_1)$ at the wake plane centerline of small bump#3, $x/H = 3.26$	253
Figure C.3 Curve fitting of $G_{uu}(\kappa_1)$ at the wake plane centerline of bump#1, $x/H = 3.46$	254
Figure D.1 The forward mode at $y_{10}^+ = 41$	256
Figure D.2 The backward mode at $y_{10}^+ = 41$	257
Figure D.3 The combination of forward and backward modes at $y_{10}^+ = 41$ for $\gamma_{N,U_1} = 0.8$	258

Figure D.4 The combination of forward and backward modes at $y_{1,0}^+ = 41$ for $\gamma_{N,U_l} = 0.6$	259
Figure D.5 The combination of forward and backward modes at $y_{1,0}^+ = 41$ for $\gamma_{N,U_l} = 0.5$	260
Figure D.6 The combination of forward and backward modes at $y_{1,0}^+ = 41$ for $\gamma_{N,U_l} = 0.4$	261
Figure D.7 The combination of forward and backward modes at $y_{1,0}^+ = 41$ for $\gamma_{N,U_l} = 0.2$	262
Figure D.8 The forward mode at $y_{1,0}^+ = 69$	263
Figure D.9 The backward mode at $y_{1,0}^+ = 69$	264
Figure D.10 The combination of forward and backward modes at $y_{1,0}^+ = 69$ for $\gamma_{N,U_l} = 0.8$	265
Figure D.11 The combination of forward and backward modes at $y_{1,0}^+ = 69$ for $\gamma_{N,U_l} = 0.6$	266
Figure D.12 The combination of forward and backward modes at $y_{1,0}^+ = 69$ for $\gamma_{N,U_l} = 0.5$	267
Figure D.13 The combination of forward and backward modes at $y_{1,0}^+ = 69$ for $\gamma_{N,U_l} = 0.4$	268
Figure D.14 The combination of forward and backward modes at $y_{1,0}^+ = 69$ for $\gamma_{N,U_l} = 0.2$	269

List of Tables

Table 4.1 Dissipation rates and macro lengthscales of each bump at the wake plane centerline, $z/H = 0$	124
Table 5.1 Locations of measurements.	151
Table 6.1 Simulation methods.	216
Table A.1 Uncertainties of 2-DTBL MiniLDV measurement in 20:1 odds.	242
Table A.2 Uncertainties of wake plane Short and Long LDV measurements in 20:1 odds.	242
Table A.3 Uncertainties of large bump#3 leeward MiniLDV measurements in 20:1 odds.	243

1

Introduction

1.1 Research Motivation

Current Computational Fluid Dynamics (CFD) programs can not accurately compute flow over complex geometries due to the difficulty of modeling non-equilibrium effects on Reynolds stresses that affect the mean flow field results. The turbulence closure problem at the current stage still requires experimental data for the development of advanced equations for defining the relations between the fluctuating and mean velocity fields. Measurements of the mean flow field and the fluctuating velocity correlations, including the Reynolds' stresses and the higher order terms, are required for each flow field separately. In addition, the turbulent flow separation from a three-dimensional (3-D) body is still not understood completely due to its complexity, even though it is quite a common phenomenon and plays an important role in practical cases. Most of previous investigations on 3-D flow separation depend on the surface topological analysis and the critical point – saddle, node and focus – theory which are based on flow visualization (Delery, 1992; Hunt et al., 1978; Tobak and Peake, 1982). However, they can only describe the flow structures qualitatively, not quantitatively. Thus, the computational analysis of this kind of flow field is difficult to be modeled and verified properly without detailed quantitative data.

In recent years, CFD researchers have extended their challenges to wall-bounded turbulent flow fields (Fureby et al., 2004). Although CFD results are qualitatively consistent with experimental data for wall-bounded turbulent flows with and without surface mounted obstacles, a more proper simulation model is necessary for complex 3-D high Reynolds number flows. Direct

Numerical Simulation (DNS) is still too expensive to apply to practical flows of interest. Although Large-Eddy Simulation (LES) seems to be better than the Reynolds-averaged Navier-Stokes (RANS) equations in flows where unsteady and large eddies are dominant, LES is also very expensive to resolve the small eddies properly near the wall. Thus, the research presented here provides detailed quantitative data for 3-D separated turbulent boundary layer (TBL) flows which are good test cases to develop better computational models for this type of flow field.

Since Hunt and Snyder (1980) have reported their experiments on flows over a 3-D hill in 1980, some studies have been performed for the flows over 2-D and 3-D hills to determine the mean velocity field and the turbulence information. However, most research motivation came from applications for environmental, atmospheric and geophysical fluid mechanics and turbulence until Webster et al. (1996) published turbulence characteristics of a boundary layer over a swept bump in 1996. Therefore, the primary objectives of the current research program are to measure and understand the formation and structure of vortical 3-D turbulent separations of a turbulent boundary layer over symmetric hills or bumps, which create strong stream-wise vortices that energize the downstream boundary layer. Of particular interest are data that describe the turbulent diffusion processes that control the momentum transfer rates that affect the vortical separation. Another objective is to provide test cases for researchers to use for comparison and to assist in modifying current turbulence models that are used to calculate such flows. For a very detailed investigation, symmetric hills were selected which have multiple separations over a large area of the leeside. Such flows are more demanding of turbulence models than attached or massively separated flow cases. Three bumps, two axisymmetric bumps of height $H = \delta$ and 2δ and one symmetric bump of height $H = 2\delta$ were considered for the present study, where δ is the boundary layer thickness.

The present work examined the flow separation pattern on each bump surface qualitatively using oilflow visualizations and surface pressure measurements. Then, the specific wake planes were measured by a 3-velocity-component fine-spatial-resolution Laser-Doppler Velocimeter (LDV). These measurements allow one to explain the structure of separated flow from bumps. However, oilflow visualizations and surface pressure distributions were not enough to understand how the turbulent flow separates and what the flow structure is around the separation regions on bump surfaces. Therefore, the flow over the bigger axisymmetric bump was finally measured using a LDV located within the bump, from the very near surface where the separations originate, mainly on the leeside of the bump.

The final goal of this dissertation is to describe the turbulent flow behavior and associated fundamental physical processes over 3-D bumps quantitatively as well as qualitatively.

1.2 Literature Review

Hunt and Snyder (1980) described the flow structure over a bell-shaped 3-D hill. The hill height was 22.9 cm and the maximum slope was about 45° . Shear stresses patterns were observed by the surface oilflow visualization. A hydrogen bubble wire technique was used to study the streamline patterns. Mean velocities and turbulence intensity were measured by hot-wire anemometers with 0.5 ~ 10 m/s free-stream velocity ranges. They reported that the flow separated on the leeside of the hill, generating a dominant horizontal recirculating flow with some vertical mixing.

Castro and Snyder (1982) performed a wind tunnel study for the nature of the separated flow fields downstream of moderately steep hills with and without surface roughness. The hills changed from an axisymmetric cone to a 2-D ridge with a constant hill height, $H = 245$ mm and 26.6° slope. The ratio of H/δ was about 0.3. All velocity and turbulence measurements were made with a pulsed-wire anemometer at a nominal free-stream velocity of 4 m/s. For the axisymmetric cone, flow separation was delayed and reversed flow region was much smaller on smooth surfaces than rough surfaces. They also concluded that the stream-wise vortices made a important role to produce downwash in the wake.

Pearse (1982) measured the flow over three conical hills of different ratios of the hill height to the base radius, 0.15, 0.25 and 0.5. A hot-wire anemometer was used to measure the stream-wise mean velocity and fluctuations along the centerline downstream of each cone at $H/\delta \approx 0.06$. The greatest increase in the mean velocity over the hills occurred at the crest of the steepest hill and the velocity fluctuations changed little over the hills.

Arya and Gadiyaram (1986) presented the effect of 3-D conical hills on the mean flow and turbulence structure. They considered two conical hills having slopes of 26.5° and 17.5° and a base radius of 470 mm. Velocity and its fluctuation were measured by a hot-wire anemometer at a free-stream velocity of 4 m/s and $H/\delta \approx 0.25$. They showed the existence of a separated recirculating flow region on the leeside of the hill and the vortex shedding from its sides for the steeper hill. They found that for both hills, the Reynolds stresses in the far wake, farther than $4H$, decreased

approximately in proportion to the stream-wise distance, $x^{-1.6}$, from the crest of the hill. They concluded that the slope and the aspect ratio of hills may be principal keys for characterizing the flow features behind a hill.

Gong and Ibbetson (1989) reported their wind tunnel measurements for mean flow and turbulence over a 2-D ridge and a 3-D circular hill. Both had a cosine-squared cross-section and about 15° maximum slope. All flow measurements were made using a hot-wire anemometer at a nominal free-stream velocity of 8 m/s and $H/\delta \approx 0.1$. They suggested that the mean flow and turbulence over the 3-D circular hill is generally similar to those over the 2-D ridge except for the wakes of the two hills. For the circular hill, there were converging motions toward the center and associated descending motions off the center. They also suggested that surface curvature effects should be considered in the flow over curved hills for a satisfactory prediction. Although they tried to describe the nature of fluid flow around hills, there was still a lack of information concerning the origin of separation and quantitative descriptions of turbulent structures and their behaviors.

Since the middle of the 1980s, there has been considerable effort studying the flow around surface mounted bodies in turbulent boundary layers. More attention was given to flow 3-dimensionality and the wake region with stream-wise vortices behind curved obstacles instead of rectangular bodies. There has been more emphasis to understand the structure of wall bounded 2-D/3-D turbulent boundary layer separations and on providing detailed quantitative information for the flow behaviors over protuberances with a development of measurement techniques. These valuable efforts were summarized in the following three articles.

Simpson (1989) defined the process of mean 2-D turbulent boundary layer separations quantitatively. He defined the set of quantitative definitions on the detachment state near the wall based on the fraction of time that the flow moves downstream, γ_{pU} such as *incipient detachment* ($\gamma_{pU} = 0.99$), *intermittent transitory detachment* ($\gamma_{pU} = 0.8$), *transitory detachment* ($\gamma_{pU} = 0.5$) and *detachment*. The last two states occur at the same location. He also mentioned that the large scale structure from separations generated larger turbulent stresses in the middle of the separated shear layer. The pressure fluctuations related to these large scale structures are relatively large and affect the mean backflow zone. He suggested that the interaction between the pressure and velocity fluctuations would be high because the backflow near the wall is re-entrained into the outer region and need to investigate this interaction.

Eaton (1995) reviewed experimental studies from his research group regarding 3-D turbulent boundary layers with the effects of 3-dimensionality. He mentioned the reduction of the magnitude of Reynolds shear stresses from a 2-DTBL as a general feature in attached 3-DTBLs. He emphasized the distortion or skewing of flow structures across the near wall region by the pressure gradient from an equilibrium 2-DTBL as this reduction, even though attached 3-DTBLs have been dominated by low and high speed streaks and quasistream-wise vortices near the wall which are similar to 2-DTBLs.

Simpson (1996) reviewed and summarized experimental research for separating 3-D turbulent flows. For the wing/body junction flow, 'closed' vortical separations occur with singular points of separation on the surface. This type of separation produces high turbulent intensities with local backflows and highly unsteady multimodal horseshoe vortex structure near the nose. For the flow around a body of revolution at incidence, 'open' or crossflow 3-D separations occur without any singular points on the surface and reversal flows. This type of separation occurs due to the crossflow pressure gradients in different regions. The converging flow by these adverse pressure gradients makes the adjacent flow more skewed and the low velocity fluid near the wall accumulated on the surface. The crossflow separations also produce stream-wise vortices which are related to reattachments and secondary separations.

Savory and Toy (1986a, 1986b and 1988) presented the wind tunnel studies of the near wake region behind a hemisphere in a turbulent boundary layer. The hemisphere diameter, D was 190 mm and the Reynolds number based on the diameter and free-stream velocity was about 1.4×10^5 . They described qualitatively the generation and development of the vortex structures around the hemisphere and the periodic formation and shedding of the vortex loops by flow visualization techniques. Using a pulsed-wire anemometer, they measured the reattachment length of about $1.2D$ along the center line and a pair of counter-rotating vortices in the wake planes. They also showed that the maximum positions of stream-wise turbulence intensity were related to the locations of the maximum velocity gradient.

Larousse et al. (1991) and Martinuzzi et al. (1993) studied the flow around a surface-mounted cube in turbulent channel flow. The Reynolds number based on the channel height was about $8 \times 10^4 \sim 10^5$. The results of flow visualizations, surface pressure distributions and laser-Doppler anemometer measurements were examined to determine separation and reattachment patterns and to investigate the flow differences between 2-D and 3-D geometries. They reported a highly unsteady

upstream flow field for a 3-D obstacle having bimodal velocity probability which generated high Reynolds shearing stresses. They also showed that the largest turbulent kinetic energy production rates occurred at the area of maximum vorticity in the shear layer.

Webster et al. (1996) presented experimental results from a turbulent boundary layer flow over a 45° swept bump. The boundary layer thickness, δ , to bump height, H , was 1.5 and the momentum thickness Reynolds number was about 3800 at a nominal velocity of 17.7 m/s. The turbulent boundary layer was affected by stream-wise pressure gradient, wall curvature and mean cross-flow so that the mean velocity was significantly different from a semi-logarithmic law. They showed great changes of the Reynolds stresses above and downstream of the bump. The Townsend structure parameter, $A1 = \sqrt{(-\overline{uv})^2 + (-\overline{vw})^2} / (\overline{u^2} + \overline{v^2} + \overline{w^2})$ showed a significant decrease compared to the typical value for a 2-D boundary layer.

Ishihara et al. (1999) examined the flow in the center plane of an axisymmetric hill that had a cosine-squared cross section and a maximum slope of 32°. The approaching boundary layer thickness δ to hill height H ratio was 9 and the Reynolds number $U_H H / \nu = 1.1 \times 10^4$, where U_H is the velocity at the hill height H for the undisturbed boundary layer. Although little was presented about the flow away from the center plane, it is clear that the flow accelerated over the top and around the sides of the hill. A leeside separation and a reattachment at the foot of the hill occurred with low frequency motions, $0.065 < fH/U_H < 0.13$, in the downstream wall layer at $x/H = 3.75$.

Willits and Boger (1999) conducted a comparative study between measured and calculated flows behind an axisymmetric bump which has the same shape as the bigger axisymmetric bump in the present study. A five-hole pitot probe and the unsteady Reynolds-averaged Navier-Stokes (URANS) equations with a $q-\omega$ model were used for the experiments and computations, respectively. Computational results of several wake planes for $\delta/H = 0.5$ were compared to measured data. There was poor agreement showing two pairs of counter-rotating stream-wise vortices in the calculations in spite of only one pair in the measurements.

After Willits and Boger (1999) reported unsatisfactory calculations from their turbulence model, several CFD research groups have tested their model on an identical larger axisymmetric bump as in the present research program as a test case to improve their turbulence models. Patel et al. (2003) and Menon et al. (2004) studied the axisymmetric bump using LES. They showed multiple separations and reattachments on the leeside of the bump. Wang et al. (2004) calculated separated flow from this bump using RANS equations with different Non-Linear Eddy-Viscosity

(NLEV) models. Temmerman et al. (2004) performed a comparative study of separation from this bump using LES and RANS. His computation, however, was conducted at half of the Reynolds number of the present study. Davidson and Dahlström (2005) have reported their hybrid LES-URANS calculations for the flow around this bump. They used the unsteady RANS near the wall and switched to LES at a specific height from the wall. They obtained relatively better agreement with experiments in the wake plane at $x/H \approx 3.6$ than the other CFD results above. Detailed comparisons are discussed later in Chapter 6.

Recently, extensive studies regarding the flow over bumps or hills in turbulent boundary layers have been performed at Virginia Polytechnic Institute and State University (Long, 2005; Pisterman, 2004 and Ma and Simpson, 2005). Long (2005) performed oilflow visualizations and surface pressure measurements for symmetric bumps. She analyzed the flow topology based on oilflow patterns on the surface of each bump and presented 'closed' 3-D separation patterns with multiple singular points of separation. She also showed the vorticity flux generated by the surface pressure gradient. She conducted LDV measurements in the wake plane inner region of the bigger axisymmetric bump, $H = 2\delta$. She captured only one-pair of counter-rotating mean stream-wise vortices in the wake plane.

Pisterman (2004) measured three-component mean velocities around the symmetric bumps using a 7-hole pressure probe and verified the possibility of use of a multi-hole pressure probe for a highly turbulent flow field. He also presented a pair of counter-rotating stream-wise vortices creating large amounts of high momentum fluid entrained toward the wall in the wake plane of each bump and compared with LDV data (Byun et al., 2004 and Long, 2005) and hot-wire probe data (Ma and Simpson, 2005). He observed the effects of the velocity gradient on the uncertainties in 7-hole probe measurements and proposed a model to explain and correct these effects. He measured the side walls and ceiling boundary layer profiles at $x/H = -3.81$ and the stream-wise free-stream velocity distribution for $x/H = -1.5 \sim 2.0$ with the presence of the axisymmetric bump, which is interested for CFD researchers. He reported a δ_{ceiling} of 32.8 mm thick and a $\delta_{\text{side wall}}$ of about 34 mm thick.

Ma and Simpson (2005) presented the downstream wake development of the symmetric bump, $H = 2\delta$, which is considered in the present study using a four-sensor hot-wire probe. They measured the flow field at $x/H = 2.62, 3.63$ and 6.59 behind the bump. They reported the similar mean vortical flow patterns at the wake planes to what Long (2005) and Pisterman (2004) measured.

The most interesting result about the flow structure at the wake planes is the contribution and distribution of low frequency ($f < 34$ Hz) fluctuations. They showed the existence of large scale and low frequency turbulent structures in the stream-wise and span-wise directions behind the bump.

1.3 Outline of Dissertation

All facilities utilized for the present measurements are described in Chapter 2. In Chapter 3, the results are discussed including the oilflow visualization, surface pressure measurements and vorticity flux on the bump surface. The wake plane Laser-Doppler velocimeter (LDV) results at $x/H \leq 3.63$ for each bump are discussed in Chapter 4. The LDV results for the flow structure over the larger axisymmetric bump are also discussed in Chapter 5. Then, further discussion and concluding remarks are finally presented in Chapter 6.

It should be noted that to accomplish the primary objective of this dissertation, some results refer to Long (2002) for oilflow visualizations and surface pressure distributions and to Ma and Simpson (2005) for the hot-wire probe measurements at the wake planes.

2

Apparatus and Instrumentation

Apparatus and instrumentation are described in this chapter including the nominal flow conditions, the shapes of three different bumps considered for the present work and the optical system for LDV measurements. Three different LDV probes that are used for the measurements of the flow field around the bumps are described.

2.1 Boundary Layer Wind Tunnel

The measurements were conducted in the Virginia Polytechnic Inst. and State Univ., Dept. of Aerospace and Ocean Engineering Low Speed Boundary Layer Tunnel, which has been used in a number of experimental studies. The wind tunnel is an open-circuit type and is powered by a 19 kW centrifugal blower. Air from the blower is supplied to a test section after first passing through a fixed setting damper, a plenum, a section of honeycomb to remove the mean swirl of the flow, seven screens to remove much of the turbulence intensity, and a 4:1 contraction to further reduce turbulence levels and accelerate the flow to test speed. The potential core of the flow entering the test section is uniform to within 0.5 % in the span-wise direction and 1 % in the vertical direction and has a turbulence intensity of 0.1 % at 27.5 m/s (Ma and Simpson, 2005).

The test section is 0.91 m wide and 7.62 m long and has a rectangular cross-section. Flow entering the test section is subjected to a further 1.5:1 contraction produced by the shape of the upper wall. A throat is reached 1.41 m downstream of the entrance where the test section is 0.25 m high. Downstream of the throat the upper wall is expanded by about 1° slope for about 0.94 m long

with 6.35 mm thick sidewall inserts. At the entrance of the test section, the flow is tripped by the 0.63 cm high blunt leading edge of the tunnel floor to make the turbulent boundary layer. Figure 2.1 shows the schematic of the side view of the wind tunnel test section for the bump measurements and the locations of the bumps.

A detailed study of the characteristics of the zero- and favorable-pressure-gradient mean two-dimensional boundary layer in this tunnel can be found in Ahn (1986). Under the nominal conditions with a speed of 27.5 m/s and a temperature of 25 ± 1.0 °C, the approaching boundary layer thickness, δ , is 39 mm and the Reynolds number based on the momentum thickness, Re_θ , is about 7300 at 2.9 m downstream of the test section entrance, which are the same conditions reported by George and Simpson (2000).

2.2 The Bumps

Experiments were conducted on three different bumps. These three bumps were referred to as large bump#3, small bump#3 and bump#1, respectively. The first two bumps are axisymmetric about the y-axis. Bump#1 is not axisymmetric, but symmetric with respect to both the x-y and y-z planes. The geometries of the bumps are described below.

2.2.1 Bump#3 (Large and Small)

The large bump#3 and the small bump#3 are of the same shape as Bump#3 in the ARL report (Willits and Bogar, 1999), which is defined by the formula,

$$\frac{y(r)}{H} = -\frac{1}{6.04844} \left[J_0(\Lambda) I_0 \left(\Lambda \frac{r}{a} \right) - I_0(\Lambda) J_0 \left(\Lambda \frac{r}{a} \right) \right] \quad (2.1)$$

where $\Lambda = 3.1962$, H is the height of the bump. The “a” is the radius of the circular base of the bump, $a = 2H$, J_0 is the Bessel function of the first kind, and I_0 is the modified Bessel function of the first kind.

For the large bump#3, the height H is 78 mm with $\delta/H = 1/2$, and the base radius, “a” is $2H$. For the small bump#3, the height H is 39 mm with $\delta/H = 1$, and the radius of the base, “a” is $2H$ as well.

There are two large bump#3 models. One is for the surface pressure measurements, the oil flow visualization and the wake plane LDV measurements. The other one is for the LDV measurements around the bump. Since LDV probes are mounted inside large bump#3 for these measurements, the 17.78 mm wide and 0.254 mm thick anti-reflection coated transparent Lexan window through which laser beams pass is mounted on the center plane of the bump between $x/H = -0.65$ and $x/H = 1.8$. This window was formed with the curvatures of the bump (Fig. 2.15).

2.2.2 Bump#1

Bump#1 is defined in the same way as in the ARL report (Willits and Bogar, 1999) by the formula,

$$\frac{y(x, z)}{H} = \frac{1}{1.1329^2} \left[\cos\left(4.73 \frac{x}{a}\right) + 0.1329 \cosh\left(4.73 \frac{x}{a}\right) \right] \times \left[\cos\left(4.73 \frac{z}{b}\right) + 0.1329 \cosh\left(4.73 \frac{z}{b}\right) \right] \quad (2.2)$$

The height, H , of bump#1 is 78 mm with $\delta/H = 1/2$. The bump#1 is not like the bump#3's, it has a rectangular base of length “a”, which is $4H$ and width “b”, which is $2H$. Figures 2.2 and 2.3 show the stream-wise shape and the 3D shape of the bump#3's and bump#1 non-dimensionalized by bump height, H , respectively.

2.3 The Coordinate Systems

Figure 2.4 shows the two right-handed, three-dimensional, Cartesian coordinate systems used for all testing and analysis. In the tunnel coordinates (x, y, z), the x -axis is parallel to the centerline of the tunnel and pointing downstream. The y -axis is normal to the tunnel floor pointing upward. The origin is fixed at the center of the bump, with $y = 0$ corresponding to the tunnel floor. In the local

coordinates (x_L, y_L, z_L) for the axisymmetric bumps, the x_L -axis is in the radial direction away from the axis of symmetry and tangent to the local surface. The y_L -axis is normal to the local surface, with $y_L = 0$ corresponding to the local bump surface. Hence, it is necessary to transform coordinates from the right-handed local coordinate (x_L, y_L, z_L) to the right-handed tunnel coordinate (x, y, z) with the pitch angle, θ and the yaw angle, ψ .

2.4 Laser Doppler Velocimeter (LDV) System

2.4.1 Optical table equipment

The optical table equipment consists of lasers, polarization rotators, mirrors, polarization beam splitter cubes, Bragg cells and laser to fiber couplers (Fig. 2.5). In the present study two lasers were used. Two beams (blue, 488 nm and green, 514.5 nm) from two lasers (1.4 W INNOVA 90-5 for green and 0.4 W INNOVA 90-6 for blue with etalons) are used to generate the 5 beams, 2 blue and 3 green, to produce three probe volumes.

Polarized laser beams emerging from the lasers pass through a polarization rotator. The green beam is further divided into two beams with a polarization-beam-splitter cube and polarization rotator couple forming a variable intensity beam splitting unit. The two green beams and one blue beam pass through Bragg cells (Acousto-optic modulator, AOM-405, IntraAction Corp.), which divide each of the beams into two beams individually and also frequency shift one of each of the two individual beams. Frequency shifting is required to distinguish the direction of the velocity vector. Frequency shifts for the green beams are 0, +50 and -30 MHz and for the blue beams are 0 and +40 MHz. In this fashion five beams are generated to form three probe volumes. The five beams, with about 170 mW for each blue beam and about 220 mW for each green beam, are input to optical fibers using laser-to-fiber couplers. The use of optical fibers permits access to cramped locations without moving the heavy equipment such as the laser or the optical table. This optical system is a sub-system of the five-velocity-component fiber optic LDV system of Ölçmen and Simpson (1995a).

2.4.2 Probe head

Three different LDV probes, “Short LDV”, “Long LDV” and “MiniLDV”, were used for measurements. For the wake plane measurements, the short and the long LDV probes were used in the near wall region and the outer layer, respectively. For the measurements around the large bump#3, the miniLDV and the long LDV probes were used in the near wall region and the outer layer, respectively.

2.4.2.1 Short and Long LDV probe

Two configurations of a three-velocity-component fiber-optic LDV system were used to obtain coincident instantaneous U, V and W components of the velocity through the transparent glass test wall. In the nearer wall region the short LDV configuration (Fig. 2.6), which is well described by Ölçmen and Simpson (1995a) including velocity measurement uncertainties, can make measurements within 40 mm from the surface. The measurement volume can traverse as close as 50 μm to the wall. The effective measurement volume of approximately 30 μm in diameter permits precise near-wall (about $y^+ = 3$) measurements. The transmitting optics consist of two 88.3 mm focal length plano-convex lenses to form three overlapping measurement volumes and five 6 mm focal length plano-convex lenses to collimate each beam. The intersection of each pair of beams is about 60 μm in diameter and 690 μm in length. The fringe spacing is about 4.9 μm in each measurement volume. The receiving optics consist of two 120 mm focal length achromatic lenses. One lens is used as a collimator and the other lens is used to focus the beam on the receiving fiber with a 50 μm core diameter.

For the outer layer the long LDV configuration (Fig. 2.6), which is well described by Ölçmen et al.(2001) including velocity measurement uncertainties, can make measurements within 160 mm from the surface with a reduced spatial resolution of 88 μm , which is of no consequence for outer layer spatial resolution. The transmitting optics consist of two 200 mm focal length plano-convex lenses to form three overlapping measurement volumes and five 6 mm focal length plano-convex lenses to collimate each beam. The intersection of each pair of beams is about 175 μm in diameter and 7.68 mm in length. The fringe spacing is about 11.1 μm in each measurement volume. The receiving optics consist of two achromatic lenses with 175 mm and 60 mm focal lengths. The 1:1 magnification ratio of the short LDV probe is reduced to 2.92:1. The same 50 μm diameter receiving fiber is used.

Without major changes to the whole system, these two probe configurations can be switched by changing transmitting lenses and receiving lenses and by inserting a 17° wedge block between the transmitting optics head and its translator. For the long LDV probe, the measured velocity components are not orthogonal to each other, unlike the short LDV probe. Figure 2.7 show a photo of the short LDV probe under the tunnel floor for the wake plane measurements.

2.4.2.2 MiniLDV Probe

In order to measure the flow field near the bump surface with a fine-spatial-resolution, the measurement probe volume has to be located very close above the bump surface. However, the usual LDV probes like the short and the long LDV probes can have limited value for measurements of flow over some complex geometries because of a relatively large probe size and difficulties locating the measurement volume where the measurement is required.

To solve these limits, several research groups have installed LDV probes inside models. Chesnakas and Simpson (1994) developed a novel 3-D fiber-optic LDV and measured three simultaneous velocity components over a 6:1 prolate spheroid from within the model. Berton et al. (2001) embedded their LDV probe into an oscillating wing for investigating unsteady flows near moving surfaces. Mouaze and Belorgey (2001) also located their LDV probe inside a cylinder, which consists of an aluminium tube with an external diameter of 0.21 m and length 2.2 m, to measure the boundary layer near the surface of the cylinder. Czarske (2001) used one laser beam and split it into two beams using a diffraction grating to minimize the size of his probe. However, the latter probes only allowed one- or two-component measurements. Therefore, a new much smaller sub-miniature, fiber-optic, high-resolution laser-Doppler velocimeter was developed for time-dependent, simultaneous three-velocity-component measurements near the bump surface.

Figure 2.8 shows a picture of the probe mounted on a traverse. The overall size of the probe head is $23.3 \text{ mm} \times 8.7 \text{ mm} \times 90.6 \text{ mm}$, which is about the width and half the height of a credit card. The calculated spherical measurement probe volume diameter is about $80 \text{ }\mu\text{m}$ and can be traversed 32 mm vertically. The probe has no moving parts. The lightweight, compact, low-profile design of the LDV probe head allows the probe head to be embedded inside vibrating models and machinery. The device can be used in either steady or unsteady and separated or attached flow regimes.

The probe head houses both the transmitting and the receiving optical units. Transmitting optics are used in forming the three overlapping probe volumes and the receiving optics are used in collecting the scattered light from the probe volumes. Three overlapping probe volumes constitute the measurement probe volume.

The probe head unit houses transmitting fiber terminators, collimator assemblies, 90° prisms, lenses, mirrors and the receiving fiber terminator. Figure 2.9 shows the schematic diagram of the miniature LDV. The five beams generated by the on-table optics are transferred to the probe head by polarization-preserving optical fibers. The three green and two blue beams emerging from the fibers pass through separate lenses for collimation. Next, all the collimated beams are reflected off 90° prisms used as mirrors and then are passed through lenses that focus them to the measurement volume. To align each blue and green beam, the collimator assemblies (Fig. 2.10) have small screws to adjust each beam terminator so that each blue and green beam can be crossed and 1 blue and 2 green probe volumes can be generated. After aligning each pair of beams, the three probe volumes can be crossed together using transmission unit adjustments (Fig. 2.9).

Each probe volume is formed by interference of 2 beams and the probe volumes are ellipsoidal in shape. Using standard optical calculations, the blue probe volume has an 80 μm diameter, 1.58 mm length and 4.8 μm fringe spacing. The Rayleigh length over which the beam radius spreads by a factor of $\sqrt{2}$ is about 10.3 mm. The two green probe volumes have 80 μm diameters, 1.81 mm lengths and 5.8 μm fringe spacing in each of them. The Rayleigh length is about 9.8 mm. However, the common overlapping region of the three probe volumes is almost spherical in shape. The probe volumes have about 80 mW and 105 mW powers for the blue and the green, respectively. Power losses are caused by optical components and are mainly at the laser-to-fiber couplers with about a 50 % loss.

The receiving optics are also housed in the probe head. The light scattered by the particles passing through the measurement probe volume is collected by a single achromatic lens and is focused to the receiving optical fiber. A multi-mode, 50 μm core-diameter receiving fiber is used to transfer the collected light to the data acquisition unit. With a 1:1 magnification ratio, the receiving optics views only a portion of the measurement probe volume where the light intensity is more uniform.

2.4.3 Data acquisition and reduction

The data acquisition and reduction unit consists of several optical filters, photo-multipliers (PM), electronic filters, amplifiers, radio frequency generators, and a 3D LDV signal processor (Fig. 2.11). This data acquisition and reduction system has been employed in many previous works since Ölçmen and Simpson (1995b).

The light collected from the measurement probe volume first passes through a dichroic filter where the collected light is color separated into blue and green wavelengths. It has about an 85 % transmission coefficient for each wavelength. Next each beam passes through separate narrow-band-pass optical filters for greater color separation.

The frequency information from the measurement probe volume is converted to electrical signals using the photo-multiplier tubes. For blue lights, a 30 mm diameter 9125B with bialkali photocathode photo-multiplier from Electron Tubes Inc. was used while a 9124B with enhanced green sensitive bialkali photocathode photo-multiplier was used for green lights. The electrical signal from the blue wavelength is amplified through an Mini-Circuits® ZFL-500 amplifier and is fed to a mixer (ZAD-6, Mini-Circuits®) in order to subtract the high frequency that was added by the Bragg cell shift to the laser beams by the on-table optical equipment. Downshifting is required to reduce the frequency range of the signal to match to that of the LDV signal processor. For this purpose a radio frequency (RF) generator (model 72-585, Tenma®) is used. The downshifted signal after a low-pass filter is fed to the LDV signal processor. The electrical signal from the green wavelength is amplified through a TSI® 10904 power amplifier. It contains the frequency information from the two probe volumes of the measurement probe volume. The signal is passed through an amplifier (ZFL-500, Mini-Circuits®) to obtain signals in the input voltage range of the LDV signal processor and is next passed through a power splitter (ZSC-2-1, Mini-Circuits®) where two electrical signals of equal power are obtained. The amplified signals pass through mixers to downmix the frequency information to the input frequency range of the LDV signal processor. The downshifted signals are next passed through low-pass filters to remove the signals from the high frequency noise content. Although the signals from the splitter consist of two green signals, one is around 50 MHz and the other is around 30 MHz, which are the Bragg cell shift frequencies. Subtracting these signals from each RF generator's signal and low pass filtering leaves only the signal coming from 50 MHz shifted probe volume or 30 MHz shifted probe volume in the bandwidth of the LDV signal processor. The three conditioned signals are fed to the LDV signal

processor to measure each frequency related to one component of the velocity of a particle passing through the probe volume. In order to obtain the velocity of the particle, the three signals need to be acquired within a time coincidence window ($10\ \mu\text{s}$).

For the wake plane measurements, the electrical signals that contain the frequency information coming from the PM tubes are processed by three Macrodyne frequency domain processors, FDP-3100. Due to the lack of the memory storage in the FDP-3100s, a 386 PC with a Dostek computer board is used for data acquisition and storage. On the other hand, for the miniLDV measurements around the large bump#3, the frequency data are obtained using a National Instrument/LabView personal computer (PC) based 3D LDV signal processor which is developed by Todd Lowe* because the FDP-3100's do not have a proper frequency bandwidth for this measurement. Two National Instruments model NI 5112 PCI 8-bit digitizers were chosen to meet the sampling requirements. Each of these boards can sample two channels at rates up to 100 MS/s. To maximize the data processing capacity of the PC, a 2 GHz Pentium-4 processor was chosen. The bus speed for this computer was 400 MHz. The software to control the data acquisition was written in LabView. This program was written to function in a very similar manner to a Macrodyne FDP3100. To acquire the Doppler bursts for each channel, the external trigger from a Macrodyne FDP3100 was used with a $10\ \mu\text{s}$ time window. For these measurements there were no other trigger sources available. However, new hardwired external trigger circuits have been constructed to be completely independent of FDP3100s. An energy validation scheme is implemented to further ensure the quality of the data and a FFT is performed by a built-in function in LabView to determine both the power of the dominant spectral peak and the center frequency of that peak for each spectrum.

The acquired Doppler frequencies were converted into velocities in the optical axes coordinate system which is defined by three vectors perpendicular to the bisector vector of each pair of beams. Also the absolute arrival time for each velocity value was recorded. The histograms of these velocities were obtained. The extreme edges of the histograms are formed by outlier points, apparently due to noise, with a level that does not vary much with velocity. Similar to the work of Ölçmen and Simpson (1995b), a parabola was fit to each side of the logarithm of the histogram ordinate in the range between 1 % and 80 % of the peak value. The data outside of the intersection

* I gratefully appreciate his help for using 3-DPCLDVDAQ.

of the parabolas with the ordinate value of the outlier points were discarded. This clean velocity information was transformed into either the tunnel coordinates for the wake plane measurements or the local coordinates for the measurements around the bump. The velocity data in these coordinates were once more cleaned using the same procedure above. The time dependent clean velocity data in these coordinates were then used to calculate the flow variables.

The data validation percentage from the LDV signal processor was at least 95 % and mostly above 98 %, which resulted in minimally noisy data. One block of 30000 samples (15000 samples for the measurements around bump) over several minutes was taken for each measurement point. The coincident sample rate varied from 40 samples/s very near the wall to 200 ~ 300 samples/s away from the wall. Since there was no correlation between the data rate fluctuation and the velocity magnitude fluctuation, no velocity bias correction was applied. Finite transit-time and instrument broadening of the signals were also negligible.

The diffraction of the light is inevitable in all optical systems. However, every optical component for this probe was chosen to not be operated below the diffraction-limited performance. Furthermore, three Doppler frequencies were captured from a portion of the overlapped measurement volumes using 10 μ s coincident triggering windows. So, the effect of the diffraction could be ignored. To avoid the signal cross-talk, the three frequency shifts from the Bragg cells were not set too close to each other, especially those for green beams. The fringe spacing and the calibration constant between velocities and Doppler frequencies, were measured within 0.03 % uncertainty by beam angles of five beams and simple trigonometry functions after probe alignments were finished.

2.4.4 Seeding system

The aerosol seeding system used dioctyl phthalate (DOP) with a measured mean particle size of about 1 μ m. The smoke generator was originally designed by Echols and Young (1963). The smoke is injected into the flow through either a row of tubes at the entrance of the test section floor or a tube at the air intake of the wind tunnel. Fig. 2.12 shows the seeding system.

2.5 Rotating turret for the measurements around large bump#3

The rotating turret was designed and manufactured for the LB3. To measure the flow around the LB3, the LDV probe is mounted inside and under the bump which is on the 11.94 mm thick rotating seat (Fig. 2.13). The rotating seat has a yaw angle graduation and is connected by several aluminum bars to the base plate on which the an entire LDV probe unit, a pitch rotation stage and a unislide linear stages are mounted. The bump and the probe rotate together about the y-axis (yaw angle, ψ) by rotating the base plate so that the entire flow field around the bump can be measured. The aluminum bar has 12.7 mm diameter but 292.1 mm length for the miniLDV and 520.7 mm length for the long LDV. Figure 2.14 shows the turret with both LDV probe before installed to the wind tunnel.

There is another rotation stage to rotate only the probe about the z_L -axis (pitch angle, θ) to locate the probe normal to the window at each measuring point. Hence, it is necessary to transform coordinates from the right-handed local coordinate (x_L, y_L, z_L) to the right-handed tunnel coordinate (x, y, z) with θ and ψ to get tunnel coordinate quantities. The miniLDV probe was used in the near wall region within about 1cm from the bump surface. In the outer-region the long LDV probe was used.

Figure 2.15 shows the LB3 and laser beams passing through the 17.78 mm wide and 0.254 mm thick anti-reflection coated transparent Lexan window.

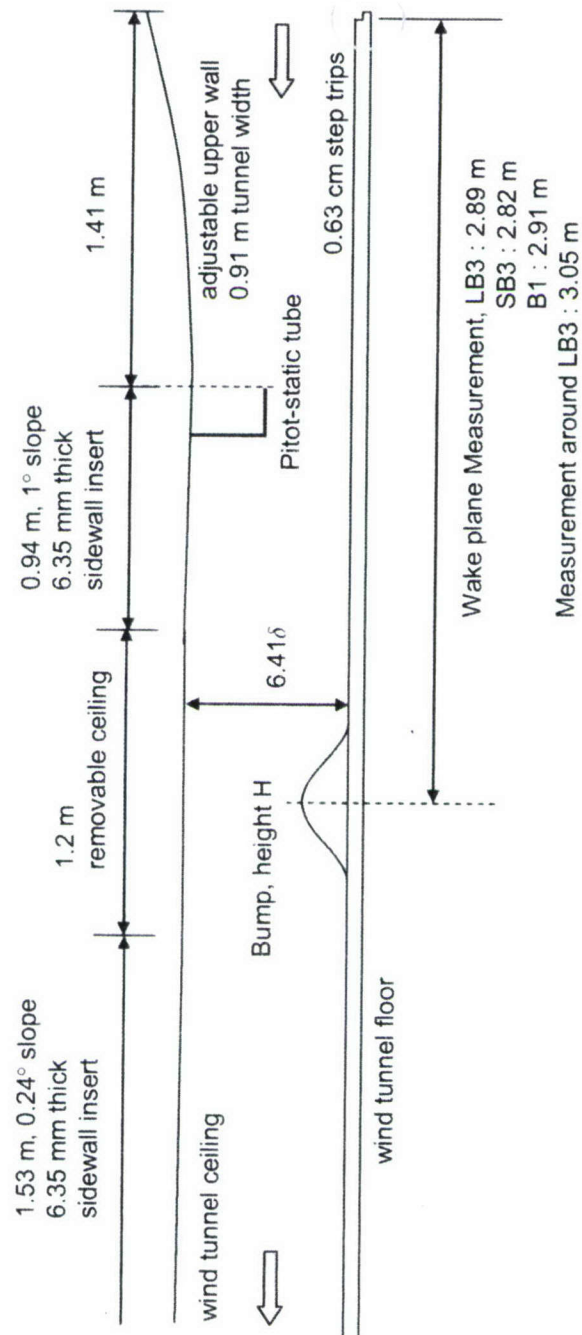


Figure 2.1 Side view schematic of the wind tunnel test section for bump measurements.

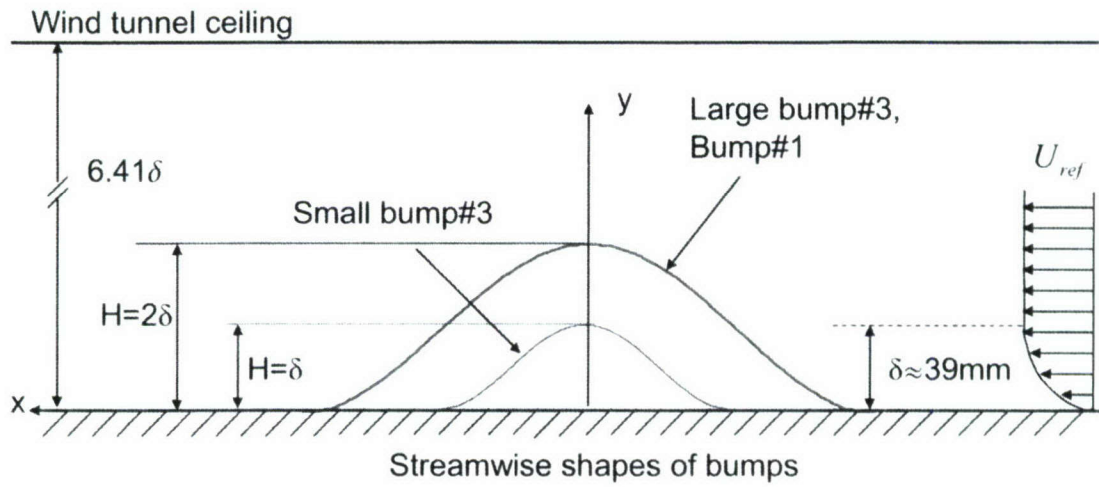


Figure 2.2 Axisymmetric shapes of bump#3 and the stream-wise shape of bump#1.

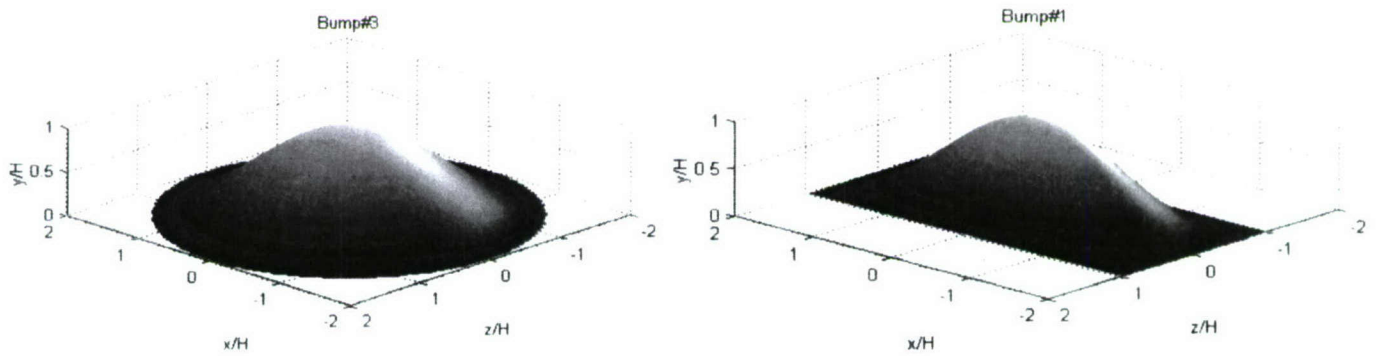
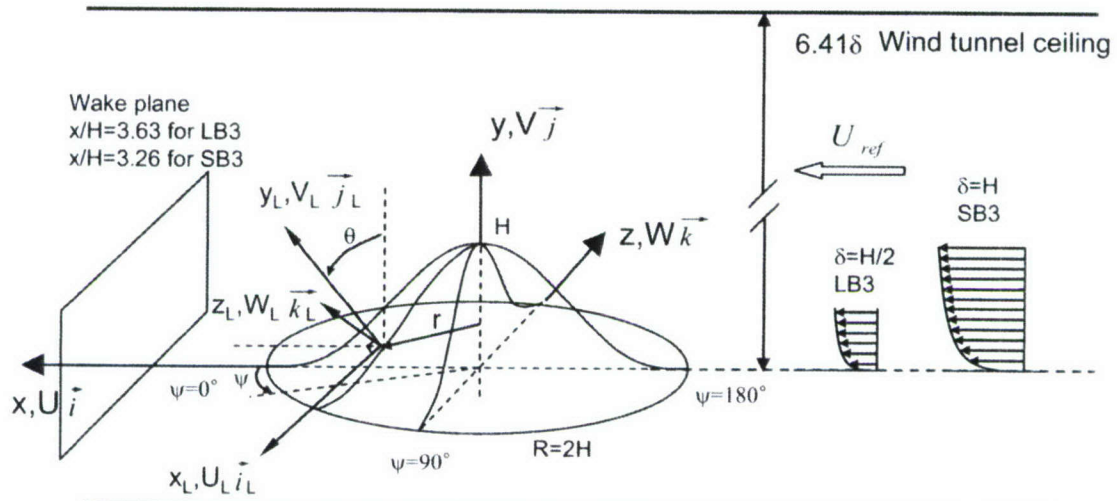
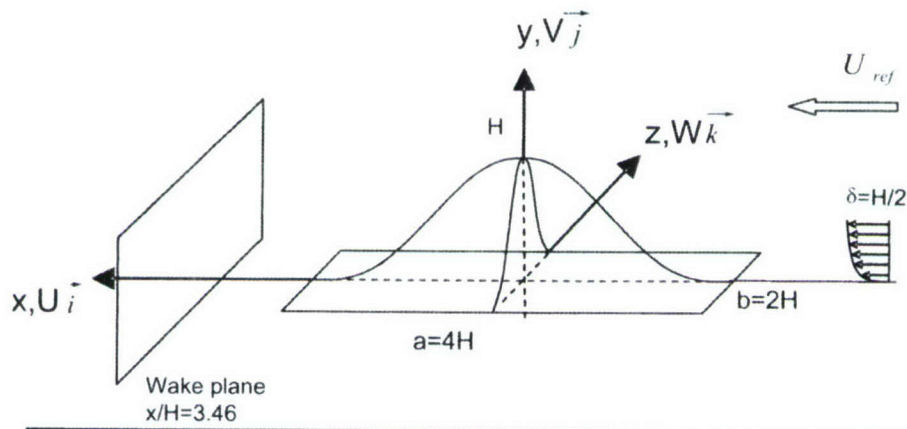


Figure 2.3 3D shapes of bumps.



(a) Tunnel coordinates (x, y, z) and Local coordinates (x_L, y_L, z_L)
pitch angle, θ and yaw angle, ψ for large bump#3.



(b) Tunnel coordinates (x, y, z) for bump#1

Figure 2.4 Schematic of bumps in the wind tunnel.

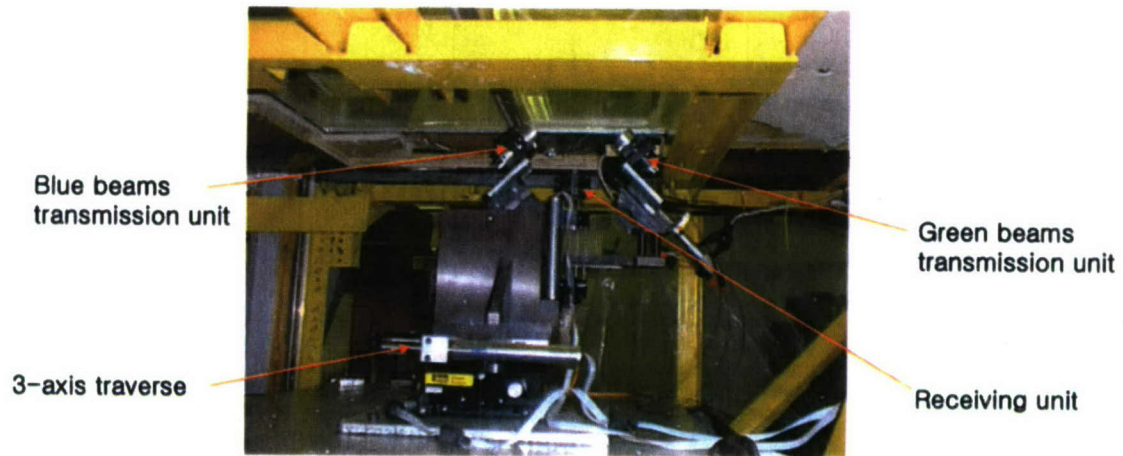


Figure 2.7 Photo of "Short" LDV probe.

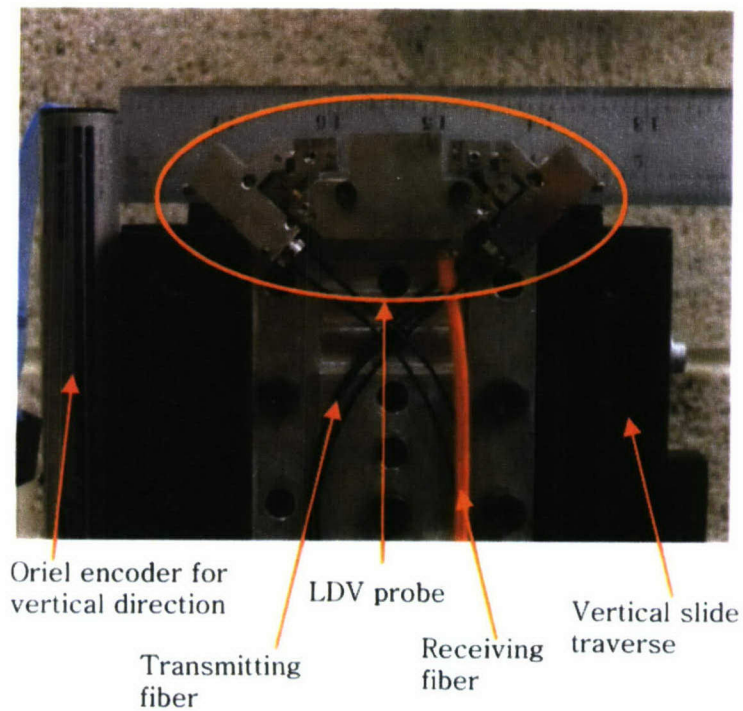
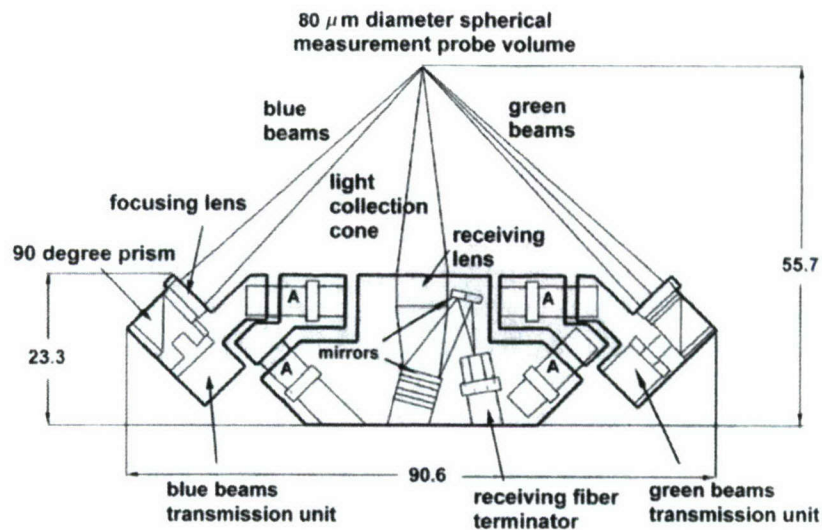
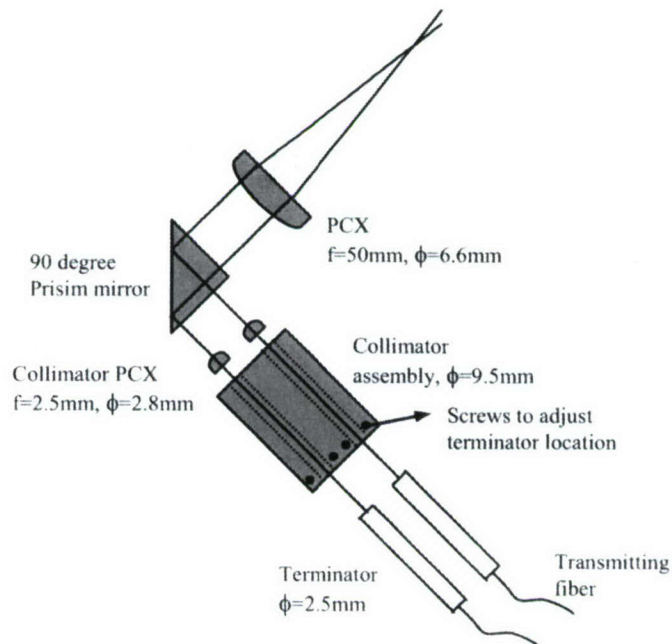


Figure 2.8 Photo of "MiniLDV" probe (scale in inches).



A : transmission unit adjustments.

Figure 2.9 Schematic of “MiniLDV” probe (unit : mm).



Terminators fit inside collimator assembly.

Figure 2.10 Optical components in the blue transmission unit.

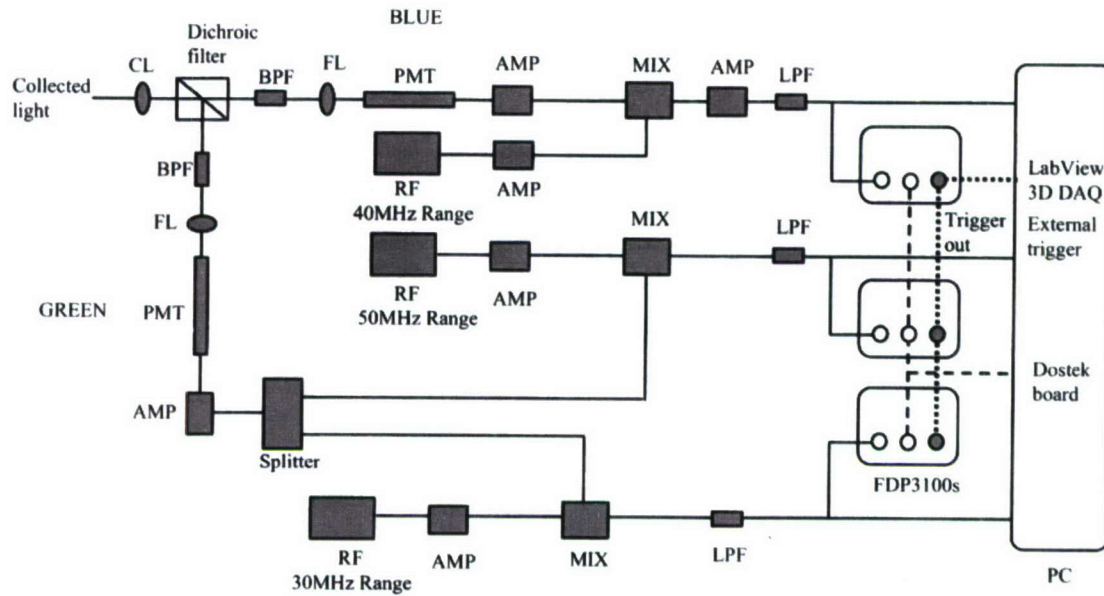


Figure 2.11 Signal processing unit. Dostek board for the wake plane measurement and Labview 3D DAQ with external trigger for the leeside measurement.

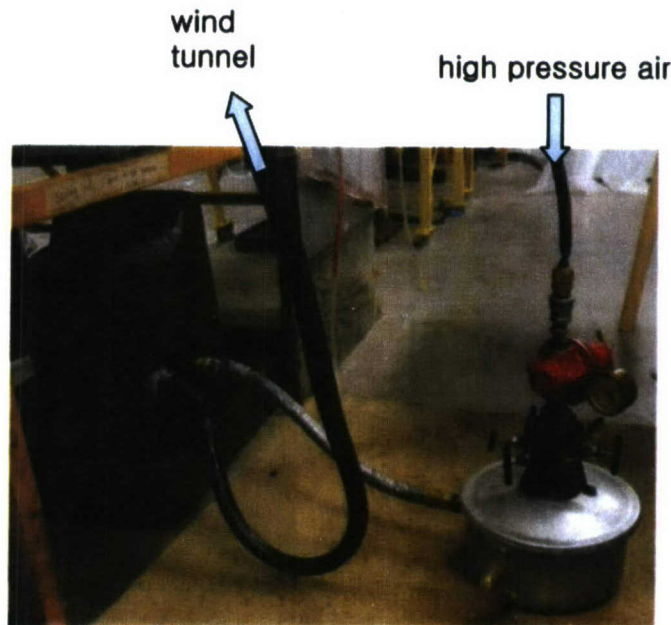


Figure 2.12 DOP seeder.

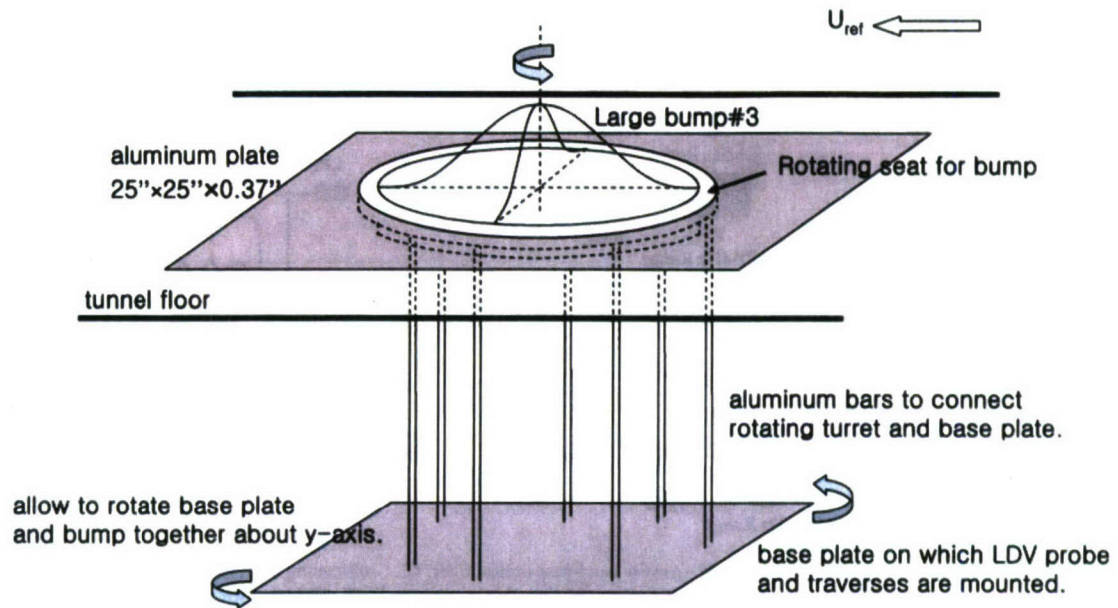
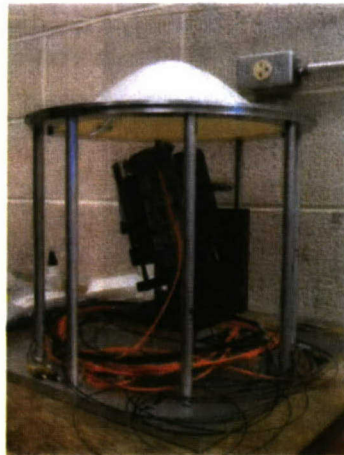
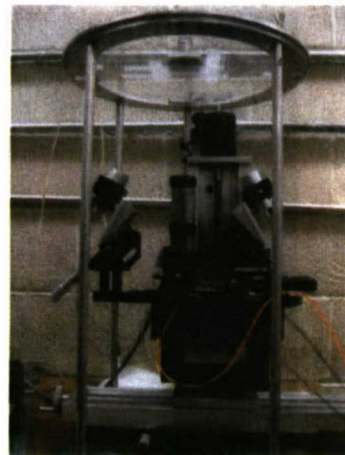


Figure 2.13 Rotating turret for large bump#3 leeside measurements.



(a) MiniLDV probe



(b) Long LDV probe

Figure 2.14 Rotating turret with LDV probes.

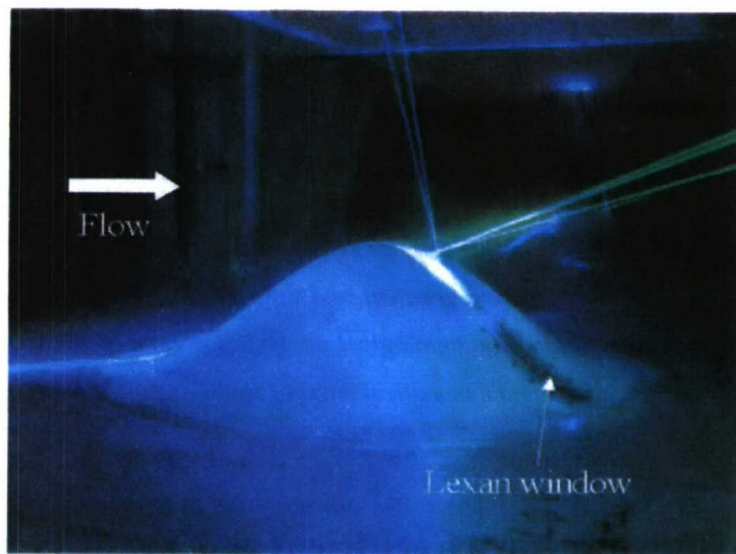


Figure 2.15 Photo of measuring large bump#3 leaside.

3

Surface Static Pressure Measurements and Oilflow Visualization

In order to provide the fundamental understanding of 3-D separation patterns on each bump, surface pressure distributions and oilflow visualizations are discussed briefly in this chapter. As mentioned in Chapter 1, all results in this chapter refer to Long (2005), Simpson et al. (2002) and Byun et al. (2004). The surface pressure gradient and the surface vorticity flux generated by the pressure gradient are presented too. The topological analyses for each bump are presented, which are based on oilflow visualizations and kinematical rules of singular points theory.

3.1 Surface Static Pressure Coefficient and Vorticity Flux

Mean static pressure distributions were measured on the surface of each bump and the plate upstream and downstream by using multiple pressure taps flush with the surface that are connected to a Scani-valve system.[†] The static pressure coefficient C_p is calculated as

$$C_p = \frac{P_{local,static} - P_{ref,static}}{P_{ref,total} - P_{ref,static}} \quad (3.1)$$

[†] Refer to Tian (2003) for details of Scani-valve system.

where $p_{\text{ref, static}}$ and $p_{\text{ref, total}}$ are the static and stagnation pressures of the undisturbed free-stream that determine U_{ref} and are measured by a Pitot-static tube mounted 1.41 m downstream from the tunnel inlet. The 0.5 mm diameter pressure taps were placed along a radial line of the bump 6.35 mm apart. For the axisymmetric bumps, the pressure measurements were made at every 10° of peripheral angle by turning the bump around the y-axis of symmetry. Three dozen pressure taps were placed on the flat Plexiglas plate. These pressure taps were only at one side of the centerline, because the flow over the plate is symmetric about the centerline as checked by the pressure data on the bump. Also the taps on the plates were only placed at one side of the bump (upstream or downstream), but the pressure data were taken for both upstream and downstream by turning the plates with the bump 180° . The contour plot of surface static pressure coefficient C_p (± 0.02 uncertain) shown in Fig. 3.1 is only for large and small bump#3, which uses data from both sides of the plane of symmetry. Differences of C_p are generally less than ± 0.02 from an average for any two symmetric locations and show good symmetry.

Because the only pressure data for bump#1 are along the centerline, there is no contour plot of bump#1. However, C_p distributions along the centerline of bump#1 are compared with Willits and Boger (1999) Applied Research Laboratory (ARL) experimental and computational data with the conditions, $U_{\text{ref}} = 24.4$ m/s and $\delta/H = 1/2$. For the upstream of the bump, the present data agree well with q- ω model results. This model has been observed to calculate two-dimensional separating flows better than some other models (Simpson, 1996). The present data show higher C_p than calculated results from $x/H > 1$, but still agrees better with ARL experimental results. It is noted that at the downstream, C_p recovers from the minimum value at the top of the bump ($x/H = 0$) to its maximum value at the edge of the bump ($x/H = 2$), which is even higher than the highest upstream value ($x/H = -1.6$). It is probably due to the strongly decelerated flow without a strong separation in that region.

The magnitude contours and vectors of surface pressure gradients are shown in Fig. 3.2 ~ Fig. 3.4 for large bump#3, small bump#3 and bump#1, respectively. For large and small bump#3, they show a similar pattern of the pressure gradient magnitude and vectors. The favorable pressure gradients appear on the windward side ($x/H < 0$) and the adverse pressure gradients on the leeward side ($x/H > 0$) of the bump. It means that the flow near the surface is accelerated until the top of the bump and then is decelerated after the top. Both bumps have the maximum pressure gradient

magnitude regions at the right before (for a favorable) and after (for an adverse) the top. However, large bump#3 has much higher maximum magnitude than small bump#3. For bump#1, the magnitude of surface pressure gradients are available only along the centerline like C_p distributions. When the pressure gradient values are negative, it means that the static pressure drops with increasing x/H , which is a favorable pressure gradient. Otherwise, if the values are positive, it is an adverse pressure gradient. The favorable pressure gradients appear on the most windward side and the adverse pressure gradients on the leeward side ($0 < x/H < 2$) too. It is noted that the pressure gradient magnitude increases for $1 < x/H < 1.7$ because of the change of C_p slope for that region (see Fig. 3.1(c)).

For incompressible flow over stationary surfaces with a unit vector normal to the surface \vec{e}_n , all vorticity, $\vec{\omega} = \text{curl} \vec{V}$ arises at the surface under the action of pressure gradients. The flux of vorticity at the surface is directly proportional to and perpendicular to the pressure gradient at the surface (Lugt, 1996) :

$$\frac{2}{\text{Re}_H} \left(\frac{\partial(\vec{\omega}H / U_{ref})}{\partial(n/H)} \right)_w = -(\vec{e}_n \times \vec{\nabla}) C_p \quad (3.2)$$

where, Re_H is the Reynolds number based on the bump height, H , n is the normal distance from the bump surface and \vec{e}_n is the unit vector normal to the bump surface and pointing out of the surface. Therefore, from Eq.(3.2), the vector plots of $-(\vec{e}_n \times \vec{\nabla}) C_p$ are the non-dimensional vorticity flux times 2, which are presented in Fig. 3.5 and 3.6 for large bump#3 and small bump#3, respectively. The vortex filaments should be created in closed loops which coincide with isobars in Fig. 3.1 from Eq.(3.2). The fresh vorticity on the upstream side of the bump is of the same sign as the approach boundary layer vorticity and it is strongly generated at the top of the bumps. On the sides of the bump the new vorticity is mainly in the stream-wise but opposite directions. Downstream of the bump top, the fresh vorticity is opposite to that of the approach boundary layer. The non-uniform generation of vorticity across the flow and the rate of diffusion of vorticity control the 3-D separation patterns.

3.2 Surface Oilflow Visualization

Surface oil flow visualization of skin friction lines, high and low velocity regions, separations and reattachments were obtained for the bumps and the tunnel floor. The oil mixture was 20 % oleic acid, 20 % titanium dioxide, and 60 % kerosene. The surface of the bump is black and the Plexiglas plate was covered with self-adhesive black plastic film. Then, the bump surface and the black plastic film on the Plexiglas plate were coated uniformly with a layer of the oil mixture. The tunnel was turned on as soon as the oil mixture was applied and kept running until the flow moved the oil into a consistent and partially dry streak. The streaks form wall shear stress lines, i.e. a limiting streamline pattern. The patterns were photographed, examined and preserved by clear acrylic spray lacquer.

The oil-flow patterns photographed during the flows (Fig. 3.7 ~ 3.9) were not definitive in the strong separation region on the leeward side of the bumps #3 because excessive oil mixture accumulated where the shear-stress lines spiraled into foci and tended to flow down the bump due to gravity. Videos were made to observe movement of the oil mixture; static pictures were made from the video for further quantitative analysis. Also, small drops of the oil mixture were placed on the leeward side of a clean bump and video was taken. This helped to determine definitively the direction of oil flow movement. The resulting oil-flow shear-stress line pattern was interpreted according to the kinematical topological rules described by Hunt et al. (1978) and is shown in Fig. 3.7 ~ 3.9. They are discussed in the following section.

3.3 Discussion of Oilflow Visualization and Surface Static Pressure Distribution

There is no separation on the windward side of each bump because the oil mixtures are not accumulated, even though the oil is left around the bump edges due to the tapes on the surface. The flow accelerates until the top of the bump, where the oil flow is dark since the shearing stress is large and there is little oil mixture left.

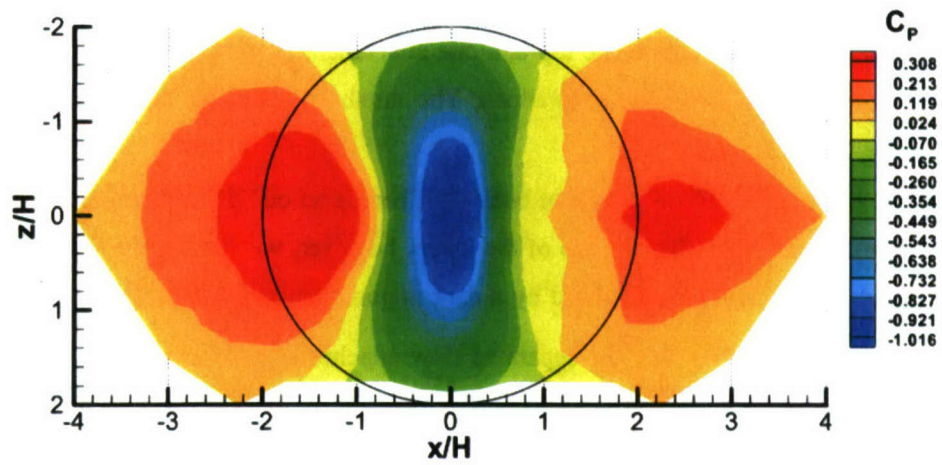
Figure 3.7 shows the oilflow results of large bump#3. Downstream on the leeside there is a region with much accumulated oil flow mixture, approximately from $x/H = 0.18$ to $x/H = 0.4$ and from $z/H = \pm 0.35$. From the shear stress lines in Fig. 3.6, there is one saddle separation S_{S1} on the x axis, followed by symmetrical foci node separations $N_{S,focus1}$ and $N_{S,focus2}$ on each side of the centerline. Just downstream a saddle attachment S_a occurs around which the oilflow is darker because of higher shearing stresses. From the C_p (Fig. 3.1) and pressure gradient distributions (Fig. 3.2), we can see that this area is also followed by a region from $x = 0.4H$ to $x = 0.5H$ with very high adverse pressure gradients. A large separation appears to start from this region with a relaxation of the pressure gradients downstream. After $x/H = 0.8$, between $\pm 30^\circ$ of the centerline, the pressure only increases slightly. Saddle separations S_{S2} and S_{S3} occur symmetrically near $x = 0.8H$ and $z = \pm 0.7H$. Foci separations $N_{S,focus3}$ and $N_{S,focus4}$ are downstream of S_{S2} and $N_{S,focus5}$ and $N_{S,focus6}$ are downstream of S_{S3} , each about $0.4H$ in diameter. Slightly downstream at about $x = 1.5H$ on the centerline, another saddle separation S_{S4} is located with a distinctly greater accumulation of oilflow mixture upstream. At the bottom of the bump near $x = 2H$, a nodal attachment N_a occurs, which supplies higher speed fluid in all directions and produces a darker oilflow. Saddle separations S_{S5} and S_{S6} are located on each side of the bottom of the bump at about $z = \pm 0.7H$. Separation lines which pass through S_{S5} and S_{S6} continue downstream and form a line between the higher velocity flow near the centerline and the lower speed flow. The number of saddles and nodes satisfy the topological rule, $\Sigma N = \Sigma S$, which is 7 here. However, as noted in Chapter 5 below, the miniLDV measurements at $y_0^+ = 6$ and 11 indicate another somewhat simpler near surface flow patterns, which suggests that the presence of the oilflow material affects the results.

Figure 3.8 shows the oilflow results of small bump#3. Because the oilflow results were not preserved well after the tunnel stopped running, the analysis was done by videos and small drops as mentioned before as well as photographs. The flow in the plane of symmetry separates near the top of the bump as indicated by the oil mixture accumulation. This area is followed by a high adverse pressure gradient region in Fig. 3.3. The lateral flow separates at the bottom of the bump. There are saddle separations S_{S2} and S_{S3} at about $x/H = 2$ and $z/H = 0.4$ on each side. Also at the bottom of the bump near $x = 2H$, the separated flow attaches at nodal attachment N_a on the centerline. The back flow from the separation together with the flow coming around the bump, forms a pair of foci node

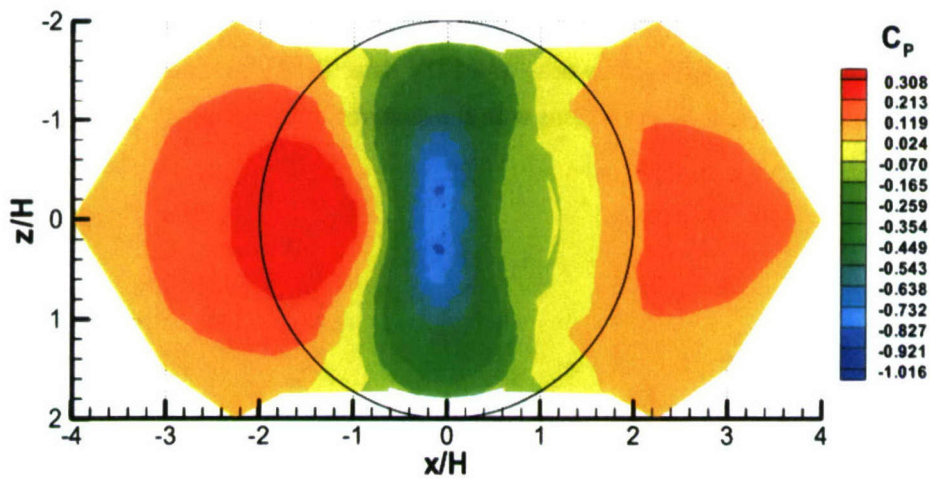
separation $N_{S1, \text{focus}}$ and $N_{S2, \text{focus}}$ at about $x/H=0.8$ and $z/H = 0.4$. Unlike large bump#3, small bump#3 shows only one strong separation at the top and one attachment at the bottom of the bump. Also there is only one pair of foci node separations. The number of saddles and nodes satisfy the topological rule, $\Sigma N = \Sigma S = 3$.

Figure 3.9 shows the oilflow results of bump#1. There is no oil mixture accumulation like the bump#3's. Downstream right after the top of the bump, however, we can see the sharp separation line like a upside-down "V". It is followed by a dark region. This means that just after the saddle separation S_{S1} at around $x/H = 0.2$, the separated flow attaches at node attachment N_{a1} . Another separation line is observed from about $x/H = 1.9$ to the downstream tunnel floor. So there is another pair of saddle separation S_{S2} and node attachment N_{a2} . The difference between bump#1 and the bump#3's is that there is no foci separation. The bump#1 also satisfies the topological rules, $\Sigma N = \Sigma S = 2$.

From a comparison between surface oilflow patterns and near-wall LDV data obtained from another complex 3-D flow, Tian et al. (2004) show that the oilflow patterns are reliable within about 1.5° uncertainty away from separation zones. Within separation zones, the oilflow separation lines are not located close to those obtained by near-wall LDV data. Thus, one must view surface oilflow visualization results in separated flow regions with some degree of uncertainty.

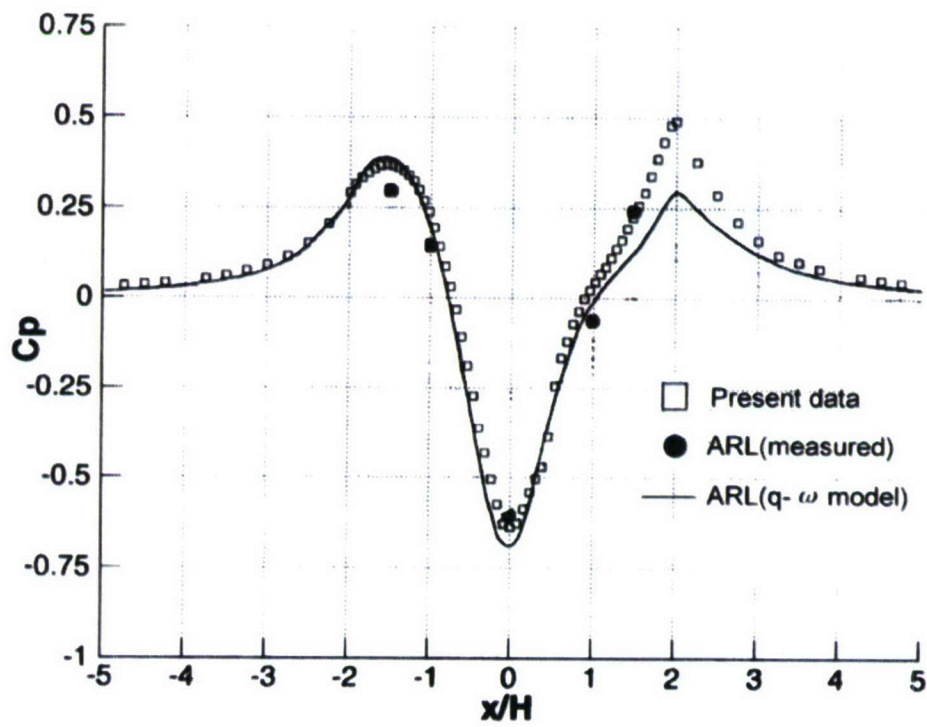


(a) Large bump#3



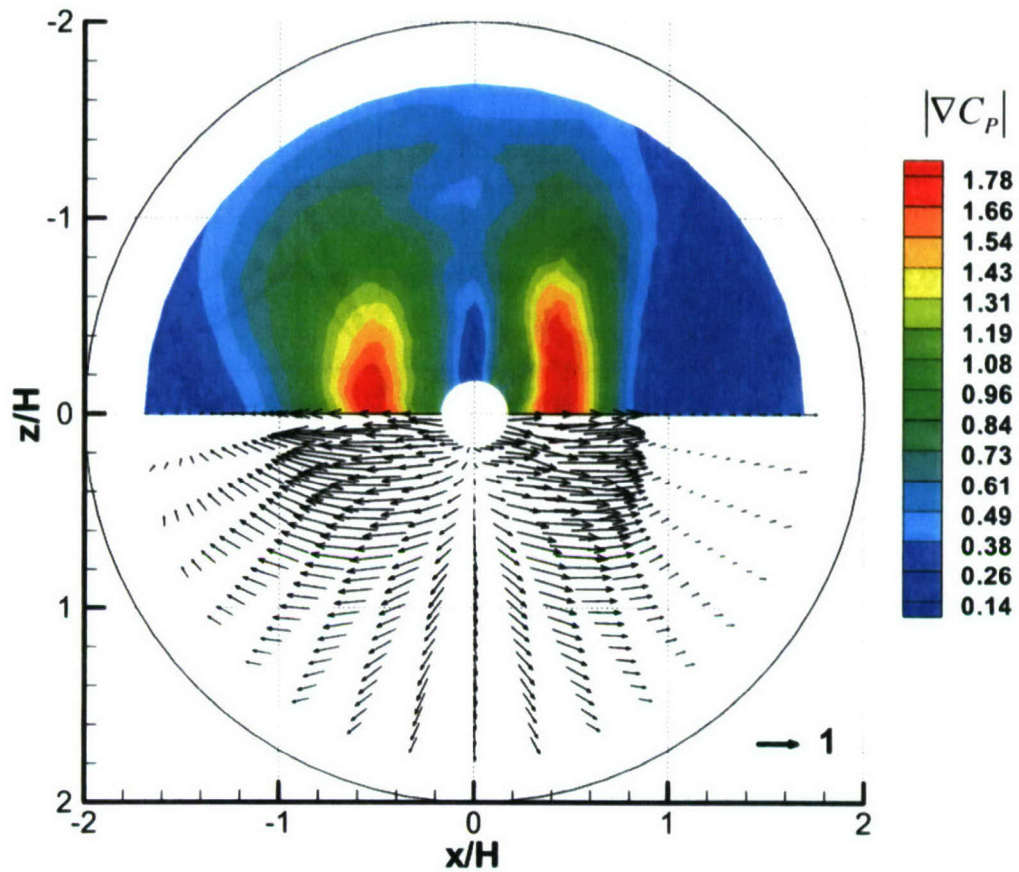
(b) Small bump#3

Figure 3.1 Surface pressure coefficient of the bumps (Byun et al., 2004).



(c) Bump#1 along the centerline. Present and ARL data (Willits and Boger, 1999)

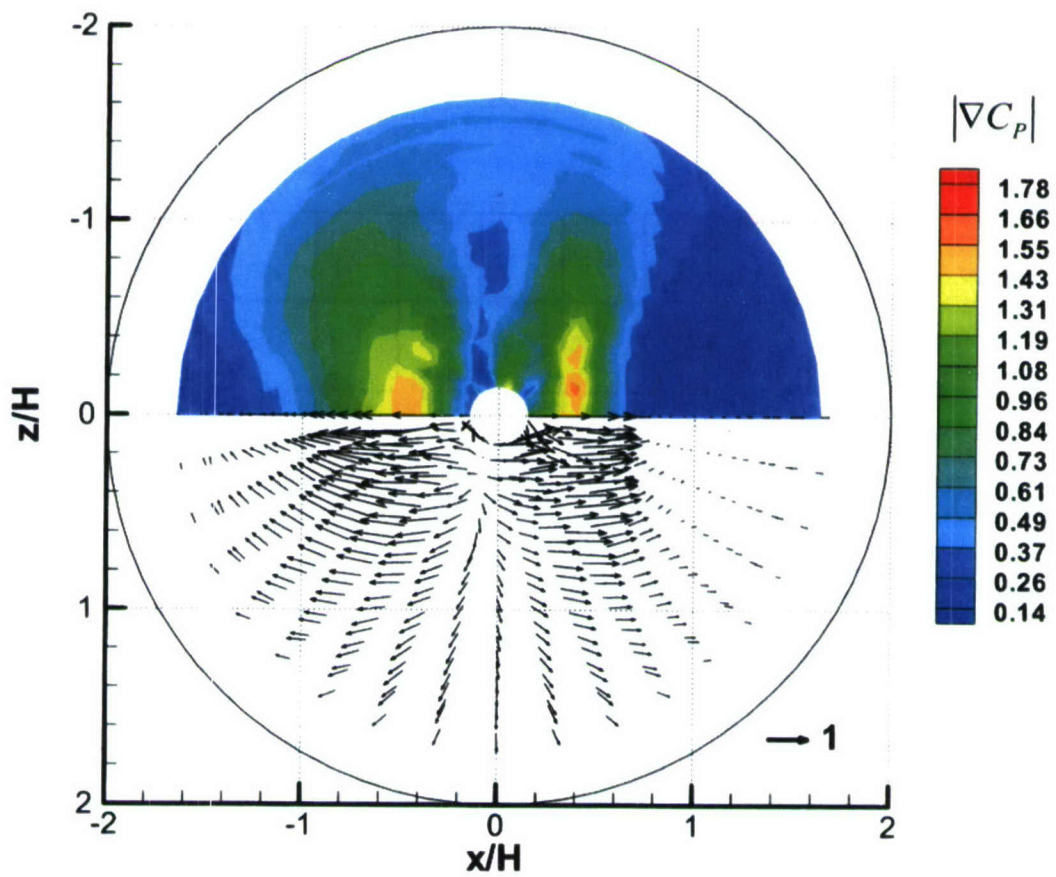
Figure 3.1 Continued.



Contours of its magnitude on negative z/H side and vectors on positive z/H side.

Figure 3.2 Surface pressure gradient of large bump#3.[†]

[†] I gratefully appreciate Long C. H. to allow using her data for Fig. 3.2 ~ 3.4.



Contours of its magnitude on negative z/H side and vectors on positive z/H side.

Figure 3.3 Surface pressure gradient of small bump#3.

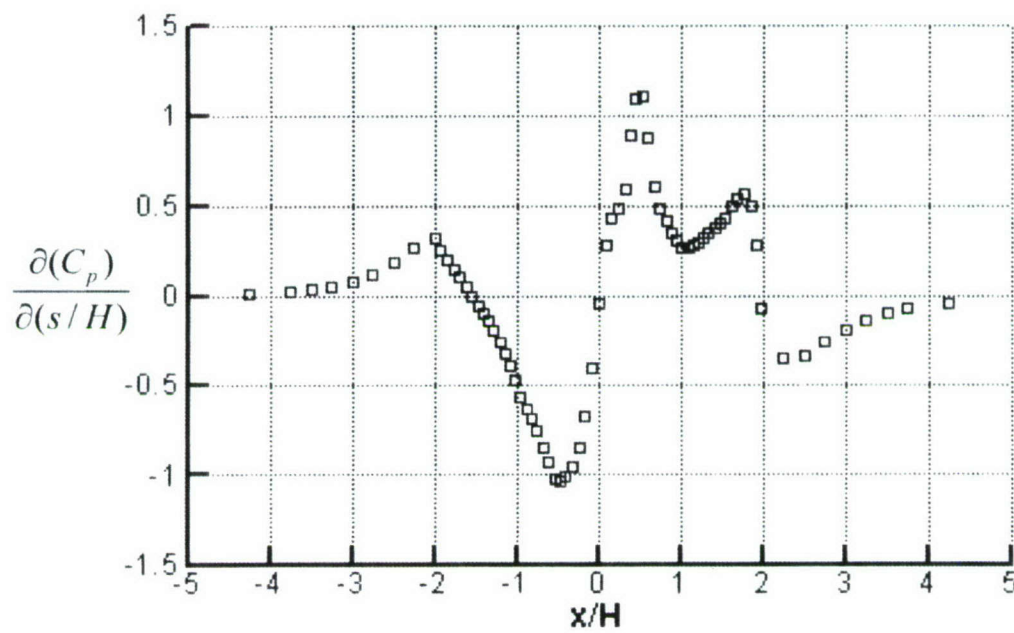
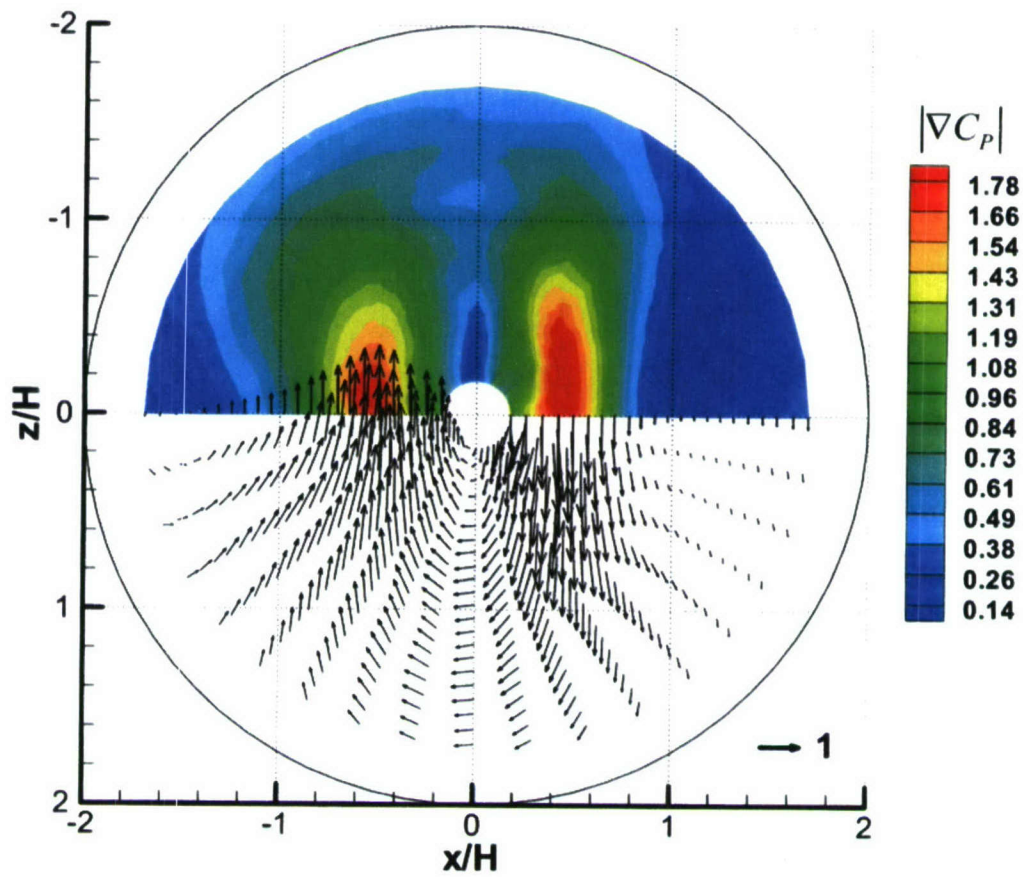
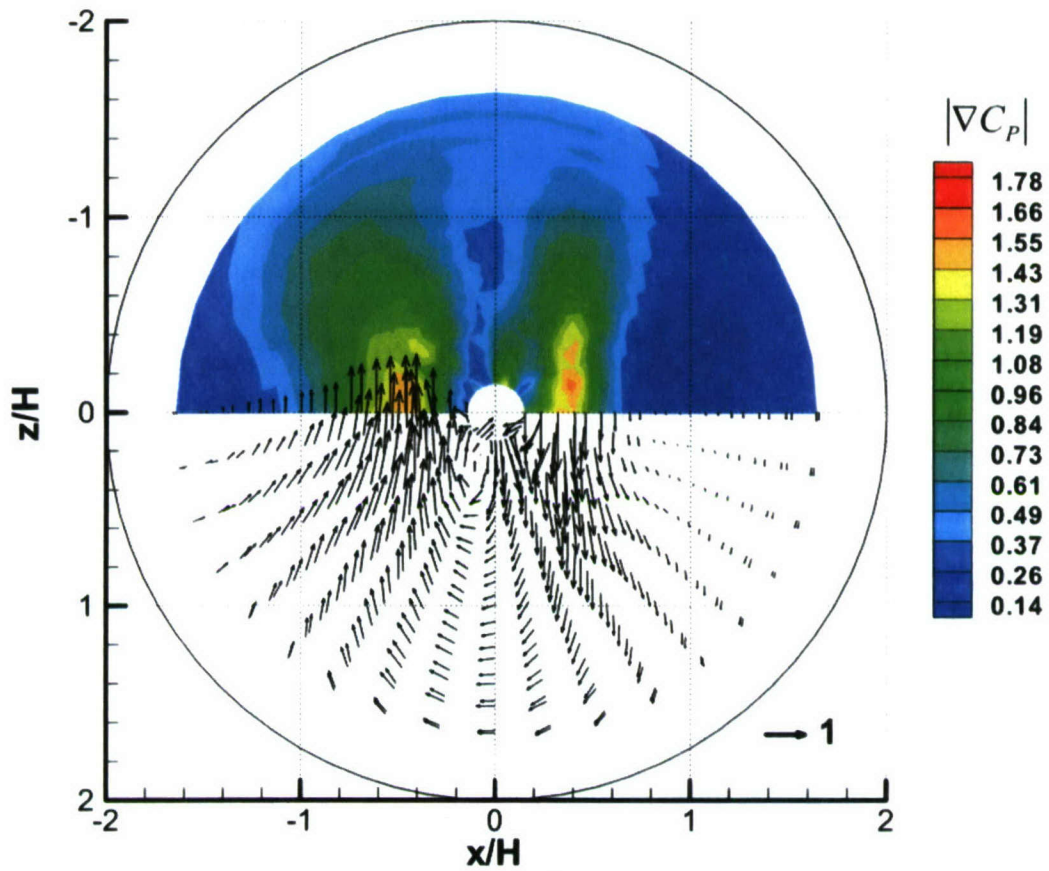


Figure 3.4 Magnitude of surface pressure gradient of bump#1.



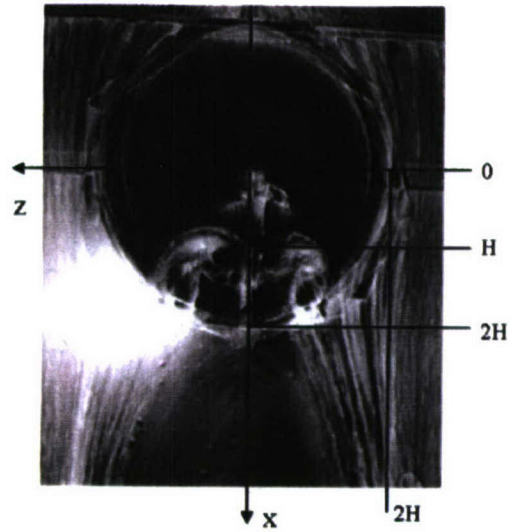
Contours of pressure gradient magnitude on negative z/H side.

Figure 3.5 Vector plot of non-dimensional vorticity flux of large bump#3.



Contours of pressure gradient magnitude on negative z/H side.

Figure 3.6 Vector plot of non-dimensional vorticity flux of small bump#3.



(a) Topview of an oilflow

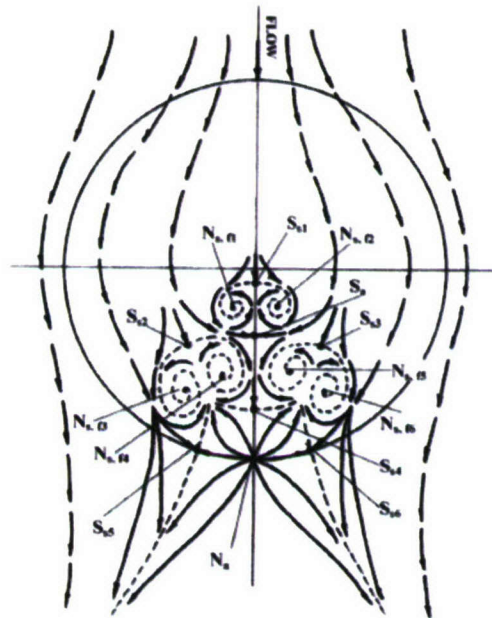
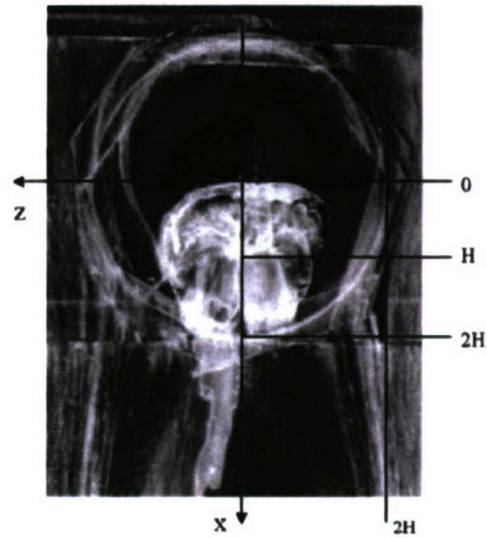
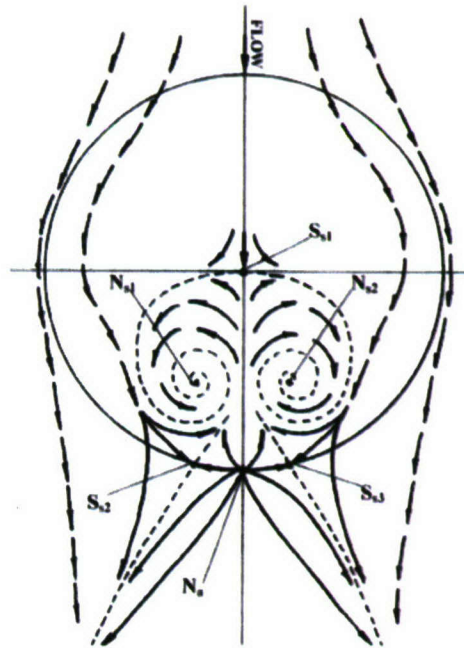
(b) Shear stress lines (bold), separation lines (dashed)
and zero shear stress points on the surface

Figure 3.7 Oilflow visualization results for large bump#3 (Simpson et al., 2002).

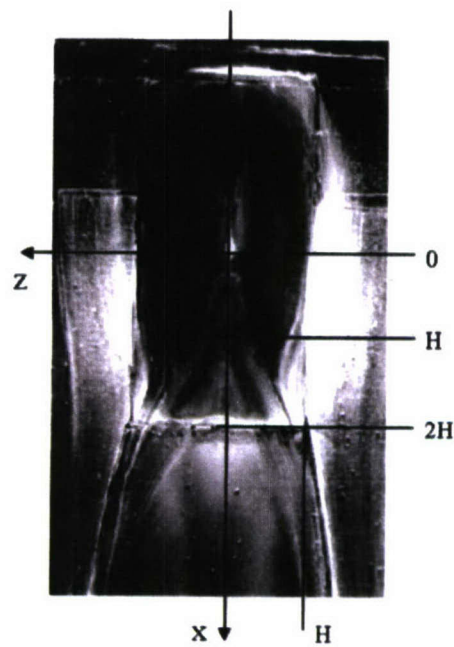


(a) Topview of an oilflow

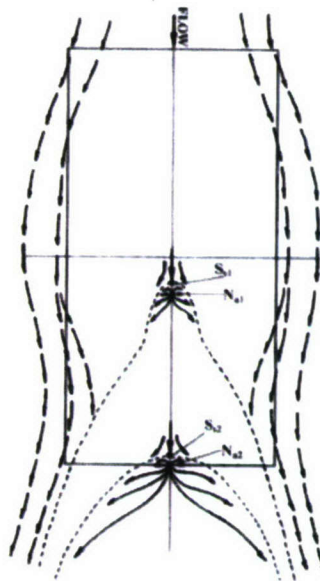


(b) Shear stress lines (bold), separation lines (dashed) and zero shear stress points on the surface

Figure 3.8 Oilflow visualization results for small bump#3 (Byun et al., 2004).



(b) Topview of an oilflow



(b) Shear stress lines (bold), separation lines (dashed)
and zero shear stress points on the surface

Figure 3.9 Oilflow visualization results for bump#1 (Byun et al., 2004).

4

Wake Plane LDV Measurements

From the flow topology of the previous chapter, each bump shows different oilflow 3-D separation patterns having multiple separation points on the leeward side. To examine the wake flow structures downstream which are separated from the bumps, LDV measurements are performed at $x/H \leq 3.63$ for each bump. The undisturbed 2-D turbulent boundary layer (2-DTBL) profile is also measured without the bump for a reference. The time-averaged mean velocities, Reynolds stresses and triple products are measured directly. Some turbulent structure and correlation parameters are evaluated in order to describe flow structures. Since LDV measurements are conducted at only one y-z plane of a specific x/H location for each bump, mean velocities from Pisterman (2004) 7-hole pitot tube results and Ma and Simpson's hot-wire results (2005) are referred to for other x/H wake planes, as well as frequency domain information such as the dissipation rate estimation.

4.1 Undisturbed 2-DTBL Measurements

A mean 2-D zero pressure gradient turbulent boundary layer 39 mm thick with $Re_\theta = 7300$ is measured at the x, z location of the center of large bump#3 without the presence of the bump to verify 2-DTBL and to use the reference profile for the comparison with 3-D profiles. The 6.35 mm thick glass plate is used for the transparent plate for the short LDV probe. For the miniLDV probe, the 71 mm long, 19 mm wide and 0.25 mm thick anti-reflection coated lexan plate was installed on the center of the Plexiglas for the transparent flat plate.

Figure 4.1 shows \overline{U}/u_τ , \overline{uv}/u_τ^2 , $\overline{u^2}/u_\tau^2$, $\overline{v^2}/u_\tau^2$, $\overline{w^2}/u_\tau^2$, $\overline{u^2v}/u_\tau^3$, $\overline{v^2w}/u_\tau^3$ and \overline{uvw}/u_τ^3 vs. $y u_\tau/\nu$ of two separate miniLDV data sets and short LDV data (George and Simpson, 2000) and DNS results (Spalart's 2-DTBL of $Re_0=1410$ and 670 (1988) and Kim et al. (1987) channel flow data at $Re_0 = 287$). The skin friction velocity u_τ ($\pm 5\%$ uncertain) was determined by the viscous sublayer data. When the measurement volume was focused just onto the surface, a strong signal determined an approximate reference location of the wall for a LDV traverse. A more refined determination of the measurement volume location relative to the wall was obtained by a least squares curve fit of the viscous sublayer mean velocity profile, $Q = C_1 y + C_2 y^4$ (Rotta, 1962), with $Q = (\overline{U}^2 + \overline{W}^2)^{1/2}$ and C_1 and C_2 as coefficients. The curve was fit through $Q = 0$ at $y = 0$. Using only the data for $y^+ < 11$, an iterative process was used to maximize the curve fit correlation coefficient by shifting the y values by Δy . This was performed at each of the profiles using at least 4 data points. Using this curve fit, the wall shearing stress $\tau_w/\rho = \nu (\partial Q/\partial y)_{\text{wall}} = u_\tau^2 = C_1 \nu$, where ν is the kinematic viscosity. The product moment of correlation coefficient, R_c between the data and the curve fit was $R_c > 0.998$.

\overline{U}/u_τ , all Reynolds stresses and triple products of two different probes agree well to each other. It is noted that the difference in $\overline{v^2}$ and some triple products between miniLDV and short LDV data sets are observed to be bigger than the presented uncertainty bounds in Appendix A. It may be due to larger uncertainties in short LDV data (George and Simpson, 2000). Comparing with DNS data sets, Reynolds normal stresses and shear stresses agree well with DNS data from near the wall, $y u_\tau/\nu \approx 5$ to the outer region. The triple product, $\overline{u^2v}/u_\tau^3$ also agrees well to Kim et al's DNS data. There are quantitative differences between LDV and DNS data in Reynolds stresses and triple products due to the different flow condition across the boundary layer. For very close to the wall, the differences between LDV and DNS data are due to the different Reynolds numbers because there are Reynolds number effects on the zero-pressure gradient flat-plate TBL except the mean velocity profile which follows the law of the wall (DeGraaff and Eaton, 2000). The $\overline{v^2w}/u_\tau^3$ and \overline{uvw}/u_τ^3 , which should be zero because the w fluctuation has no preferred direction in a 2-

DTBL, are very close to zero through the measured region even though they fluctuated around zero. All data satisfy the realizability conditions (Schumann, 1977).

4.1.1 Velocity Gradient Broadening

To investigate the velocity gradient broadening of $\overline{u^2}$ and the effective measurement volume diameter, the correction of $\overline{u^2}/u_\tau^2$ suggested by Fischer et al. (2000) was used. However, it is hard to tell that the correction is correct by comparing with Spalart's DNS data ($Re_\theta=1410$) without enough sublayer data ($yu_\tau/\nu < 5$) because the magnitude of $\overline{u^2}/u_\tau^2$ grows with increasing Reynolds number. Fernholz and Finley (1996) showed the peak value of $\overline{u^2}/u_\tau^2$ was about proportional to $Re_\theta^{1/8}$ and DeGraaff and Eaton (2000) used an equivalent scaling of $\overline{u^2}$, $\overline{u^2} \sqrt{C_f/2}/u_\tau^2$ vs. yu_τ/ν which showed good collapse up to $yu_\tau/\nu \approx 30$ between $Re_\theta=1430$ and 31000.

Figure 4.2 shows $\overline{u^2} \sqrt{C_f/2}/u_\tau^2$ vs. yu_τ/ν for miniLDV data with and without the small velocity gradient broadening correction. The data presented in Fig. 4.1 are not corrected for the velocity gradient broadening. However, Fig. 4.2 shows that the maximum gradient broadening effect on $\overline{u^2}/u_\tau^2$ is only 4.6% in $yu_\tau/\nu < 10$ and the coincident effective measurement probe volume diameter is approximately $50\mu\text{m}$.

According to Ölçmen and Simpson (1995a) and Ölçmen et al. (2001), the short and the long LDV probe have about 30 and $88\mu\text{m}$ effective measurement volumes, respectively. Therefore, the velocity gradient broadening effect on the short LDV probe data in the near wall region must be less than that on miniLDV data. The long LDV just was used for outer layer measurements where the velocity gradient broadening is negligible (see Fig. 4.2). So, it could be concluded that the velocity gradient broadening is negligible for the present data within measurement uncertainties.

4.2 Wake Plane LDV Measurements

The LDV results presented here for the bumps were obtained in a y-z plane located downstream from the center of the bumps ($x/H = 3.63$ for the large bump#3, $x/H = 3.26$ for the small bump#3 and $x/H = 3.46$ for the bump#1) with profiles for $-2.85 \leq z/H \leq 0.81$. The short and long LDV probes are used. Note that “2-D flow” profiles were measured at $x/H = 0$ for the large bump#3 without the bump. The 20 to 1 odds uncertainties calculated as mentioned above are in Table 4.2.

4.2.1 Skin Friction Velocity

Figure 4.3 shows the magnitude of u_τ / U_{ref} that was determined by the viscous sublayer data. The u_τ is calculated by the same method mentioned in Section 4.1 for 2-DTBL measurements. Most of the optimum Δy shifts were less than 50 μm . The effect of pressure gradient on u_τ was considered too. Thus the model equation would be $Q = C_1 y + C_2 y^2 + C_3 y^4$ in which $C_2 = (\vec{n}_Q \cdot \vec{\nabla} P) / 2\mu$ was determined by the magnitude of the pressure gradient in the Q direction (Rotta, 1962). The \vec{n}_Q is the unit vector in the Q direction and μ is the viscosity. Unfortunately, no pressure data were available at each LDV measurement locations except the centerline ($z/H = 0$). The nearest upstream pressure data from the LDV measurement location were used for curve fitting of off-center points as mentioned earlier ($x/H = 2.75$ for $z/H = \pm 0.49$ and $x/H = 2.5$ for $z/H = -0.98, -1.47$). Although these pressure data were not measured at the location where LDV data were taken and these pressure gradients are larger than downstream, it is possible to estimate how much the pressure gradient affects $|u_\tau|$. $|u_\tau|$ was changed less than 1.5 % by the pressure gradient. However, the product moment of correlation coefficient between the data and the curve fit was $R_c > 0.999$ for all stations that were calculated. This indicates a better fit than when the pressure gradient was not considered. It increased around the center ($z/H = 0$) due to a favorable pressure gradient and decreased away from the center by an adverse pressure gradient.

The results show a maximum at the centerline that is due to the strong downwash of the trailing vortices. On each side of the centerline where data are available, there is an almost symmetric variation for $|x|/H < 0.81$. Thus, the other variations at greater $|x|/H$ appear credible.

Closely the same results from multiple profiles at the same z/H confirm these variations. A local minimum occurs for each case near where low velocity flow is observed from the oilflow. For the 2-D flow without the bump, $|u_\tau|/U_{ref} \approx 0.036$, so the 3-D flow has lower wall stresses across the span except near the centerline.

4.2.2 Mean Velocity

Figure 4.4 ~ 4.6 show the stream-wise mean velocity \bar{U} for large bump#3, small bump#3 and bump#1, respectively. It is normalized by U_{ref} and bump height H and by wall variables on the local u_τ from Fig. 4.3 as well. Except for small bump#3, there are much higher \bar{U}/U_{ref} values near the centerline because of the downwash of the trailing vortices bringing high velocity fluid down toward the wall while the flow outside the vortex pair is much slower. All profiles of small bump#3, however, have lower \bar{U}/U_{ref} values for the same y/H than that of the 2-D flow. An interesting feature of bump#1 is at $|z|/H < 0.65$. In this region \bar{U}/U_{ref} reaches more than $0.55 U_{ref}$ at about $y/H = 10^{-2}$ then decreases up to $y/H = 10^{-1}$. The \bar{U}/u_τ shows the similar trend in $60 < yu_\tau/\nu < 400$. This generates different \bar{uv} in that region from other bumps #3. It will be discussed later.

Plots of \bar{U}/u_τ vs. yu_τ/ν profiles using the local u_τ from Fig. 4.3 do not collapse well onto a single line except in $yu_\tau/\nu < 8 \sim 9$ since there is no law of the wall for mean 3-D flows. In these plots, most of the apparent asymmetry between data on opposite sides of the centerline is due to the different local u_τ to form \bar{U}/u_τ .

Figure 4.7 ~ 4.9 show the span-wise mean velocity \bar{W} for large bump#3, small bump#3 and bump#1, respectively. They are also normalized by two variables like \bar{U} . Bump#1 generates much higher span-wise velocity than bumps #3. The \bar{W}/U_{ref} is about zero at $y/H \approx 0.2$ ($yu_\tau/\nu \approx 900$) for large bump#3 and at $y/H \approx 0.2$ ($yu_\tau/\nu \approx 900$) for bump#1 for all z/H , which is the apparent height of the vortex center. In the case of small bump#3 the height where $\bar{W}/U_{ref} \approx 0$ is not nearly

the same for all z/H and increases away from the center. All bumps reach their maximum \overline{W}/U_{ref} at $y/H \approx 10^{-2} \sim 2 \times 10^{-2}$ for all z/H and show good symmetry about the centerline. In bump#1 there is a relatively huge reduction of \overline{W}/U_{ref} between $z/H = -0.81$ and 0.98 because the vortex center is at $z/H \approx 0.8$, which is shown clearly in Fig. 4.10. The magnitude of \overline{W} is much higher in the inner region ($yu_\tau/\nu \approx 1000$) than the outer region for large bump#3 and bump#1 near the centerline, especially for bump#1.

Figure 4.10(a) and (b) show contours of the mean stream-wise \overline{U}/U_{ref} velocity component and secondary flow velocity component vectors for the 3 bumps with the linear y/H scale and the $\log_{10}(y/H)$ scale, respectively. The tail of each vector is located at the y/H and z/H for that data point. The $\log_{10}(y_0^+)$ scale also was used to show the near-wall region in terms of wall variables and y_0^+ , which is the $y^+ (= yu_\tau/\nu)$ value based on the 2-D flow u_τ . One is able to see the outer region flow behavior more clearly with the linear scale in Fig. 4.10(a), while Fig. 4.10(b) magnifies the nearer wall behavior. The contours show the relatively large \overline{U}/U_{ref} for large bump#3 and bump#1 and the relatively low \overline{U}/U_{ref} in small bump#3 around the centerline, as shown in Fig. 4.4 ~ 4.6. Bump#1 is clearly more effective in bringing high velocity fluid down toward the wall than the other 2 bumps #3. In these plots, there is good apparent symmetry between data on opposite sides of the centerline.

The circulation, Γ was calculated for the measurement plane for each bump using a numerical integration along the closed loop around the outer edge of the y - z plane, $0 \leq y/H \leq 1.23$ and $-2.85 \leq z/H \leq 0$. It was normalized by U_{ref} and H . Bump#1 has the highest circulation, Γ/HU_{ref} as -0.25 . Large bump#3 and small bump#3 have -0.21 and -0.13 , respectively. Therefore, bump#1 generates the strongest stream-wise vorticity at the measured wake plane among three bumps.

Figure 4.11 shows the stream-wise vorticity,

$$\omega_x = \frac{\partial \overline{W}}{\partial y} - \frac{\partial \overline{V}}{\partial z} \quad (4.2)$$

normalized by U_{ref} and H for each bump with the $\log_{10}(y/H)$ and the $\log_{10}(y_0^+)$ scales. Solid lines indicate positive values and dashed lines denote negative values. As expected, bump#1 generated the strongest $\omega_x H / U_{ref}$, having at least 2 times stronger peak vorticity than the other bumps. Most $\omega_x H / U_{ref}$ was generated behind bumps and close to the wall up to $y/H \approx 0.2$ ($\log_{10}(y/H) \approx -0.7$, $y_0^+ \approx 790$) due to strong $\partial \bar{W} / \partial y$ values near the wall (Fig. 4.7 ~ 4.9 and Fig. 4.10(b)). For the $z/H < 0$ region, the contours show the large negative $\omega_x H / U_{ref}$ near the wall around the stream-wise vortex center because of the wall no-slip condition. The sign of $\omega_x H / U_{ref}$ changed at $y/H \approx 0.02$ ($\log_{10}(y/H) \approx -1.7$, $y_0^+ \approx 80$) for all 3 bumps, since the sign of $\partial \bar{W} / \partial y$ was changed around that height. For small bump#3, unlike the other 2 bumps, $\omega_x H / U_{ref}$ is positive for $-0.4 < z/H < 0$ then negative for $z/H < -0.4$ near the wall. This is because \bar{W} is still toward the centerline in $-0.4 < z/H < 0$. It is noted that the stream-wise vorticity is stronger and more concentrated in bump#1 than other bumps. This might be related to the span-wise meandering motions for the two bump#3, which are discussed later.

Figure 4.12 shows the helicity density, $h = \bar{U} \omega_x$ normalized by U_{ref} and H for each bump with the $\log_{10}(y/H)$ and $\log_{10}(y_0^+)$ scales. It represents three-dimensional flowfields that contain concentrated vortices. Solid lines indicate positive values and dashed lines denote negative values. The sign of the helicity density indicates the direction of the stream-wise vorticity relative to the stream-wise velocity. All three bumps show very strong three-dimensional coherent helical structures near the wall. For large bump#3 and bump#1, hH / U_{ref}^2 shows similar distributions to $\omega_x H / U_{ref}$ in Fig. 4.11, indicating higher hH / U_{ref}^2 near the wall, $y/H < 0.03$ ($\log_{10}(y/H) \approx -1.5$, $y_0^+ \approx 140$). Like for $\omega_x H / U_{ref}$, bump#1 has a peak hH / U_{ref}^2 that is at least 2 times larger than for the other 2 bumps.

The total helicity,

$$\mathcal{H} = \iint h dy dz \quad (4.3)$$

was calculated for the area bounded by the contour used to determine Γ for each bump using a numerical integration of the helicity density. It was normalized by U_{ref} and H . Like circulations, Bump#1 has the highest helicity, \mathcal{H}/HU_{ref}^2 as 0.22. Large bump#3 and small bump#3 have 0.18 and 0.09, respectively.

4.2.3 Reynolds Stresses

Figure 4.13 ~ 4.15 show Reynolds normal stresses $\overline{u^2}/u_\tau^2$, $\overline{v^2}/u_\tau^2$ and $\overline{w^2}/u_\tau^2$ vs. yu_τ/ν for each bump, respectively. For the bumps #3, $\overline{u^2}/u_\tau^2$ values are much higher than 2-DTBL and reach maxima in the outer region for $|z|/H < 0.81$. In these span-wise locations, $\overline{u^2}/u_\tau^2$ values increase significantly from $yu_\tau/\nu \approx 300 \sim 400$. The $\overline{u^2}/u_\tau^2$ values approach to zero as the height is close to the boundary layer edge. It is noted that $\overline{u^2}/u_\tau^2$ values near the centerline are almost constant for $20 < yu_\tau/\nu < 200 \sim 300$. However, for bump#1, $\overline{u^2}/u_\tau^2$ values are much smaller than the bumps #3 and show very similar behavior like the 2-DTBL for most z/H locations. They show maximum values at $yu_\tau/\nu \approx 10 \sim 20$ and change slowly in $100 < yu_\tau/\nu < 500$. For very near the centerline, $|z|/H < 0.33$, $\overline{u^2}/u_\tau^2$ values are even smaller than 2-DTBL in $40 < yu_\tau/\nu < 1000$.

The $\overline{v^2}/u_\tau^2$ values show a similar trend for all three bumps, increasing significantly from $yu_\tau/\nu \approx 100$ near the centerline due to the downwash by stream-wise vortices even though bump#1 has much smaller $\overline{v^2}/u_\tau^2$ values and reaches maximum values in the inner layer.

For all bumps, the $\overline{w^2}/u_\tau^2$ values increase significantly from the very near wall and especially near the centerline due to the counter-rotating stream-wise vortices. For large bump#3, in $0 < |z|/H < 0.81$, $\overline{w^2}/u_\tau^2$ values are higher than the centerline. However, for small bump#3, the maximum values appear in $|z|/H < 0.16$ and then $\overline{w^2}/u_\tau^2$ values decrease as z/H moves away from the centerline. It is noted that for bump#1, the lowest $\overline{w^2}/u_\tau^2$ values appear at the centerline within

the inner region. The maxima values of $\overline{w^2}/u_\tau^2$ appear at $yu_\tau/\nu \approx 30$ and 500 at $z/H = -0.81$, which is very close to the vortex center. In between the centerline and the vortex center, $\overline{w^2}/u_\tau^2$ values change slowly in $20 < yu_\tau/\nu < 300$.

Figure 4.16 ~ 4.18 shows Reynolds shear stresses, $-\overline{uv}/u_\tau^2$, $-\overline{vw}/u_\tau^2$ and $-\overline{uw}/u_\tau^2$ vs. yu_τ/ν for each bump, respectively. For large bump#3 $-\overline{uv}/u_\tau^2$ has similar profiles between the wall and the height of $yu_\tau/\nu \approx 80$ for all z/H . Near the centerline, $|z/H| > 0.98$, $|\overline{uv}/u_\tau^2|$ increases as y increases and shows the maximum at $yu_\tau/\nu \approx 3000$ ($y/H \approx 0.8$) and $|z/H| = 0.33$. The height of the maximum $|\overline{uv}/u_\tau^2|$ decreases as z/H is away from the center. Small bump#3 also has similar profiles up to $yu_\tau/\nu \approx 30$ at $|z/H| > 0.98$ and shows the maximum value which is greater than one of large bump#3 at $yu_\tau/\nu \approx 1000$ ($y/H \approx 0.6$) and $|z/H| = 0.08$ and 0.16. The height of the maximum $|\overline{uv}/u_\tau^2|$ decreases as z/H is away from the center like large bump#3. Large bump#3 and small bump#3 have much higher stream-wise Reynolds shear stresses than 2-DTBL because of larger eddies generated by the separation from the leeside of bumps.

However, bump#1 shows different $-\overline{uv}/u_\tau^2$ profiles from other two bumps #3 as shown in Fig. 4.16(c). The magnitudes are much smaller than bumps #3. Although they have a similar trend up to $yu_\tau/\nu \approx 20$ for all z/H , they decrease from $yu_\tau/\nu > 20$ and reach minima about $yu_\tau/\nu \approx 100$ for $|z/H| > 0.81$ between two mean stream-wise vortices. They show two different trends with respect to the span-wise location of the mean stream-wise vortex center. These $-\overline{uv}/u_\tau^2$ profiles within $|z/H| = 0.81$ come from the unusual stream-wise mean velocity as shown in Fig. 4.6 which shows zero and even negative velocity gradient with respect to y and lower Reynolds normal stress, $\overline{v^2}$ in $20 < yu_\tau/\nu < 1000$, resulting in a much lower $-\overline{uv}$ production rate. Therefore, $|\overline{uv}/u_\tau^2|$ in $|z/H| \leq 0.81$ is lower than 2DTBL while it is higher for $|z/H| > 0.81$.

The Reynolds span-wise shear stress, $-\overline{vw}$ normalized by u_τ is shown in Fig. 4.17 for each bump. Large bump#3 and bump#1 have a similar trend between the wall and the height up to

$yu_\tau / \nu \approx 1000 \sim 2000$ which is around the mean stream-wise vortex center of each bump (see Fig. 4.7). For large bump#3, $|\overline{vw}/u_\tau^2|$ increases from $yu_\tau / \nu \approx 80$ for in $|z|/H < 1$ as z/H is away from the centerline. After reaching a maximum value, it decreases up to $yu_\tau / \nu \approx 2000$. It is noted that there is a sign change of $-\overline{vw}/u_\tau^2$ at $yu_\tau / \nu \approx 80$ where the maximum span-wise mean velocity appears (see Fig. 4.7). The higher $|\overline{vw}/u_\tau^2|$ in $80 < yu_\tau / \nu < 2000$ than 2-DTBL for $|z|/H < 1$ results from the span-wise velocity gradient with respect to y and the significant increase of Reynolds normal stress, $\overline{v^2}$. Above $yu_\tau / \nu \approx 2000$, $|\overline{vw}/u_\tau^2|$ increases again mainly due to much higher $\overline{v^2}$ produced by large eddies from the separation on the bump. The $-\overline{vw}/u_\tau^2$ profiles for bump#1 also can be explained by the similar mechanism. Bump#1 has the maximum span-wise mean velocity at $yu_\tau / \nu \approx 80$ and the increase of $\overline{v^2}$ up to $yu_\tau / \nu \approx 1000$. However, $|\overline{vw}/u_\tau^2|$ approaches to zero above $yu_\tau / \nu \approx 1000$ unlike large bump#3. It is noted that bump#1 shows larger $|\overline{vw}/u_\tau^2|$ for $|z|/H < 1$ than large bump#3 as z/H is away from the centerline in the inner region. It is even true in $yu_\tau / \nu < 80$ where bump#1 has higher span-wise mean velocity gradient with respect to y than large bump#3 while $\overline{v^2}$ is not much different from large bump#3. This indicates that the span-wise momentum transfer by the velocity fluctuation is higher than the stream-wise momentum transfer in bump#1.

Unfortunately, $-\overline{vw}/u_\tau^2$ for small bump#3 does not show symmetric profiles for $|z|/H < 1$ as shown in Fig. 4.17(b). There were several trials to adjust and check flow symmetry changing by the bump span-wise location within 2 mm. However, \overline{vw} and $\overline{w^3}$ did not show symmetric distributions within experimental uncertainties while mean velocities, other Reynolds stresses and triple products were much better. Generally, $|\overline{vw}/u_\tau^2|$ seems to be higher near the centerline and in the inner region.

Figure 4.18 shows $-\overline{uw}/u_\tau^2$ vs. $y u_\tau / \nu$ for each bump. It is one parameter of flow 3-dimensionality. For large bump#3, $|\overline{uw}/u_\tau^2|$ shows high value in the outer region for $|z|/H < 1$ as z/H is away from the centerline. For small bump#3 it is high in the inner region for $|z|/H < 1$ as z/H is away from the centerline and shows a maximum at $y u_\tau / \nu \approx 200$. The maximum value is much higher than one of large bump#3 as close to the centerline. However, bump#1 has high $|\overline{uw}/u_\tau^2|$ within $y u_\tau / \nu \approx 100$ for $|z|/H < 1$ and show a maximum at $y u_\tau / \nu \approx 10$ which is higher than $|\overline{uv}/u_\tau^2|$. Although $-\overline{uw}$ is not a major term in the Reynolds-averaged momentum equations, it show high values near the centerline for all bumps and even very near wall for bump#1.

Figure 4.19 shows the magnitude of Reynolds shear stress, $\tau / \rho u_\tau^2$ for each bump. Large bump#3 and small bump#3 have much higher values for $|z|/H < 1$ in the outer region than bump#1. They show significant increases from $y u_\tau / \nu \approx 100$. Two bumps #3 show higher $\tau / \rho u_\tau^2$ values than 2-DTBL for all y except $|z|/H \leq 0.16$ for large bump#3. However, as expected, bump#1 has very low $\tau / \rho u_\tau^2$ values for $|z|/H \leq 0.33$ where it reaches minima at $y u_\tau / \nu \approx 100$. For bump#1, $\tau / \rho u_\tau^2$ shows higher values than the 2-DTBL at most y locations for $|z|/H > 0.33$ and has maxima at $y u_\tau / \nu \approx 400 \sim 500$ for $0.65 \leq |z|/H \leq 0.98$, which are close to the mean stream-wise vortex center.

For a better understanding of behaviors of Reynolds stresses at the measured wake planes for each bump, the contour plots of all Reynolds stresses at the wake planes are shown in Appendix B.

4.2.4 1/S Parameter and Correlation Coefficient, R_{uv}

The 1/S parameter defined as

$$\frac{1}{S} = \frac{\sqrt{(-\overline{uv})^2 + (-\overline{vw})^2}}{v_\tau^2} \quad (4.4)$$

for each bump in Fig. 4.20 shows some similarities of trends across the flow at almost all z/H locations for each bump. It is noted that the magnitude of both Reynolds shear stresses and $\overline{v^2}$ are going to zero with y^3 and y^4 , respectively as approaching to the wall so that $1/S$ must be very high at the very near wall. Thus, the present $1/S$ profiles below $yu_t/\nu < 10 \sim 20$ are not reliable.

This parameter has about 0.6 for $100 < yu_t/\nu < 1000$ for a 2-DTBL. It has been found to have closely the same behavior for 3-D flows as 2-D flows, if there are no embedded stream-wise vortices (Ölçmen and Simpson, 1995b). There are embedded stream-wise vortices for these three bumps at these locations. Near the wall region bump#1 has a higher $1/S$ value because of higher $-\overline{vw}$ than other bumps. There are two similarities in two z/H regions above $yu_t/\nu \approx 40$. For locations further from the centerline than the mean vortex, the level of $1/S$ up to $yu_t/\nu \approx 1000$ ($y/H < 0.3$) is close to that for the 2-D flow and is about the same level as observed in 3-D flows without embedded vortices. Near the centerline where the downwash effects are large, a different similarity is observed.

These two similarities in these two regions are much better than the similarity of the $R_{uv} = -\overline{uv}/\overline{u'v'}$ correlation coefficient across the flow as shown in Fig. 4. 21. This indicates that the relationship between $\overline{v^2}$ and the shear stress is stronger than the relationship between the u' and v' that appear in the R_{uv} correlation coefficient. It is interesting that R_{uv} for large bump#3 and small bump#3 is unusually lower than 0.25 in the region of $|z|/H < 1$ and around $yu_t/\nu \approx 100$, while it is above 0.35 for the outer region and for the 2-DTBL. It is mainly due to the larger $\overline{u^2}$ present there, since the $-\overline{uv}$ values do not appear to be large in this zone. The R_{uv} for the larger $|z|/H$ behaves more like those for the undisturbed 2-DTBL.

4.2.5 Turbulent Kinetic Energy and its Diffusion Velocity Vector

Figure 4.22 show the turbulent kinetic energy,

$$TKE = \frac{\overline{q^2}}{2} = \frac{\overline{u^2} + \overline{v^2} + \overline{w^2}}{2} \quad (4.5)$$

normalized by U_{ref}^2 vs. yu_r/ν for each bump. Large bump#3 and small bump#3 have much higher TKE values across the flow in $|z|/H < 1$ than bump#1. The maximum TKE for bumps #3 shows about 4 % of a free-stream kinetic energy near the centerline. Away from the wall, the large turbulence levels are produced by the stream-wise vortices. However, for bump#1, the highest TKE values appear at $|z|/H = 0.81$ about 1.5 % of a free-stream kinetic energy. The span-wise locations close to and below the mean stream-wise vortex center show high TKE level instead of near the centerline. Bump#1 has lowest TKE distributions at the centerline for $100 \leq yu_r/\nu \leq 1000$. Bump#1 does not have an unsteady separation on the leeside which generates high velocity fluctuations. It has the strongest stream-wise vortices among three bumps which bring lower turbulence level flows toward the wall around the center. The relatively high TKE values produced near the stream-wise vortex center between the wall and the height of vortex center are mainly due to higher $\overline{w^2}$. There are no plateau nearly constant level regions for all three bumps.

Figure 4.23 shows contours of the turbulent kinetic energy, and the TKE transport velocity vectors in the y-z plane

$$\vec{V}_q = \frac{V_{qv}\vec{j} + V_{qw}\vec{k}}{U_{ref}} = \frac{\overline{vq^2}\vec{j} + \overline{wq^2}\vec{k}}{q^2 U_{ref}} \quad (4.6)$$

derived from the triple products which show the flow transport velocity vectors of the TKE by the turbulent diffusion. For the bumps #3 away from the wall in the region behind the bump, the large turbulence levels are generated by the massive separation from the leeside of bumps. However, bump#1 has much lower TKE and has the maximum level just below the vortex center instead of behind the bump. Large bump#3 doesn't show the maximum TKE near the center like small bump#3 because it brings high mean flow momentum more effectively from the free-stream. The transport vectors show the large transport of TKE away from where it has the greatest values. The TKE is transported mainly by the w' near the wall apparently due to the wall damping of v' . As the height increases, the transport by v' becomes dominant, especially around the centerline. The region $|z|/H > 1.6$ shows low values of the TKE and the transport velocity for each bump.

The large magnitude of these TKE transport velocity vectors shows some unsteadiness and jitter of the instantaneous flow. Their directions are about opposite to the mean velocity vectors when the instantaneous velocity is occasionally much lower than the mean velocity. Small bump#3 shows the most unsteady flow around the height of bump near the centerline. Asymmetric TKE transport velocity vectors appear again near the wall and the center due to asymmetric $\overline{w^3}$ distributions for small bump#3.

4.2.6 Townsend's Structural Parameter, A1

Figure 4.24 shows Townsend's structural parameter

$$A1 = \frac{\sqrt{(-\overline{uv})^2 + (-\overline{vw})^2}}{2TKE} \quad (4.7)$$

for each bump. It is a measure of the correlation between the magnitude of Reynolds shear stress and the twice of turbulent kinetic energy. It is about $0.1 \sim 0.13$ for $100 \leq yu_\tau / \nu \leq 1000$ in a 2-DTBL. All three bumps show lower A1 values than 2-DTBL in $|z|/H < 1$ in the inner region due to higher TKE generation and/or lower Reynolds shear stress magnitude in separated 3-DTBL than undisturbed 2-DTBL. It is interesting that large bump#3 and small bump#3 have approximately plateau A1 regions in $10 \leq yu_\tau / \nu \leq 100$ for $|z|/H < 1$ even though this parameter includes some inactive motions contributes to the TKE through $\overline{u^2}$, which are low frequency and long wavelength structures that produce little Reynolds shear stresses. That is why 1/S parameter in Eq.(4.4) is a better measure of the correlation for Reynolds shear stresses because $\overline{v^2}$ contains little contribution from these inactive turbulent motions. Finally, the TKE representation for the magnitude of Reynolds shear stresses which is the main purpose of this parameter in 2-DTBL (Bradshaw, Ferris and Atwell, 1967) does not work for the wake flow behind bumps since A1 is not constant across the flow.

4.2.7 Flow Angle, Flow Gradient Angle and Shear Stress Angle

Figure 4.25 ~ 4.27 show the flow angle(FA), the flow gradient angle(FGA) and the shear stress angle(SSA) for each bump, respectively.

The FA is calculated using

$$FA = \tan^{-1} \left(\frac{\overline{W}}{\overline{U}} \right). \quad (4.8)$$

It shows the degree of 3-dimensionality of the flow. It is approximately constant up to $yu_\tau/\nu \approx 100$ for large bump#3 and bump#1. However, for small bump#3, it varies semi-logarithmically in $20 < yu_\tau/\nu < 400$ and the flow seems to be almost collateral at most z/H within $yu_\tau/\nu \leq 10$. For large bump#3 and bump#1, the FA values are close to zero at $yu_\tau/\nu \approx 1000$ in all z/H like \overline{W} profiles. Bump#1 has the largest FA variation within about $\pm 37^\circ$ at $|z|/H = 0.65$ among three bumps. Generally, for all bumps, the FA values tend to increase with the z/H moving from the centerline to the stream-wise vortex center. Then, for the z/H farther from the vortex center, the FA values reduce to nearly zero.

The FGA is calculated using

$$FGA = \tan^{-1} \left[\frac{\partial \overline{W} / \partial y}{\partial \overline{U} / \partial y} \right]. \quad (4.9)$$

These mean velocity gradients in the y -direction are computed by least-square fitting parabolas to \overline{U} and \overline{W} profiles at each successive five points and the derivatives are computed from the derivative of the parabolas at the middle point. The FGA gives the flow strain change associated with the flow in the x - z plane.

The SSA is calculated using

$$SSA = \tan^{-1} \left(\frac{-\overline{vw}}{-\overline{uv}} \right) \quad (4.10)$$

which gives the directions of the Reynolds shear stress vectors in the x - z plane. It is noted that the SSA for small bump#3 shows asymmetry due to \overline{vw} as mentioned before. For all bumps, the FGA

shows a similar trend across the flow. Large bump#3 and bump#1 has almost constant FGA values between the wall and the height up to $yu_\tau/\nu \approx 40$ for all z/H . After this height, the FGA values reduce to nearly zero at $yu_\tau/\nu \approx 80$. From this height, the FGA values begin to increase significantly and reach maximum at $yu_\tau/\nu \approx 300 \sim 500$ in z/H between the centerline and the stream-wise vortex center. As the height increases, the FGA values reduce to almost zero again at $yu_\tau/\nu \approx 2000$. For small bump#3, the FGA values show a slow decrease up to $yu_\tau/\nu \approx 30$ where most z/H profiles have a nearly zero FGA. Above this height, the FGA values increase and have maximum at $yu_\tau/\nu \approx 150$ in z/H between the centerline and the stream-wise vortex center. As the height increases, the FGA values reduce up to $yu_\tau/\nu \approx 1200$. For all bumps, like the FA behavior, the FGA values tend to increase with the z/H moving from the centerline to the stream-wise vortex center. For large bump#3 and bump#1, the span-wise flow changes faster than the stream-wise flow at $300 \leq yu_\tau/\nu \leq 900$.

The SSA profiles have a similar behavior as the FGA for all bumps. However, one can see that there are differences and misalignments between the FGA and SSA vectors, which indicate that the flow is anisotropic.

4.2.8 Anisotropy factor, N

Figure 4.28 show the anisotropy factor N for each bump. The N is calculated using

$$N = \frac{\tan(SSA)}{\tan(FGA)} = \frac{-\overline{vw}/(\partial\overline{W}/\partial y)}{-\overline{uv}/(\partial\overline{U}/\partial y)} = \frac{\nu_{Tz}}{\nu_{Tx}} \quad (4.11)$$

where ν_{Tx} and ν_{Tz} are the stream-wise and span-wise eddy viscosity which are discussed later. The FGA and SSA vectors are in the same direction if the effective eddy viscosity is isotropic. The difference between FGA and SSA gives the anisotropy of the flow and how the anisotropy develops with increasing 3-dimensionality of the flow. Many eddy viscosity turbulence models still use the isotropic eddy viscosity in which the N is equal to unity to calculate 3-D turbulent flows. However, as expected from the FGA and SSA distribution in Fig. 4.26 and Fig. 4.27, the N is not unity except

at some y locations for any of the bumps. The N values are scattered where the \overline{W} derivatives in y -direction are close to zero because the N values go to infinity as the \overline{W} derivatives in the y -direction approach zero. The N values have between 0 and 1 since the Reynolds shear stresses lag the mean velocity gradient. The decorrelation between \overline{uv} and \overline{vw} causes the negative N values. Therefore, the isotropic eddy viscosity models are not proper in order to predict the wake flow of these bumps.

4.2.9 Mixing Length and Eddy Viscosity

The mixing length and the stream-wise and span-wise eddy viscosity are calculated using

$$L_m = \frac{\sqrt[4]{(-\overline{uv})^2 + (-\overline{vw})^2}}{\sqrt{(\partial \overline{U} / \partial y)^2 + (\partial \overline{W} / \partial y)^2}} \quad (4.12)$$

$$\nu_{Tx} = \frac{-\overline{uv}}{\partial \overline{U} / \partial y} \quad (4.13)$$

$$\nu_{Tz} = \frac{-\overline{vw}}{\partial \overline{W} / \partial y} \quad (4.14)$$

Figure 4.29 and Figure 4.30 ~ 4.31 show the normalized mixing length and eddy viscosity for each bump. It is noted that $L_m u_\tau / \nu$ is plotted within the range from 0 to 500 even though bump#1 has the negative values at some locations. For all three bumps, $L_m u_\tau / \nu$ values increase as the height increases from the wall. The two bumps #3 show a significant difference in $L_m u_\tau / \nu$ values between $|z|/H \leq 0.81$ and $|z|/H \geq 0.98$ above $y u_\tau / \nu \approx 100$ while in bump#1 most z/H profiles collapse together except very close to the centerline. The ν_{Tx} / ν values also are much higher in $|z|/H \leq 0.81$ for two bumps #3. However, for bump#1, the ν_{Tx} / ν values are smaller in $|z|/H \leq 0.49$ below $y u_\tau / \nu \approx 200 \sim 300$ than the farther z/H from the centerline. Near this height, the ν_{Tx} / ν shows negative values due to negative \overline{U} derivatives in the y -direction. As shown in Fig. 4.28 the

span-wise eddy viscosity ν_{Tz} / ν values are scattered and relatively large which means that there are the strong interactions along the span-wise direction as well.

In order to evaluate algebraic eddy viscosity models, several models are tested and plotted in Fig. 4.30 ~ 4.31 only for the inner layer. Even though many advanced turbulence models have been developed, these models are the simplest to use because they do not have to solve the continuity, momentum and other turbulent transport equations. The selected isotropic models are Van Driest's model (Schetz, 1993), Patel's model (Chen and Patel, 1988) and Johnson-King's model (J-K, 1985). There are two more models, Cebeci-Smith's model (1984) and Rotta's model (1980) which were tested by Ölçmen and Simpson (1993) for 3-DTBL. These two models were also evaluated for three bumps. However, they use Van Driest damping function and show little improvement from the first three models even though Rotta's model includes the anisotropic constant T . Therefore, the predictions of the first three models are plotted. Patel's model uses TKE in order to define the eddy viscosity and mixing length while Johnson-King's model uses the maximum Reynolds shear stress in the layer to define the eddy viscosity and the Van Driest damping function. All necessary quantities like the mean velocities, their gradients in the y -direction and maximum Reynolds shear stress are taken from present data.

Two span-wise locations are selected, $z/H=0$ and -0.98 for comparisons because several simulations for large bump#3 introduced in Chap. 1 have shown the poor agreement with present data especially near the centerline. For the mixing length, only the Van Driest model shows fair agreement below $yu_\tau / \nu \approx 40$ and other models show over estimations for large bump#3 and bump#1. For small bump#3, the Van Driest model agrees well with data up to $yu_\tau / \nu \approx 100$ for $z/H = -0.98$. Patel's estimations are worst for all three bumps.

For the eddy viscosity, the Van Driest model is better in the very near wall below $yu_\tau / \nu \approx 20 \sim 30$ and other models are better in $100 < yu_\tau / \nu < 400$ for bumps #3. For bump#1, near the wall region, the Van Driest model shows over estimations, especially at the centerline. Evidently, no selected algebraic eddy viscosity model is proper for the bump flow.

4.2.10 Span-wise Velocity Spectra

In order to examine the large scale unsteadiness of the separated flow, a spectrum analysis of the span-wise velocity fluctuation w data at $z/H = 0$ was performed for each bump using a slotting technique (Roberts, 1986). Figure 4.32 shows the w spectra G_{ww} which is defined as

$$\overline{w^2} = \int_0^{\infty} G_{ww}(f) df \quad (4.15)$$

where, f is the frequency, Hz. The spectra, G_{ww} are normalized by the bump height H and U_{ref} for large bump#3 at $y/H = 0.2$ ($yu_{\tau}/\nu \approx 900$), small bump#3 at $y/H = 0.12$ ($yu_{\tau}/\nu \approx 244$) and bump#1 at $y/H = 0.17$ ($yu_{\tau}/\nu \approx 700$), respectively, which are at the heights of the mean vortex center of each bump. The maximum $\overline{w^2}$ at the centerline occurred at about the same height. Although the LDV coincident data rate was about 200 Hz, low frequencies with high spectral levels could be examined.

For large bump#3 the spectrum has a peak at $fH/U_{ref} \approx 0.003$ and a f^{-1} slope for $0.003 < fH/U_{ref} < 0.1$. For small bump#3 the spectrum also has local peaks at $fH/U_{ref} \approx 0.009$ and 0.05 . These results suggest low frequency large amplitude span-wise meandering of the large shed vortex structures in the bumps #3, such as suggested by Ishihara et al. (1999) and perhaps a large eddy simulation (Patel et al., 2003). Ma and Simpson (2005) also captured these large amplitude spectra in low frequencies for the same bump. Small bump#3 shows higher meandering frequency motion and more unsteadiness. Bump#1, however, shows much lower spectrum levels in the entire frequency range. It indicates that the span-wise meandering motion of bump#1 is much weaker than for bumps #3.

4.3 Estimation of Dissipation Rate

The stream-wise spectra G_{uu} defined as

$$\overline{u^2} = \int_0^{\infty} G_{uu}(f) df \quad (4.16)$$

is used in order to examine the turbulent kinetic energy dissipation rate by the smallest turbulent eddies in separated turbulent boundary flows at the wake plane of each bump. Even though the LDV time series data were used for the w spectra previous section, it is definitely not enough to estimate the dissipation rate ε from the spectra because much higher frequency information is necessary. Therefore, hot-wire data measured at the same wake planes of each bump are used instead.

Ma and Simpson (2005) measured identical flow fields for each bump using hot-wire anemometer probes and reported large scale and low frequency turbulence structures for large bump#3. They used a miniaturized four-sensor hot-wire with an approximate 0.5 mm^3 measurement volume. For spectral measurements, the 60 records of 2^{18} samples were recorded at each measurement point with a sampling rate of 25.6 kHz. So, the frequency range is from 0.1 Hz to 12.8 kHz with a resolution of a 0.1 Hz. However, they did not calculate the dissipation rate. The following estimation and analysis have been done using their hot-wire probe data.**

A possible error in spectrum measurements and the estimation of dissipation rate is due to the hot-wire length. There are many papers concerning the effect of finite hot-wire length on the spectrum measurement. When the finite hot-wire length l , is greater than the transverse Taylor's microscale, it tends to attenuate the spectral level in high frequency (high wavenumber) region and the estimation of dissipation rate as well. Wyngaard (1968) and Elsner et al. (1993) proposed the correction function based on Pao's (1965) 3-D spectrum. However, Pao's spectrum is true only in the case of isotropic and homogeneous turbulent flows with sufficiently high Reynolds number, which means that Pao's spectrum is not an adequate representation of the true spectrum.

Therefore, Derksen and Azad (1983) suggest another correction method for dissipation rate which does not use any spectrum models. Actually it came from a correction for the integral length scale given by Hinze (1975). However, their method also was based on the assumption which the

** I appreciate Dr. Ruolong Ma allowing to use his hot-wire probe data.

transverse integral lengthscale was nearly equal to the transverse Taylor microscale. This assumption is not reasonable for the present study because Ma and Simpson (2005) estimated the transverse integral lengthscale of $1.5H$ at the wake plane of large bump#3 and the transverse Taylor microscale is calculated as about $0.02H$ in the present study even though it depends on the accuracy of estimated ε .

The last correction method considered was given by Azad and Kassab (1989). They calculated the dissipation rate from the integration of the 1-D spectra from the different lengths of hot-wire and then extrapolated the dissipation rate to zero length. Even though it seems to be the most reasonable correction method, the spectrum from the different hot-wire length are not available from Ma and Simpson (2005). Finally, the dissipation rates for each bump presented here are not corrected for the length effect. It should be noted that the spectral attenuation due to the finite hot-wire length appears in the very high wavenumber region, mainly in the dissipation region. However, the spectra used here do not completely cover the entire dissipation frequency range. Therefore, the calculation of dissipation rate from the inertial range curve fitting would be little affected by the hot-wire length.

The dissipation rate ε can be estimated by several methods. The integration of 1-D stream-wise spectra is able to give the dissipation rate.

$$\varepsilon = 15 \int_0^{\infty} \nu \kappa_1^2 G_{uu}(\kappa_1) d\kappa_1 \quad (4.17)$$

In Eq.(4.17), κ_1 is the stream-wise wavenumber. The κ_1 and $G_{uu}(\kappa_1)$ can be calculated from f and $G_{uu}(f)$ using Taylor's hypothesis.

$$\kappa_1 = \frac{2\pi f}{U} \quad (4.18)$$

$$G_{uu}(\kappa_1) = \frac{\overline{U} G_{uu}(f)}{2\pi} \quad (4.19)$$

Actually, Eq.(4.17) comes from the assumption of homogeneous isotropic turbulence. Therefore, it can not be used for non-isotropic turbulence. However, the κ_1^{-2} in the integral magnifies the influence of high frequencies which are more like isotropic and reduces the influence of low frequency motions. Therefore, as Larssen (2005) mentioned, the dissipation rate has to be taken as the asymptotic value of the integral. Figure 4.33 shows the cumulative sum of the integrand in Eq.(4.17) for the large bump#3 stream-wise spectra. Unfortunately, it does not converge, which means that there is not enough high frequency range to estimate the dissipation rate. Therefore, the inertial subrange curve fitting has used to calculate the dissipation rate instead.

The inertial subrange is the intermediate range of the energy spectrum between the energy containing range and the dissipation range. According to Kolmogorov hypotheses, this inertial subrange depends only on the dissipation rate and has a -5/3 power-law spectrum for turbulent flows at relatively high Reynolds number given by (Pope, 2000):

$$G_{uu}(\kappa_1) = 0.49\varepsilon^{2/3}\kappa_1^{-5/3} \quad (4.20)$$

Finally, the dissipation rate ε was estimated by the least square curve fitting of 1-D stream-wise spectra. Figure 4.34 shows an example of a curve fit in a Kolmogorov scaling. The solid line is corresponding to Eq.(4.20) and the dashed lines indicate the curve fitting range. The model equation is fitted well in the inertial subrange with the correlation coefficient $R_c = 0.994$. It should be noted that the goodness of least square fit is dependent on the fitting range which is indicated by the dashed lines. Pope (2000) showed that the $-5/3$ power-law and local isotropic behavior of $G_{uu}(\kappa_1)/(\varepsilon\nu^5)^{1/4}$ appeared in $2 \times 10^{-3} < \kappa_1\eta < 10^{-1}$ for many different turbulent flows measured by Saddoughi and Veeravalli (1994).^{††} He also showed that the $G_{uu}(\kappa_1)/(\varepsilon\nu^5)^{1/4}$ value began to depart from the -5/3 power-law around at $\kappa_1\eta = 10^{-1}$ and to decay faster in $\kappa_1\eta > 10^{-1}$ as shown in Fig. 4.34. It may be a simple method to verify the estimation of the dissipation rate from the curve fitting. However, $G_{uu}(\kappa_1)$ at some wake plane locations have the -5/3 power behavior in smaller wavenumber range or it does not show the -5/3 law, especially for bump#1 (see Appendix C),

^{††} See pp.234 – 240 in Pope (2000).

which results in lower correlation coefficients and relatively higher uncertainties of ε . It may be because the Taylor Reynolds number is not much higher than 100 which is the condition for the existence of an inertial subrange in turbulent flows suggested by Bradshaw (1969).

Table 4.1 presents the dissipation rates and macro lengthscales of each bump estimated at the centerline ($z/H = 0$) in wake planes. The uncertainty of estimated ε was calculated from the root mean square difference σ between each $G_{uu}(\kappa_1)$ calculated from Eq.(4.20) which is a least squares curve fit of these same points, and its corresponding measured $G_{uu}(\kappa_1)$ value. The 95 % confidence level uncertainties are 1.96σ . The dissipation and longitudinal integral lengthscales in Table 4.1 are defined by

$$L_\varepsilon = TKE^{3/2} / \varepsilon \quad (4.21)$$

$$L_{11} = \frac{\pi}{2u^2} \lim_{\kappa_1 \rightarrow 0} G_{uu}(\kappa_1) \quad (4.22)$$

The lowest wavenumber spectrum is used for the limiting $G_{uu}(\kappa_1)$ value in Eq.(4.22). As Larssen (2005) mentioned, the estimation of the integral lengthscale using Eq.(4.22) depends too much on the lowest wavenumber spectrum which is highly uncertain for the limiting value because of the limited samples. In spite of this imperfection, Eq.(4.22) is used to obtain the integral lengthscale because of limited available hot-wire spectrum data.

Figures 4.35 and 4.36 show the normalized dissipation rates and macro lengthscales of each bump at the centerline of wake planes. The small bump#3 generates the highest dissipation rate among three bumps across the centerline at the wake plane while bump#1 shows much lower dissipation rate than bumps #3. Compared with the dissipation rate of a reference 2-DTBL

estimated by $-\overline{uv} \frac{\partial \overline{U}}{\partial y}$ in a semi-logarithmic region assuming the convection and diffusion of TKE

are negligible, the dissipation rates in the wake plane of bumps #3 are higher than in a 2-DTBL. However, the dissipation rates of bump#1 are even much smaller than of a 2-DTBL. The bumps #3 which generate strong 3-D separations on the wide leeside region have large macro lengthscales at the wake plane centerline. The larger dissipation lengthscales appear for large bump#3 than other bumps. Bumps #3 show relatively large dissipation lengthscales across the centerline about 1.6 ~

2.8 times of δ which is a boundary layer thickness of a reference 2-DTBL. It is interesting that for large bump#3, the longitudinal integral lengthscales are bigger than the dissipation lengthscales across the centerline. It may be due to much higher limiting $G_{int}(\kappa_1)$ values in Eq.(4.22) which result from dominant large scale low frequency flow structures in the wake plane. The presented separated 3-DTBLs in the wake planes of each bump show much higher L_x / δ values than in a separated 2-DTBL measured Simpson et al. (1977).

4.4 Summary of Flow Structures of Each Bump at Wake Plane

Figure 4.37 and 4.38 illustrate the flow structures at the measured wake planes for bumps #3 and bump#1. The mean flow appears to be closely symmetric about the centerline for each case. Vortical separations occur on the leeside and merge into 2 large stream-wise vortices downstream. These stream-wise vortices generate non-equilibrium 3-D turbulent flows behind each bump.

The LDV and oilflow results downstream of the bump are clearly consistent with one another. For each bump, the flow along the stream-wise centerline is a downwashing reattachment flow with only one mean vortex on each side of the centerline away from the wall showing higher skin friction velocity magnitude in large bump#3 and bump#1.

In spite of a different height between large and small bump#3, they show similar flow structures compared with bump#1. For large and small bump#3 having the massive 3-D separations on the leeside, at the downstream measurement plane, the near-wall flow is dominated by the wall, while the vortices in the outer region produce large turbulence levels near the centerline and appear to have low frequency motions that contribute to turbulent diffusion. Bump#1, which has a different flow separation pattern showing a relatively sharper separation on the surface than from the bumps #3, creates a stronger stream-wise vortex with very low turbulence levels and more steadiness. Bump#1 is a much more effective vortex generator than bumps #3 for producing higher span-wise mean velocity flow near the wall.

The bumps #3 produce much higher Reynolds shear stress in outer region than bump#1 due to large eddies with the stream-wise vortices near the centerline. Bump#1 shows much lower Reynolds shear stress magnitude across the flow and even lower than a 2-DTBL in the inner region near the centerline. However, bump#1 shows relatively high Reynolds shear stress related w

fluctuations in inner region near the vortex center. The selected correlation parameters like $1/S$, R_{uv} and $A1$ are not correlated well in inner layer near the centerline even though they show similar behavior. It makes the turbulent modeling for these flows difficult.

The FA, FGA and SSA change much across the flow for each bump due to the effect of high three-dimensionality with the stream-wise vortices. All bumps show a misalignment between FGA and SSA suggesting the flow is nonisotropic. Therefore, any mixing length and eddy viscosity models tested here do not show good agreement with presented data.

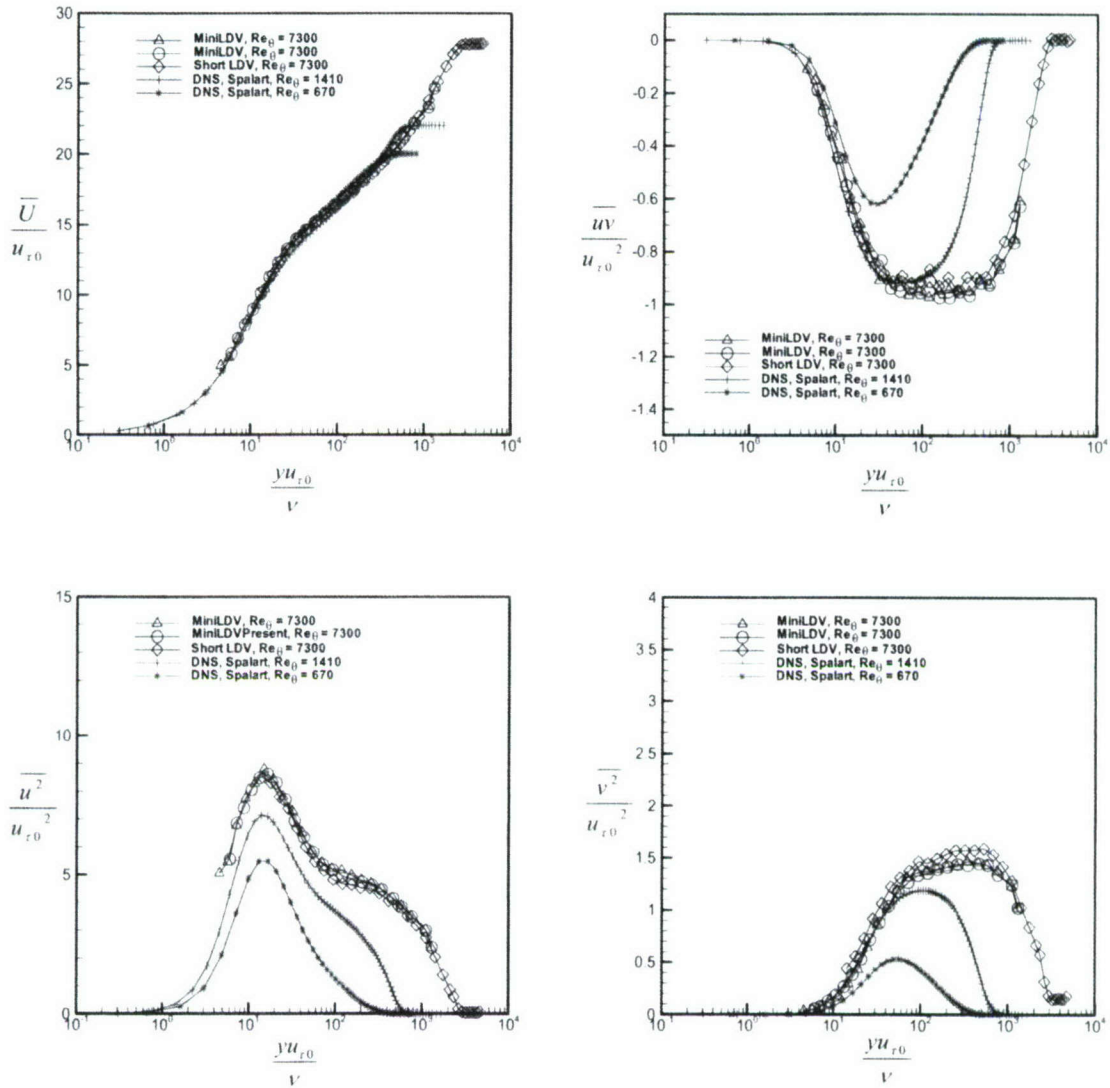
From the 1-D stream-wise and span-wise spectrum of the hot-wire (Ma and Simpson, 2005) and the presented LDV measurements, the bumps #3 show much higher spectral levels in lower wavenumbers than bump#1, which means they have large eddies containing higher TKE. The longitudinal integral lengthscales which is characterizing the larger eddies are larger than the bump height in size near the centerline. Therefore, the low frequency large scale eddies are more dominant in the wake of bumps #3 than bump#1.

Dr. Ma conducted two-point hot-wire probe measurements at the wake plane of large bump#3. The probes were located at near the center of stream-wise vortices on each side. He captured much higher u component coherency below 7 Hz than other components. It may indicate that the large scale flow structures are generated by the unsteady separations on the large portion of bump leeside. It may also suggest that there are no correlations of the leeside separations representing that the one side is separated and the other side attached. More details are discussed in his paper near future.^{††}

From the TKE profiles and its transport vectors in y - z plane, it can be expected the TKE production and its dissipation are not balanced for bumps #3 because the TKE values increase as the height from the wall increases and there are no plateau regions across the flow. Furthermore, its transport vectors have a large magnitude near the centerline. This suggests that their occasional jittering motions increase the turbulent diffusion which is not negligible behind the bumps. Thus, the triple velocity correlations for turbulent models are important to predict these flows properly. However, for bump#1, the TKE profiles show some plateau regions in the log layer near the centerline and the magnitude of TKE transport vectors is much smaller than bumps #3. This means

^{††} Personal communication with Dr. Ruolong Ma.

that the TKE production rate and its dissipation rate are more balanced and the TKE diffusion by turbulent motions are less significant.



Two miniLDV data sets (Δ, O). Short LDV data from George and Simpson (2000).

Figure 4.1 Comparison of 2-DTBL data with miniLDV, short LDV data and DNS results.

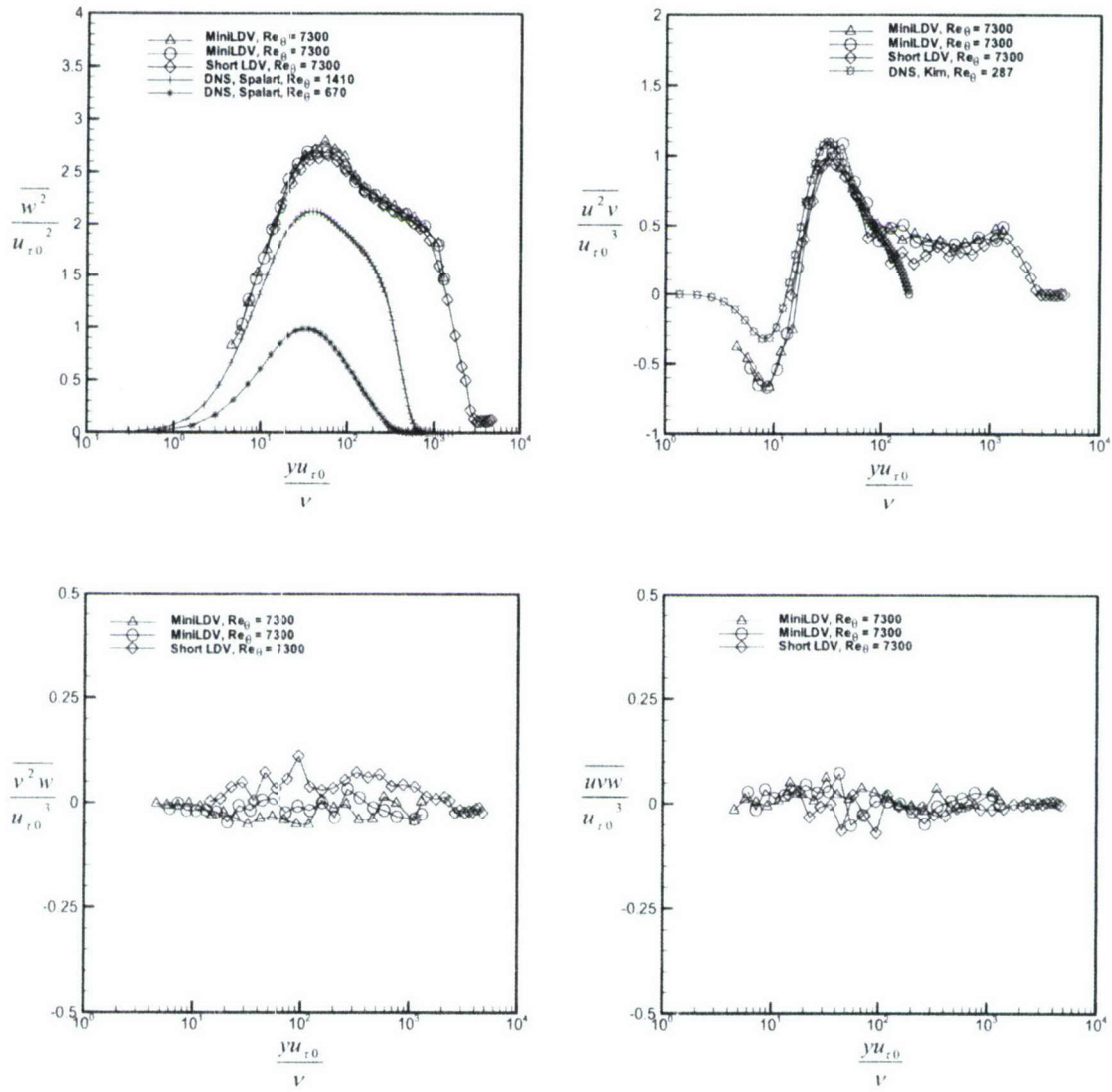


Figure 4.1 Continued.

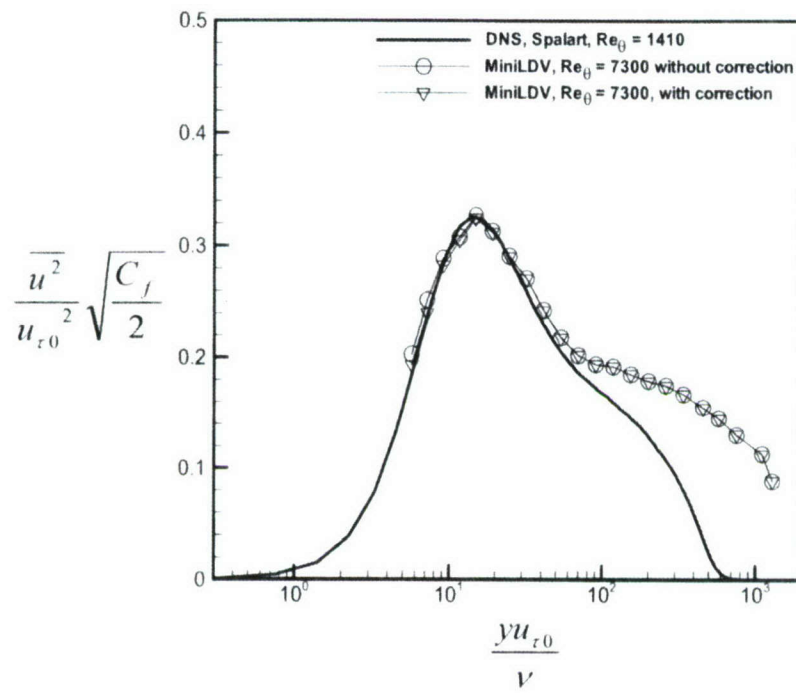
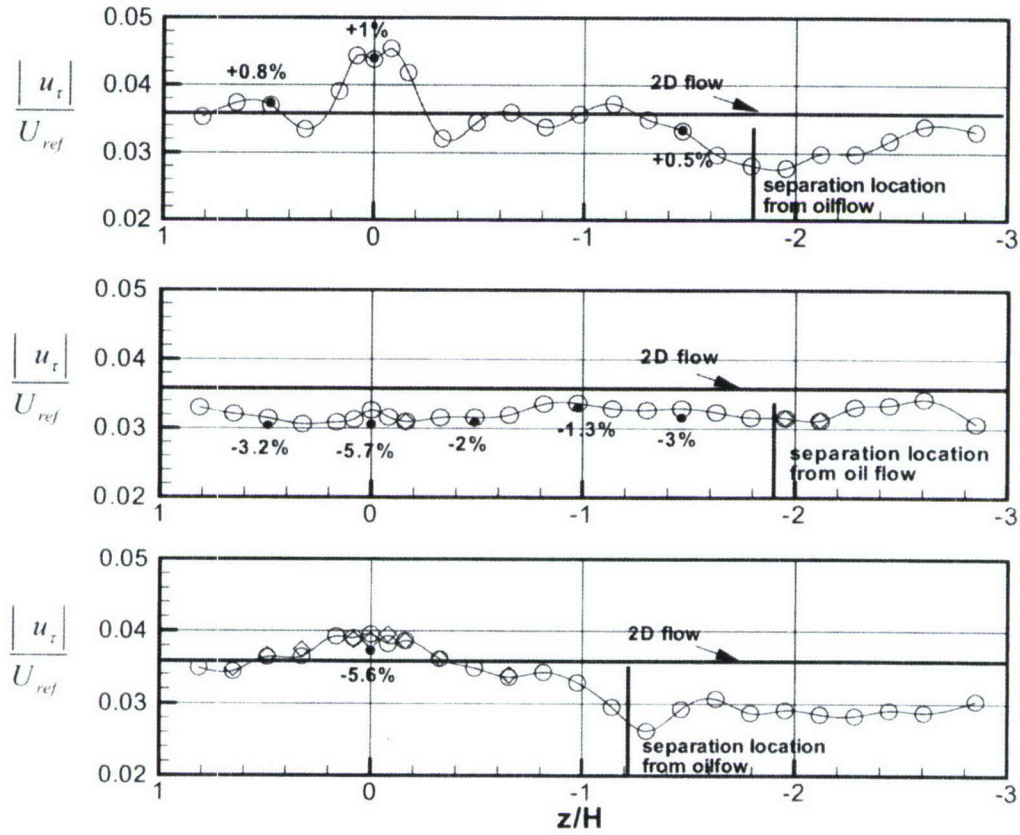


Figure 4.2 Effect of velocity gradient broadening.

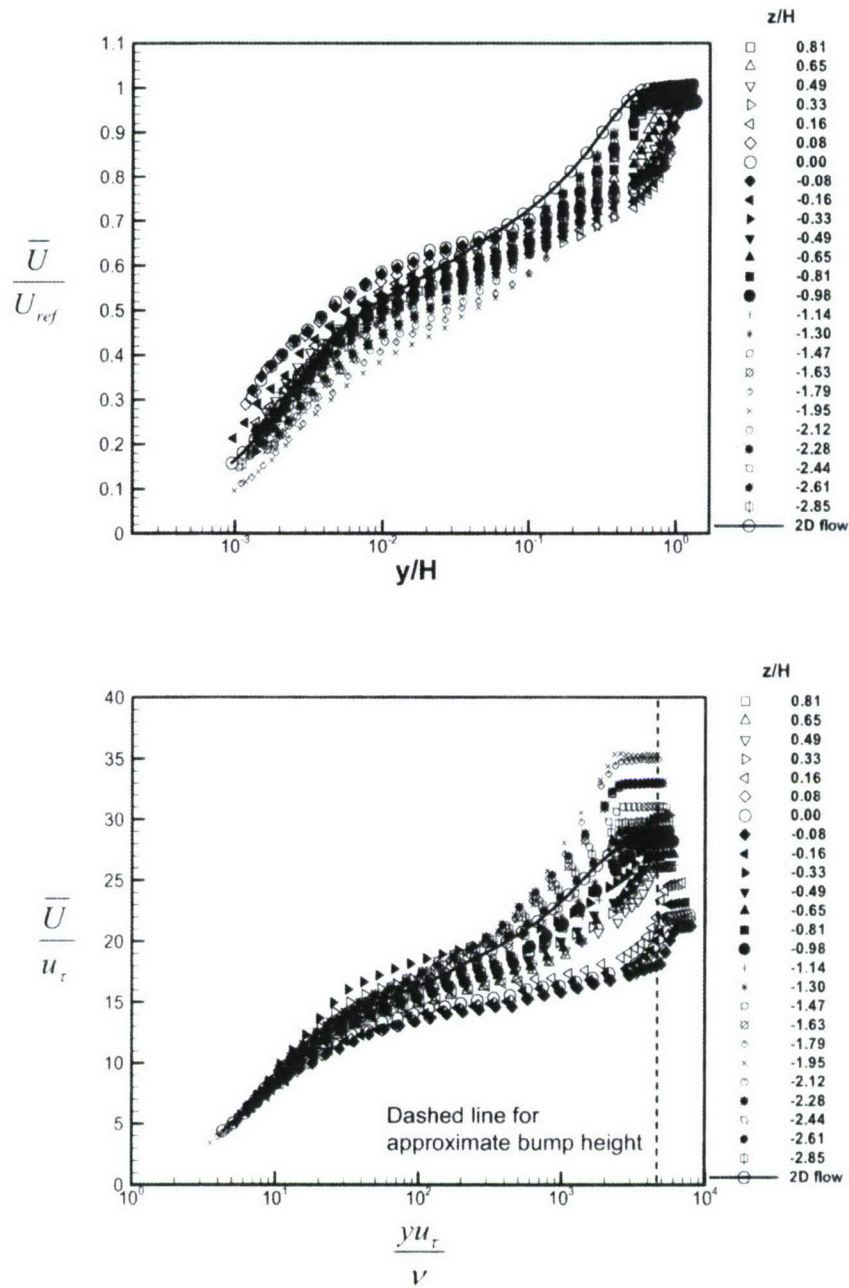


Top to bottom : large bump#3 ($x/H=3.63$), small bump#3 ($x/H=3.26$) and bump#1 ($x/H=3.46$).

Results from multiple profiles shown as multiple symbols.

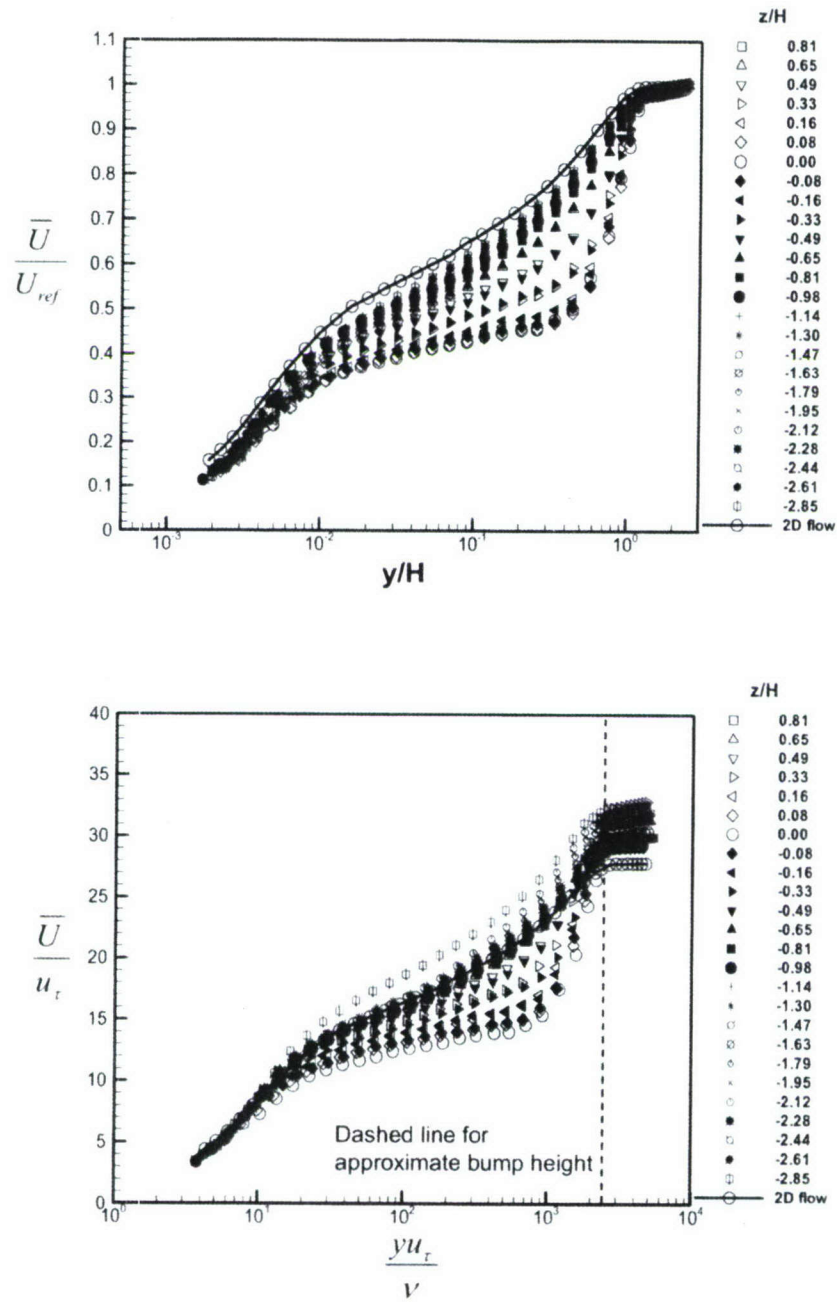
Filled circles and percentage show results with pressure gradient effect.

Figure 4.3 $|u_\tau|/U_{ref}$ vs. z/H for 3 different bumps.



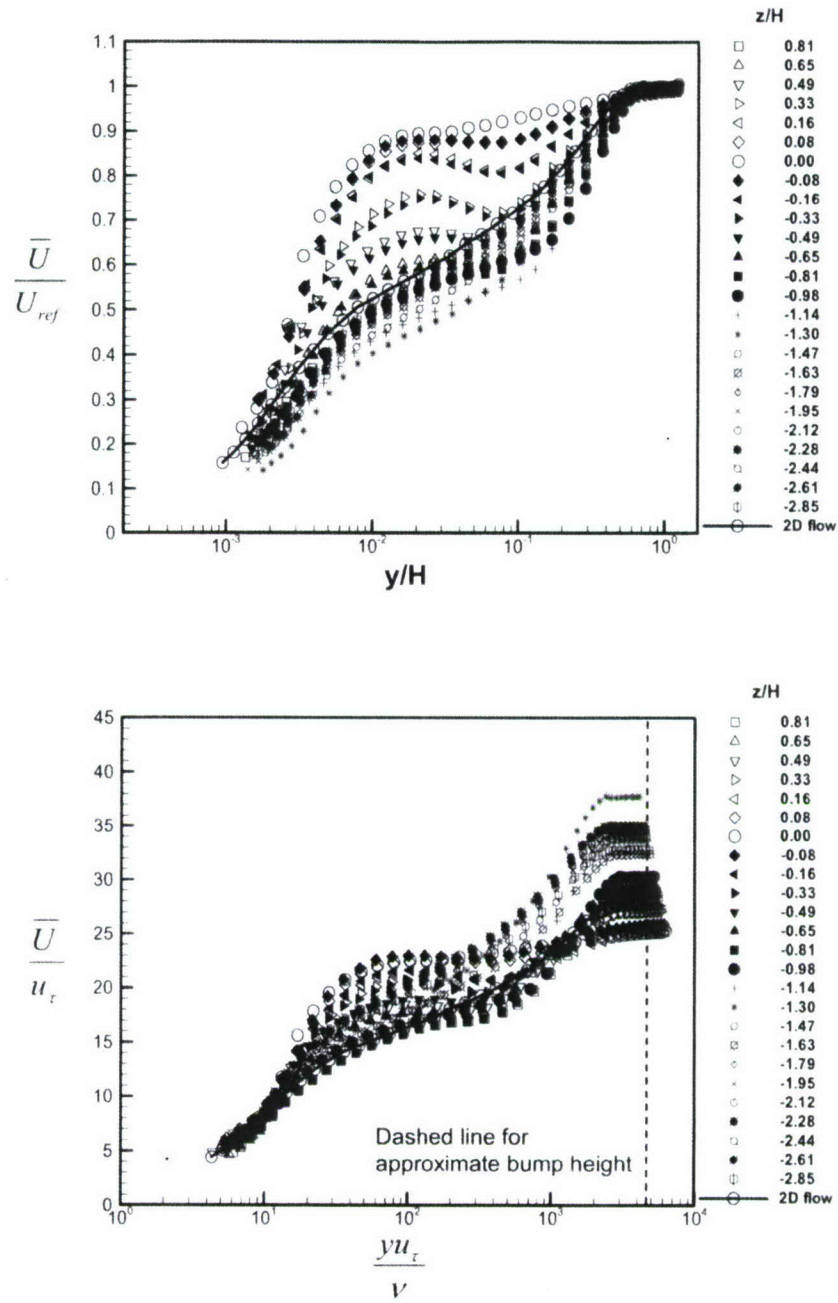
Top : normalized by U_{ref} and H . Bottom : normalized by u_τ .

Figure 4.4 Large bump#3 Mean velocity \bar{U} at wake plane, $x/H=3.63$.



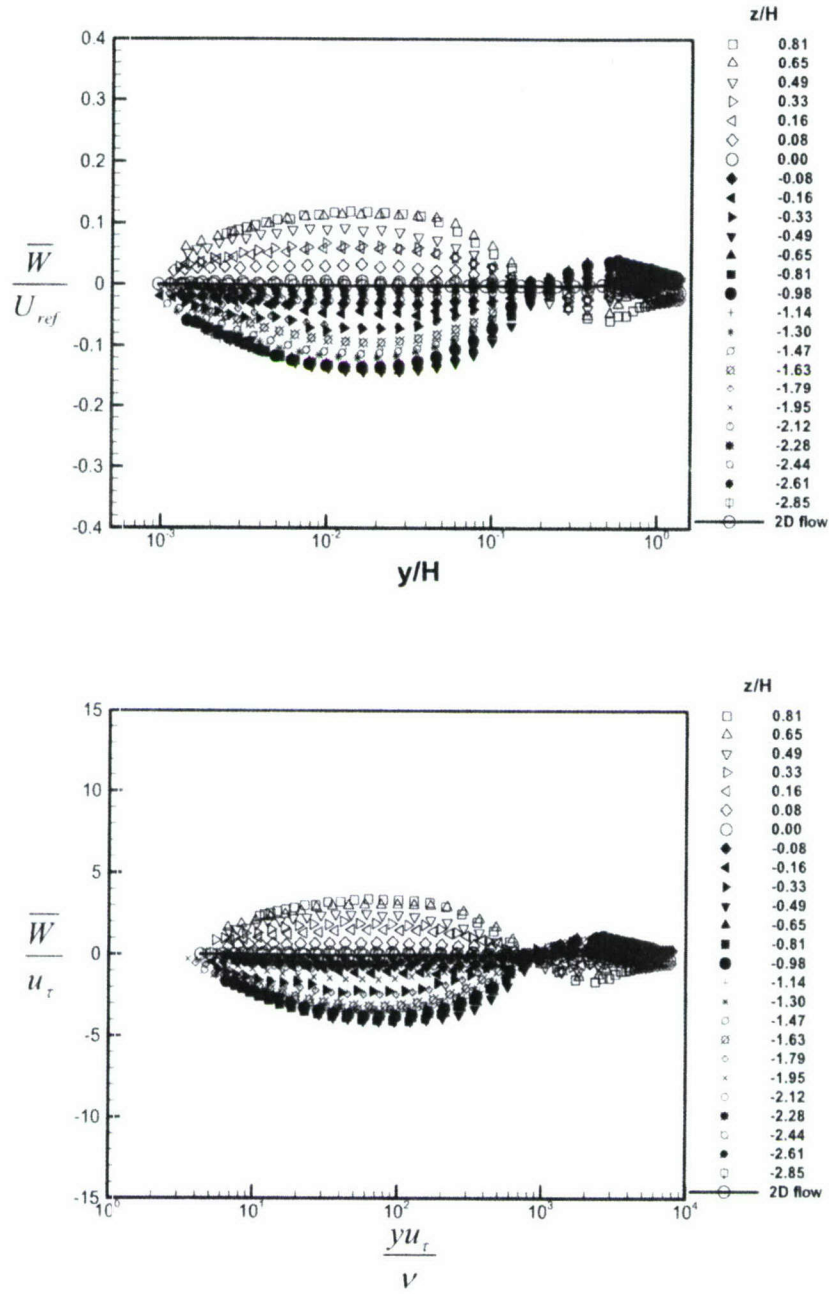
Top : normalized by U_{ref} and H . Bottom : normalized by u_τ .

Figure 4.5 Small bump#3 Mean velocity \bar{U} at wake plane, $x/H=3.26$.



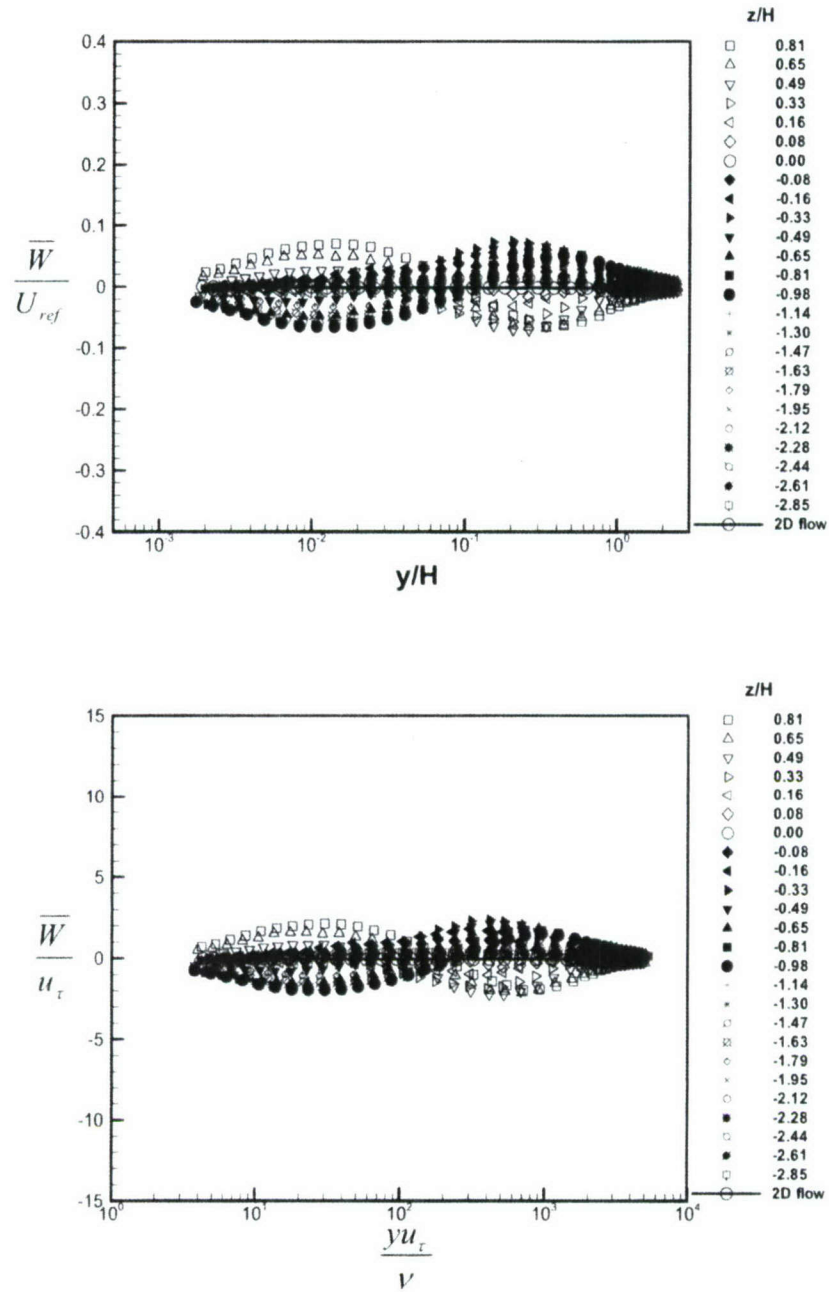
Top : normalized by U_{ref} and H . Bottom : normalized by u_τ .

Figure 4.6 Bump#1 Mean velocity \bar{U} at wake plane, $x/H=3.46$.



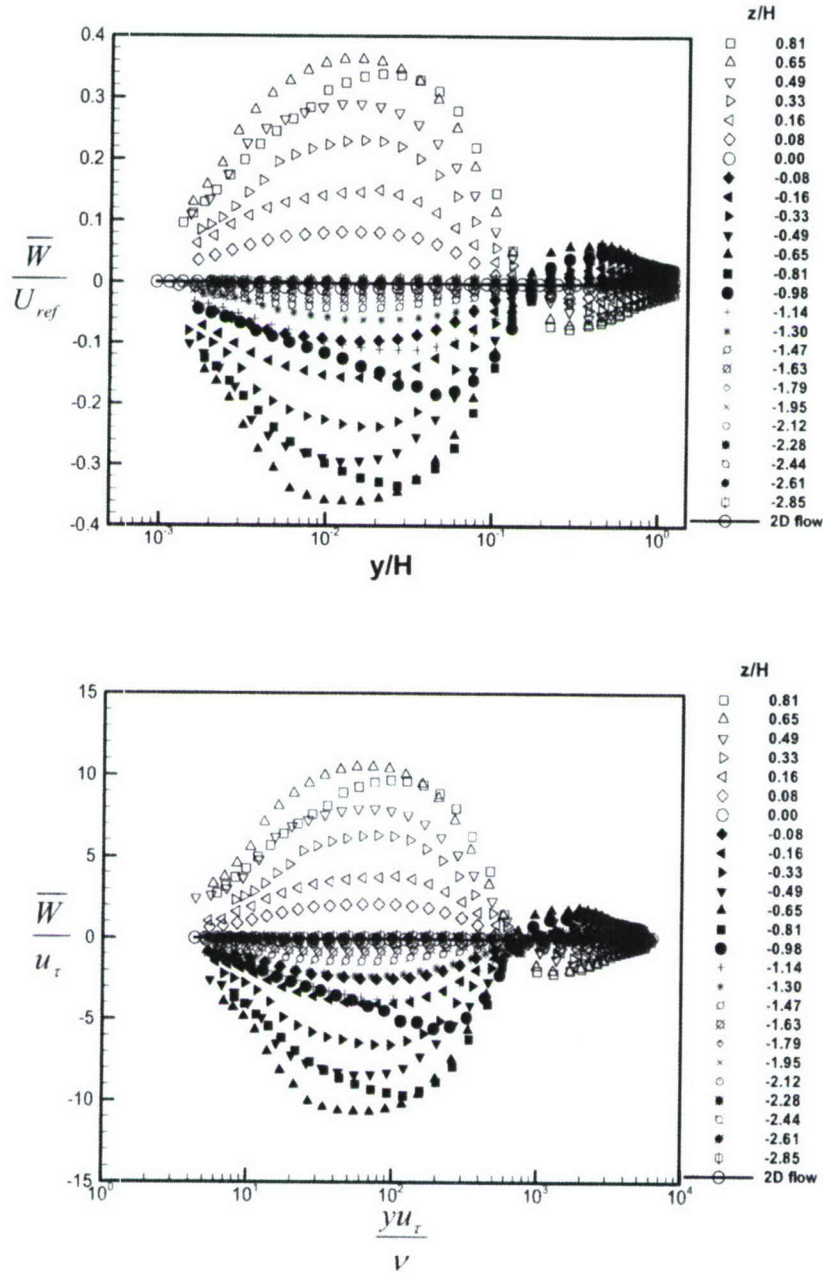
Top : normalized by U_{ref} and H . Bottom : normalized by u_τ .

Figure 4.7 Large bump#3 Mean velocity \overline{W} at wake plane, $x/H=3.63$.



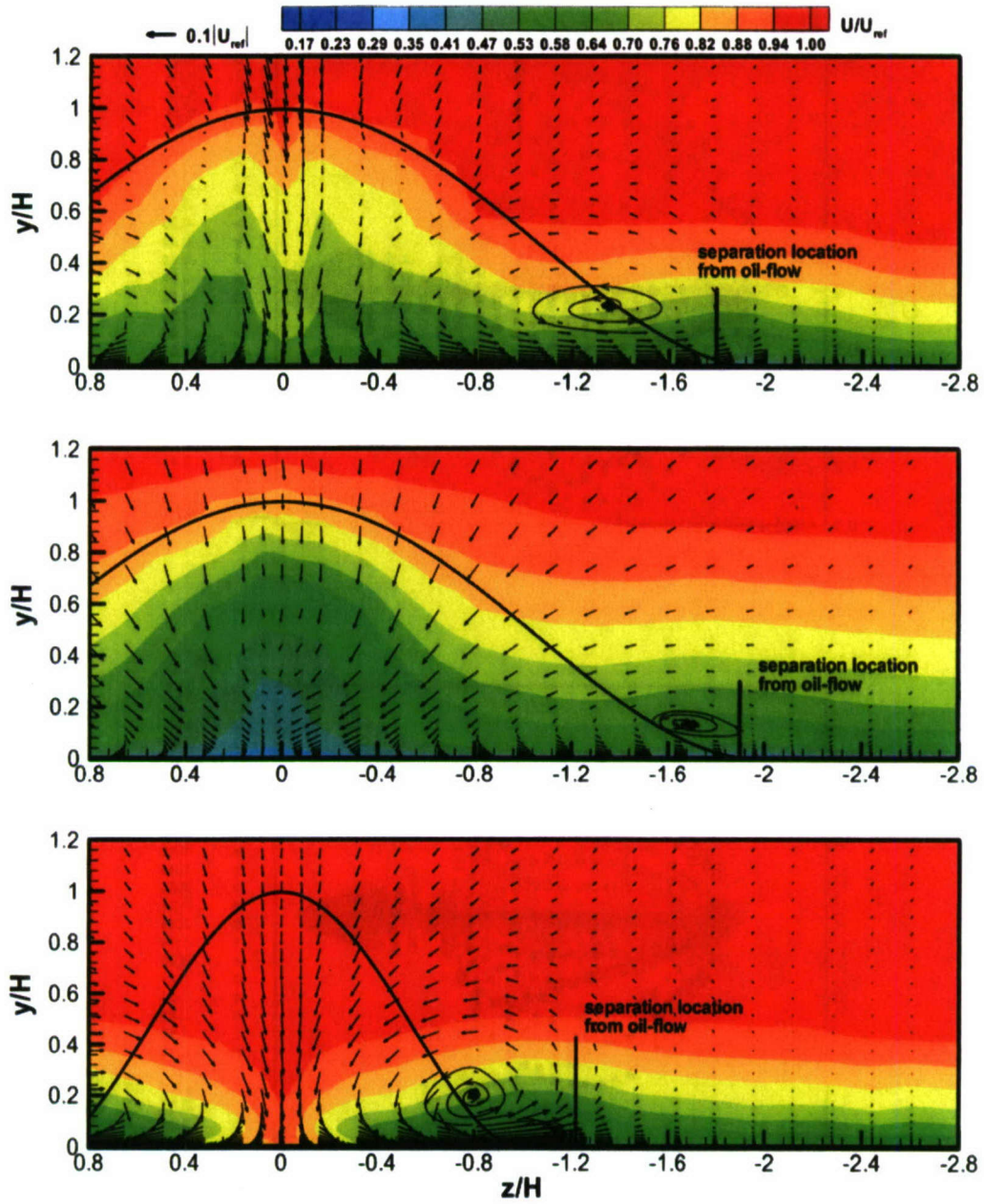
Top : normalized by U_{ref} and H . Bottom : normalized by u_τ .

Figure 4.8 Small bump#3 Mean velocity \overline{W} at wake plane, $x/H=3.26$.



Top : normalized by U_{ref} and H . Bottom : normalized by u_τ .

Figure 4.9 Bump#1 Mean velocity \overline{W} at wake plane, $x/H=3.46$.



(a) Linear scale

Top to bottom : large bump#3 ($x/H=3.63$), small bump#3 ($x/H=3.26$) and bump#1 ($x/H=3.46$).

Figure 4.10 Mean velocity pattern. \bar{U} contour and \bar{V} , \bar{W} vectors.

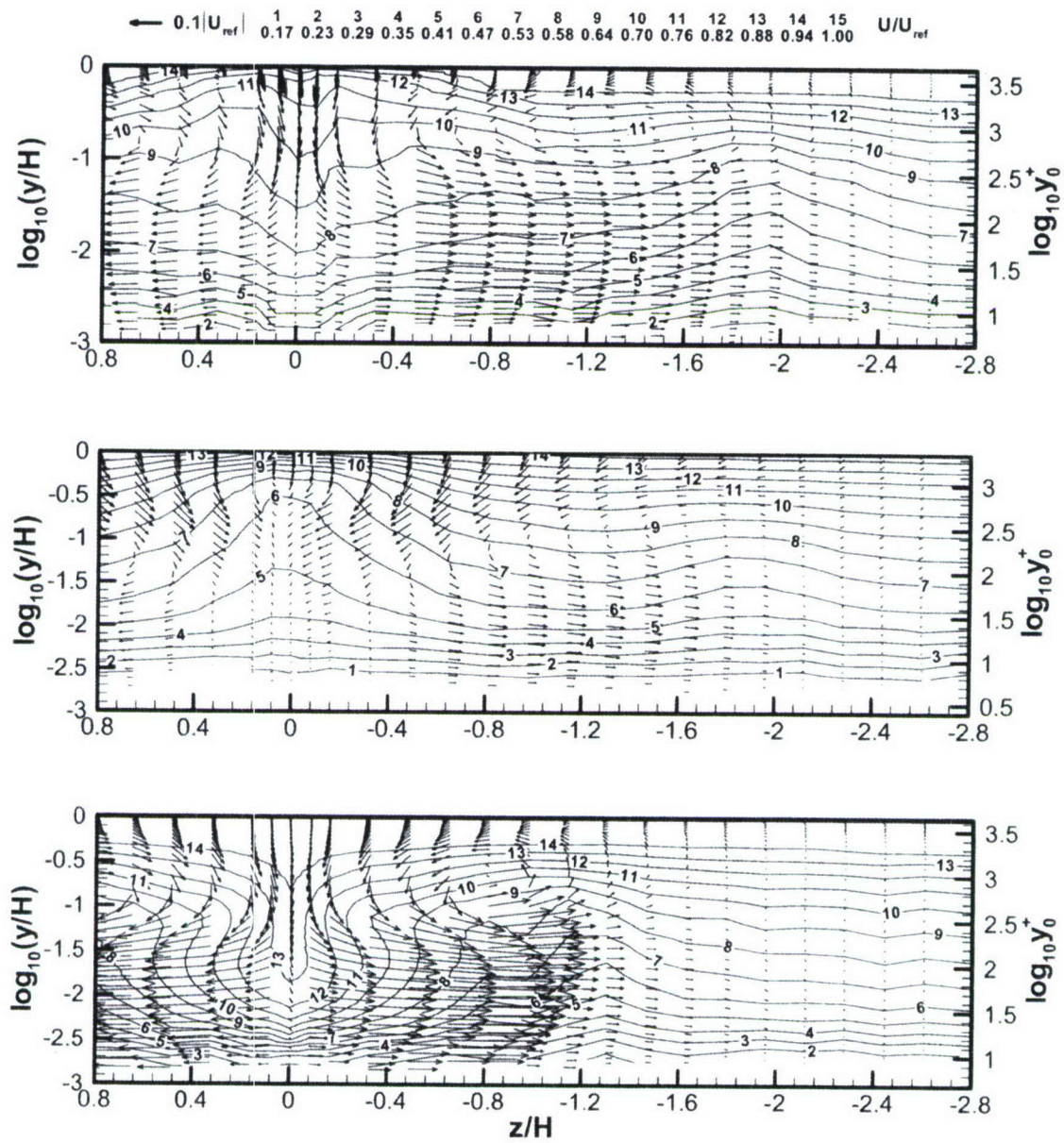
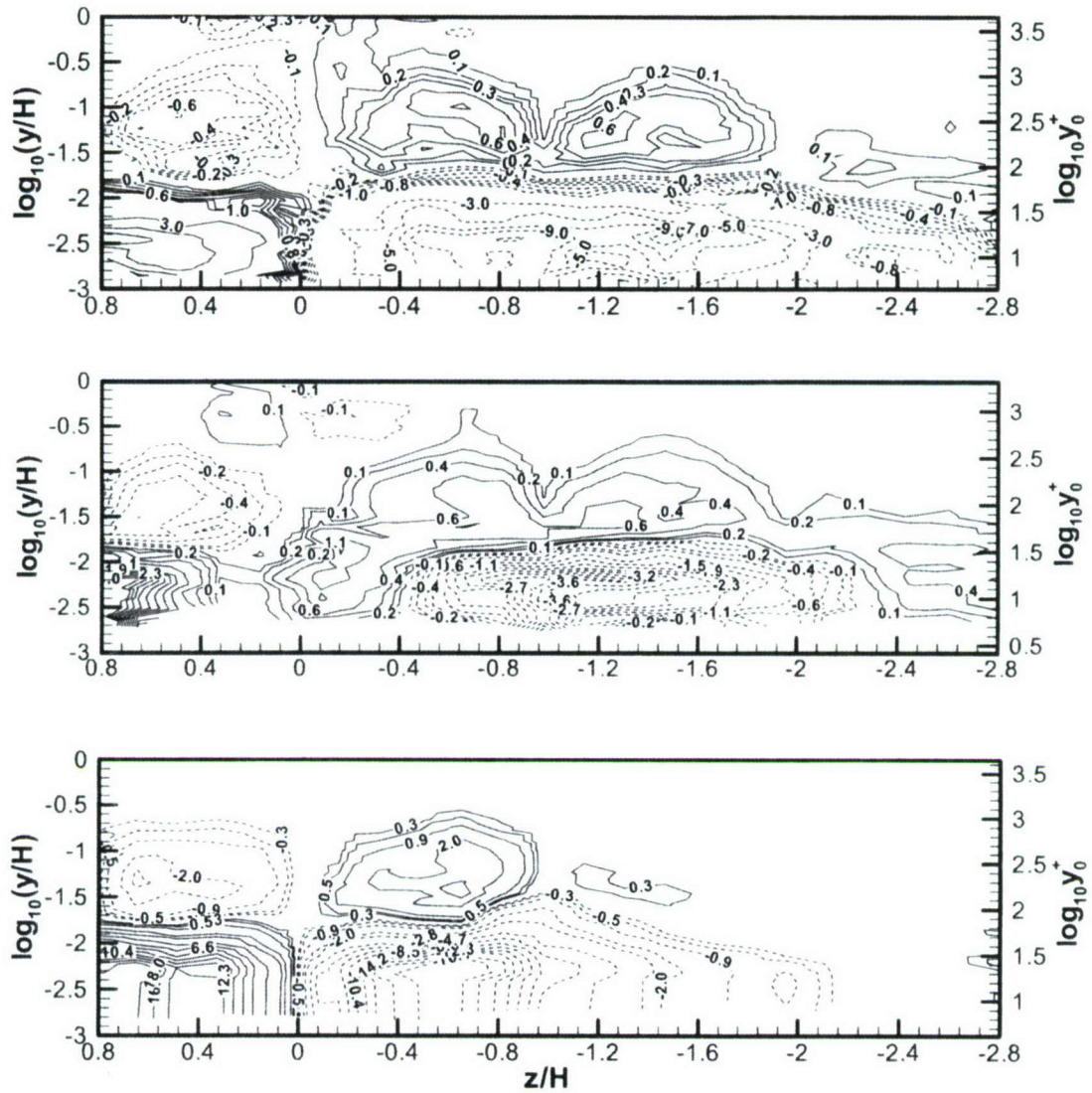
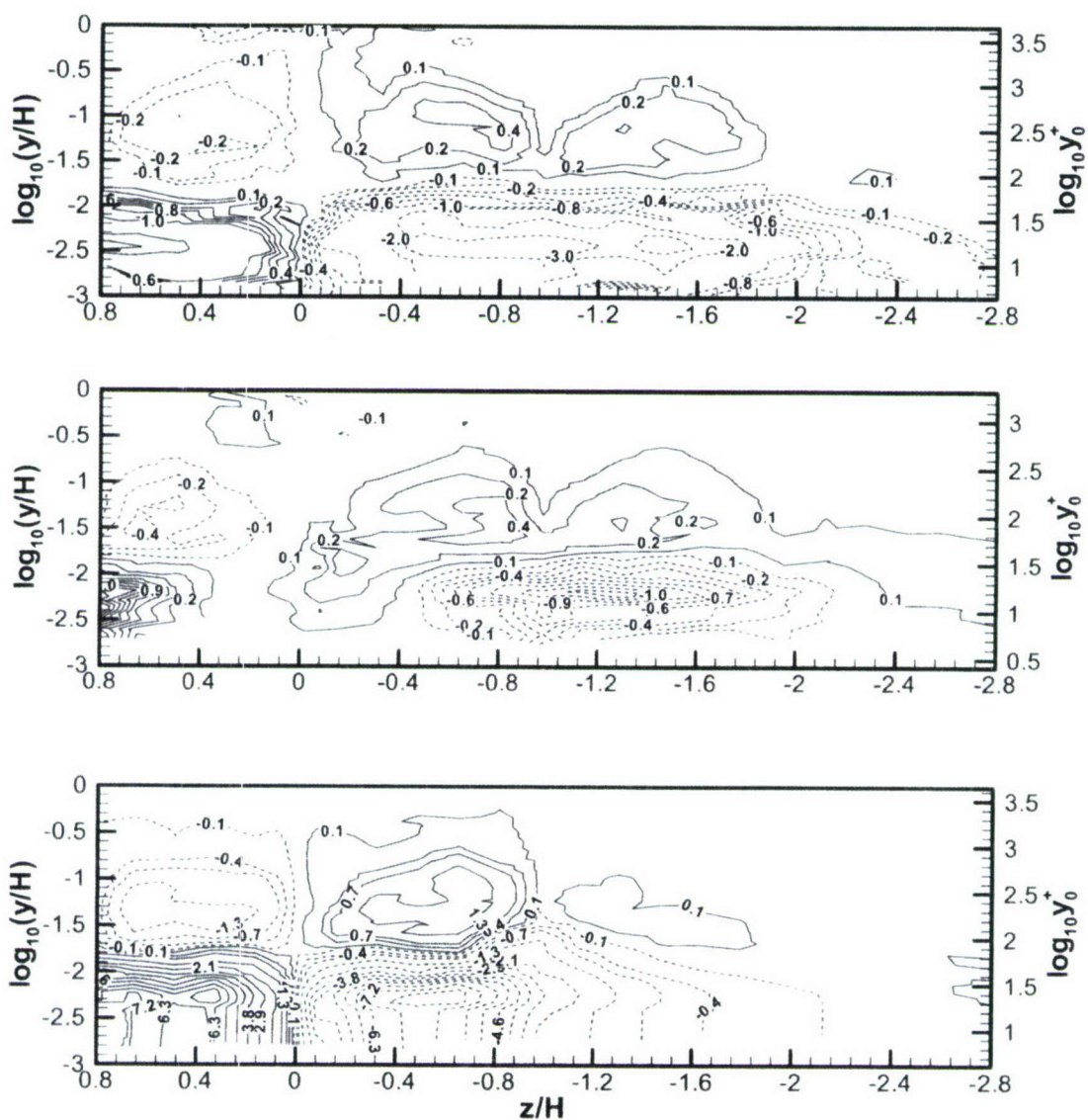
(b) $\log_{10} y/H$ and $\log_{10} y_0^+$ scale

Figure 4.10 Continued.

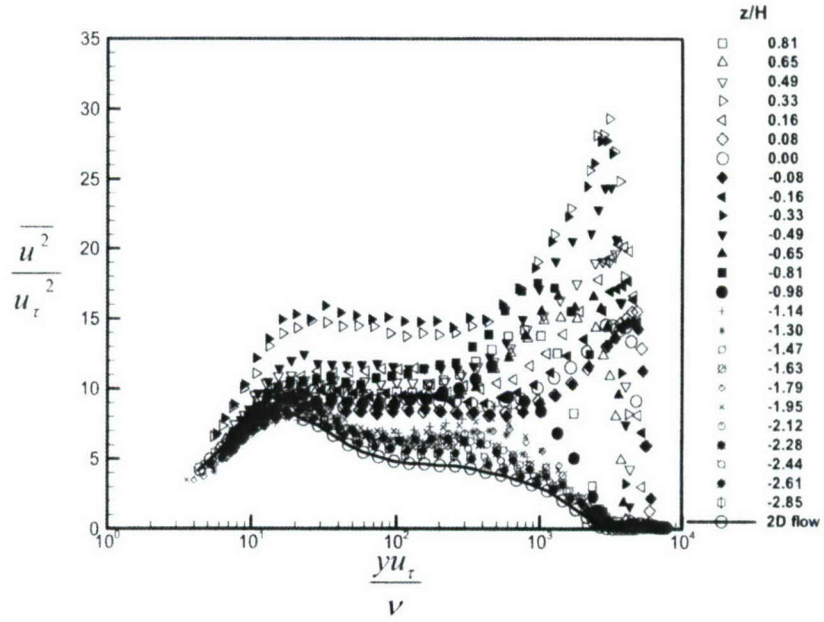
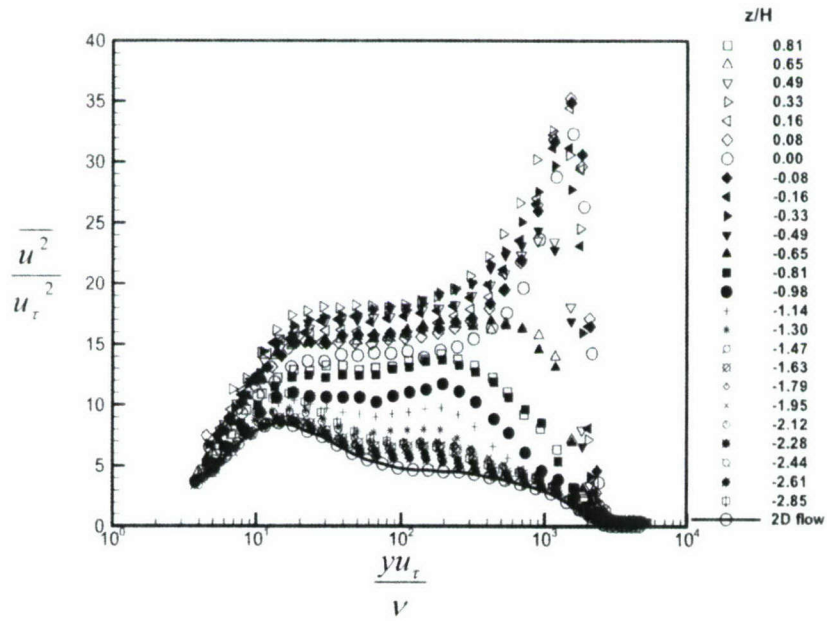




Log₁₀ y/H and Log₁₀ y₀⁺ scale, Top to bottom : large bump#3 (x/H=3.63),
small bump#3 (x/H=3.26) and bump#1 (x/H=3.46).

Solid lines are positive values and dashed lines are negative value.

Figure 4.12 Contour of normalized helicity density, hH/U_{ref}^2 .

(a) Large bump#3 at $x/H=3.63$ (b) Small bump#3 at $x/H=3.26$ Figure 4.13 Reynolds stress $\overline{u^2}$ at wake planes.

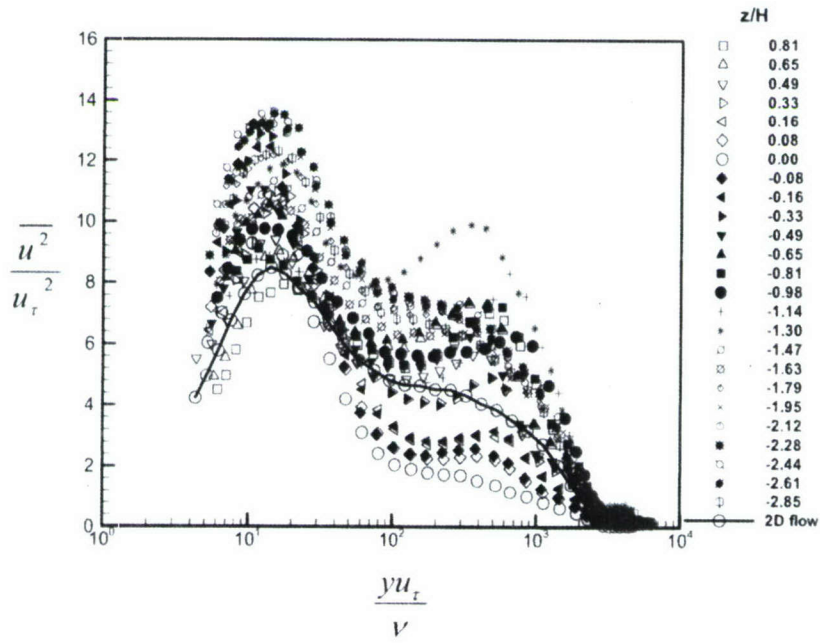
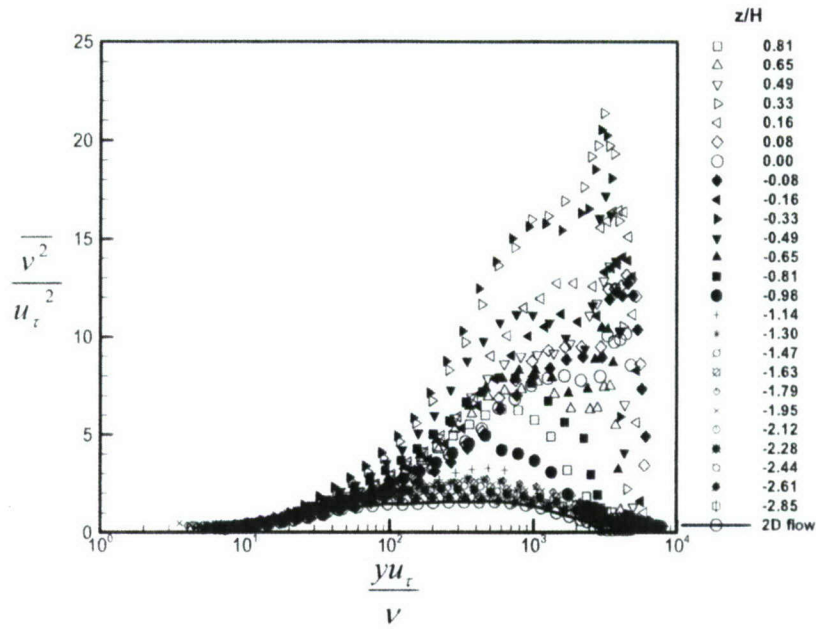
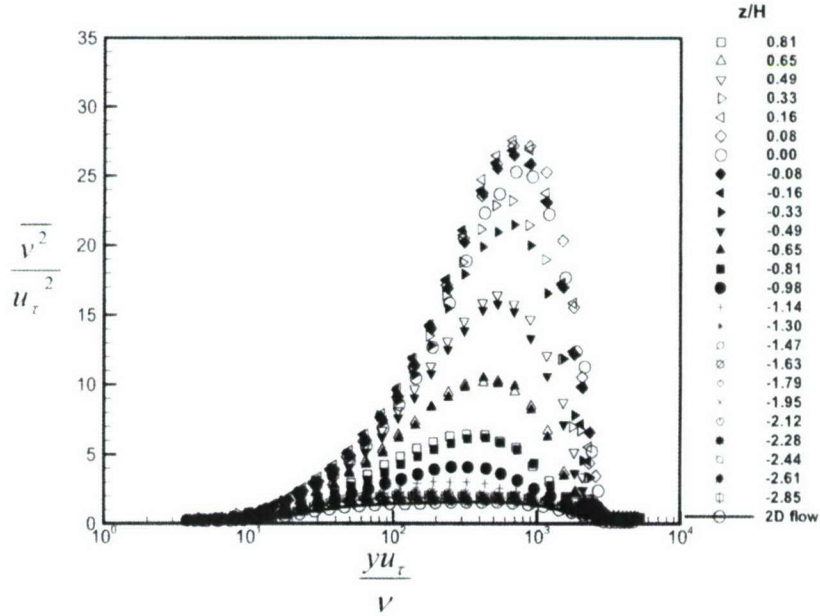
(c) Bump#1 at $x/H=3.46$

Figure 4.13 Continued.

(a) Large bump#3 at $x/H=3.63$ (b) Small bump#3 at $x/H=3.26$ Figure 4.14 Reynolds stress $\overline{v'^2}$ at wake planes.

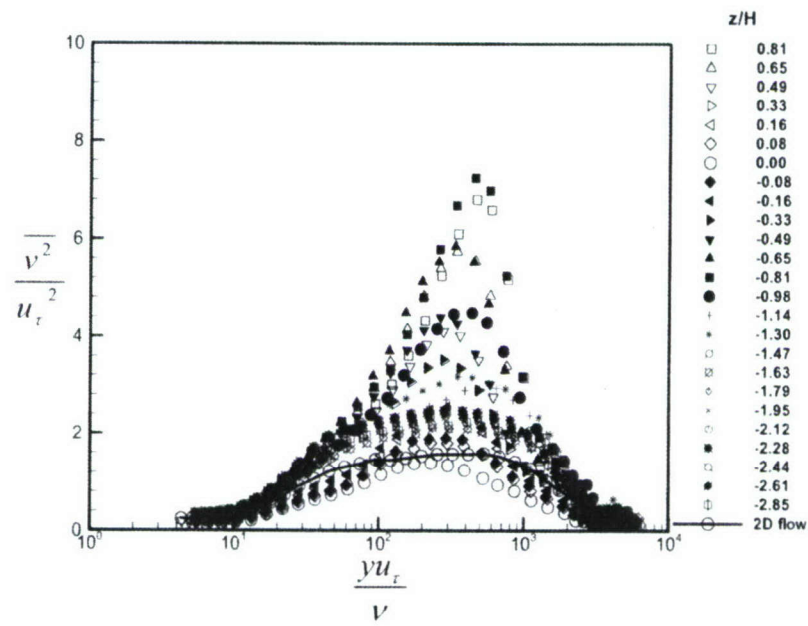
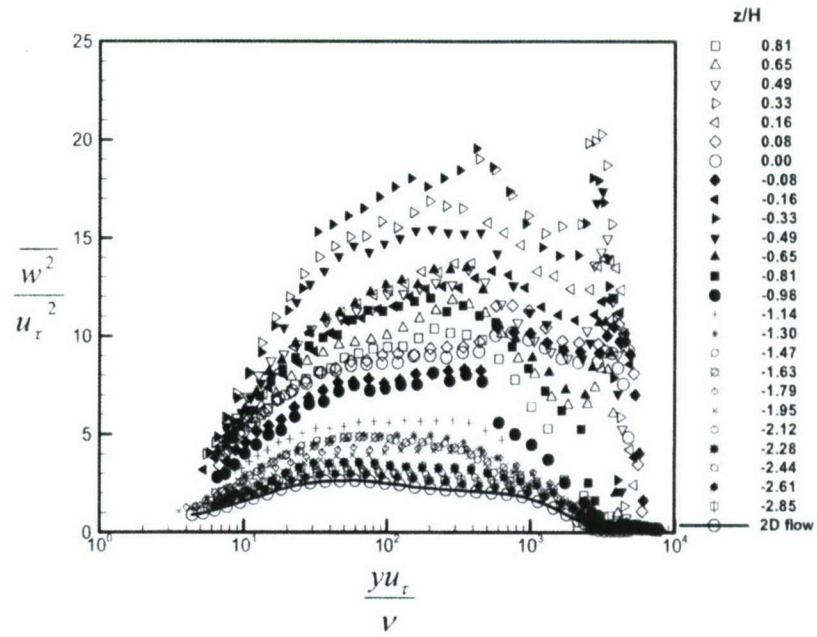
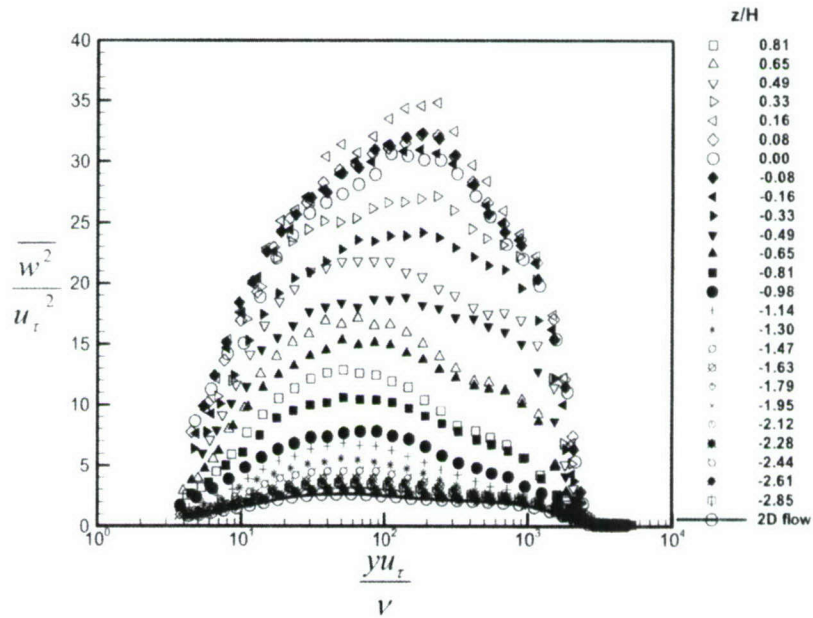
(c) Bump#1 at $x/H=3.46$

Figure 4.14 Continued.

(a) Large bump#3 at $x/H=3.63$ (b) Small bump#3 at $x/H=3.26$ Figure 4.15 Reynolds stress $\overline{w'^2}$ at wake planes.

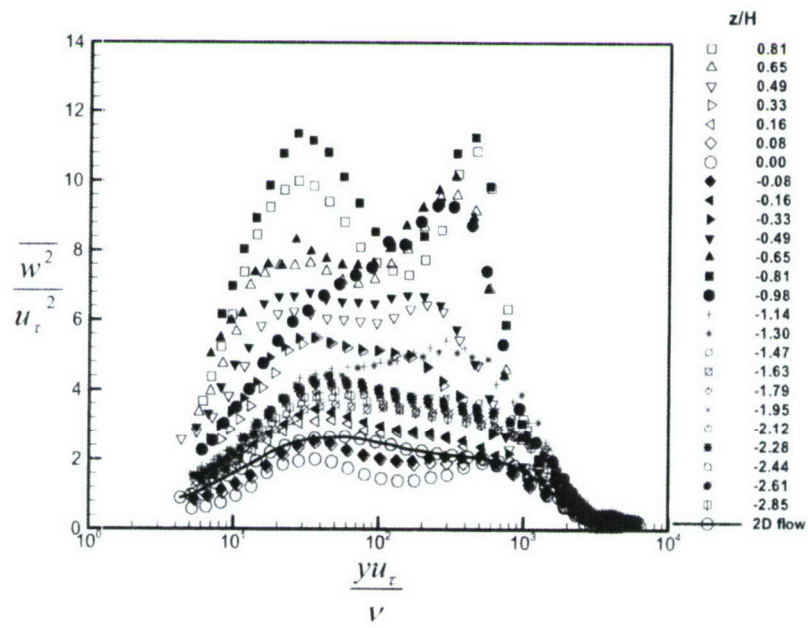
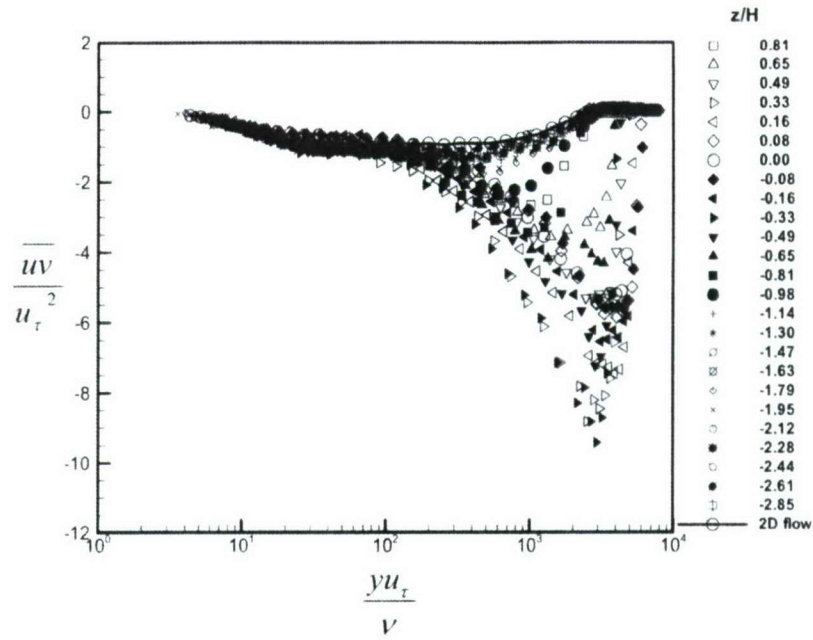
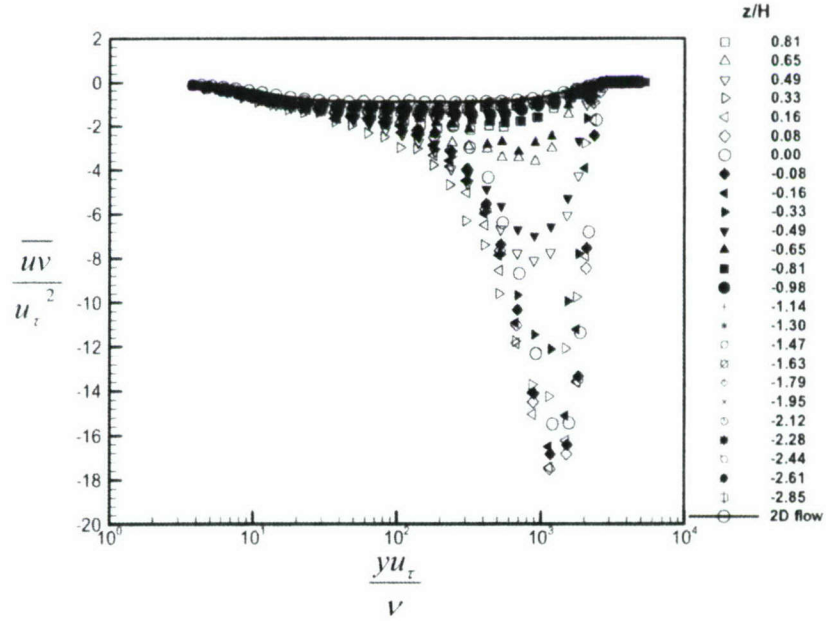
(c) Bump#1 at $x/H=3.46$

Figure 4.15 Continued.

(a) Large bump#3 at $x/H=3.63$ (b) Small bump#3 at $x/H=3.26$ Figure 4.16 Reynolds stress $-\frac{uv}{u_\tau^2}$ at wake planes.

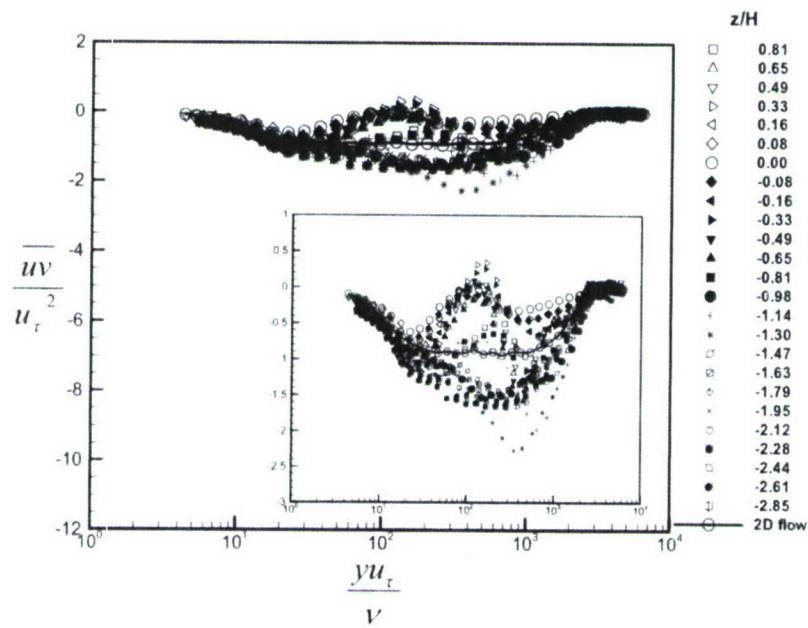
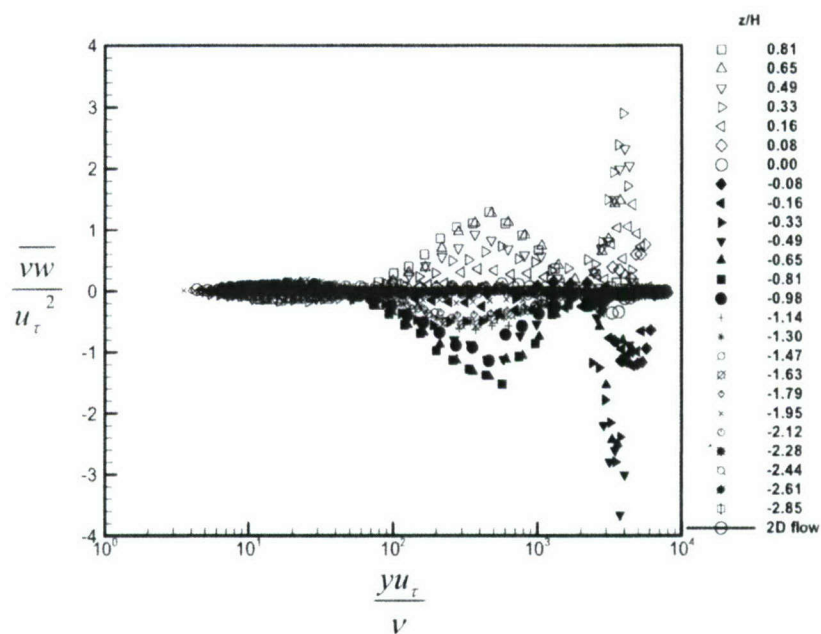
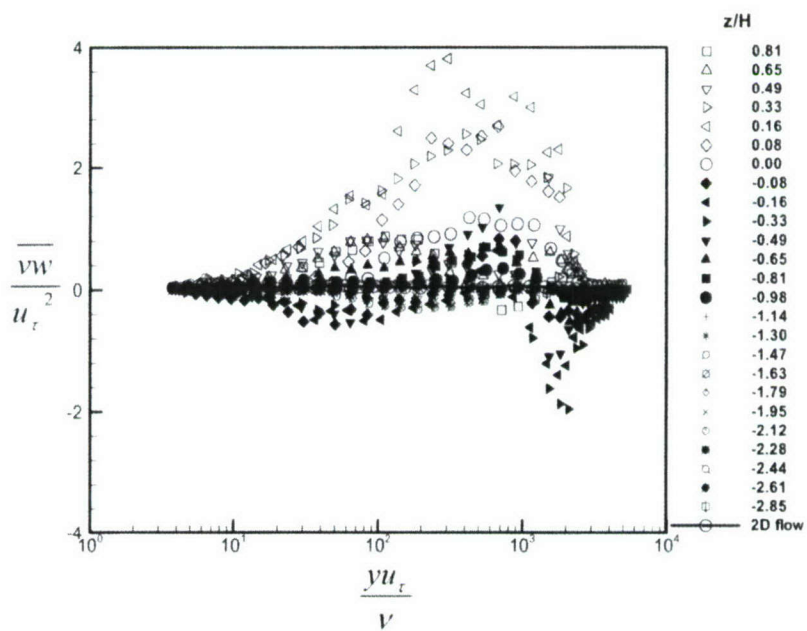
(c) Bump#1 at $x/H=3.46$

Figure 4.16 Continued.

(a) Large bump#3 at $x/H=3.63$ (b) Small bump#3 at $x/H=3.26$ Figure 4.17 Reynolds stress $-\overline{vw'}$ at wake planes.

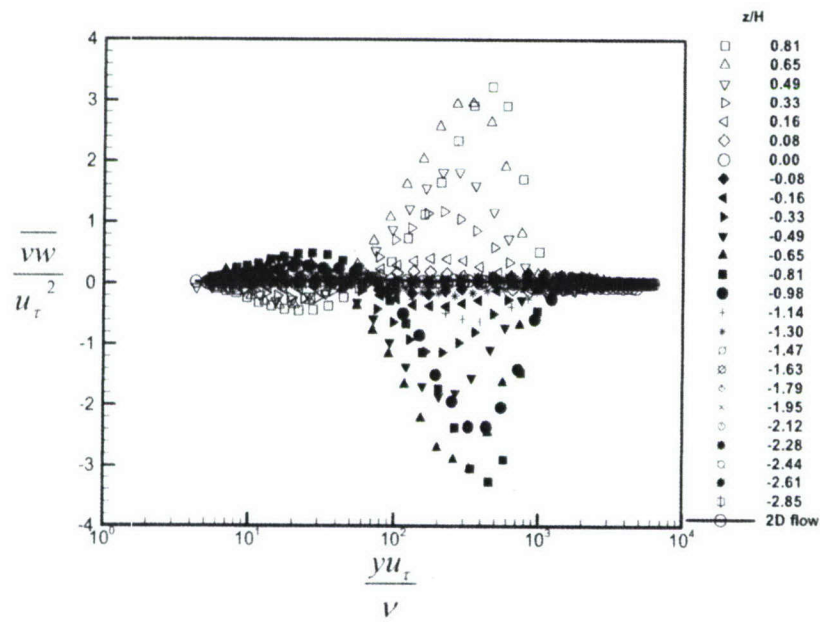
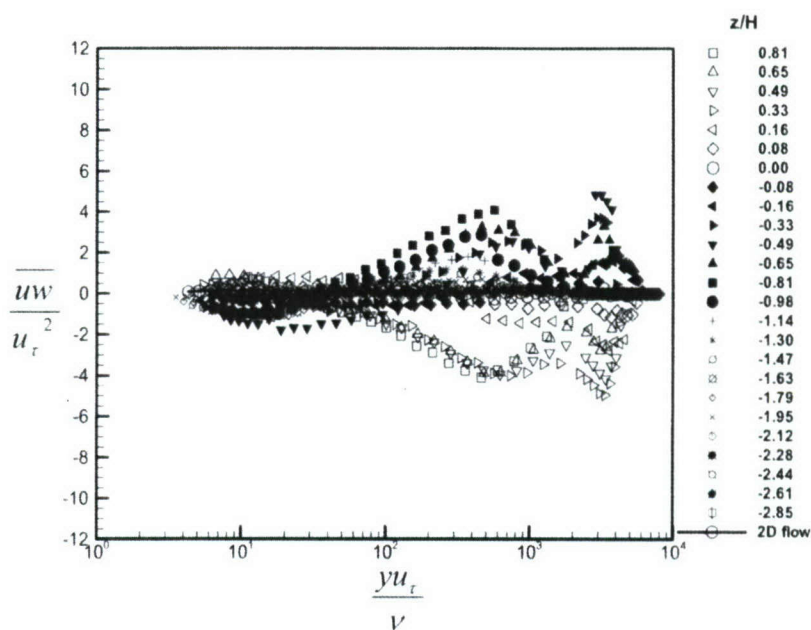
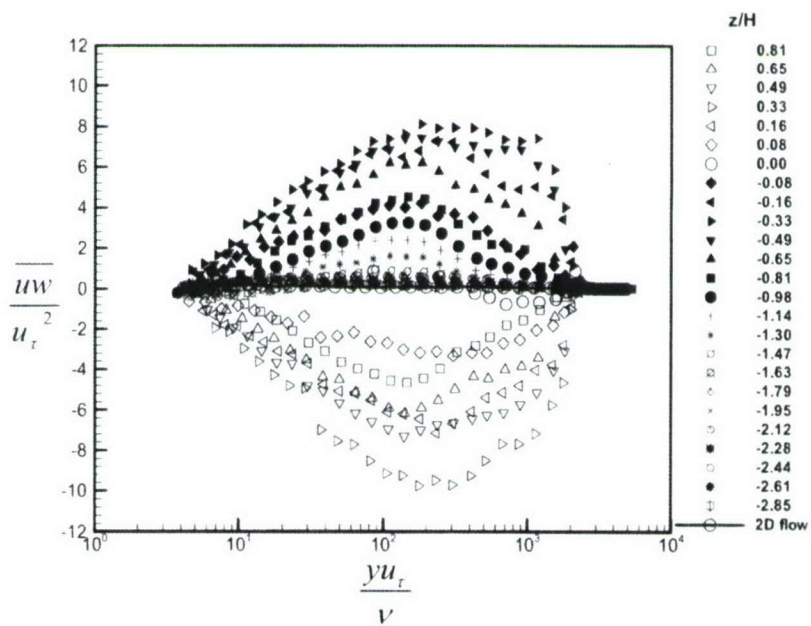
(c) Bump#1 at $x/H=3.46$

Figure 4.17 Continued.

(a) Large bump#3 at $x/H=3.63$ (b) Small bump#3 at $x/H=3.26$ Figure 4.18 Reynolds stress $-\overline{u'w'}$ at wake planes.

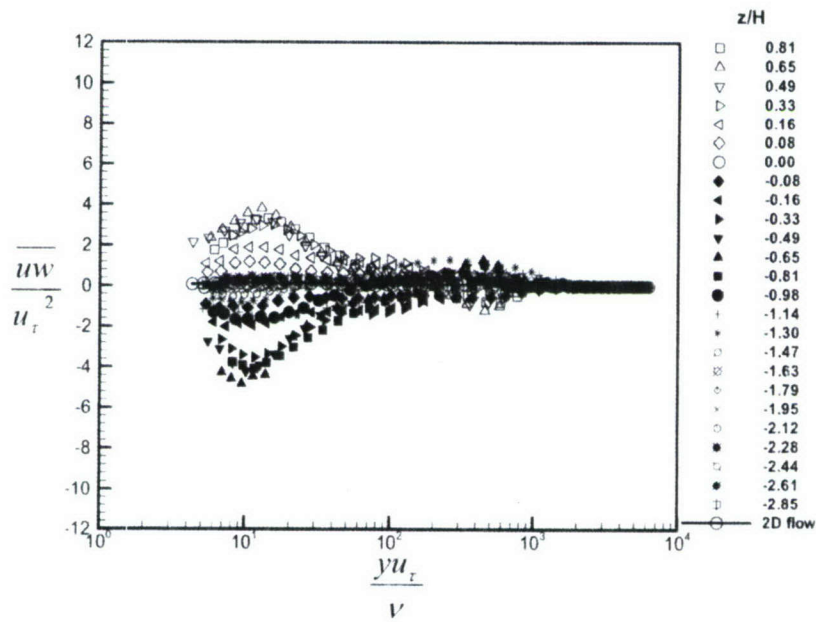
(c) Bump#1 at $x/H=3.46$

Figure 4.18 Continued.

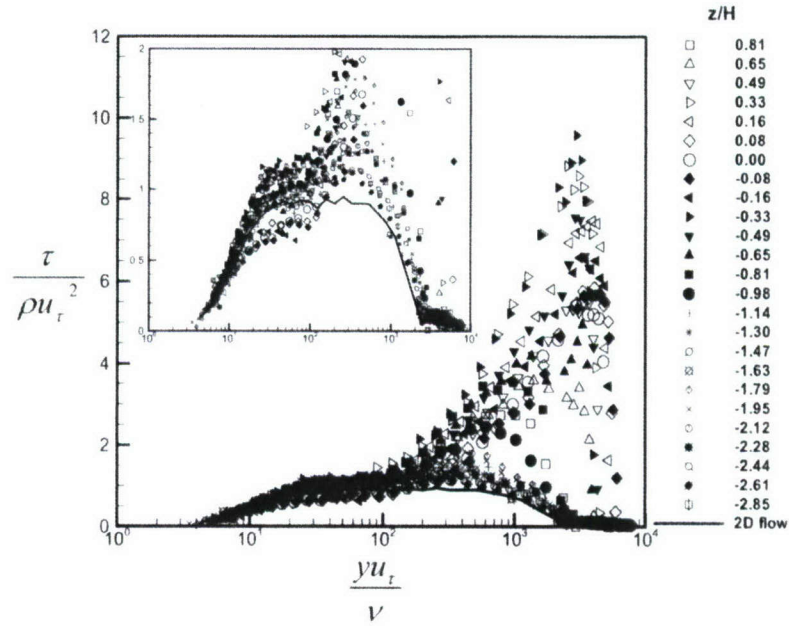
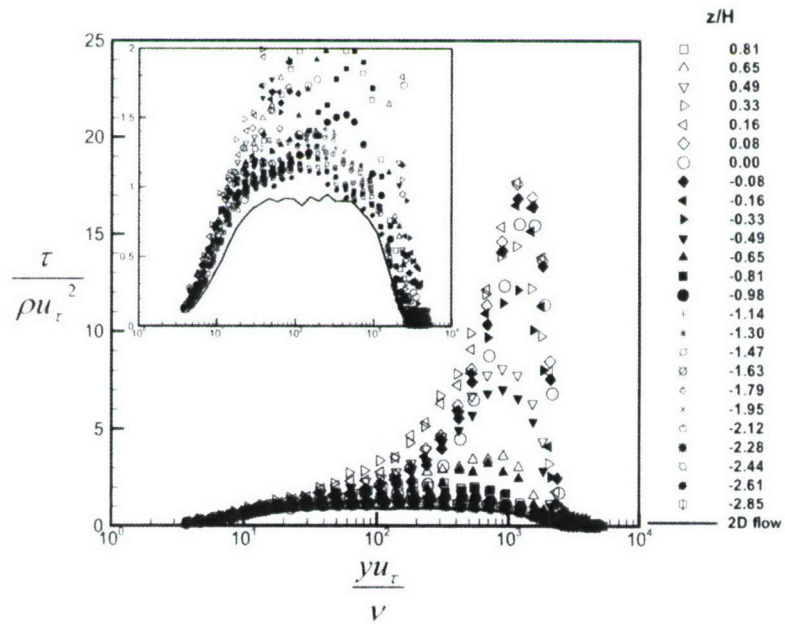
(a) Large bump#3 at $x/H=3.63$ (b) Small bump#3 at $x/H=3.26$

Figure 4.19 Magnitude of Reynolds shear stresses at wake planes.

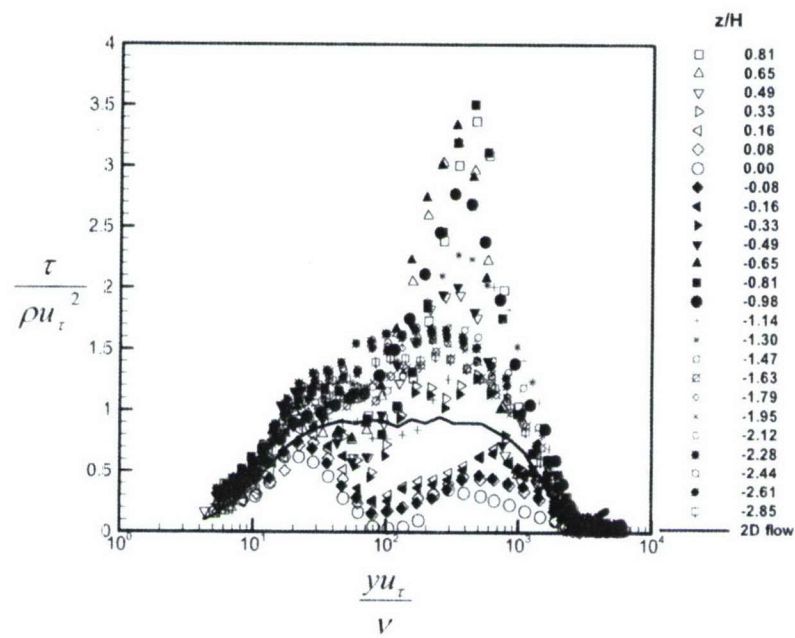
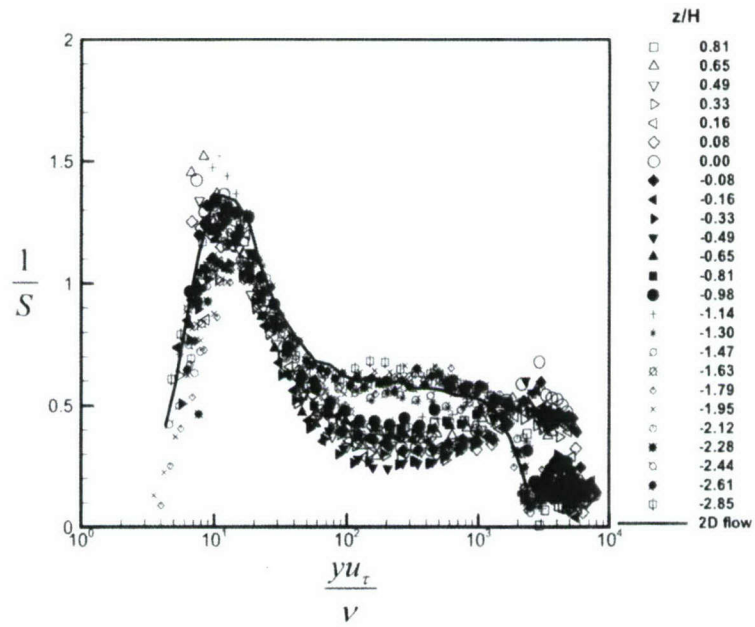
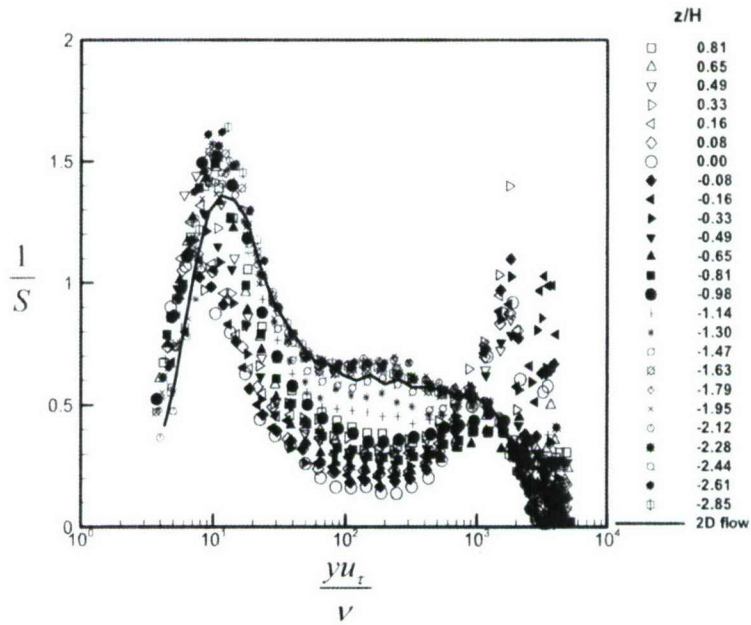
(c) Bump#1 at $x/H=3.46$

Figure 4.19 Continued.

(a) Large bump#3 at $x/H=3.63$ (b) Small bump#3 at $x/H=3.26$ Figure 4.20 Parameter $1/S = \sqrt{(-uv)^2 + (-vw)^2} / v^2$ at wake planes.

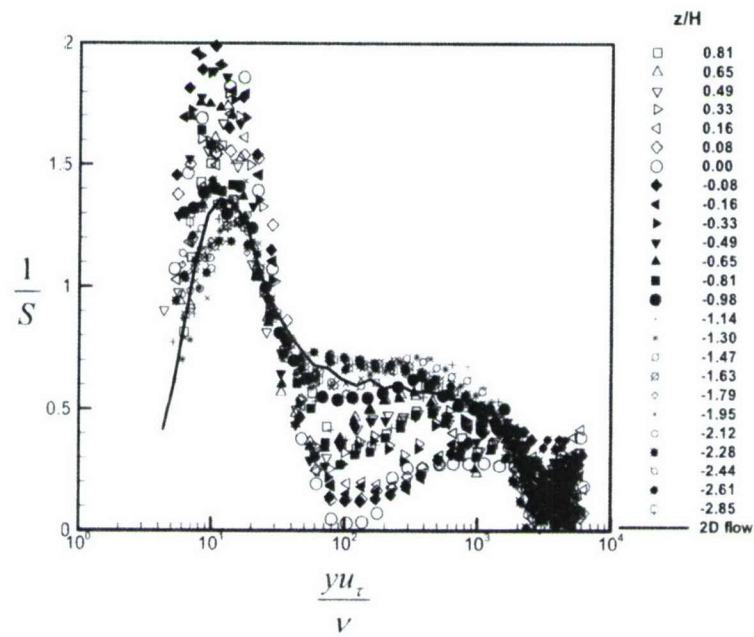
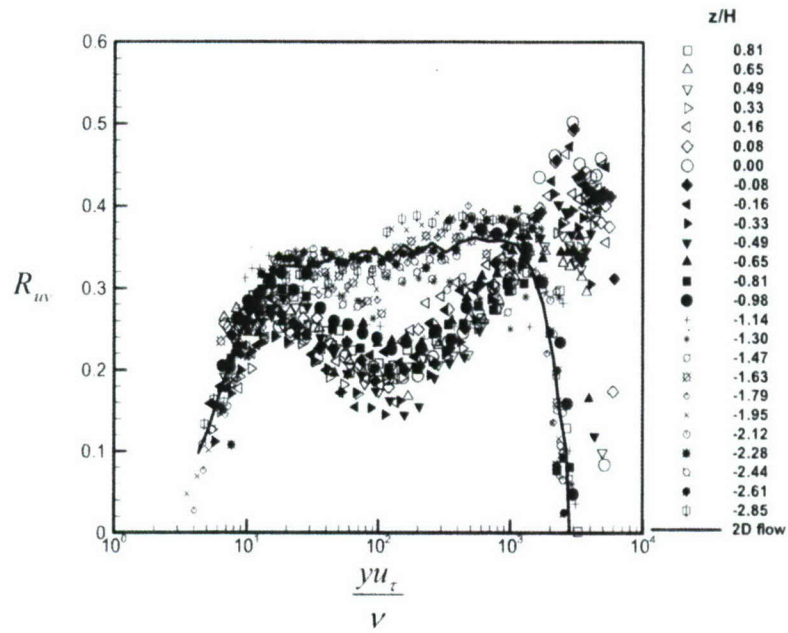
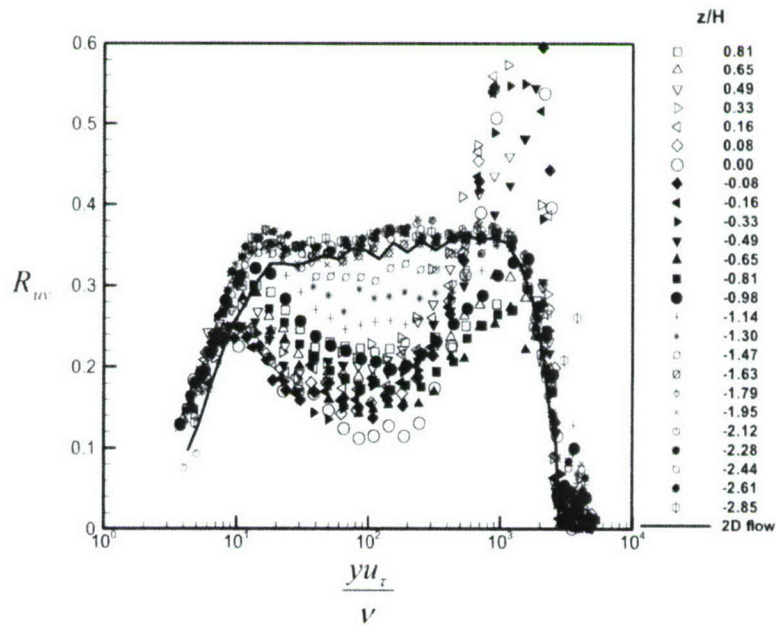
(c) Bump#1 at $x/H=3.46$

Figure 4.20 Continued.

(a) Large bump#3 at $x/H=3.63$ (b) Small bump#3 at $x/H=3.26$ Figure 4.21 Correlation coefficient $R_{uv} = -\overline{uv}/\overline{u'v'}$ at wake planes.

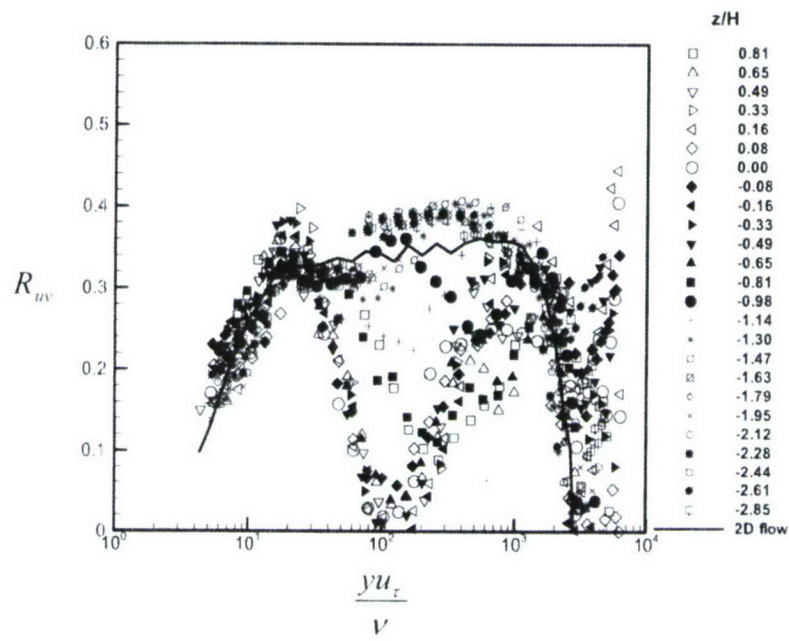
(c) Bump#1 at $x/H=3.46$

Figure 4.21 Continued.

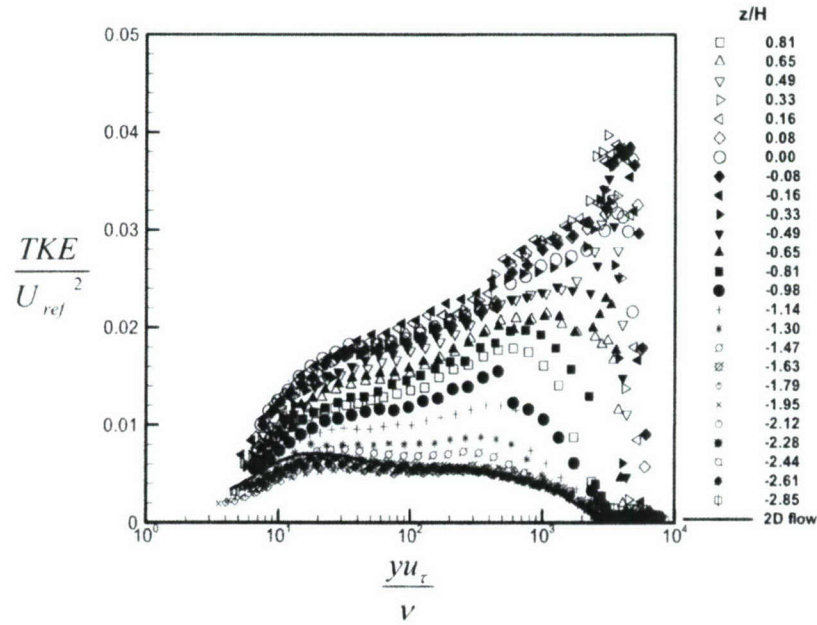
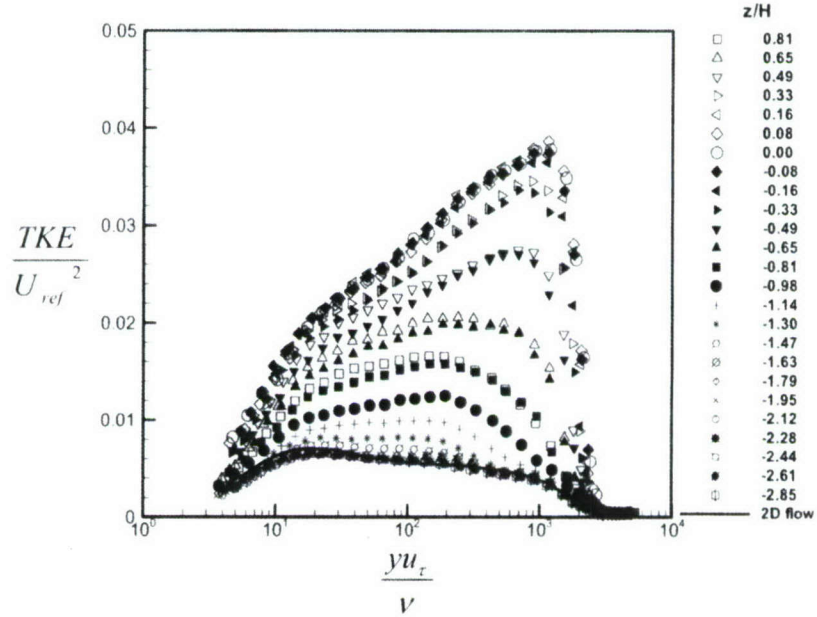
(a) Large bump#3 at $x/H=3.63$ (b) Small bump#3 at $x/H=3.26$

Figure 4.22 Turbulent kinetic energy at wake planes.

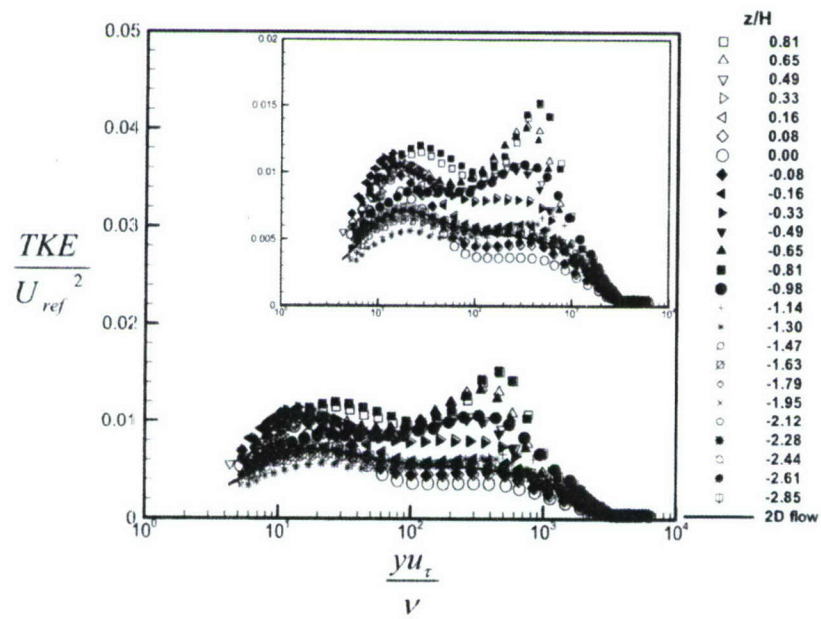
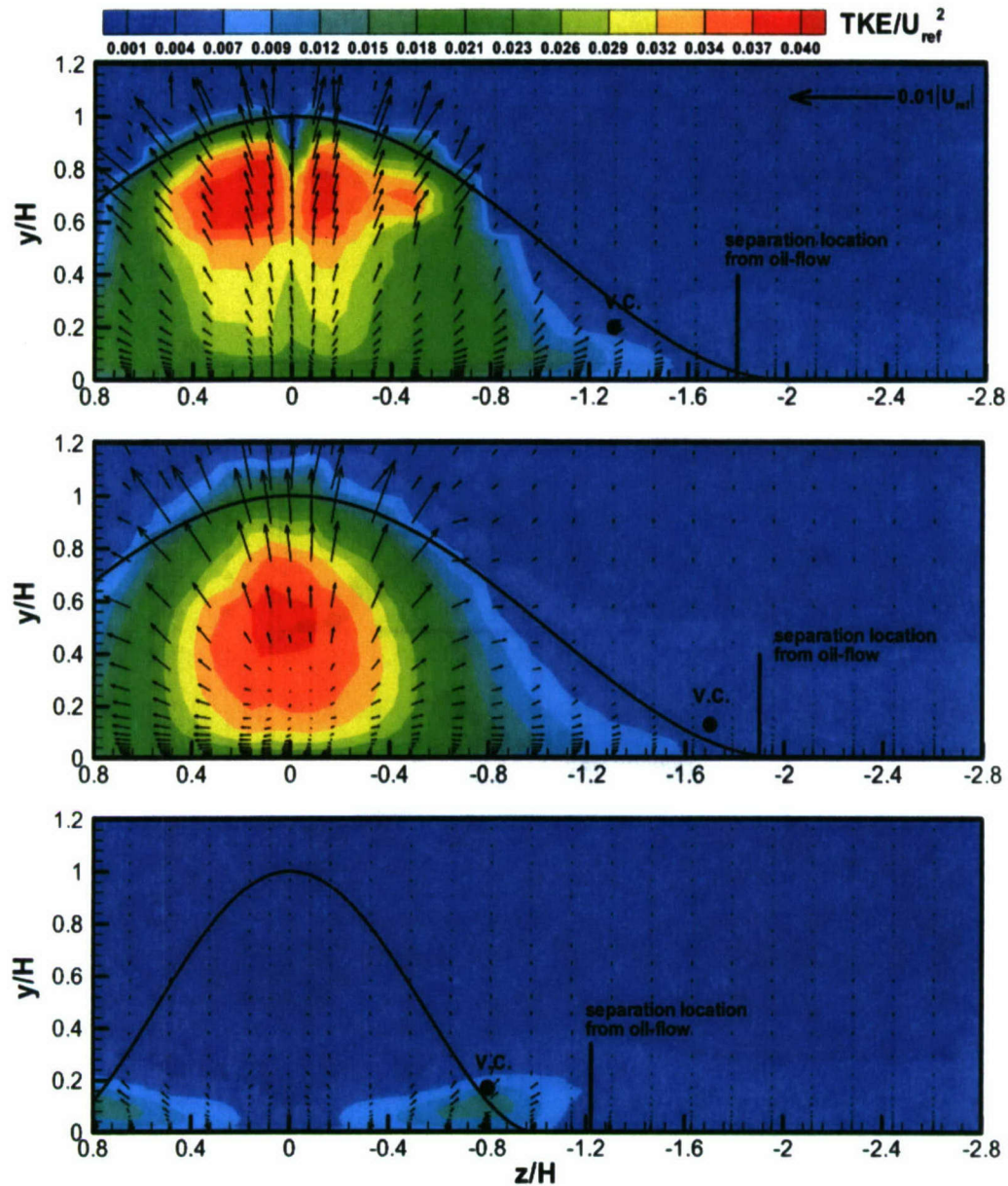
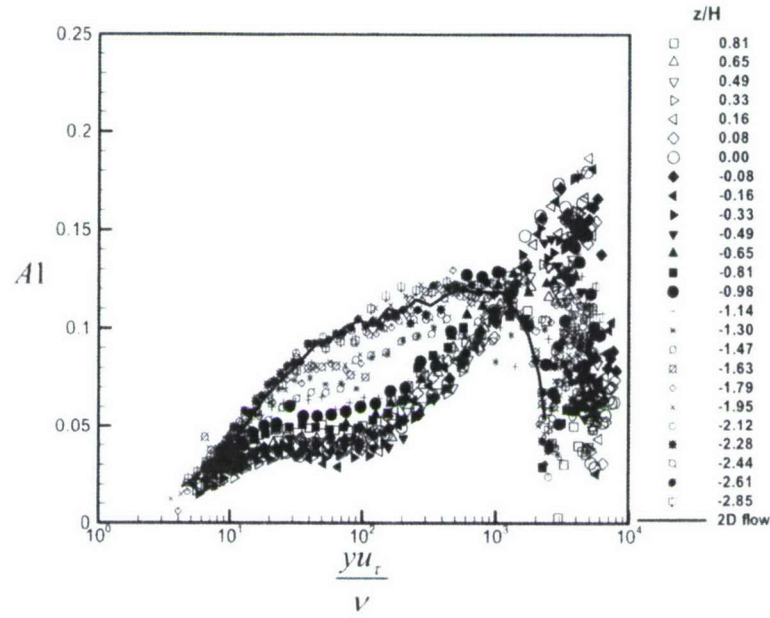
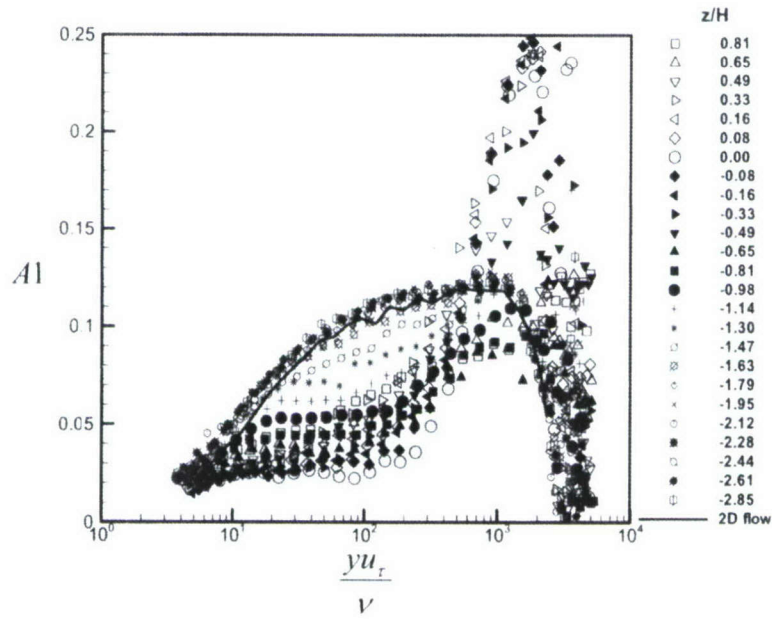
(c) Bump#1 at $x/H=3.46$

Figure 4.22 Continued.



Top to bottom : large bump#3($x/H=3.63$), small bump#3($x/H=3.26$)
and bump#1($x/H=3.46$). V.C. : Vortex Center.

Figure 4.23 Contours of turbulent kinetic energy and its transport velocity vectors.

(a) Large bump#3 at $x/H=3.63$ (b) Small bump#3 at $x/H=3.26$ Figure 4.24 Parameter $A1 = \sqrt{(-\overline{uv})^2 + (-\overline{vw})^2} / 2TKE$ at wake planes.

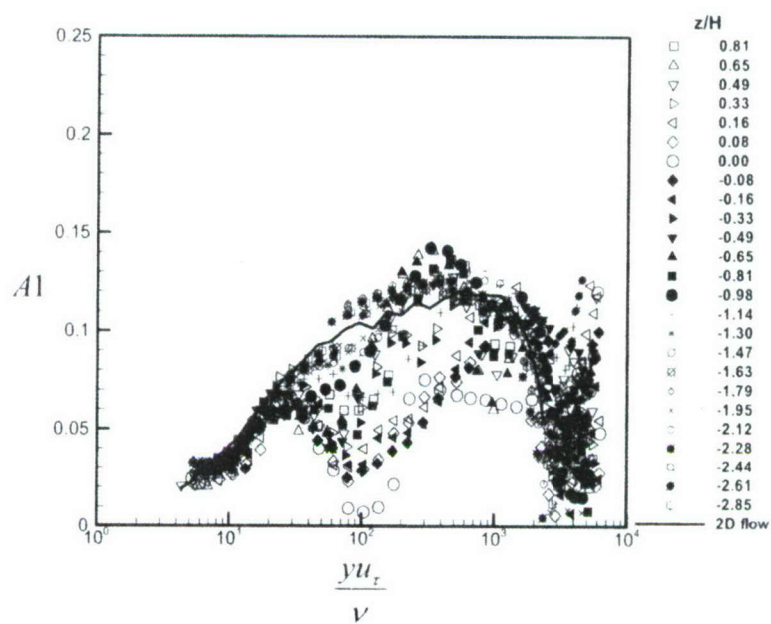
(c) Bump#1 at $x/H=3.46$

Figure 4.24 Continued.

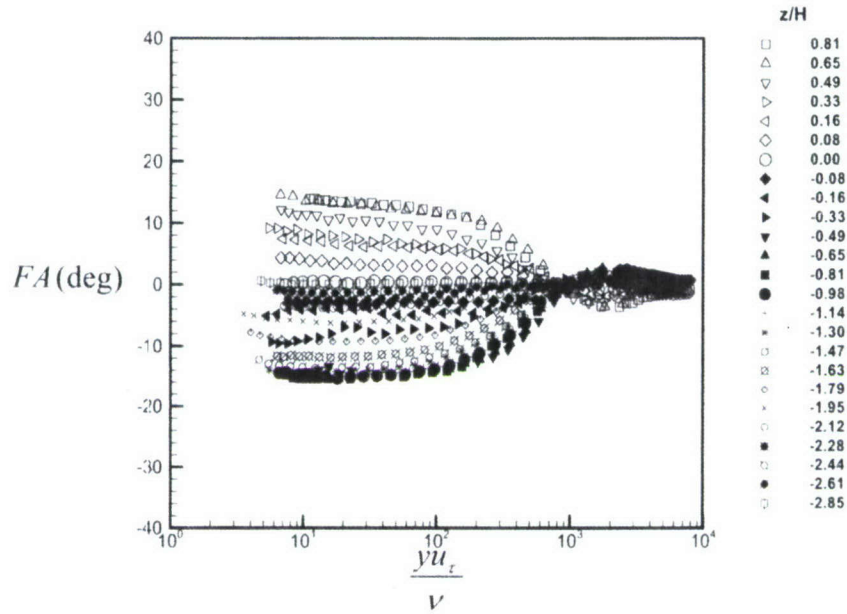
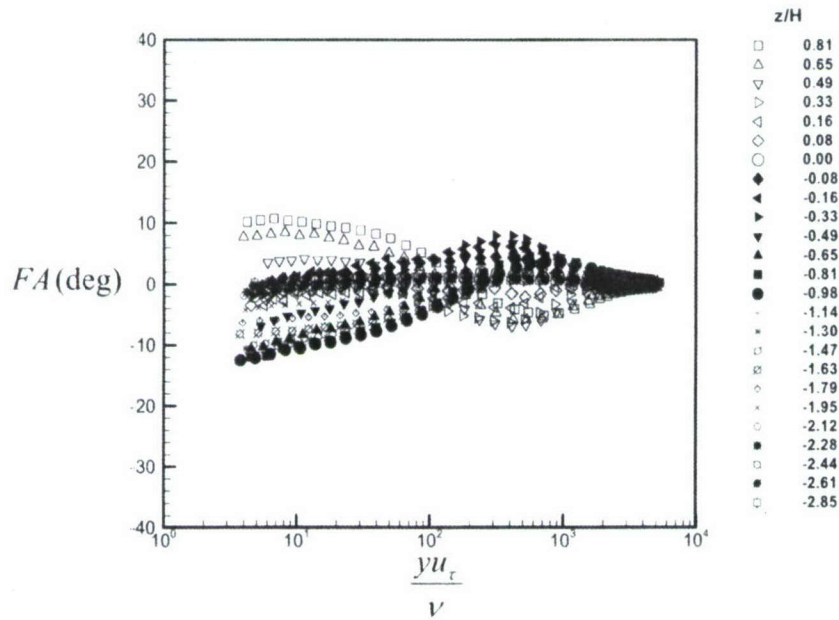
(a) Large bump#3 at $x/H=3.63$ (b) Small bump#3 at $x/H=3.26$

Figure 4.25 Flow angle (FA) at wake planes.

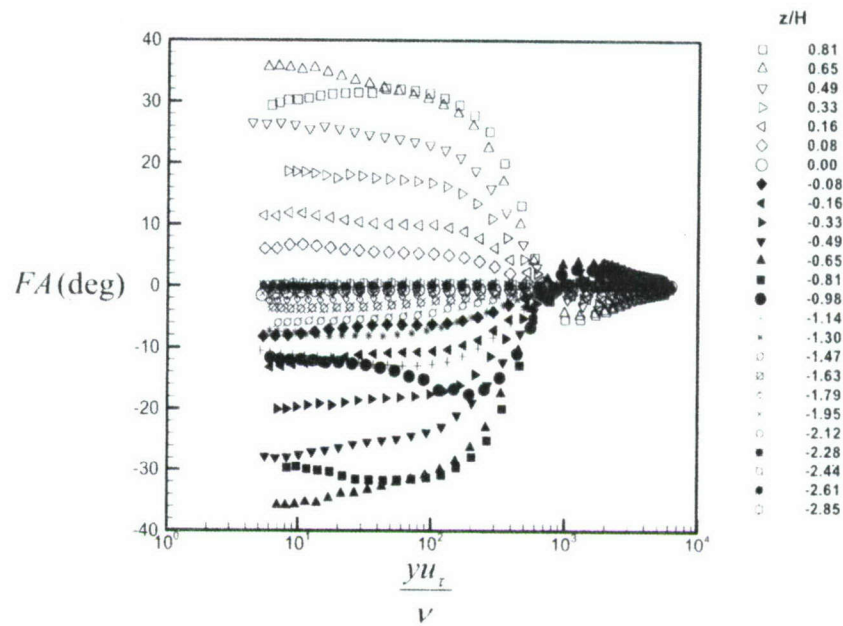
(c) Bump#1 at $x/H=3.46$

Figure 4.25 Continued.

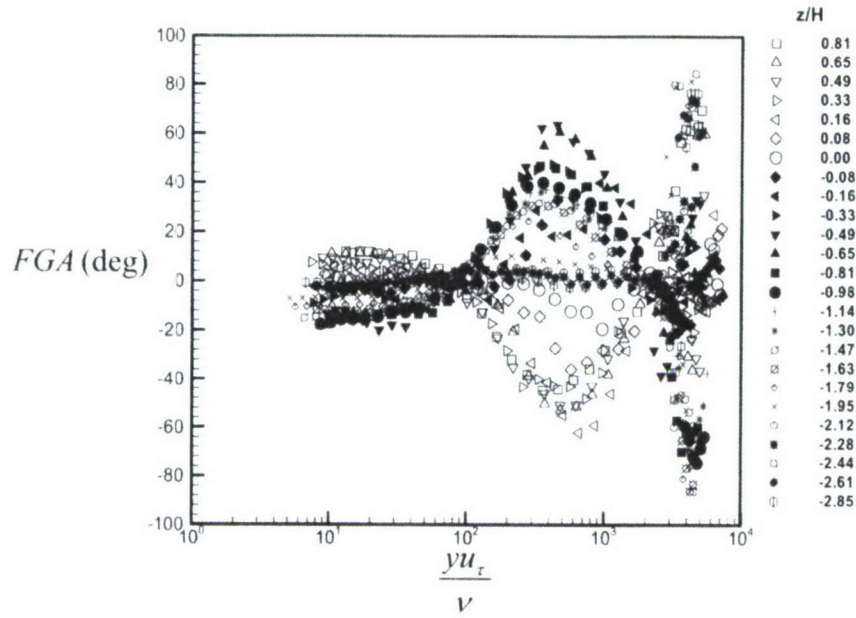
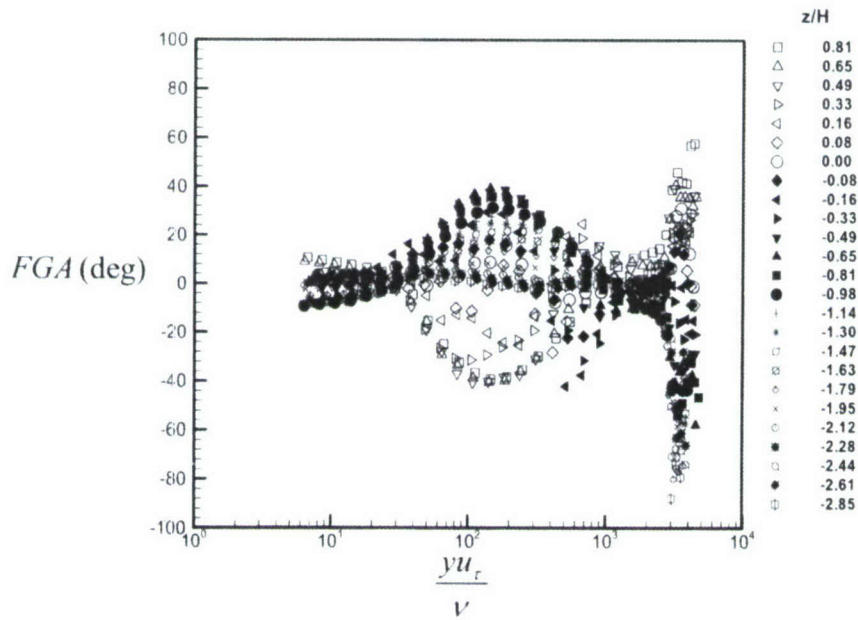
(a) Large bump#3 at $x/H=3.63$ (b) Small bump#3 at $x/H=3.26$

Figure 4.26 Flow gradient angle (FGA) at wake planes.

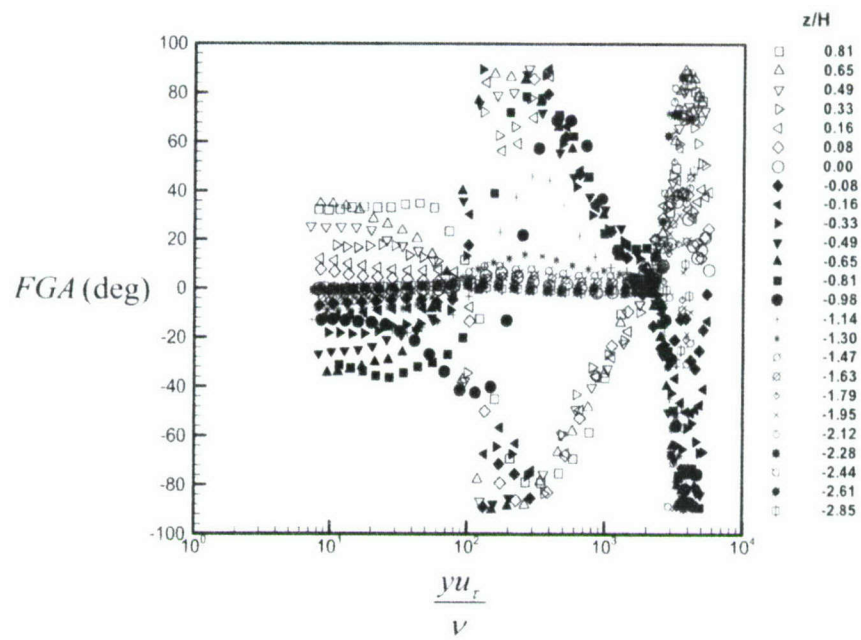
(c) Bump#1 at $x/H=3.46$

Figure 4.26 Continued.

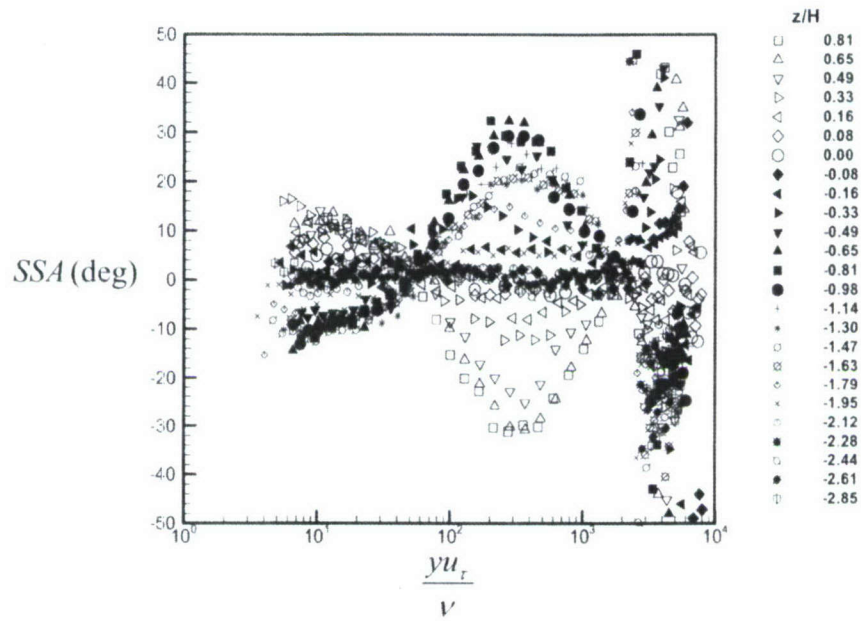
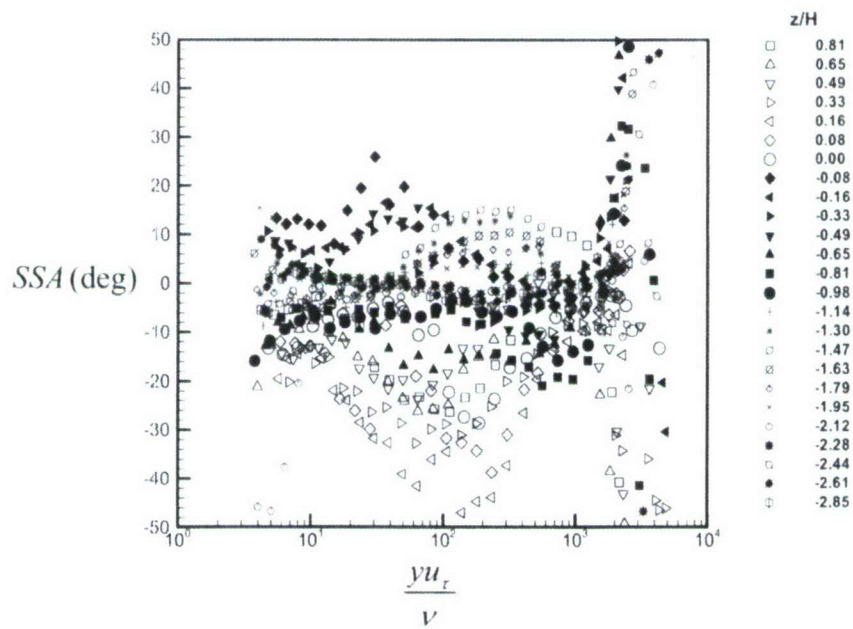
(a) Large bump#3 at $x/H=3.63$ (b) Small bump#3 at $x/H=3.26$

Figure 4.27 Shear stress angle (SSA) at wake planes.

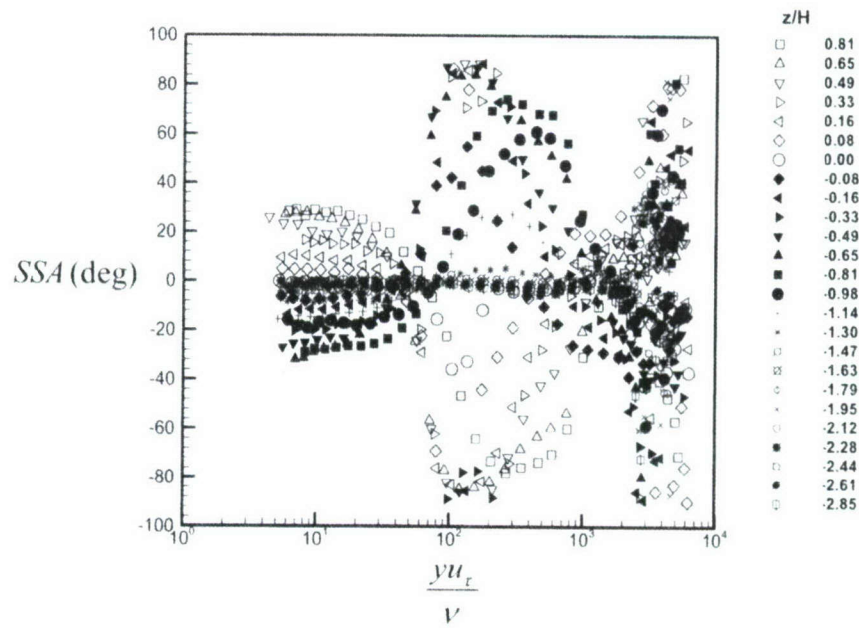
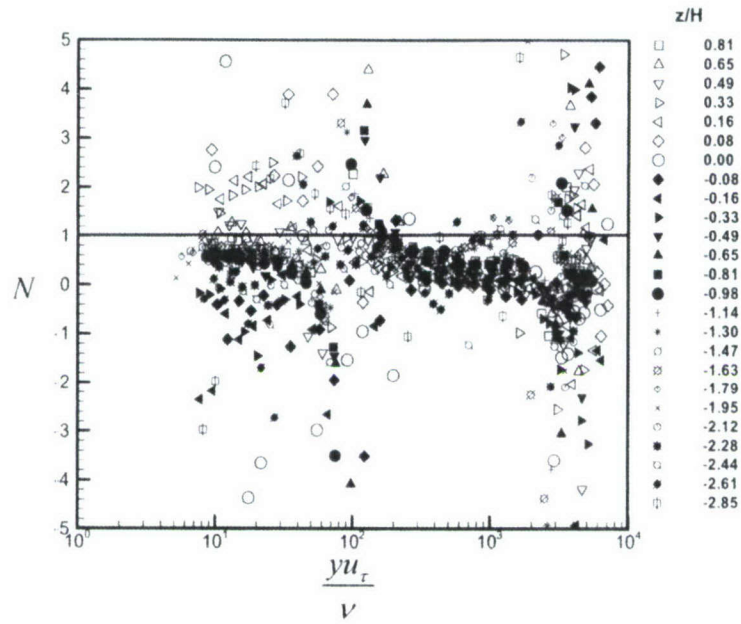
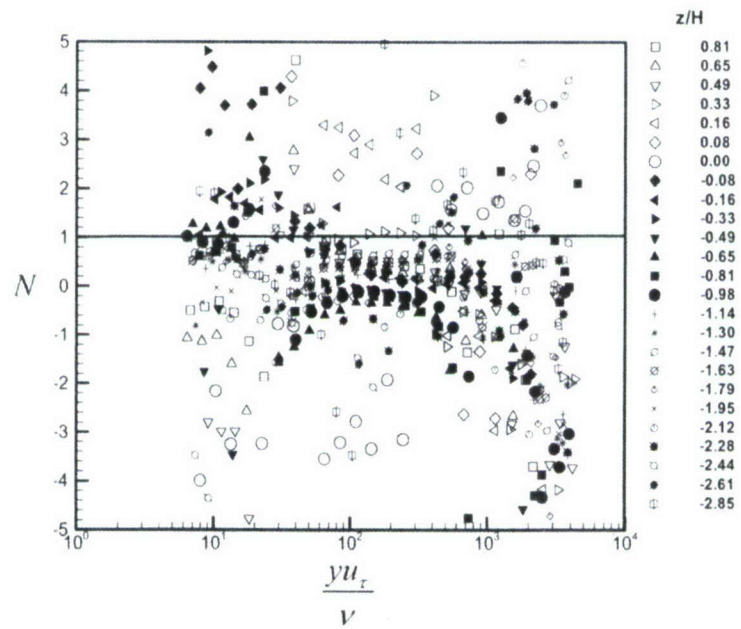
(c) Bump#1 at $x/H=3.46$

Figure 4.27 Continued.

(a) Large bump#3 at $x/H=3.63$ (b) Small bump#3 at $x/H=3.26$ Figure 4.28 Anisotropy constant, N at wake planes.

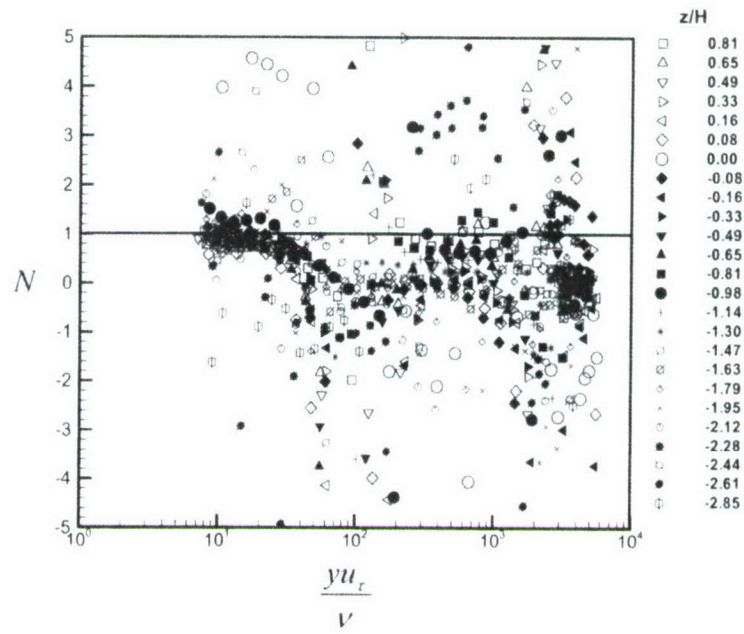
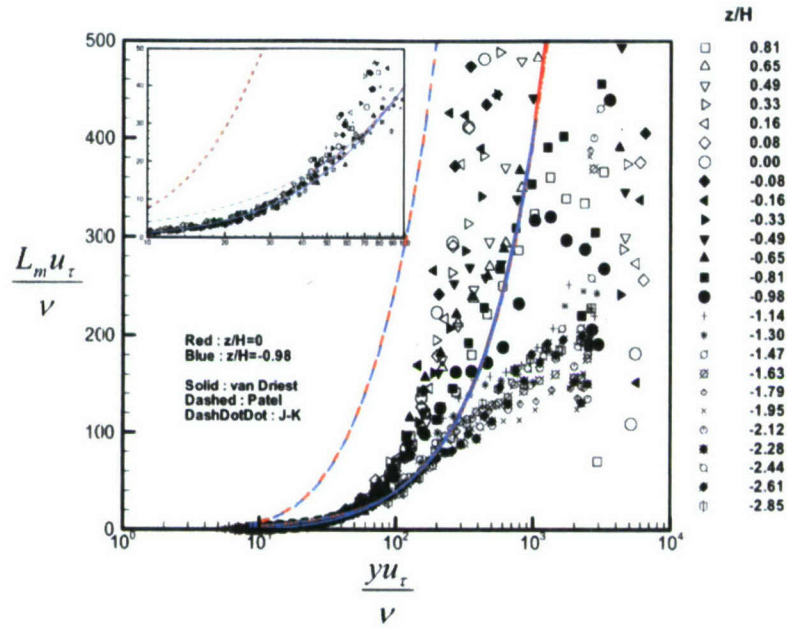
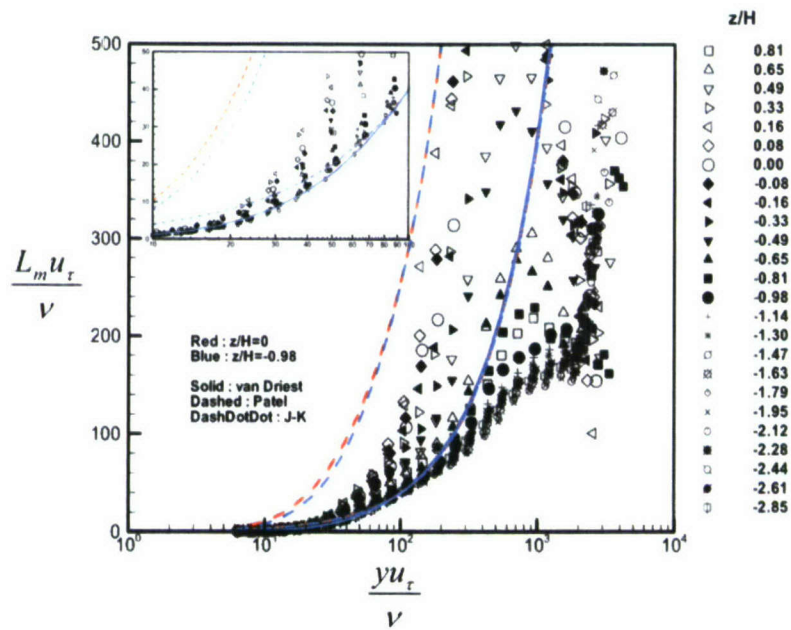
(c) Bump#1 at $x/H=3.46$

Figure 4.28 Continued.

(a) Large bump#3 at $x/H=3.63$ (b) Small bump#3 at $x/H=3.26$ Figure 4.29 Mixing length (L_m) at wake planes.

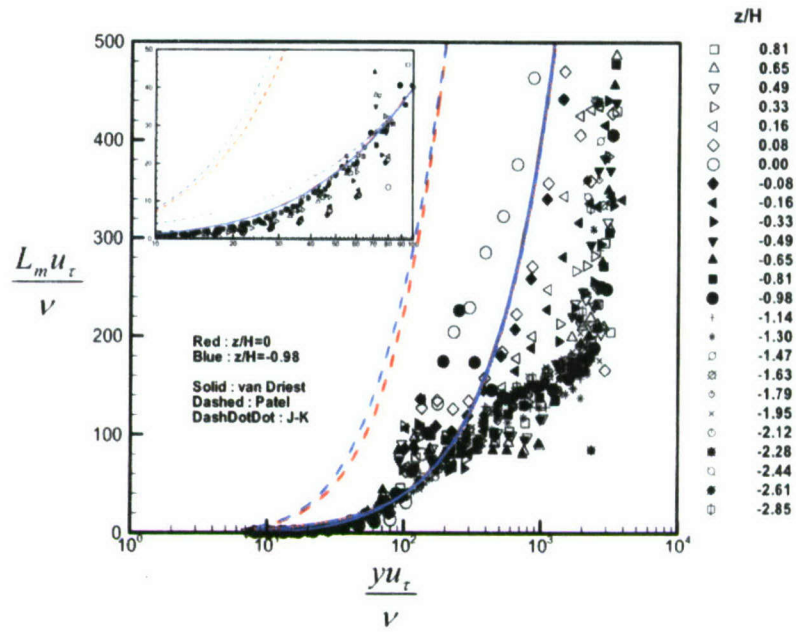
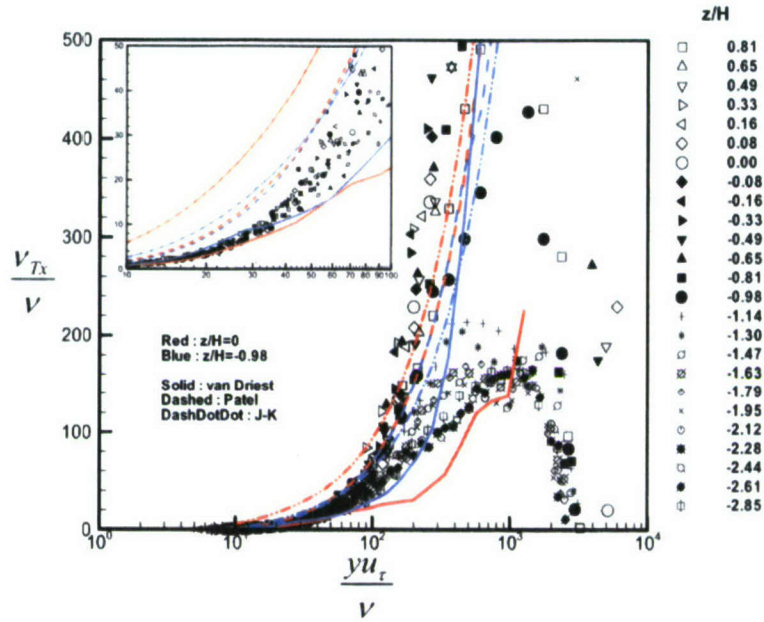
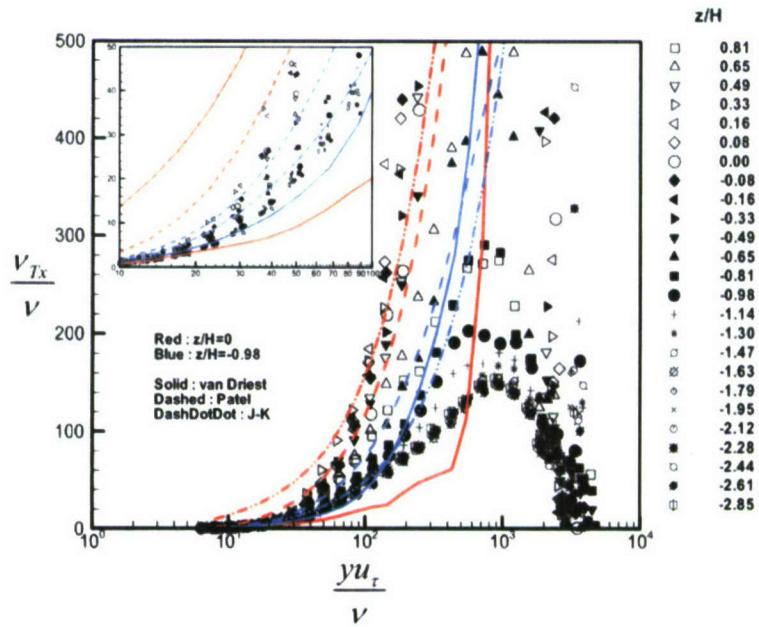
(c) Bump#1 at $x/H=3.46$

Figure 4.29 Continued.

(a) Large bump#3 at $x/H=3.63$ (b) Small bump#3 at $x/H=3.26$ Figure 4.30 Stream-wise eddy viscosity (v_{Tx}) at wake planes.

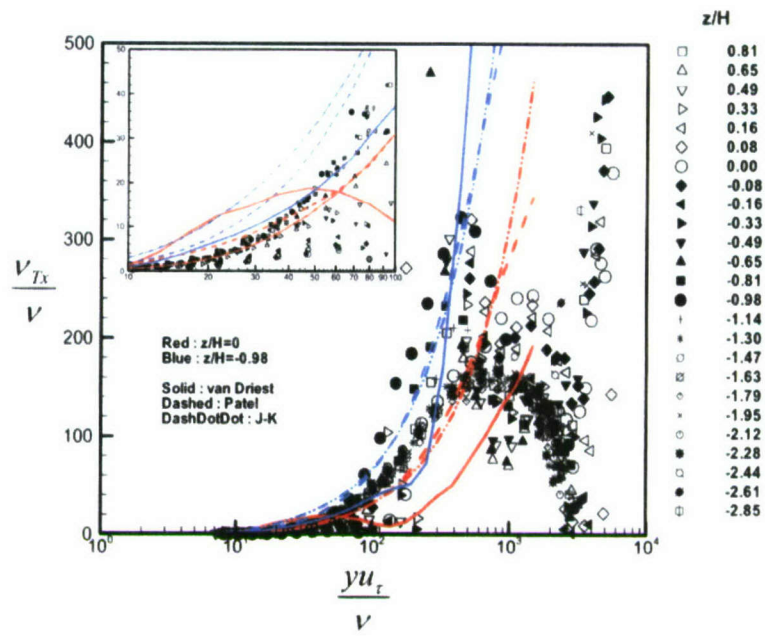
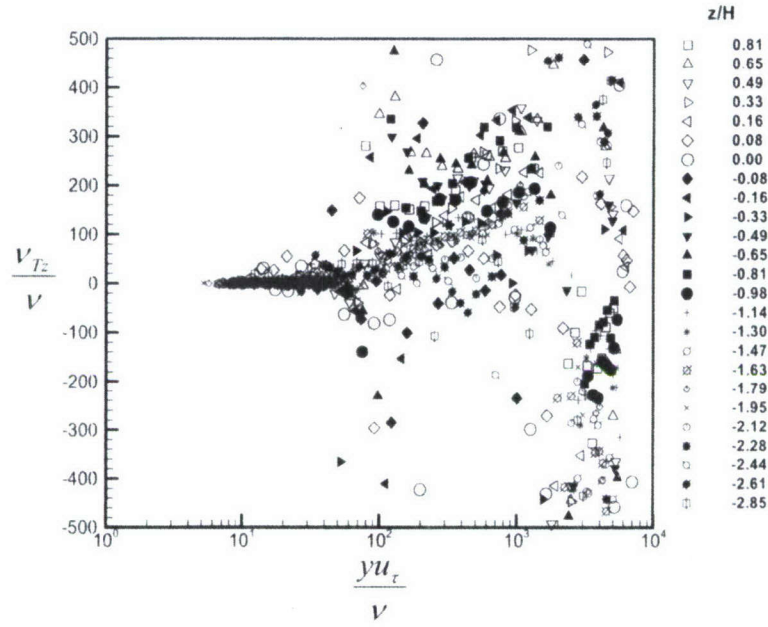
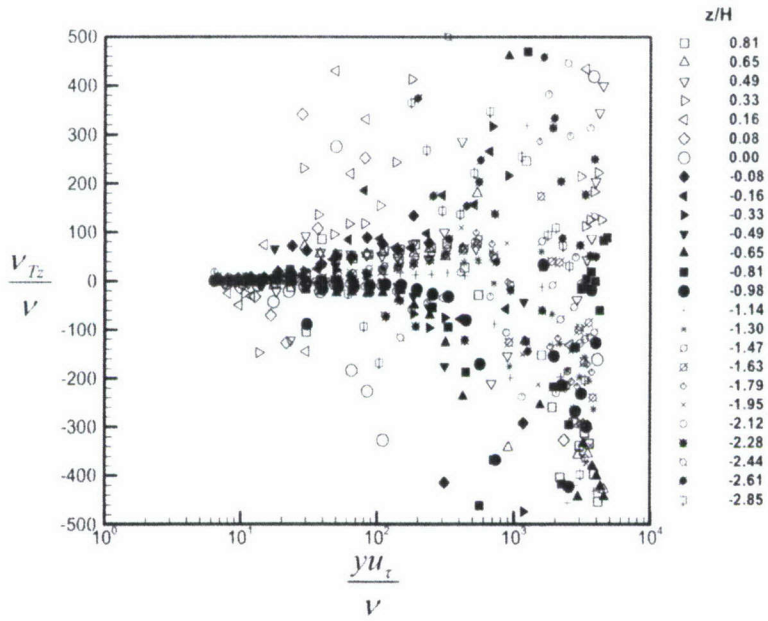
(c) Bump#1 at $x/H=3.46$

Figure 4.30 Continued.

(a) Large bump#3 at $x/H=3.63$ (b) Small bump#3 at $x/H=3.26$ Figure 4.31 Span-wise eddy viscosity (v_{Tz}) at wake planes.

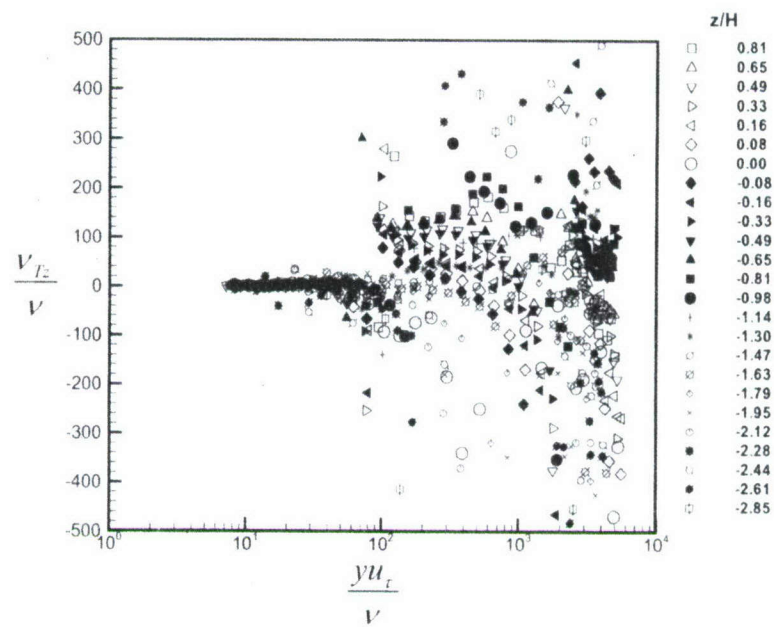
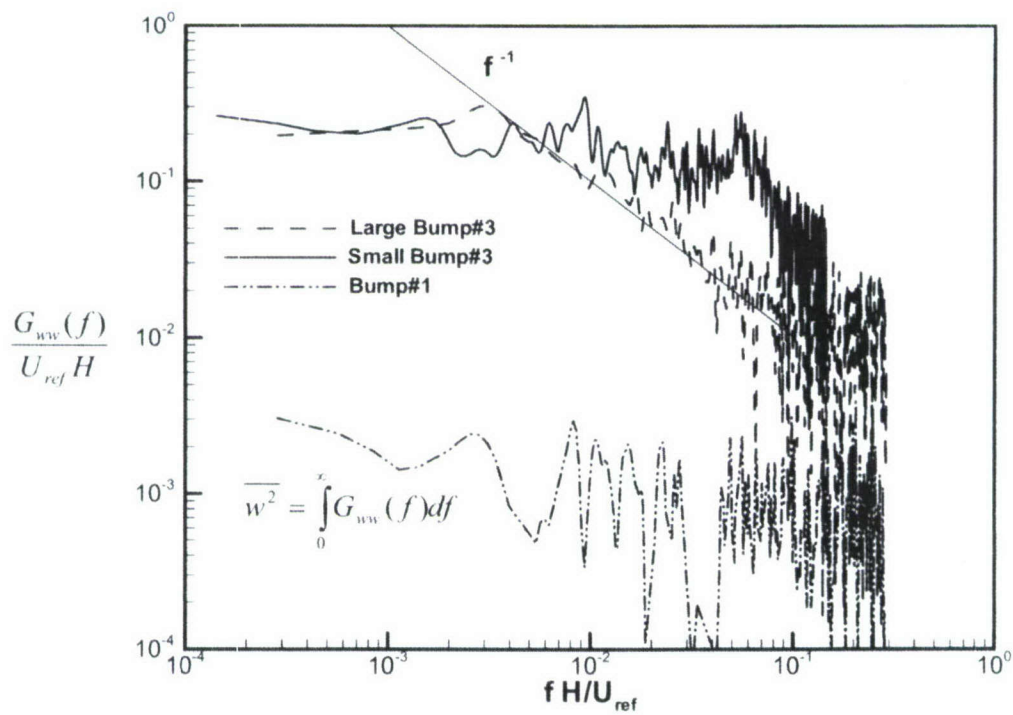
(c) Bump#1 at $x/H=3.46$

Figure 4.31 Continued.



large bump#3 at $y/H=0.2$, small bump#3 at $y/H=0.12$ and bump#1 at $y/H=0.17$.

Figure 4.32 Normalized w spectra of each bump at the centerline.

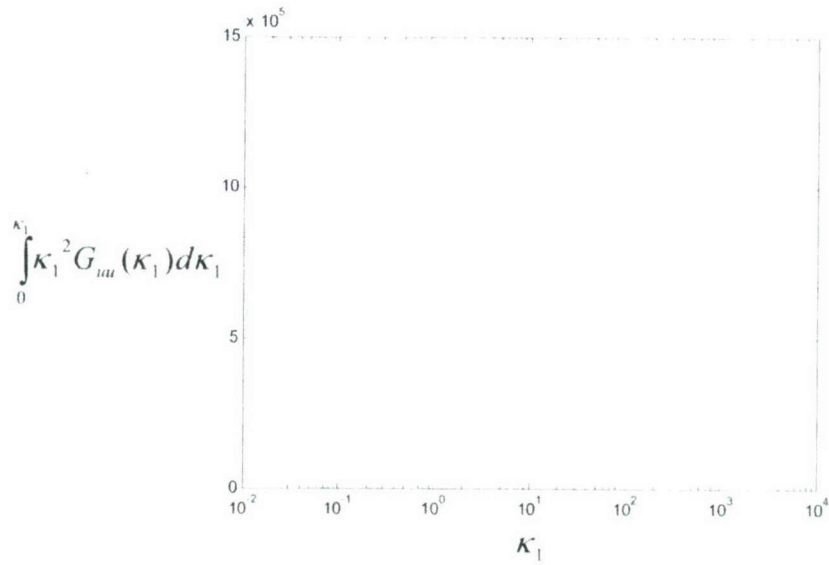
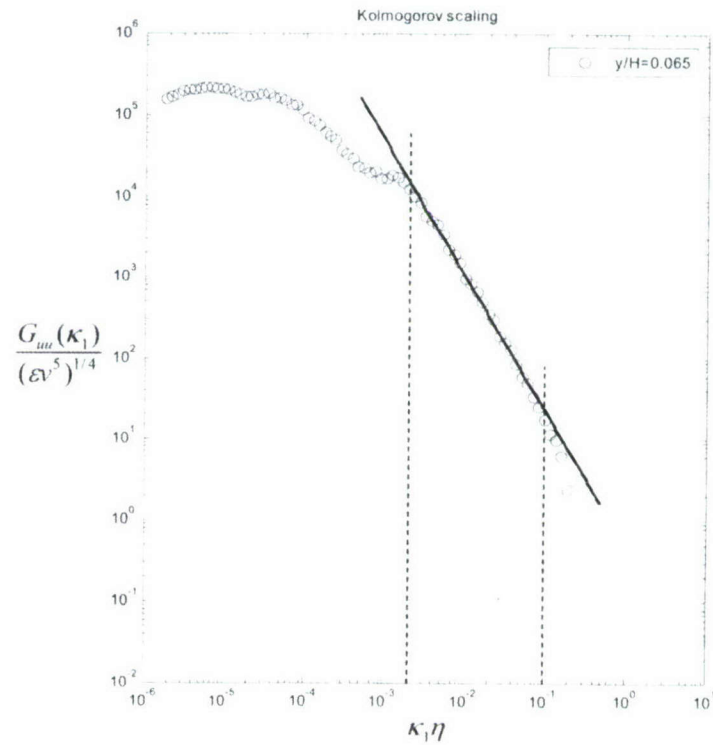


Figure 4.33 Integration of $G_{uu}(\kappa_1)$ at large bump#3 wake plane, $y/H = 0.065$, $z/H = 0$.



Solid line for Eq.(4.20). Dashed lines show fitting range.

Figure 4.34 Curve fitting of $G_{uu}(\kappa_1)$ at the wake plane centerline of large bump#3.

**Table 4.1 Dissipation rates and macro lengthscales of each bump
at the wake plane centerline, $z/H = 0$.**

	y/H	$yu_{\tau 0}/\nu$	$\varepsilon\nu/u_{\tau 0}$	R_C	L_ε/H (L_ε/δ)	L_{11}/H (L_{11}/δ)	$\varepsilon_0\nu/u_{\tau 0}$
LB3 ($x/H = 3.63$)	0.065	293	0.017 ± 0.001	0.994	0.95 (1.9)	1.42 (2.84)	0.008
	0.199	893	0.02 ± 0.001	0.996	0.95 (1.9)	2.21 (4.42)	0.003
	0.358	1610	0.013 ± 0.0005	0.999	1.1 (2.2)	2.45 (4.9)	
	0.782	3513	0.0005 ± 0.0003	0.994	1.4 (2.8)	1.68 (3.36)	
SB3 ($x/H = 3.26$)	0.065	146	0.03 ± 0.0048	0.997	1.66 (1.66)	0.16 (0.16)	0.015
	0.199	447	0.037 ± 0.0031	0.99	1.62 (1.62)	0.16 (0.16)	0.006
	0.358	805	0.037 ± 0.0037	0.99	1.77 (1.77)	0.19 (0.19)	0.0034
	0.782	1757	0.034 ± 0.0013	0.997	1.58 (1.58)	0.23 (0.23)	
B1 ($x/H = 3.46$)	0.033	146	0.0025 ± 0.0009	0.996	0.29 (0.58)	0.12 (0.24)	0.015
	0.166	745	0.0008 ± 0.0005	0.994	0.36 (0.72)	0.1 (0.2)	0.0036

LB3 : large bump#3, SB3 : small bump#3, B1 : bump#1.

$u_{\tau 0}$: skin friction velocity of reference 2-DTBL, 0.97.

δ : boundary layer thickness of reference 2-DTBL, 39 mm.

ε_0 : estimated dissipation rate of reference 2-DTBL assuming TKE convection and diffusion ≈ 0 .

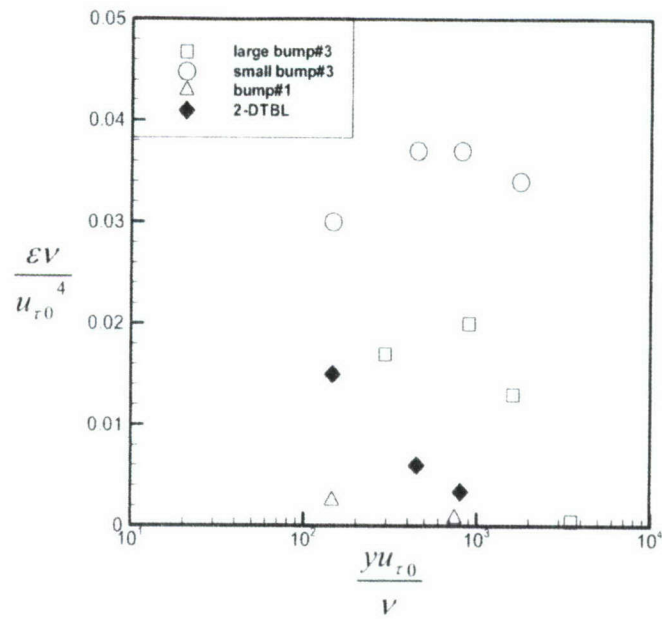
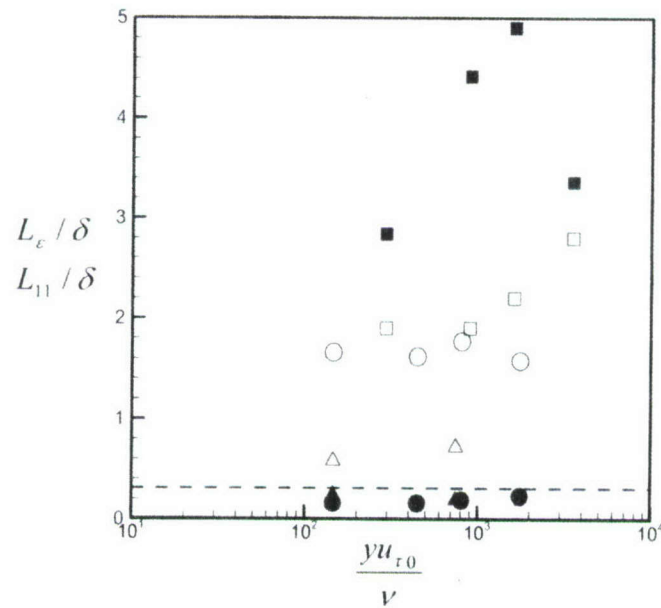


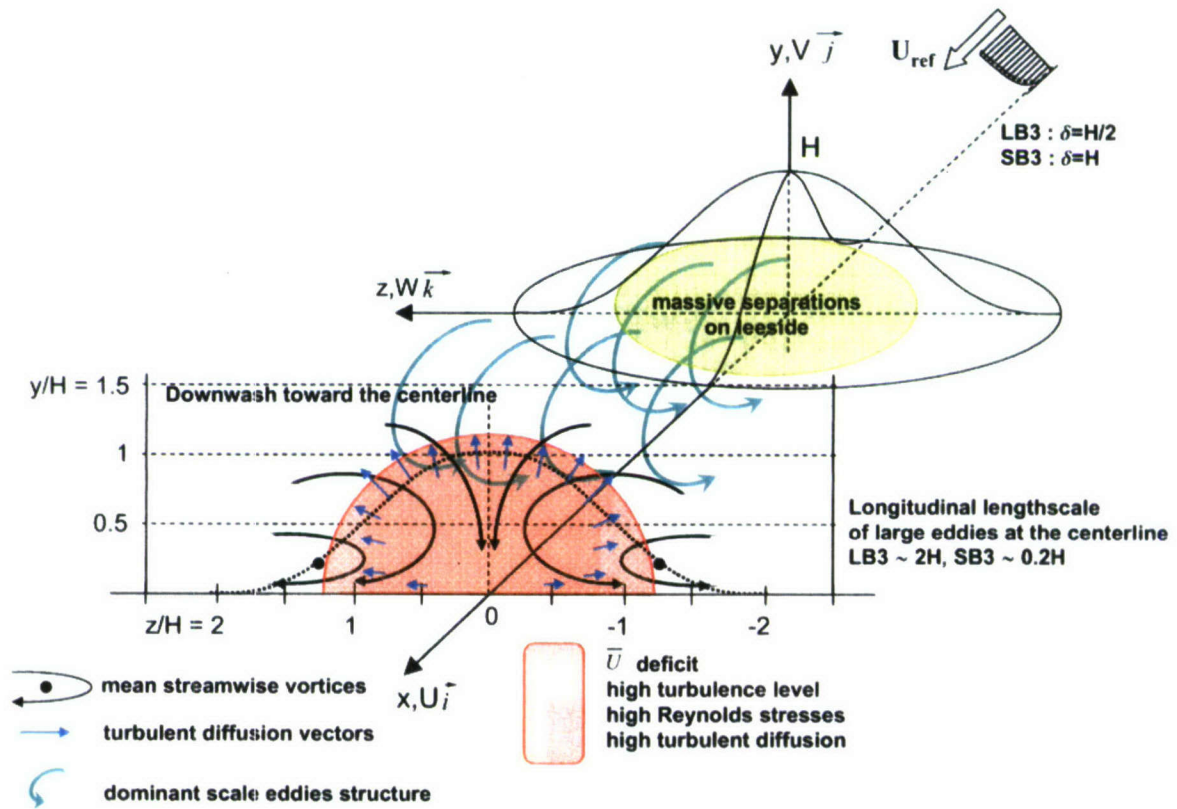
Figure 4.35 Normalized dissipation rate at the centerline of wake plane.



Dashed line for maximum L_ε / δ of separating 2-DTBL measured by Simpson et al. (1977).

□ : large bump#3, ○ : small bump#3 and △ : bump#1. Filled for L_{11} / δ and open for L_ε / δ .

Figure 4.36 Normalized macro lengthscales at the centerline of wake plane.



Large bump#3 at $x/H = 3.63$, small bump#3 at $x/H = 3.26$. A few eddies are drawn for clarity.

Figure 4.37 Illustration of flow structures at measured wake plane for bumps #3.

5

LDV Measurements near Large Bump#3 Surface

In previous chapters, the separation patterns and the structures and features of separated flow from the bumps at wake planes are described. However, they are still not well described enough to understand the origin of 3-D separations. Therefore, more detailed LDV measurements were performed around large bump#3 because this bump generates highly unsteady turbulent flow with multiple separations on the leeward surface. Data were measured from the very near surface and in the vicinity of separation region shown in the oilflow visualization in Chapter 3 in order to examine and describe the separation phenomena and associated physical processes.

Measurements have been performed over half of the bump at various yaw(ψ) and pitch(θ) angles with the miniLDV probe volume above the surface. The yaw angle changes by 10° for $0^\circ \leq \psi \leq 90^\circ$ and by 30° for $90^\circ < \psi \leq 180^\circ$. The miniLDV probe volume was traversed perpendicularly from the bump surface between about $y_L \approx 100 \mu\text{m}$ and $y_L \approx 1 \text{ cm}$ ($y_{L0}^+ \approx 6 \sim 578$ based on 2-D $u_\tau = 0.96$ at the center location of bump). The long LDV probe was used for locations farther from the surface. It should be noted that the symmetric pressure data are from Long(2002) and Simpson et al.(2002). All miniLDV data satisfy the realizability conditions (Schumann, 1977).

5.1 Mean Flow Symmetry

Since detailed measurements were conducted only on half of the bump, it was necessary to examine the mean flow symmetry over the bump. Several measurements have been conducted changing yaw angles at fixed locations from the bump surface. The bump was also moved in the span-wise direction within ± 2 mm to get symmetric mean flow, such as was done previously the wake plane measurements. In Fig. 5.1, the mean velocities, Reynolds stresses and triple products within $\psi = \pm 60^\circ$ at $r/H = 1.112$ and $y_L = 4$ mm away from the wall, show good symmetry within the experimental uncertainties. After the flow symmetry was acquired, detailed measurements were begun. Table 5.1 shows the locations of measurement. It is noted that the locations near the top of bump ($x/H = 0$) could not be measured because of the support of lexane window blocking laser beams.

5.2 Mean Velocities and Separations

5.2.1 Across the Center Plane

Figure 5.2(a) shows the measured \overline{U}_i and \overline{V}_j vectors normalized by U_{ref} of the center plane. The flow accelerates past the top region and decelerates near the wall due to the adverse pressure gradient. This decelerated flow reaches the stagnation point at about $x/H \approx 0.96$, even though the location is not exact because the velocity magnitude is small within uncertainties. The large mean backflow region is shown from this point below the dashed line, which indicates locations at $\overline{U}_i = 0$. The mean stream-wise flow from upstream and the backflow from downstream converge toward $x/H \approx 0.96$ and finally move away in the span-wise direction from this point to satisfy the continuity equation. Figure 5.2(b) shows the velocity field across the center plane by the combined LES-RANS calculation (Tessicini et al., 2005). It is combined with the log-law wall function and dynamic SGS (sub-grid scale) model. This simulation calculates the separation region reasonably well compared with present experimental data shown in Fig. 5.2(a), even though the reattachment appears around $x/H = 1.8$ for the simulation, which is apparently too far upstream. More simulation results and comparisons with present experimental results will be discussed in Chapter 6.

Figure 5.3 shows \overline{U}_L normalized by U_{ref} in local coordinates along the centerline. As shown in Fig. 5.3(a), it is highly accelerated from the windward side and reaches about 1.22 at $y_{L0}^+ \approx 50$ for $r/H = -0.254$. The \overline{U}_L values reduce after the top of the bump and approach to zero as r/H moves downstream. As shown in Fig. 5.3(b), most \overline{U}_L values are negative downstream from the separation below $y_{L0}^+ \approx 100$. The local maximum negative \overline{U}_L value increase farther downstream from the separation and it reduces up to about $-0.15 U_{ref}$ at $r/H = 1.615$.

Figure 5.4 shows the intermittency, $(\gamma_{pU})_L$ which is the fraction of time that the flow moves downstream (positive velocity) in local coordinates. Simpson (1989) defined quantitatively the detachment location as $\gamma_{pU} = 0.5$ for separating mean 2-DTBLs. The instantaneous reverse flow first appears at $r/H = 0.644$ near the wall. For downstream r/H , the time fraction of backflow increases up to 46 % at $r/H = 0.91$. There is more than 50 % backflow for $r/H \geq 0.976$ and downstream and the backflow region also increases from the wall further downstream. The $(\gamma_{pU})_L$ has a minimum of about 0.14 at $r/H = 1.615$. Since $(\gamma_{pU})_L$ is never zero, the large eddies supply the intermittently forward flow in this mean backflow region similar to a 2-D separated TBL (Simpson, 1987).

Simpson (1983) also suggested the simple model of mean backflow in 2-DTBL separation. For downstream of detachment, the model equation is

$$\frac{\overline{U}}{\overline{U}_N} = A \left(\frac{y}{y_N} - \ln \left| \frac{y}{y_N} \right| - 1 \right) - 1 \quad (5.1)$$

where $A = 0.3$ and \overline{U}_N and y_N are the maximum negative velocity and its corresponding distance from the wall, respectively. The equation above describes the mean backflow velocity profile of the middle region, $0.02 < y/y_N < 1.0$. It is curious how well this model works for presented mean backflow profiles. Figure 5.5 shows the normalized mean backflow velocity profiles in local coordinates for several r/H locations along the bump centerline. The solid lines represent the model equation with $A = 0.35$ instead of 0.3. Generally, the mean backflow model works well even though it does not describe the velocity profiles well where are close to the separation at $r/H \approx 0.96$. It might be due to the increase of 3-dimensionality spreading the mean backflow away from the

centerline in this region (see Fig. 5.6 and 5.7). However, for farther downstream from separation location, the agreement between modeled and measured profiles becomes better for $0.02 < y/y_N < 1.0$. This means that the structure and behavior of mean backflow in the centerline is very similar to one of 2-DTBL separation which is a function of only y/y_N , A and the result of the time average of large turbulent fluctuations induced by large-scale outer region eddies.

5.2.2 On the Leaside of the Bump

Figure 5.6(a) shows the surface pressure gradient contour, its vectors and lines connecting tangential velocity vectors of $\overline{U}i_t + \overline{W}k_t$ at $y_{L0}^+ = 11$. It shows clearly that the flow converges toward $x/H \approx 0.96$ along the centerline and then moves away in the span-wise direction. If the mirror image is used in the negative z side, this flow pattern is a typical 3-D saddle separation. For $|z/H| < 0.8$, the stream-wise flow from the upstream and the mean backflow from the downstream move away from the saddle point and converge into one trajectory which is the separation line. For $|z/H| > 1$, the stream-wise flow from the upstream is deflected toward the centerline due to the span-wise adverse pressure gradient and backflow continuity requirement and is spiraled into the backflow region, $x/H > 1$. Finally, the stream-wise flow from the upstream and the backflow from the downstream spiral and converge toward $x/H \approx 1.2$ and $z/H \approx 0.7$. The flow at this point forms a “focus separation” and satisfies the continuity equation. The separation line from the saddle point ends at the focus. This saddle-foci structure, with another focus on the positive z -side because of the symmetric flow, is not only on the nearest surface but also in the flow field up to $y_{L0}^+ \approx 340$ (see Fig. 5.7). A separation surface emanates from the separation line and the vortical rolling-up from the foci. Delery (1992) called this vortical structure a “Tornado-like vortex”. As y_{L0}^+ increases more, this vortex is not shown in Fig. 5.7(d).

It is noted that the LDV data show a different near surface flow pattern from the oilflow visualization presented in Chapter 3. They do not show foci separations between $x/H \approx 0.18$ and 0.4 because there is no backflow in this region. In addition, there is no clockwise focus on the negative z side between $x/H \approx 1$ and 1.5 because of no separation about $x/H \approx 1.5$ and no mean stream-wise flow in this region from the LDV data. These differences probably come from the effect of gravity (the maximum slope of the bump is about 38°), the flow unsteadiness on the finite thickness oil mixture, and the shear stress of the backflow. Unlike the oilflow visualization, the LDV data show

only one focus on each side, which is similar to the flow topology of the small bump#3 with the height, $H = \delta$ (see Fig. 3.8). Using a quadratic eddy-viscosity model, Wang et al. (2004) calculated very similar results for the leeside near wall region, as shown in Fig. 5.6(b) by the skin friction lines on the negative z/H side. However, the saddle separation on the centerline is calculated much upstream of the experimentally measured location. In these days, their calculations have been improved and will be discussed more in Chapter 6.

Figure 5.8 and 5.9 show the intermittency of U_L and W_L in local coordinates along several r/H locations. For upstream from $r/H \approx 0.96$ the $(\gamma_{pu})_L$ values are above 0.5 for $10^\circ \leq \psi \leq 60^\circ$. However, for downstream from $r/H \approx 0.96$, its values drop below 0.5 for $10^\circ \leq \psi \leq 30^\circ$ and reach about 0.1 at $r/H = 1.386$ and $\psi = 20^\circ$. The $(\gamma_{pw})_L$ values also show a similar behavior but their local minima are around 0.2 and 0.3 for $\psi = 10^\circ$ and 20° which are greater than that of $(\gamma_{pu})_L$. The intermittently forward flow of U_L and W_L in the mean backflow region corresponds to the effects of span-wise sweeping and ejection motions as well as stream-wise motions.

Figure 5.10 show the law of mean backflow \overline{U}_L in local coordinates along $r/H = 1.386$ and $\psi = 10^\circ, 20^\circ$ and 30° . The solid line also represents the model equation Eq.(5.1) like Fig. 5.5. For $\psi = 10^\circ, 20^\circ$ the modeled and measured profiles agree well even though there are larger \overline{W}_L values than along the centerline. However, For $\psi = 30^\circ$, which is almost at the center location of the focus, the law of mean backflow model does not work. It might be because the \overline{U}_L values for $\psi = 30^\circ$ are much smaller and closer to zero up to $y_{L0}^+ \approx 100$ than those for $\psi = 10^\circ, 20^\circ$.

5.2.3 Three-Dimensional Mean Streamlines

To understand the mean flow structures better, Figure 5.11 shows 3-D mean streamlines using \overline{U} , \overline{V} and \overline{W} . Streamlines "a" to "j" start from $x/H = 0.645$, upstream from the saddle separation, at $y/H = 0.781$ and $-0.05 \geq z/H \geq -0.5$ with $\Delta z/H = 0.05$. Note that the y_{L0}^+ at the beginning of each streamline increases span-wise as indicated in Fig. 5.11. Streamline "k" starts from $x/H = 0.63$, $y/H = 0.549$ and $z/H = -0.751$. It should be emphasized that they show mean velocity flow patterns, not instantaneous flow features. Streamlines "a" to "c" near the wall ($y_{L0}^+ \leq 53$) and close to the centerline ($z/H \leq -0.15$) move span-wise as they approach the saddle separation and separate near $x/H \approx 1$ around the separation line originating from the saddle separation. These separated flow

mean streamlines are entrained into the mean backflow region downstream, even though we know from Fig. 5.4 that the backflow is intermittent and some forward flow is supplied by the large eddies. They spiral toward the focus and then separate. A little further from the centerline and the surface, mean streamlines “d” and “e”, which start from $y_{L0}^+ = 91$ and 139 and $z/H = -0.2$ and -0.25 , respectively, move almost straight downstream, but they are entrained by large eddies toward the centerline and the surface after $x/H \approx 1.5$. Especially, after the entrainment, streamline “d” moves backward upstream and spirals toward the focus. Downstream from the saddle separation, the large eddies sweep fluid into the near surface frequently like for separated 2-D mean TBLs (Simpson, 1989). Streamlines “f” to “j” ($y_{L0}^+ \geq 197$) roll downstream counter-clockwise toward the centerline over top of mean streamlines “a” to “e” and show the positive stream-wise vortices as measured at the wake planes in Chapter 4. Streamline “k”, starting further span-wise from the centerline near the wall ($z/H = -0.751$, $y_{L0}^+ = 31$), moves toward the center downstream and spirals upstream toward the focus. Thus, the mean backflow zone is supplied by the large eddy structure and by flow from the sides of the bump.

5.3 Reynolds Stresses and Correlation Parameters

5.3.1 Reynolds Stresses

All 6 Reynolds stresses are presented here at typical r/H locations, 0.644, 0.91, 1.386 and 1.615 for x - y plots. They are shown in tunnel coordinates for contours at typical y_{L0}^+ , 11, 41, 200 and 456 as well. The solid lines in contour plots are mean streamlines tangent to bump surface.

Figure 5.12 and 5.13 shows the normalized $\overline{u_L^2}$ in local coordinates and $\overline{u^2}$ contours in tunnel coordinates, respectively. The $\overline{u_L^2}$ values increase near the wall region right after the top of bump for $\psi \leq 40^\circ$. Its maximum normalized value reaches up to 0.05 at $y_{L0}^+ \approx 30$ for $r/H = 0.338$. However, as farther downstream, the $\overline{u_L^2}$ values decrease near the wall region and have local maximum values in the semi-logarithmic mean velocity profile overlap region, $100 \leq y_{L0}^+ \leq 1000$ for $\psi \leq 40^\circ$. They approach zero in the outer region for all ψ values. For downstream from the separation, $r/H \geq 0.976$, the u_L fluctuations are much higher in the outer region and the local

maximum $\overline{u_L^2}$ values appear at $500 \leq y_{L0}^+ \leq 1000$ for $\psi \leq 30^\circ$. The normalized $\overline{u^2}$ contours in tunnel coordinates give a better view of $\overline{u^2}$ distributions for different y_{L0}^+ . As mentioned before, the $\overline{u^2}$ values are higher around the top of the bump near the wall and their higher region moves downstream where the separated flow is dominant as y_{L0}^+ increases.

Figure 5.14 and 5.15 shows the normalized $\overline{v_L^2}$ in local coordinates and $\overline{v^2}$ contours in tunnel coordinates, respectively. The $\overline{v_L^2}$ distribution in local coordinates are similar to that of $\overline{u_L^2}$ even though its magnitude is smaller than $\overline{u_L^2}$. The $\overline{v_L^2}$ values are higher near the wall region around the top of the bump for $\psi \leq 60^\circ$. It is related to large sweeping motions ($u_L > 0$ and $v_L < 0$) near the wall region. The local maximum normalized $\overline{v_L^2}$ values are about 0.015. As farther downstream, the $\overline{v_L^2}$ values also decrease near the wall and increase in the overlap region. For downstream from the separation, $r/H \geq 0.976$, they have local maximum in the outer region for $\psi \leq 30^\circ \sim 40^\circ$. The normalized $\overline{v^2}$ contours in tunnel coordinates show very similar trends to $\overline{u^2}$ contours. Their higher value region moves downstream as y_{L0}^+ increases and large eddies from the leeside separations increase the v fluctuation significantly in the outer region.

Figure 5.16 and 5.17 shows the normalized $\overline{w_L^2}$ in local coordinates and $\overline{w^2}$ contours in tunnel coordinates, respectively. The $\overline{w_L^2}$ values increase up to $y_{L0}^+ \approx 100$ in the inner region around the top of bump where the flow is attached like $\overline{u_L^2}$ and $\overline{v_L^2}$. However, The $\overline{w_L^2}$ values are relatively higher for $\psi \geq 50^\circ$ than for $\psi \leq 40^\circ$ because of the definition of local coordinates. As farther downstream, the $\overline{w_L^2}$ values for $\psi \leq 40^\circ$ are increasing up to the overlap region while they are decreasing near the wall for $\psi \geq 50^\circ$. For downstream from the separations, $r/H \geq 0.976$, the $\overline{w_L^2}$ values have local maxima at $y_{L0}^+ \approx 1000$ for $\psi \leq 30^\circ$ and the highest $\overline{w_L^2}$ value appear at $\psi = 20 \sim 30^\circ$ and $r/H = 1.386$ where is near the focus separation. As farther downstream, $r/H > 1.386$, the $\overline{w_L^2}$ values increase gradually up to the semi-logarithmic mean velocity profile overlap region for $\psi \leq 30^\circ$ and approach to zero as y_{L0}^+ increases. The contours of normalized $\overline{w^2}$ in tunnel

coordinates show a wider range of high w fluctuation near the bump surface around the downstream as well as the top than $\overline{v^2}$. It is noted that the contour level of $\overline{v^2}$ and $\overline{w^2}$ is much smaller than $\overline{u^2}$. In the mean backflow and near the wall region, $r/H \geq 0.976$ and $\psi \leq 30^\circ$, the u and w fluctuations are relatively higher than the v fluctuations due to the wall damping effect on v and the skewed large eddies originated from the leeside separations which generated forward and backward flows instantaneously in the mean backflow region.

Figure 5.18 and 5.19 show the normalized $\overline{uv_L}$ in local coordinates and \overline{uv} contours in tunnel coordinates, respectively. The $\overline{uv_L}$ values are large negative near the wall around the top of the bump for $\psi \leq 40^\circ$ due to the large sweeping motions. At farther downstream, the $\overline{uv_L}$ shows locally maximum negative values at $y_{L0}^+ \approx 90$ for $\psi \leq 40^\circ$ mainly due to the ejection motions ($u < 0$ and $v > 0$) while its values nearer the wall decrease. However, as r/H approaches to the saddle separation at $r/H \approx 0.96$, the $\overline{uv_L}$ values in $y_{L0}^+ \leq 100$ decrease and the large positive $\overline{uv_L}$ values begin to appear in the overlap region for $\psi \leq 30^\circ$. It might be due to the reduced ejection motions in $y_{L0}^+ \leq 100$ and the increased interactions ($u_L < 0$ and $v_L < 0$) in the overlap region. For downstream from near the separation, $r/H \geq 0.841$, the $\overline{uv_L}$ value in $y_{L0}^+ \leq 100$ appear to be close to zero or even to be positive for $\psi \leq 30^\circ$. In this region, most $\overline{U_L}$ profiles show the mean backflow which is the result of time-averaging velocity fluctuations induced by the skewed large eddies structure coming from the separation. Therefore, u and v are not correlated to produce Reynolds shear stress. However, the negative $\overline{uv_L}$ values increase in the overlap region, $100 \leq y_{L0}^+ \leq 1000$ due to the sweeping motions. In the outer region, $y_{L0}^+ \geq 1000$, the large positive $\overline{uv_L}$ values appear but they do not appear in $r/H \geq 1.615$. As shown in the contours of normalized \overline{uv} in tunnel coordinates, the lower \overline{uv} values appear in the mean backflow and near the wall region. The larger negative \overline{uv} values appear downstream from the saddle separation as y_{L0}^+ increases farther in $r/H \geq 0.96$ and $\psi \leq 30^\circ$.

Figure 5.20 and 5.21 show the normalized $\overline{vw_L}$ in local coordinates and \overline{vw} contours in tunnel coordinates, respectively. The $\overline{vw_L}$ values are generally small near the wall region $y_{L0}^+ \leq$

100 for $\psi \leq 30^\circ$. They increase in larger ψ region due to the increase of flow 3-dimensionality in local coordinates. For $\psi \geq 40^\circ$ the high $\overline{vw_L}$ values downstream from the top decrease with r/H increase and the $\overline{vw_L}$ profiles for these ψ regions show a similar trend downstream from the saddle separation. As r/H approaches the saddle separation and downstream from the separation, the large positive $\overline{vw_L}$ values appear in the outer region for $\psi = 20^\circ \sim 30^\circ$ like $\overline{uv_L}$. It might be mainly due to the increase of span-wise outward interaction ($u_L < 0$, $v_L < 0$ and $w_L < 0$). However, the $\overline{vw_L}$ values for $\psi = 10^\circ$ downstream from the saddle separation appear to be negative in the semi-logarithmic mean velocity profile overlap region which is due to the span-wise sweeping motions toward the centerline ($u_L > 0$, $v_L < 0$ and $w_L > 0$). As shown in the contours, the normalized \overline{vw} values in tunnel coordinates are very small in most leeward. They are positive near the wall around the separation lines coming from the saddle separation. The negative \overline{vw} values appear downstream from the separation and where the mean backflow disappear.

Figure 5.22 and 5.23 show the normalized $\overline{uw_L}$ in local coordinates and \overline{uw} contours in tunnel coordinates, respectively. The $\overline{uw_L}$ values are higher for $\psi \geq 60^\circ$ near the wall downstream from the top of bump. At farther downstream r/H approaching the saddle separation, the $\overline{uw_L}$ values for $10^\circ \leq \psi \leq 40^\circ$ increase positively in $y_{L0}^+ \geq 100$. For downstream from the separation, the $\overline{uw_L}$ profiles for $\psi \geq 50^\circ$ are close to zero and have a similar behavior. However, $\overline{uw_L}$ for $\psi = 20^\circ \sim 30^\circ$ have significant positive values in the outer region. However, the $\overline{uw_L}$ values for $\psi = 10^\circ$ are negative in the inner region. It means that the u_L and w_L fluctuations are correlated oppositely between $\psi = 10^\circ$ and $\psi = 20^\circ$. As shown in Fig. 5.23, the \overline{uw} in tunnel coordinates are negatively high in the mean backflow region near the centerline and its sign changes about midway between the centerline and the focus separation.

Comparing the magnitude of three Reynolds shear stresses, the $\overline{vw_L}$ is the smallest for $\psi \leq 40^\circ$ and the $\overline{uw_L}$, one of the major features of 3-D turbulence, is not negligible at all for $\psi \leq 40^\circ$. Figure 5.24 shows the ratio of $\overline{vw_L}$ to $\overline{uw_L}$ in local coordinates. The ratio is much less than one for

profiles of $\psi \leq 40^\circ$. The $\overline{uw_L}$ is more significant than $\overline{vw_L}$ in this region, which means that u_L and w_L are more correlated than v_L and w_L .

Figure 5.25 shows the normalized Reynolds shear stress magnitude $|\tau_L / \rho U_{ref}^2| = \sqrt{(-\overline{uw_L})^2 + (-\overline{vw_L})^2}$ in local coordinates. This quantity is independent of the coordinate rotation about the axis which is normal to the surface. The solid line is for 2-DTBL. The $|\tau_L|$ values are much higher than 2-DTBL near the wall, $y_{1,0}^+ \leq 100$ for most profiles around the top of bump. For farther downstream, as r/H approaches the saddle separation, the $|\tau_L|$ values decrease and become lower than 2-DTBL for $\psi \leq 40^\circ$ within $y_{1,0}^+ \leq 100$ while they are still much higher than 2-DTBL for $\psi \geq 50^\circ$. However, the $|\tau_L|$ values begin to increase significantly for $y_{1,0}^+ > 100$ and to be much higher than for a 2-DTBL in the outer region for $\psi \leq 40^\circ$. For farther downstream from the separation, the $|\tau_L|$ values for $\psi \leq 40^\circ$ and $y_{1,0}^+ \leq 100$ are still lower than a 2-DTBL. Actually, this region is the mean backflow area. In the outer region, the $|\tau_L|$ values are much higher and reach local maxima at $y_{1,0}^+ \approx 800$ for $\psi \leq 30^\circ$. The $|\tau_L|$ values for $\psi \geq 50^\circ$ are still higher than for the 2-DTBL near the wall region, $y_{1,0}^+ \leq 100$, but they reduce gradually as r/H increases. They are lower than the 2-DTBL in the outer region and increase up to 2-DTBL magnitude with ψ increase.

5.3.2 The Correlation Coefficients related to Reynolds Stresses

Figure 5.26 shows the parameter $1/S \equiv [(-\overline{uw_L})^2 + (-\overline{vw_L})^2]^{0.5} / \overline{v_L^2}$ vs. $y_{1,0}^+$ in local coordinates. It is independent of the coordinate rotation about y_L -axis, which is normal to the wall. As mentioned in Chapter 4, since $\overline{v^2}$ contains little contribution from “inactive” turbulent motions, this parameter is a type of Reynolds stress correlation coefficient. “Inactive” motions are low frequency, long wavelength structures that produce little Reynolds shearing stresses. It should be noted that this parameter is almost constant at about 0.6 for $100 \leq y^+ \leq 1200$ in a 2-DTBL and has a similar behavior for 3-D flows as for 2-D flows if there are no embedded stream-wise vortices (Ölçmen and Simpson, 1995). For $r/H < 0.781$, $1/S$ is lower than a 2-DTBL below $y_{1,0}^+ \approx 100$ within $\psi \leq 40^\circ$ due to much higher $\overline{v^2}$ in spite of relatively high Reynolds shearing stresses. For $\psi \leq 40^\circ$, $1/S$ in the inner layers ($20 \sim 30 \leq y_{1,0}^+ \leq 400 \sim 500$) is much lower than a 2-DTBL for $r/H \geq 0.781$ and reaches

the local minima at $y_{L0}^+ \approx 80 \sim 100$ because of strong 3-D flows with vortices which are generated by the pressure gradient and spiral around the focus. For $\psi \geq 50^\circ$, $1/S$ is relatively high in these layers due to higher Reynolds shearing stresses. As shown in Fig. 5.25, for $\psi \leq 40^\circ$ in these layers the numerator in $1/S$, the Reynolds shearing stress magnitude, is much lower downstream from the separation because of the lower production rates in the backflow zone and the decorrelation of turbulent structures with different locally upstream histories. It does not change much up to $y_{L0}^+ \approx 100$ downstream of the separation and begins to increase significantly above this height within $0^\circ \leq \psi \leq 40^\circ$ because of the higher production rates due to the higher Reynolds normal stress and positive velocity gradient in the backflow region for $y_{L0}^+ > 100$. It shows higher values in this region from $y_{L0}^+ \approx 456$ where the saddle-focus structure disappears than for $\psi \geq 50^\circ$.

Figure 5.27 shows the correlation coefficient between u_{LSS} and v_{LSS} , $(R_{uv})_{LSS} \equiv -\overline{uv_{LSS}} / \sqrt{\overline{u_{LSS}^2}} \sqrt{\overline{v_{LSS}^2}}$ in local shear stress coordinates in which there is $-\overline{vw_{LSS}} = 0$. It is less correlated and has local minimum, less than 0.1, at around $y_{L0}^+ \approx 80 \sim 100$ within $0^\circ \leq \psi \leq 40^\circ$ than for $\psi \geq 50^\circ$ for $r/H \geq 0.91$. From these two parameters, there is less correlation between u_L and v_L and lower Reynolds shearing stress generated by the rotational motions with respect to $\overline{v_L^2}$ in the saddle and focus structure region than in a 2-DTBL.

5.4 Turbulent Kinetic Energy and its Transport Velocity Vectors

Contours of the turbulent kinetic energy, $TKE \equiv \overline{q^2}/2 = (\overline{u^2} + \overline{v^2} + \overline{w^2})/2$ normalized by U_{ref} and its transport velocity vectors, $\vec{V}_q/U_{ref} \equiv (V_{qu}\vec{i} + V_{qv}\vec{j})/U_{ref} \equiv (\overline{uq^2}\vec{i} + \overline{vq^2}\vec{j})/\overline{q^2}U_{ref}$ at the center plane are shown in Fig. 5.28. Figure 5.29 shows the normalized TKE contours and its transport velocity vectors, $\vec{V}_q/U_{ref} \equiv (V_{qu}\vec{i}_L + V_{qv}\vec{k}_L)/U_{ref} \equiv (\overline{uq^2}\vec{i}_L + \overline{wq^2}\vec{k}_L)/\overline{q^2}U_{ref}$ which are locally tangent to the surface for several $y_{L0}^+ = 11, 41, 200$ and 456. Near the wall, the high turbulent shear stresses and velocity gradients generate the highest TKE level around $x/H \approx 0.3$ after the apex of the bump. As y_{L0}^+ increases, however, the TKE level in this region decreases because of lower TKE production rates. On the other hand, the separated and backflow region ($x/H > 1$ and $|z/H| < 1$) from the saddle and the focus shows the high TKE level as y_{L0}^+ increases due to large production rates.

The TKE transport velocity vectors, \vec{V}_{qt}^+ / U_{ref} in Fig. 5.28 and Fig. 5.29 which are derived from the triple products show the flow transport velocity vectors of the TKE by the turbulent diffusion. Their large magnitudes show some unsteadiness and jitter of the instantaneous flow. Generally, their directions are about opposite to the mean velocity vectors, indicating that occasionally the instantaneous velocity is much lower than the mean velocity. For $x/H > 1$, their magnitudes are less near the wall than away from the wall because, as y_{L0}^+ increases, the TKE increases in this region and the unsteady and occasional jittering motions also increase by the vortical separated flow. These meandering motions are outward from the focus along $\psi = 20^\circ$ and 40° . However, they are stream-wise toward the centerline before the focus and opposite after the focus along $\psi = 30^\circ$. Around the bump apex, the magnitudes of TKE transport vectors are very strong and have about the same directions as the mean velocity vectors near the wall. This is due to the very high positive $\overline{u^3}$ generated by turbulent sweeping motions toward the wall under the effects of the adverse pressure gradient and the curvature. As y_{L0}^+ increases, the \vec{V}_{qt}^+ / U_{ref} magnitude becomes smaller and the directions changes opposite to the mean velocity vectors because of turbulent ejection motions from the wall.

Figure 5.30 shows the normalized TKE profiles for several $r/H = 0.644, 0.91, 1.386$ and 1.615 with the comparison with 2-DTBL TKE profile which is a solid line. As shown in Fig. 5.28 and 5.29, the TKE values for downstream from the top of bump are very high near the wall, $y_{L0}^+ \leq 100$. As r/H increases approaching the saddle separation, the TKE level in these layers decreases while it increases significantly in the outer region for $\psi \leq 40^\circ$. However, the TKE level for $\psi \geq 50^\circ$ is still higher than for $\psi \leq 40^\circ$ very near the wall, $y_{L0}^+ \leq 20$. For downstream of the separation, $r/H \geq 0.976$, the TKE level for $\psi \leq 40^\circ$ increases from the wall with increasing y_{L0}^+ and reaches local maxima values at $y_{L0}^+ \approx 1000$. It does not show a plateau in the overlap region for $\psi \leq 40^\circ$. The TKE level for $\psi \geq 60^\circ$ is very close to that of a 2-DTBL from the overlap region, $y_{L0}^+ \geq 100$ even though it is still higher below that height. It is noted that for downstream from the separation the maximum TKE values appear near where $(\gamma_{PU})_L$ is close to 1.0 shown in Figs. 5.4 and 5.8 for $\psi \leq 30^\circ$ like a 2-D separating TBL.

Figure 5.31 shows the turbulence intensity, $TI = \sqrt{\overline{u^2} + \overline{v^2} + \overline{w^2}} / (\overline{U} + \overline{V} + \overline{W})$ contours. It may be a better parameter than TKE normalized by U_{ref} to show the local turbulence level on the leeside of

the bump. Near the wall, the TI has a very high level of more than 20 along the separation line from the saddle point to the focus point because of very low mean velocities. As y_{L0}^+ increases above $y_{L0}^+ \approx 150$, the high TI zone moves and spreads downstream because of the separated flow, which has higher Reynolds normal stresses as well as low mean velocities.

5.5 Structural Parameters A1, B and B2

Figure 5.32 shows Townsend's structural parameter $A1 \equiv [(-\overline{uv_L})^2 + (-\overline{vw_L})^2]^{0.5} / \overline{q^2}$ vs. y_{L0}^+ in local coordinates. This quantity is also independent of the coordinate rotation about the vertical axis which is normal to the surface. It is the ratio of the magnitude between Reynolds shearing stress and 2TKE. It is about 0.1 ~ 0.13 for $70 \leq y^+ \leq 1000$ in a 2-DTBL although some "inactive" motions contribute to the TKE through $\overline{u^2}$. The A1 shows very similar behavior as $1/S$ in Fig. 5.26, having much lower value and local minimum at about $y_{L0}^+ \approx 80 \sim 100$ within $\psi \leq 40^\circ$ than for $\psi \geq 50^\circ$ for $r/H \geq 0.91$. The TKE relative to the magnitude of the Reynolds shearing stress is higher than in a 2-DTBL. The A1 reduction in the inner region for $\psi \leq 40^\circ$ is mainly due to the reduced Reynolds shear stresses in the mean backflow region compared with 2-DTBL.

Figure 5.33 and 5.34 show $B = \overline{v_L^3} / (\overline{u^2 v_L} + \overline{v_L^3} + \overline{v w_L^2})$ and $B2 = \overline{v_L^3} / \sqrt{(\overline{u v_L^2})^2 + (\overline{v^2 w_L})^2}$ parameters vs. y_{L0}^+ in local coordinates, respectively. They are invariant with the coordinate rotation about the axis which is normal to the surface. The B parameter indicates the relation between the turbulent transport of TKE and the $\overline{v_L^2}$ transport by the v fluctuations. It is more scattered near the wall due to higher measurement uncertainties and less number of samples. In general, the B parameter collapses well to 0.2 ~ 0.4 values in the overlap region and it is much higher near the wall which means that the TKE is transported less effectively by the normal fluctuations. For $r/H \geq 1.615$, it becomes higher for $\psi \leq 30^\circ$ than for $\psi \geq 40^\circ$.

The B2 parameter indicates the correlation between the turbulent transport of Reynolds shear stresses, $\overline{uv_L}$, $\overline{vw_L}$ and the $\overline{v_L^2}$ transport by the v fluctuations. The B2 parameter shows a different behavior from the B parameter. It increases almost semi-logarithmically within ± 1 from the wall for downstream from the bump apex. As r/H approaches to the saddle separation, $r/H \approx 0.96$, it has two different trends for $\psi \leq 30^\circ$ and $\psi \geq 40^\circ$. The B2 parameter for $\psi \leq 30^\circ$ is a negative value in the

inner region while it for $\psi \geq 40^\circ$ is positive value. These two behaviors become significant as r/H moves downstream. For $r/H = 1.386$, the B2 values is about -0.6 in the inner region for $\psi \leq 30^\circ$. However, as $r/H \geq 1.615$, it increases negatively in the inner region with $y_{1,0}^+$ increase. Compared with B parameter in Fig. 5.33, the transport of Reynolds shear stresses by v fluctuations is more effective than the TKE transport for $\psi \leq 30^\circ$ and it must be toward the near wall region from high Reynolds shear stresses in the outer region where large scale structures are dominant.

5.6 Flow Angle, Flow Gradient Angle and Shear Stress Angle

As mentioned in Chapter 4, the isotropic eddy viscosity model has been used in many turbulence closure problems and even for this bump flow. It is related to velocity strains and Reynolds shear stresses. Therefore, the flow angle, $FA = \tan^{-1}(\overline{w'_l}/\overline{u'_l})$, the flow gradient angle, $FGA = \tan^{-1}[(\partial \overline{w'_l}/\partial y_l)/(\partial \overline{u'_l}/\partial y_l)]$ and the shear stress angle, $SSA = \tan^{-1}(-\overline{vw'_l}/-\overline{uv'_l})$ in local coordinates are presented here, especially for the leeside separations region. Figure 5.35 ~ 5.37 show these three angles vs. $y_{1,0}^+$ typically for $r/H = 1.179, 1.386$ and 1.615 . The absolute FA values greater than 90° represent the mean backflow in local coordinates. It is noted that the angle values, 180° and -180° represent the same direction. For $\psi \leq 20^\circ \sim 30^\circ$, all three angles show huge variations within $\pm 180^\circ$ across $y_{1,0}^+$ because of the mean backflow and spiral flow due to the saddle-focus separation. The FA and SSA values change dramatically in the overlap region for $\psi \leq 30^\circ$ while the FGA values change significantly around $y_{1,0}^+ \leq 100$ due to the mean backflow gradient in that layer. As usual in 3-DTBLs, there is the lag between FGA and SSA variation across the layer. Therefore, the isotropic eddy viscosity is improper to represent the leeside flow of bump. For $\psi \geq 50^\circ$, the FA values do not change much across the layer while FGA and SSA values become greater than 90° around $y_{1,0}^+ = 100$, which means that the flow gradient and Reynolds shear stress vectors are backward in local coordinates.

These three angles at $\psi = 30^\circ$ of each r/H are also presented for clearer comparison of each other. The difference between FGA and SSA values are observed. The FA and FGA appear to be close to each other about 40° in the outer region. The FGA values change toward about 40° up to $y_{1,0}^+ \approx 100$ and do not change much above that height while FA values change toward 40° up to $y_{1,0}^+ \approx 300 \sim 400$. The large SSA variations are still observed above $y_{1,0}^+ \approx 100$ where FA and FGA

seem to be almost constant. Figure 5.37(d) is for the closet location to the focus center near the wall. All three angles vary gradually from the wall and change significantly below $y_{L0}^+ \approx 100$. The FA and FGA values reach to about 40° as farther y_{L0}^+ . However, the SSA value decreases negatively after it reaches to 0° at $y_{L0}^+ \approx 100$ with y_{L0}^+ increase due to large negative $-\overline{vw_L}$ values in the overlap region.

5.7 Bimodal Histogram

One of the most interesting features of the leeside flow structure is the bimodal velocity histogram. Devenport and Simpson (1990) reported first the bimodal features in U and V for their wing-body junction flow. They captured bimodal probability histograms in the vicinity of the wing nose. Larousse et al. (1991) also reported similar bimodal features in front of the surface mounted cube.

In the leeside of bump, there are bimodal velocity probability histograms in U_L and W_L in local coordinates. Double peak histograms in U_L appear downstream of $r/H = 0.841$, a little upstream from the saddle separation, and are significant along the centerline. Bimodal histograms in W_L appear from downstream from the saddle separation in $\psi \leq 40^\circ$ as well as U_L . Figure 5.38 shows bimodal histograms of U_L and W_L at specific locations. The V_L probability histogram has no bimodal feature. In this bimodal region, velocity fluctuations are switched between two dominant peak values so that the flow is highly unsteady and may be meandering with a low frequency.

Figure 5.39 shows the contour of the joint probability density function (JPDF) of U_L and W_L , $P(U_L, W_L)$ along the centerline. A 50×50 bins grid was used. There are also two dominant contour level peaks of U_L along $W_L \approx 0$. The JPPDFs, $P(U_L, W_L)$ of several locations in the leeside bump are shown in Fig. 5.40. There are significant two pairs of (U_L, W_L) with high probability. It is noted that the bimodal JPPDF depends on the coordinate system. Figure 5.39 and 5.40 represent that the bimodal U_L and W_L are highly correlated each other and that the focus

location may move sequentially in x_L - z_L plane. Figure 5.41 shows the coherency functions in a frequency domain at $r/H = 1.386$, $\psi = 30^\circ$ and $y_{L0}^+ = 261$.^{††} It also indicates that the u and w is much higher coherent below 50 Hz than the u and v and the v and w . It must be the source of high Reynolds shearing stress \overline{uw} production in these bimodal regions as shown in Fig. 5.22.

5.7.1 Forward and Backward Modes

These bimodal histograms having two peaks in U_L and W_L indicate that the instantaneous velocity has two preferred values. It may be very interesting if these bimodal histograms could be separated into two independent histogram distributions. The mode-averaged results from two independent histograms may represent some limited instantaneous flow features and unsteadiness in the bimodal region.

Devenport and Simpson (1990) separated each bimodal histogram in their flow into two modes. They assumed that one histogram was symmetric with the larger peak of original bimodal histogram. Then, the other histogram could be obtained by the subtraction of this symmetric histogram from the original. However, this method does not work well to separate two modes especially for the cases that two peaks in original bimodal histogram are too close. Therefore, the least square fit of two Gaussian functions in Eq.(5.2) has been used for the present data analysis.

$$PDF(x) = \sum_{i=1}^2 A_i \exp \left[- \left(\frac{x - B_i}{C_i} \right)^2 \right] \quad (5.2)$$

The original bimodal probability density function (PDF) of U_L or W_L is the summation of two Gaussian functions, where x is the given data U_L or W_L , A_i is the amplitude, B_i is the peak position and C_i is the full width at half the peak amplitude. The least square fit for Eq.(5.2) depends on the bin width of histograms. Therefore, the optimum bin width suggested by Scott (1979) is used for bimodal histograms.

^{††} I gratefully appreciate that Mr. Todd Lowe allowed me to use his codes for the coherency calculation.

$$\text{Bin width} = 3.49\sigma N^{-1/3} \quad (5.3)$$

In Eq.(5.3), σ is the standard deviation of samples and N is the number of samples, respectively.

There are two different bimodal histogram features between the flow of bump leeside and the flow around surface mounted obstacle like Devenport and Simpson (1990) and Larousse et al. (1991). The bump flow has bimodal histograms in U_L and W_L but they have bimodality in U or V instead. Also, one peak is almost always very close to zero velocity and the other is at large negative velocity in their U PDF. However, for the bump flow, two peaks are always at negative and positive velocity values and the minimum probability between two peaks are very close to zero velocity in both U_L and W_L . Therefore, two independent probability histograms from Eq.(5.2) are defined as “forward mode” with positive peak and as “backward mode” with negative peak, respectively. Figure 5.42 shows the example case for separating two modes. The blue line is for the forward mode and the green line for the backward mode. The red line is for the original bimodal PDF by summing two modes. Even though the correlation coefficient R^2 for least square fit is about 0.97 ~ 0.99, the model equation (5.2) seems to work reasonably for most bimodal histograms such as having two dominant symmetric peaks like Fig. 5.42(a) and having asymmetric peaks with one of larger and the other of smaller like Fig. 5.42(b).

Now the averaged velocities of two modes can be estimated. However, the question is how these averaged two velocities in U_L and W_L , total four velocities, are related to each other. As mentioned earlier, Fig. 5.39 ~ 5.41 represent that U_L and W_L in the bimodal region are highly correlated to each other. Therefore, the averaged forward velocity in U_L must be related to the one in W_L and the backward mode must be too. In other words, the forward velocity mode has positive (U_L, W_L) values and the backward velocity mode has negative (U_L, W_L) values. It is noted that some locations do not have bimodal histograms or one of peaks are too small to fit Eq.(5.2). For these locations, the time-averaged velocities of original bimodal histograms are used. Figures 5.43 and 5.44 show the velocity vectors which are tangent to the bump surface for the forward and backward modes at $y_{1,0}^+ = 11$. For $y_{1,0}^+ = 41$ and 69, the forward and backward modes are shown in Appendix D. In these figures, the blue lines connect the time-averaged velocity vectors which are

tangent to surface from the original bimodal histograms. The contours are for γ_{N,U_L} , the time fraction of negative U_L in bimodal region. The black vectors are for the forward or the backward mode velocity vectors only in bimodal region and the black lines are connecting these vectors for visual aid. As expected, the two flow patterns are totally different from the original bimodal histograms. They do not show any saddle-focus separation structure. The flow just moves forward and toward the center in the forward mode and backward and outward from the center in the backward mode. However, as Devenport and Simpson (1990) suggested, these forward and backward modes may be the kind of ideal cases and may not occur dominantly. On the other hand, the combination of these two modes may represent the more possible preferred flow patterns. The similar analysis for present data will be discussed in the following section.

5.7.2 Combination of Forward and Backward Modes

In order to combine two modes, it is necessary to decide where the forward or the backward mode is possible. For this criterion, the contour of time fraction γ_{N,U_L} is used for the backward mode region because it represents the possible region where the backflow occurs. Figures 5.45 ~ 49 show the possible flow patterns by the combination of two modes in the bimodal region at $y_{10}^+ = 11$ for specific γ_{N,U_L} levels. In these figures, the backward mode velocity vectors are presented where γ_{N,U_L} is above the specific level. The possible flow patterns by mode combination for $y_{10}^+ = 41$ and 69 are shown in Appendix D. They show large unsteady flow patterns in the bimodal region.

These estimated flow patterns are different as y_{10}^+ increases. However, they have similar patterns as γ_{N,U_L} level decreases, which means that the backflow region becomes larger. Generally, the converging streamlines appear along the boundary between forward and backward modes and it moves inward downstream. They seem to generate a nodal separation around $x/H = 1.3 \sim 1.4$ at the centerline for $\gamma_{N,U_L} = 0.8$. As γ_{N,U_L} decreases ($\gamma_{N,U_L} = 0.6$), the inward converging lines and the nodal separation at the centerline appear farther upstream and they are getting closer to those from the result of original bimodal histograms. The outward converging streamlines also appears around $r/H > 1$ and $\psi \approx 20^\circ$ and they generate weak focus (foci). For lower γ_{N,U_L} levels ($\gamma_{N,U_L} = 0.5$ and 0.4), the converging lines appear even upstream from the original separation lines coming from the saddle separation at the centerline and move outward generating a focus around the original focus of

time averaging bimodal histograms. For $\gamma_{N,U_L} = 0.2$, there is no separation line from the centerline while it appears around $\psi = 30^\circ$. It must come from the center upstream of bimodal region, the boundary between the forward and the backward flows. The locations of these saddle-focus separations and separation lines depend on γ_{N,U_L} levels.

According to the above modal analysis, the 3-D separations on curved bump surface occur time-dependently in a wide region of the leeside. Therefore, the CFD models which are trying to simulate this bump flow have to be able to represent these bimodal features. It should be noted that in their time-averaged results, such as Tessicini et al. (2005) and Wang et al. (2004), the locations of saddle separation at the centerline and focus on the leeside are farther upstream and more toward the centerline than in the presented measurement, which is similar as explained in the combination of two modes for lower γ_{N,U_L} levels.

5.7.3 Time Dependence of Bimodal Histograms

In the previous section, the mode-averaged velocity results are discussed for the region having bimodal velocity probability histograms. The analysis for time dependence of bimodal histograms has been performed in order to investigate the time of switching two modes. Figure 5.50 shows the time dependence of bimodal U_L and W_L at $r/H = 1.386$, $\psi = 30^\circ$ and $y_{1.0}^+ = 261$. It is the closet location to the center of focus at the wall and the strong bimodal probabilities appear at this height as shown in Fig. 5.50(a). Figure 5.50(b) shows the time series of $(uw/u'w')_L$ and the dashed line is for the threshold value in order to measure Δt , the time between the events exceeding the thresholds value. The u and w correlation must be positive since they are highly correlated with each other with the forward and backward modes. The resulting Δt distributions are shown in Fig. 5.50(c). It is of course dependent on the threshold values. However, the Δt has an exponential distribution for selected threshold values. It is a similar distribution as Martinuzzi et al. (1992) reported for their flow around the cube mounted on the floor. Even though the above analysis suggests that the u and w fluctuations show organized motions occurring with the forward and backward modes, it does not represent the switching time between two modes because both two motions generate the positive u and w correlation.

In order to examine the time related mode switching, the coordinates are rotated about the y_L axis to get a bimodal histogram only in U velocity. Figure 5.51(a) and (b) show JPDF of U_{LR} , W_{LR} and PDF of U_{LR} in locally rotated coordinates at the same location as Fig. 5.50. In these coordinates, we can tell one mode from the other because the forward mode has positive u fluctuations and the backward mode has negative fluctuations. Now, the threshold band begins with b1 and b2 which are peak values of each distribution as shown in Fig. 5.51(b). The band increases such as b1 and b3, b1 and b4 to avoid the effect of the edge of forward distribution. Therefore, the Δt in Fig. 5.51(c) is the time between the event exceeding one threshold value and the other event exceeding the other threshold value. The resulting Δt distributions for several threshold bans are shown in Fig. 5.51(d). They are fitted better with log-normal distributions instead of exponential distributions and have preferred peak times about 0.01 ~ 0.025 s for switching two modes.

5.8 Skewness and Flatness Factors

To investigate the effect of bimodality of U_L and W_L on higher order structure functions, the skewness and flatness factors are examined in this section. Figure 5.52 and 5.53 show the skewness factor, $(S_u)_L \equiv \overline{u_L^3} / (\overline{u_L^2})^{3/2}$ and the flatness factor, $(F_u)_L \equiv \overline{u_L^4} / (\overline{u_L^2})^2$ of U_L along the centerline upstream and downstream of separation ($r/H \approx 0.96$), respectively. They are 0 and 3, respectively, for a Gaussian distribution.

For upstream of separation along the centerline, the skewness factors decrease to negative values as y_{L0}^+ moves away from the wall. In the outer region, they have much less than the Gaussian value because the intermittent large amplitude negative u fluctuations occurred by the large eddies driving the low velocity fluid away from the wall. This makes the flatness factor large too. The skewness and flatness factors become larger as r/H moves downstream toward the separation location. For very near the separation, $r/H = 0.841$ and 0.91 , the skewness near the wall is a positive value. It might be due to the increase of positive u fluctuations bringing the high velocity fluid toward the wall. However, the amplitude of these occasional fluctuations is not too big so that the flatness values are almost minima along the centerline upstream of separation.

For downstream of separation and near the wall, all locations are positively skewed and the skewness increases further downstream as well as away from the wall. It has a local maximum around $y_{L0}^+ \approx 100$. The local minimum of $\overline{U_L}$ appears at very close to this location. The almost symmetric bimodal histograms appear where the skewness changes its sign and the flatness shows a local minimum at this height. In the case of symmetric double peaks in a histogram, there are relatively infrequent two dominant amplitude fluctuations so that the edges in the probability histogram are a smaller fraction as compared to non-bimodal histograms. Closer to the wall than y_{L0}^+ for $(S_u)_L \approx 0$, the skewness increases positively because one peak in the positive fluctuation is reduced and consequently this edge is larger. It also increases the amplitude of intermittent positive fluctuations and increases the flatness too. Similarly, farther than y_{L0}^+ for $(S_u)_L \approx 0$ the skewness decreases up to $y_{L0}^+ \approx 500 \sim 600$, but the flatness increases from its local minimum value because of larger negative edge. There are no bimodal features farther than this height and the skewness and the flatness have very high negative values due to large magnitude occasional negative fluctuations generated by the large eddies interaction motions ($u_L < 0$, $v_L < 0$) bringing the low velocity fluid toward the wall region. In the overlap region, the skewness factors change the sign and the flatness factors are small. The \overline{uv}_L values are large and negative in this region. It represents that the intense mixing occurs with smaller amplitude but much higher probability of fluctuations.

In order to examine higher order structure functions on the leeside away from the center line, the skewness and flatness factors of U_L and W_L , $(S_w)_L \equiv \overline{w_L^3} / (\overline{w_L^2})^{3/2}$, $(F_w)_L \equiv \overline{w_L^4} / (\overline{w_L^2})^2$ along $r/H = 1.386$ in local coordinates are shown in Fig. 5.54 and 5.55, respectively. Note that the focus is located around $r/H = 1.386$ and $\psi = 30^\circ$. The $(S_w)_L$ is very close to zero for $\psi = 0^\circ$. The $(S_u)_L$ and $(S_w)_L$ show similar trends for $10^\circ \leq \psi \leq 30^\circ$, where they have relatively high positive values up to $y_{L0}^+ \approx 400$ even though the $(S_u)_L$ values are much larger than $(S_w)_L$ near the wall. They increase away from the surface and the largest positive skewness appears at $y_{L0}^+ \approx 200$ for $\psi = 20^\circ$ in both U_L and W_L . This means that there are large amplitude motions ($u_L > 0$, $w_L > 0$) toward the centerline up to $y_{L0}^+ \approx 400$ for $10^\circ \leq \psi \leq 30^\circ$. Above this height, they decrease negatively in both U_L and W_L , which means large amplitude outward span-wise motions ($u_L < 0$, $w_L < 0$). For $\psi \geq 40^\circ$, the skewness decreases to negative values as the height moves from the near wall. The $(S_w)_L$ of $\psi = 40^\circ$ has negative values from the wall and shows significant differences from $\psi = 20^\circ$ and 30° .

This might be due to the opposite effect of focus structure on inner and outer locations. The $(F_u)_L$ has a similar trend as along the centerline but the $(F_w)_L$ are almost constant in the inner region.

5.9 Summary of the Flow Structure of Large Bump#3 Leaside

Figure 5.56 illustrates flow features in the leaside of bump. The mean flow pattern on the leaside shows a saddle type 3-D separation at $x/H \approx 0.96$ on the centerline of bump. The downstream backflow and the stream-wise flow from upstream of the saddle separation spread span-wise outward and generate one focus separation on each side at $x/H \approx 1.2$ and $z/H \approx \pm 0.7$. The saddle-focus separated flow structure is not only on the nearest wall surface but also extends up to $y_{L,0}^+ \approx 350$. In the mean backflow region within $0^\circ \leq \psi \leq 30^\circ$, more TKE is generated than Reynolds shearing stresses in local coordinates because u_L and v_L fluctuations are less correlated and w_L fluctuations are correlated better with u_L .

The 3-D mean streamtraces show that the mean stream-wise vortex generated by the focus separation on each side is an opposite sense to what is observed in the wake plane. The mean stream-wise vortex in the wake plane is generated by the downwash flow which is passing over the bump and toward the centerline and is not entrained into the backflow region.

The $1/S$ parameter, the correlation coefficient $(R_{uv})_{LSS}$ and the structural parameter $A1$ are much lower than a universal 2-DTBL in this region. A general explanation for low $1/S$, $A1$ and $(R_{uv})_{LSS}$ values can be given for regions where the mean flow angle, $\tan^{-1}(\overline{W_L}/\overline{U_L})$ varies with the distance from the wall, $y_{L,0}^+$. The turbulent flow at different $y_{L,0}^+$ comes from different directions and is not well correlated with the turbulence at other $y_{L,0}^+$. Thus, the correlation coefficients and the Reynolds shearing stresses are low while the skewed eddies out of x_L - y_L plane generate significant $-\overline{uw_L}$ which is one of the major indicators for the three-dimensionality.

The large eddies and the flow from the bump side supplies the mean backflow. Since $(\gamma_{pu})_L$ is never zero, the large eddies supply the intermittently forward flow in this mean backflow region similar to a 2-D separated TBL. Bimodal probability distributions of U_L and W_L appear in this region due to the unsteady and highly correlated meandering of U_L and W_L in the flow field.

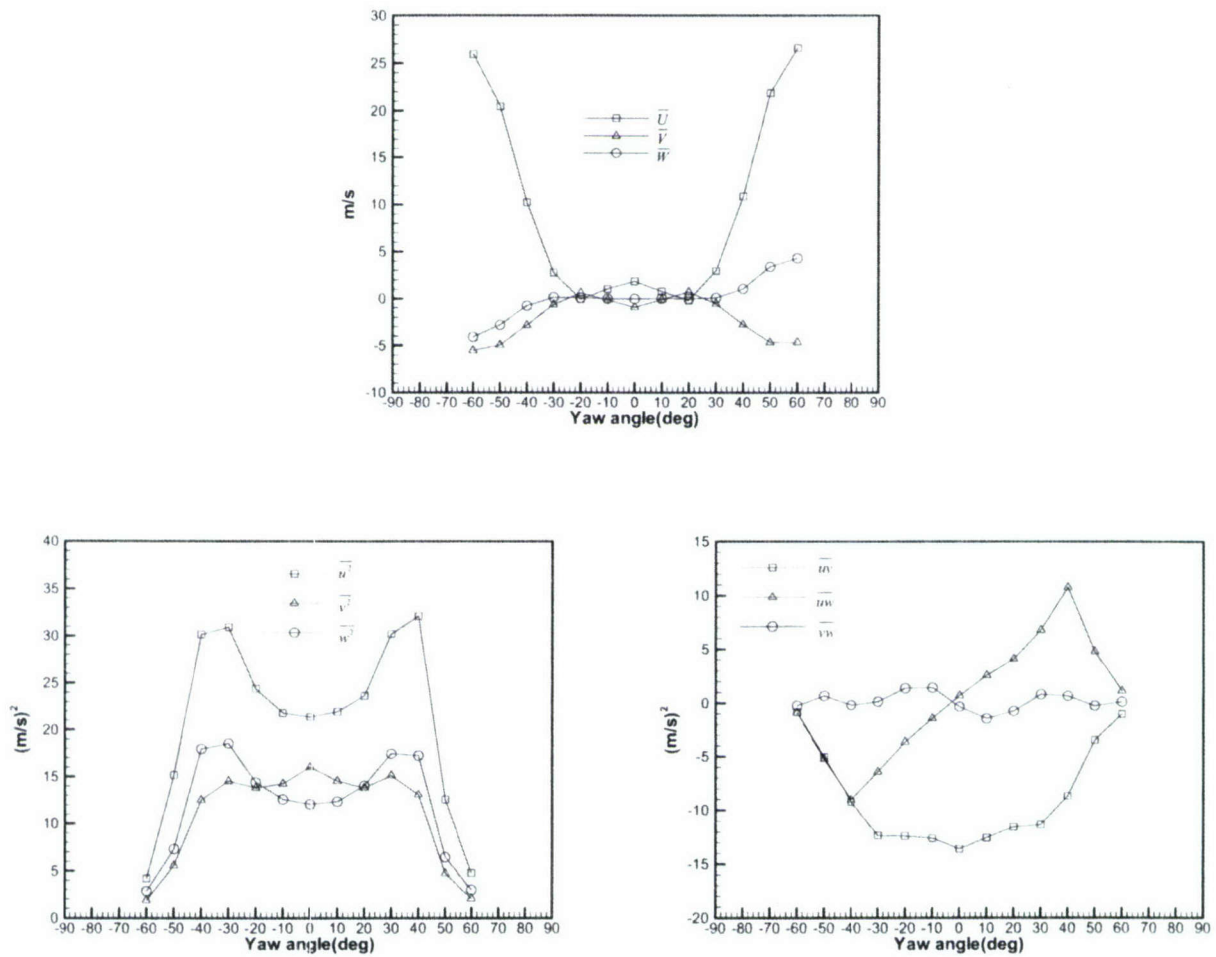
Significant symmetric bimodal histograms make the histogram edges smaller so that they occur with close to zero skewness and minimum flatness factors.

By the mode-averaged analysis of bimodal histograms, highly unsteady flow structures are estimated and unsteady 3-D separations seem to be occurring in a wide range on the bump leeside. The process of these separations has a very complex dynamics having intermittent large portion of attached and detached flow region which is varying in time. These bimodal features with highly correlated u_L and w_L fluctuating motions are the major source of large Reynolds stresses $\overline{u_L^2}$, $\overline{w_L^2}$ and $-\overline{uw_L}$. It might also result in the decorrelation between u_L and v_L .

The flow angles show huge variations across the height from the wall near the centerline due to the spiral motion and backflow. In the separation region on the leeside, there are large lags between the flow gradient angles and the shear stress angles like in the wake flow implying anisotropic turbulence.

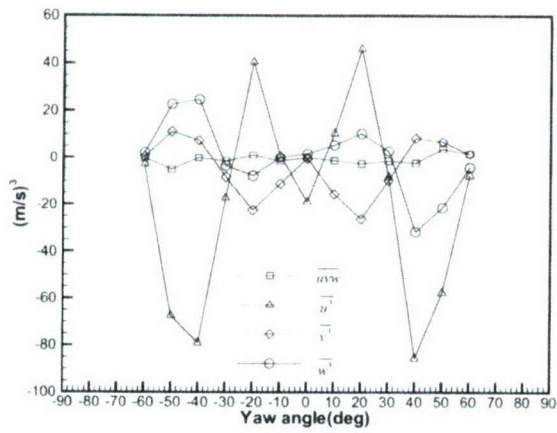
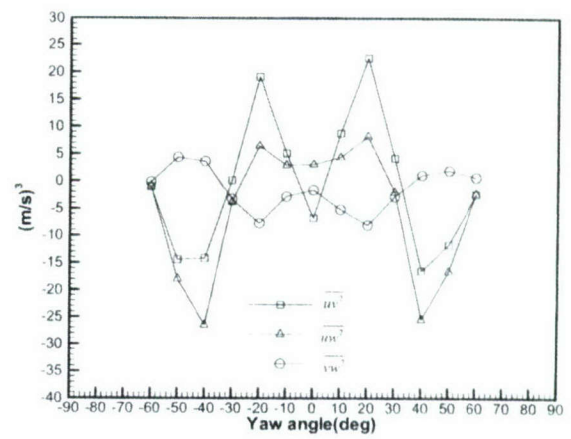
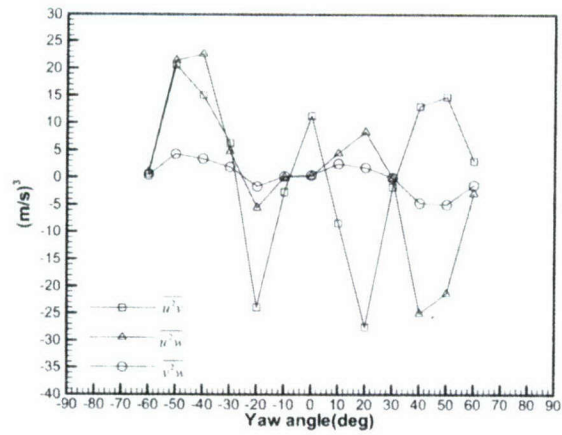
Table 5.1 Locations of measurements.

x/H	y/H	Pitch angle, θ (°)	Yaw angle, ψ (°)
0.177	0.982	-11	0° ~ 80°, 20° increment 120°, 150°, 180° only at x/H = 0.254
0.254	0.964	-15	
0.338	0.936	-21	
0.421	0.902	-24	
0.496	0.866	-27	
0.573	0.823	-29	
0.644	0.78	-32	0° ~ 90°, 10° increment 120°, 150°, 180° only at x/H = 0.976, 1.615
0.706	0.74	-33	
0.781	0.688	-36	
0.841	0.645	-37	
0.91	0.593	-37	
0.976	0.543	-38	
1.044	0.491	-38	
1.112	0.438	-38	
1.179	0.387	-37	
1.244	0.338	-37	
1.313	0.288	-36	
1.386	0.237	-34	
1.46	0.189	-32	
1.532	0.146	-30	
1.615	0.102	-27	
1.692	0.067	-21	
1.769	0.039	-17	



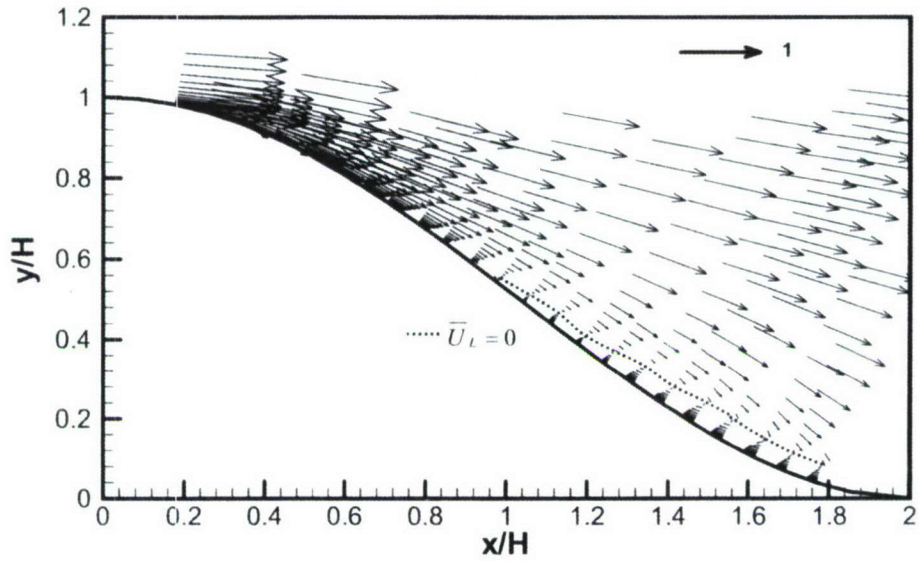
(a) Mean velocities and Reynolds stresses

Figure 5.1 Mean symmetric flow around large bump#3 at $r/H=1.112$ and $y_L=4$ mm.

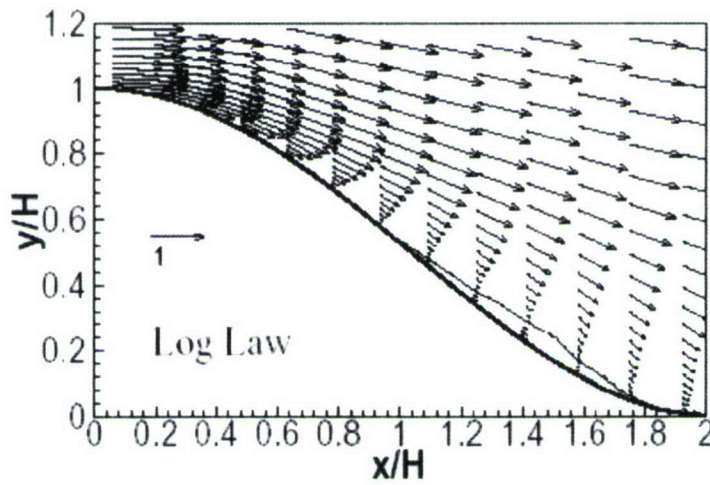


(b) Triple products

Figure 5.1 Continued.



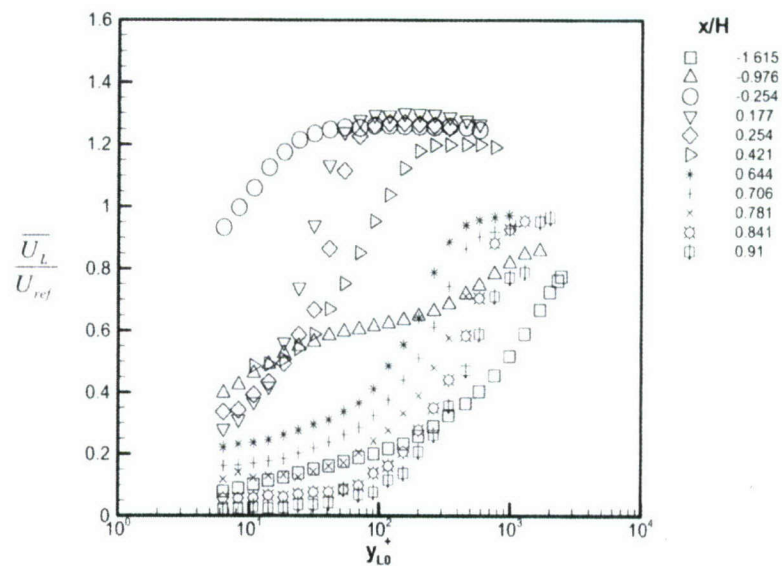
(a) Present measurements



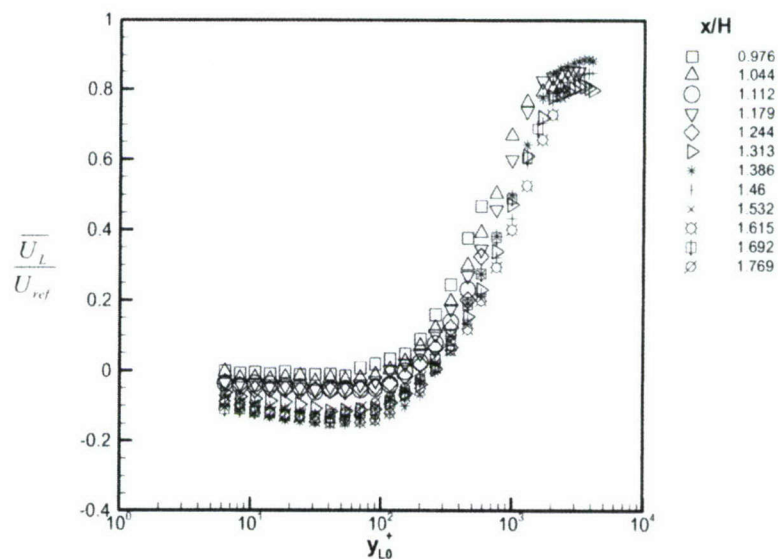
(b) Combined LES-RANS calculation by Tessicini et al. (2005)

Dotted line for $\overline{U}_L = 0$

Figure 5.2 Normalized $\overline{U}_i + \overline{V}_j$ vectors in the center plane.

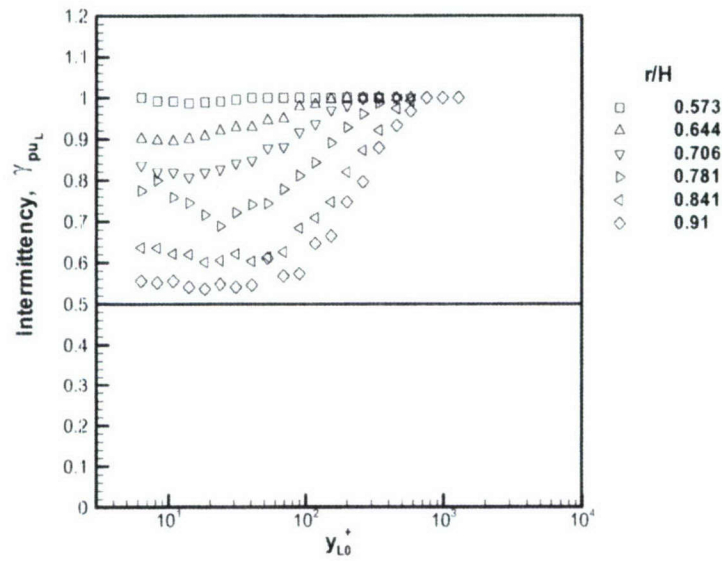


(a) Upstream from separation

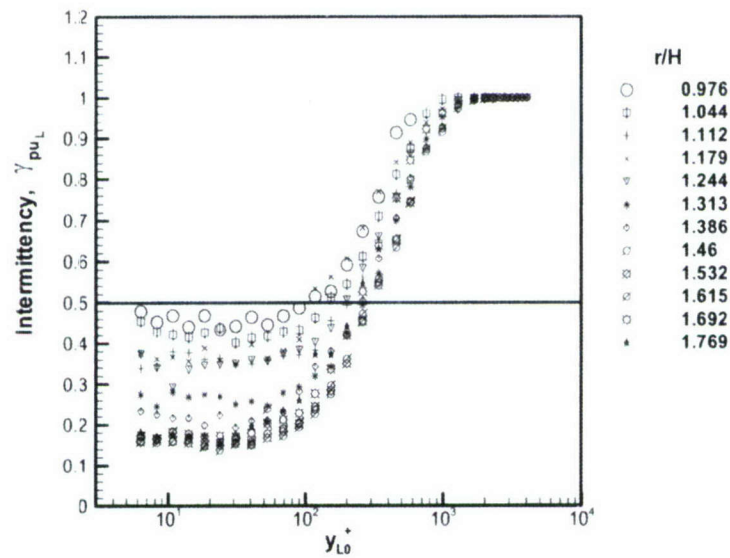


(b) Downstream from separation

Figure 5.3 $\overline{U_L}$ in local coordinates along the centerline.

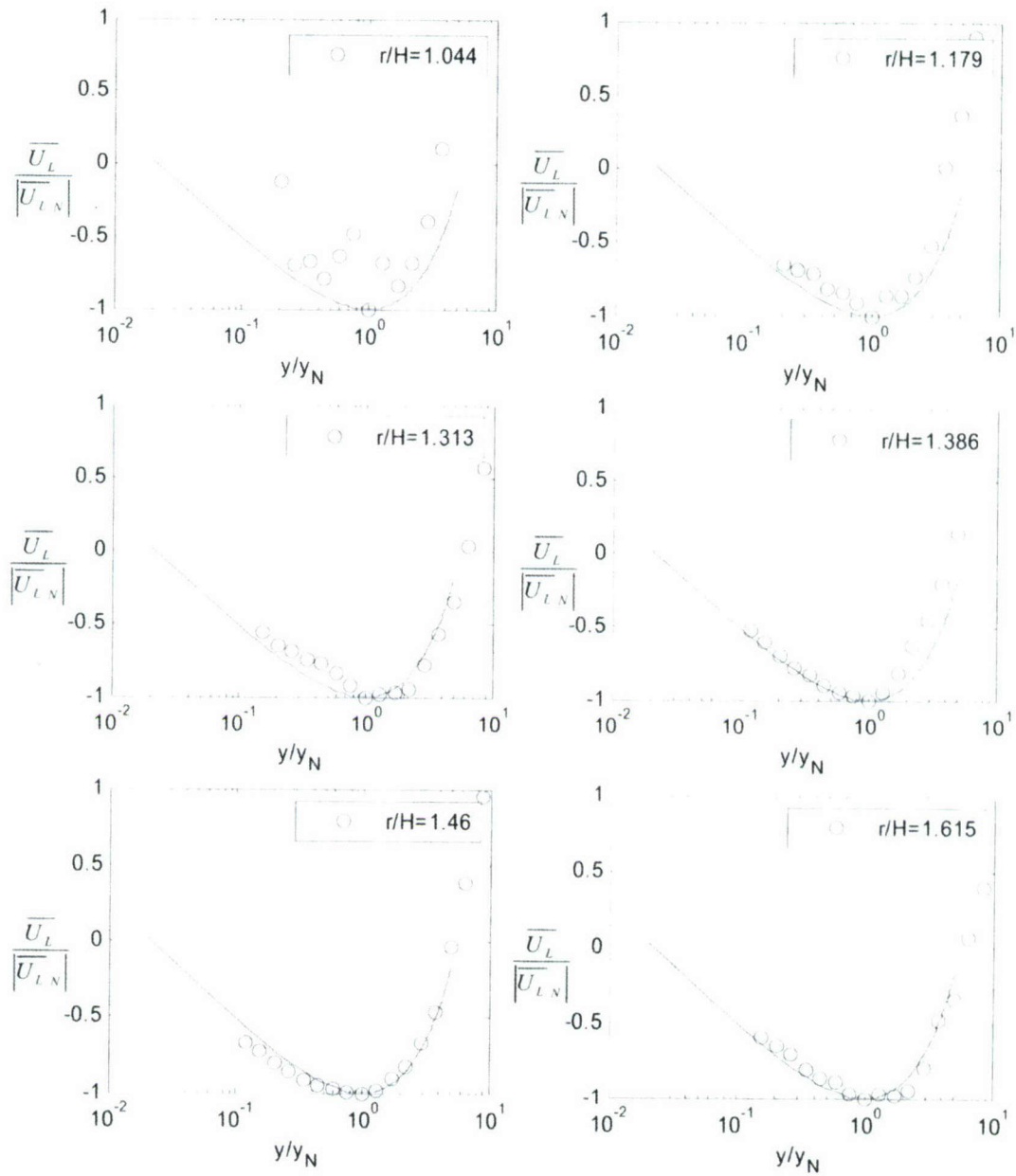


(a) Upstream from separation



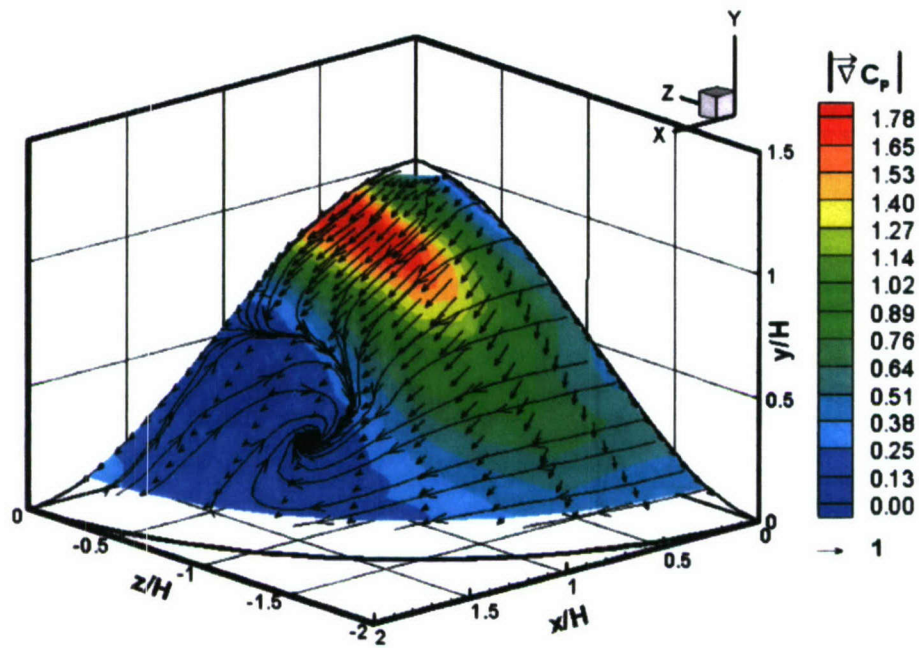
(b) Downstream from separation

Figure 5.4 Intermittency of U_L in local coordinates along the centerline.

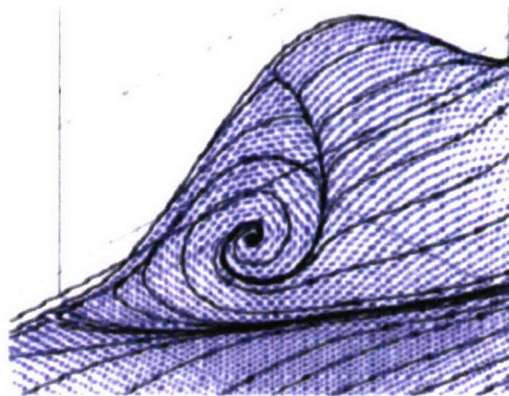


Solid line for the law of mean backflow.

Figure 5.5 Law of mean backflow $\overline{U_L}$ in local coordinates along the centerline.

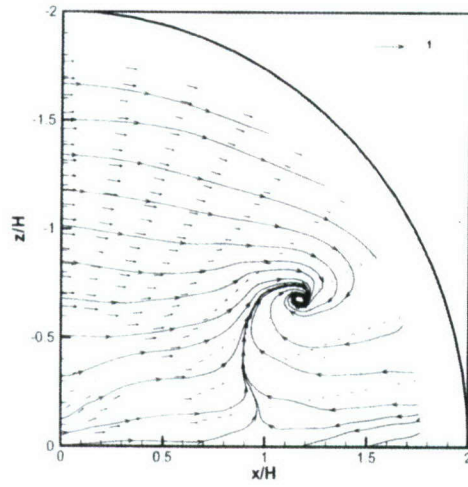
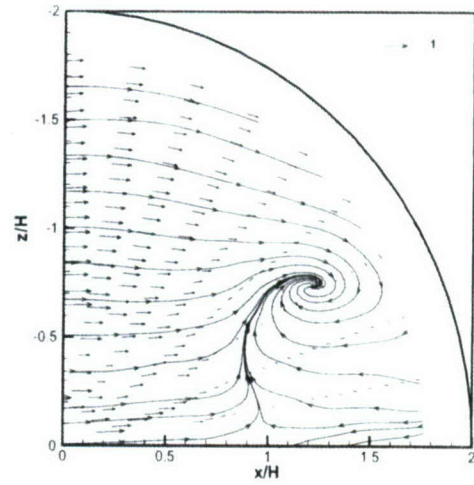
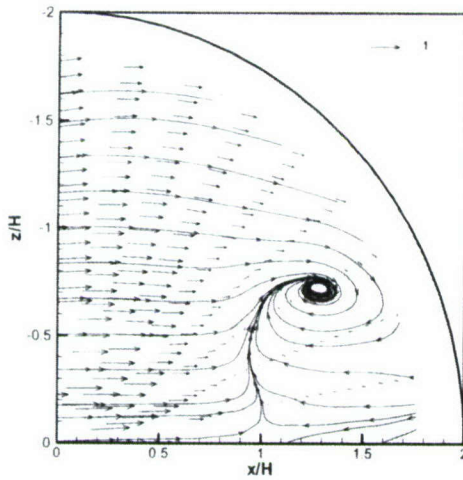
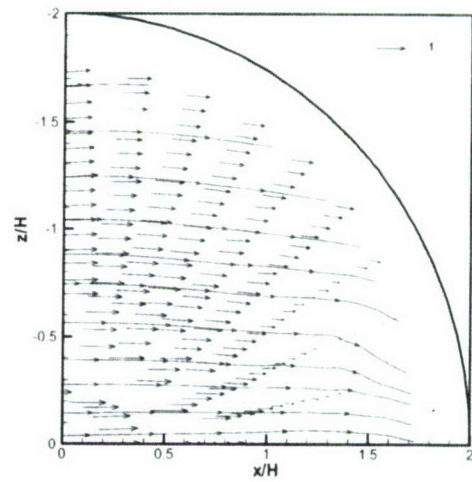


(a) Surface pressure gradient contour, its vectors and lines connecting $\overline{U}i_L + \overline{W}k_L$ vectors locally tangent to surface at $y_{L,0}^+ = 11$



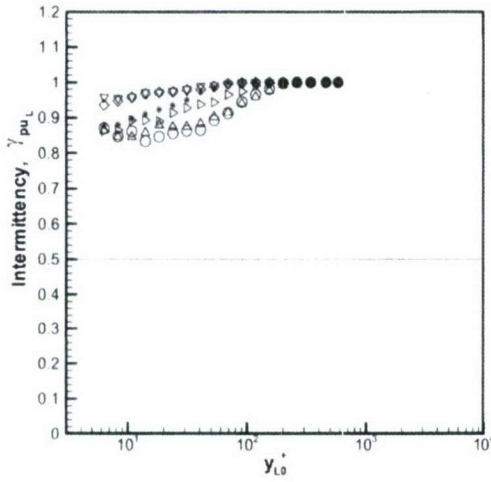
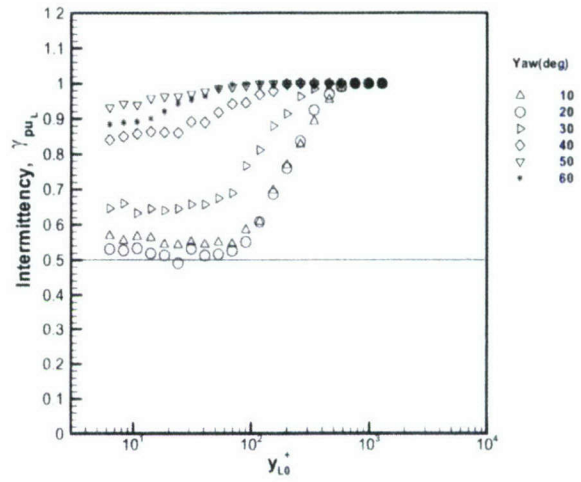
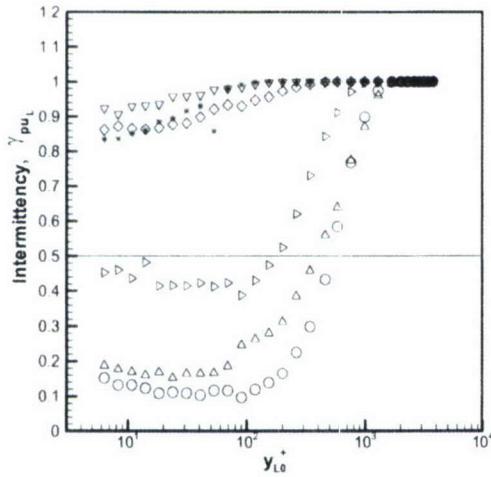
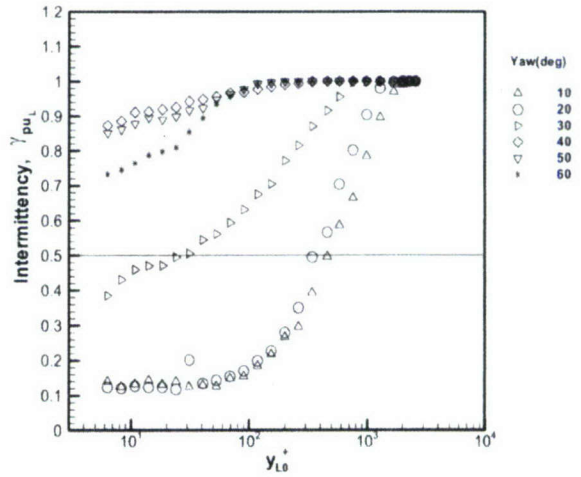
(b) Skin friction lines from quadratic eddy-viscosity model from Wang et al. (2004)

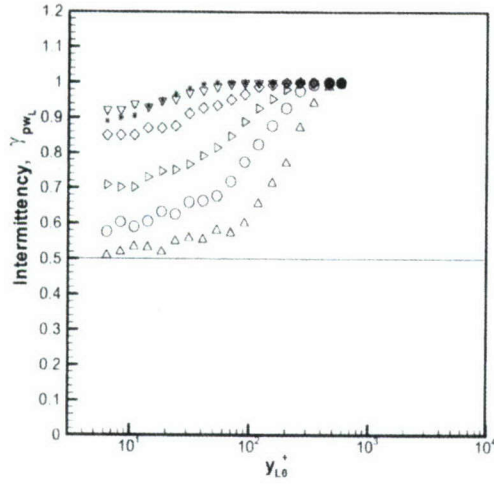
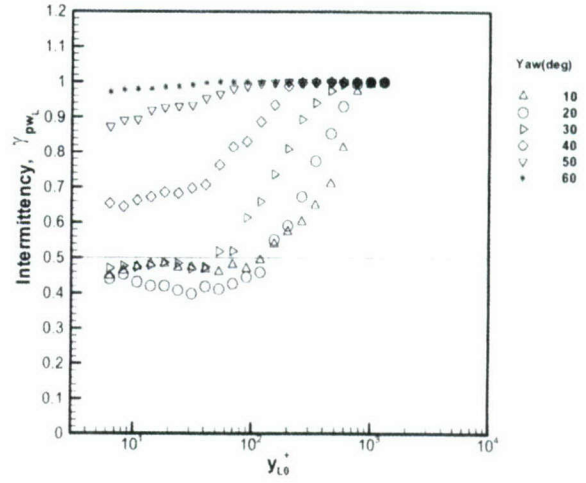
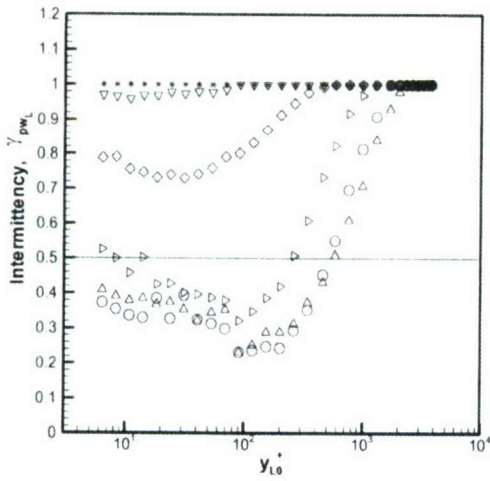
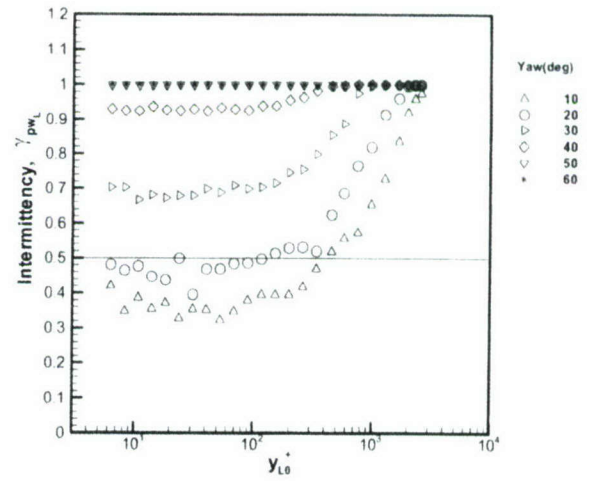
Figure 5.6 Near wall flow field.

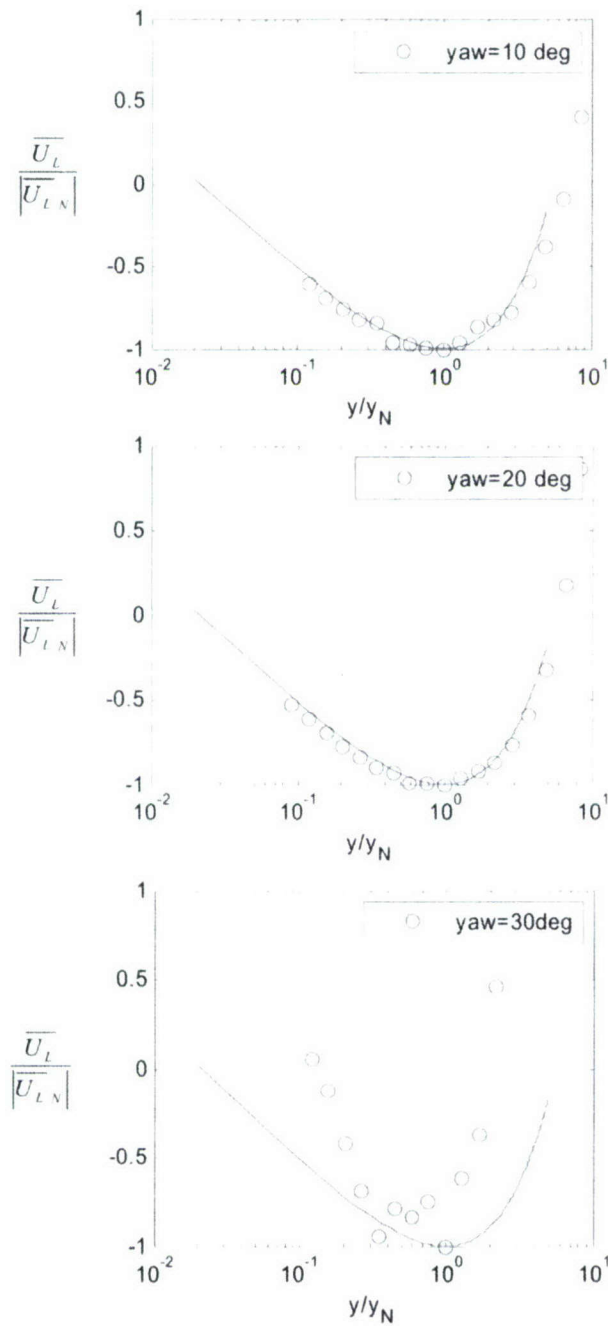
(a) $y_{L,0}^+ = 6$ (b) $y_{L,0}^+ = 24$ (c) $y_{L,0}^+ = 90$ (d) $y_{L,0}^+ = 456$

Lines connecting vectors for visual aid only at different $y_{L,0}^+$.

Figure 5.7 Normalized $\overline{U}i_L + \overline{W}k_L$ vectors locally tangent to surface.

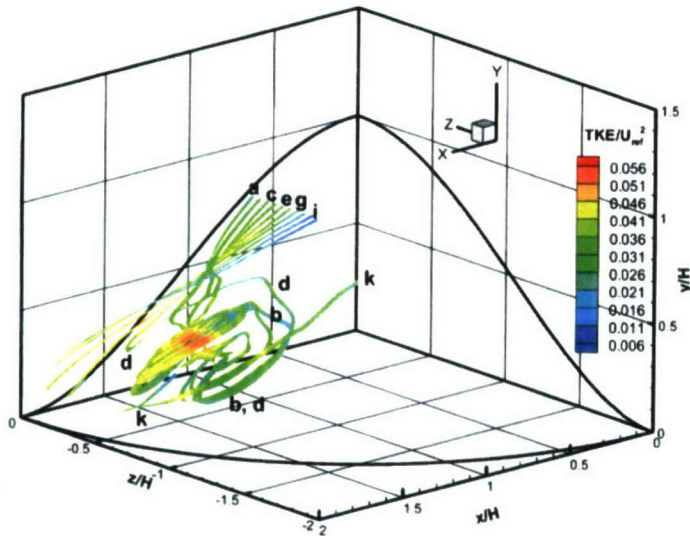
(a) $r/H = 0.706$ (b) $r/H = 0.91$ (c) $r/H = 1.386$ (d) $r/H = 1.615$ Figure 5.8 Intermittency of U_L in local coordinates along r/H .

(a) $r/H = 0.706$ (b) $r/H = 0.91$ (c) $r/H = 1.386$ (d) $r/H = 1.615$ Figure 5.9 Intermittency of W_L in local coordinates along r/H .

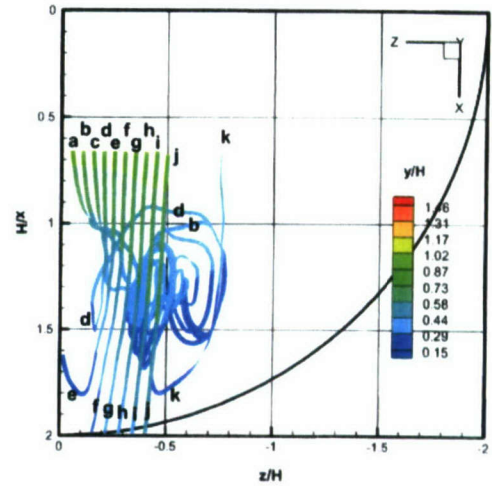


Solid line for the law of mean backflow.

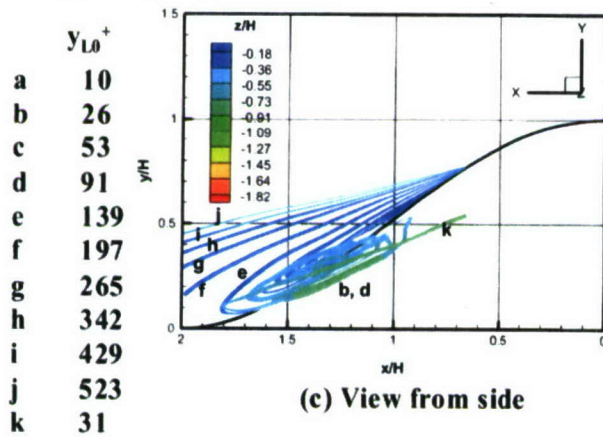
Figure 5.10 Law of mean backflow $\overline{U_L}$ in local coordinates along $r/H = 1.386$.



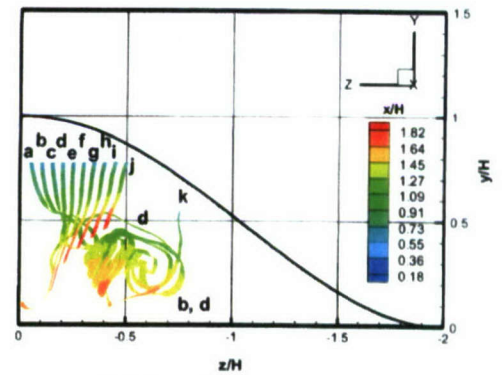
(a) 3-D perspective view



(b) View from top



(c) View from side

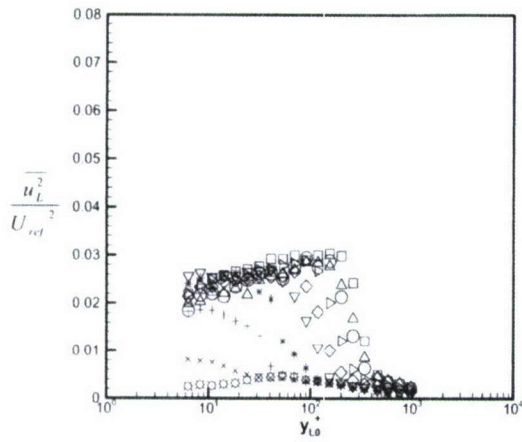
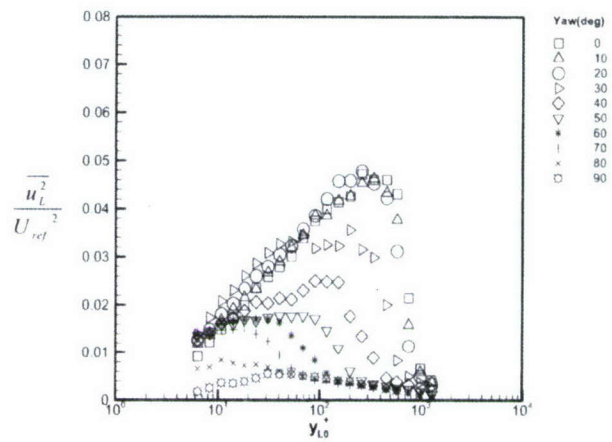
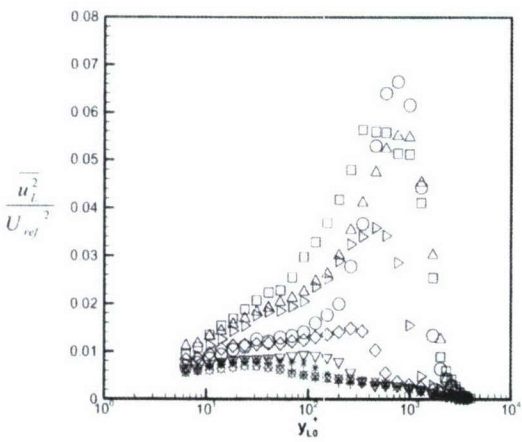
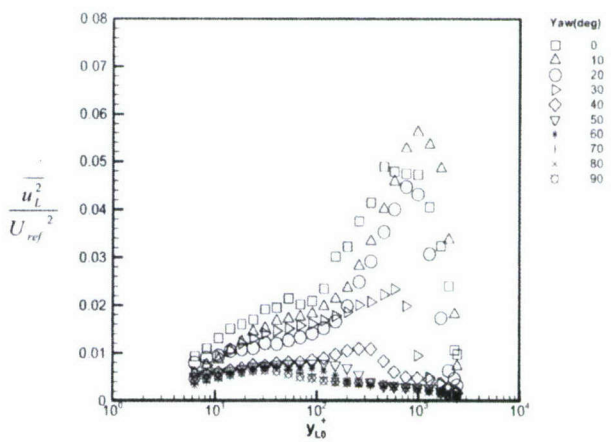


(d) View from downstream

	$y_{L,0}^+$
a	10
b	26
c	53
d	91
e	139
f	197
g	265
h	342
i	429
j	523
k	31

Contours show TKE levels and out-of-plane positions.

Figure 5.11 Some 3-D streamlines using \bar{U} , \bar{V} and \bar{W} from various $y_{L,0}^+$ starting points.

(a) $r/H = 0.644$ (b) $r/H = 0.91$ (c) $r/H = 1.386$ (d) $r/H = 1.615$ Figure 5.12 Normalized $\overline{u_L^2}$ in local coordinates.

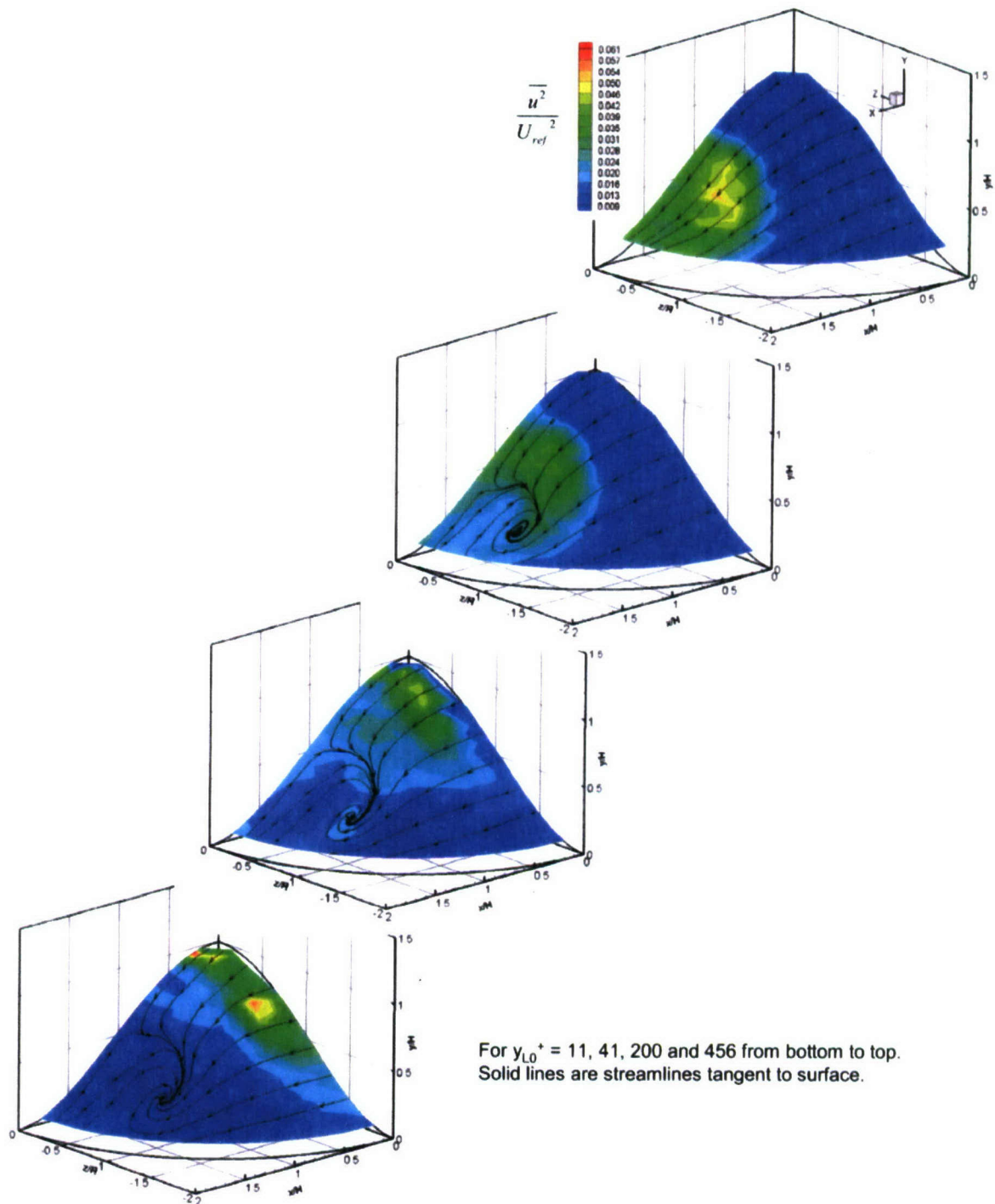
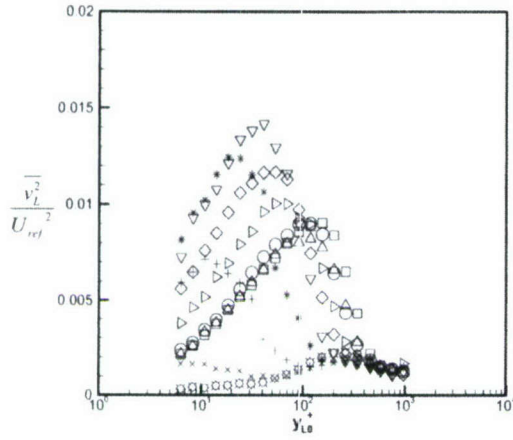
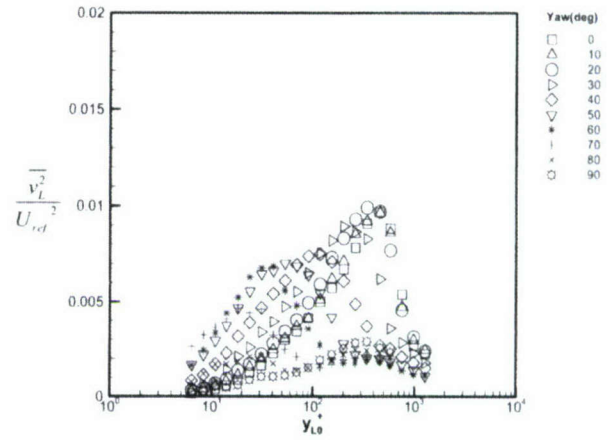
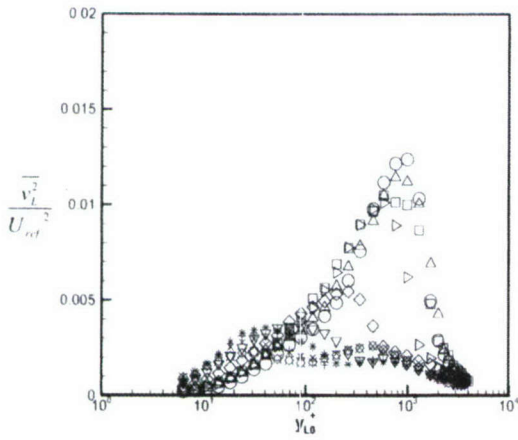
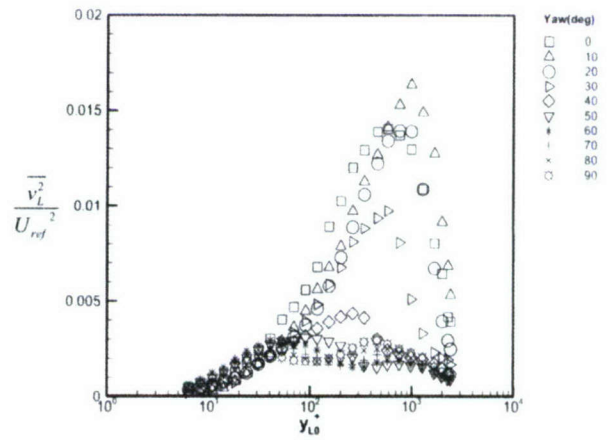


Figure 5.13 Contours of normalized $\overline{u^2}$ in tunnel coordinates.

(a) $r/H = 0.644$ (b) $r/H = 0.91$ (c) $r/H = 1.386$ (d) $r/H = 1.615$ Figure 5.14 Normalized $\overline{v_L^2}$ in local coordinates.

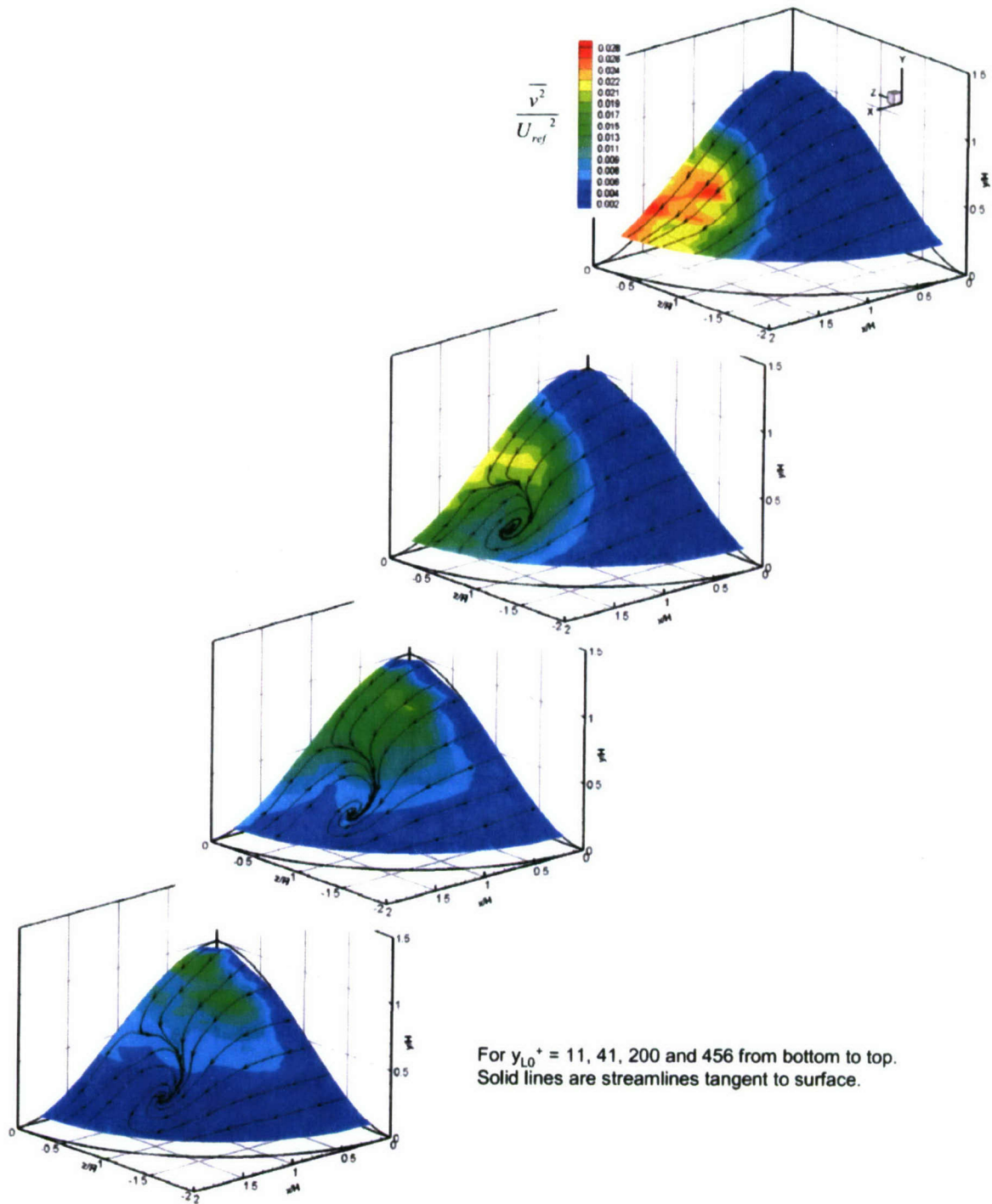
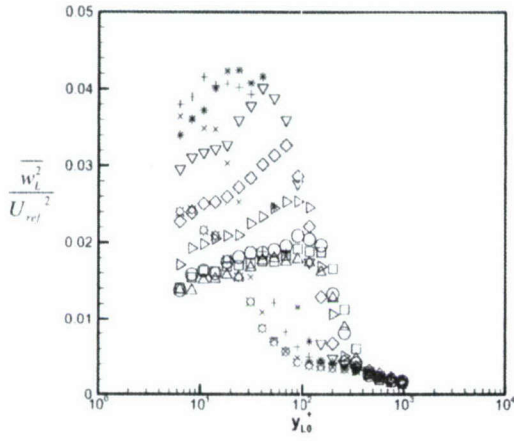
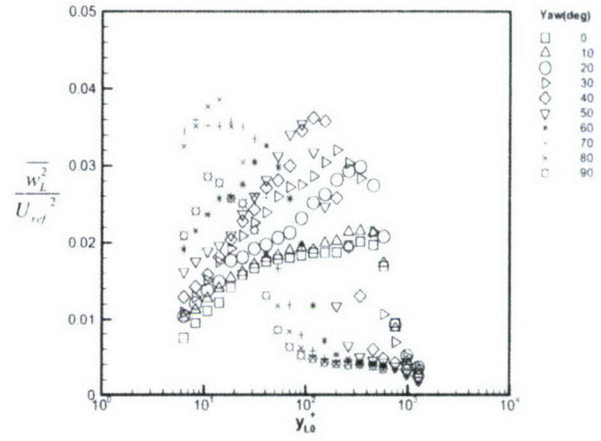
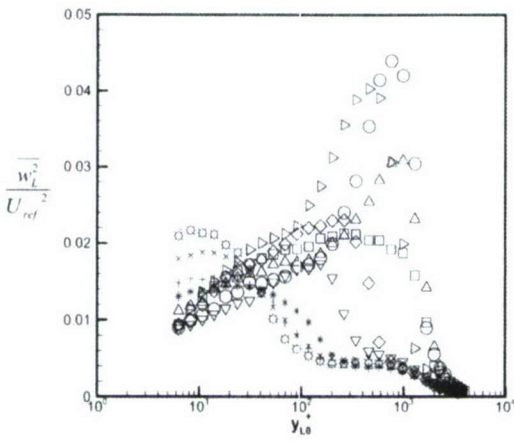
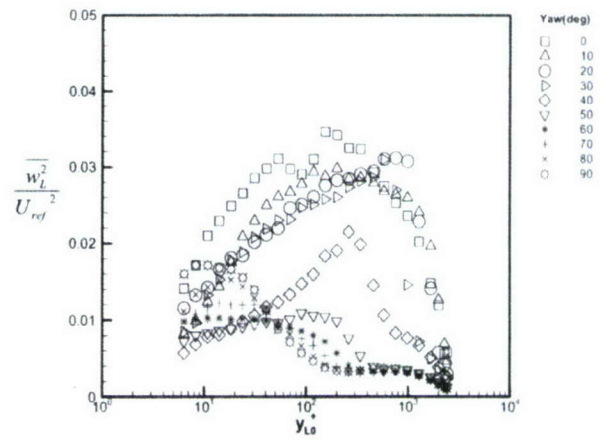


Figure 5.15 Contours of normalized $\overline{v^2}$ in tunnel coordinates.

(a) $r/H = 0.644$ (b) $r/H = 0.91$ (c) $r/H = 1.386$ (d) $r/H = 1.615$ Figure 5.16 Normalized $\overline{w_L^2}$ in local coordinates.

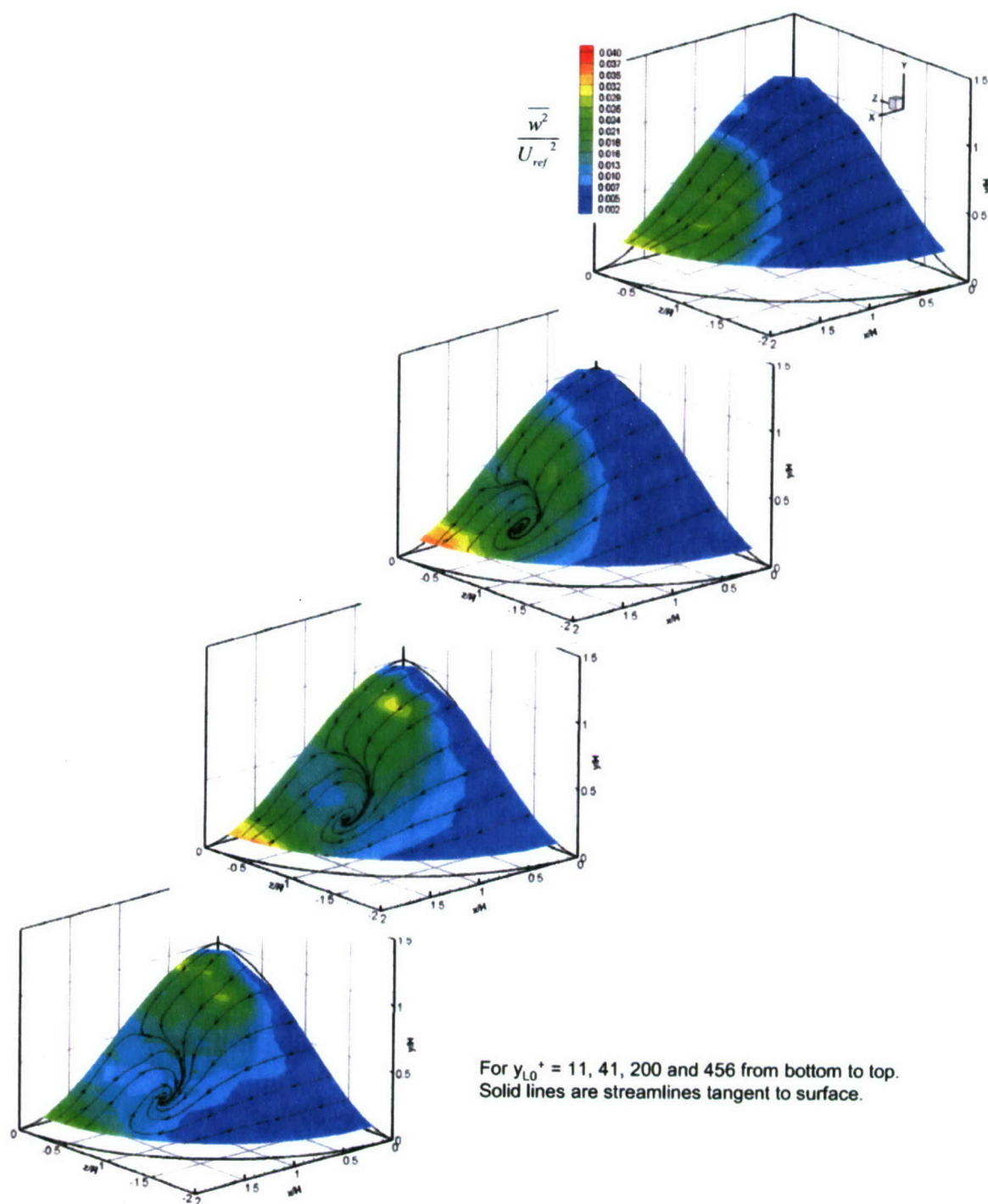
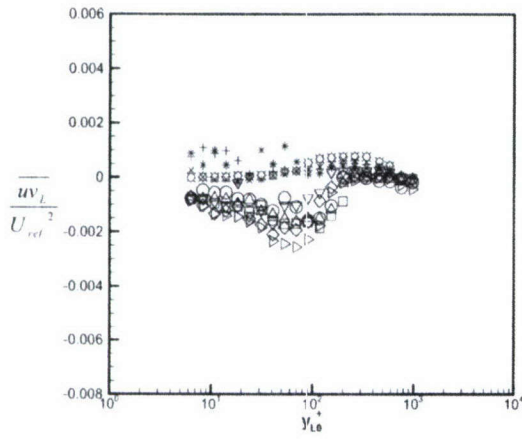
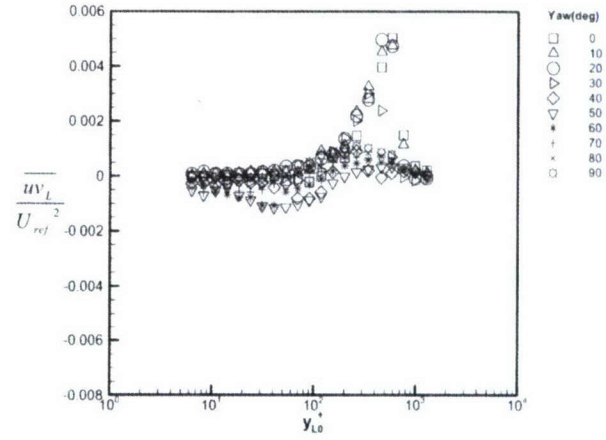
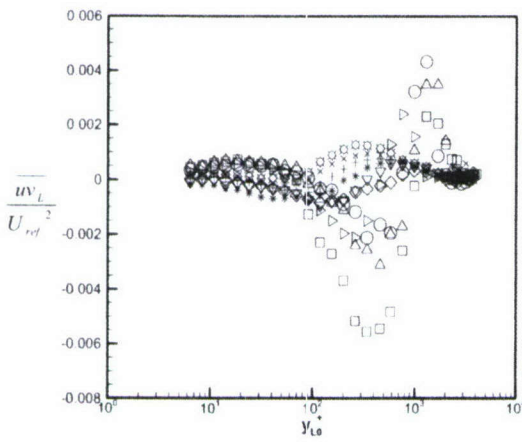
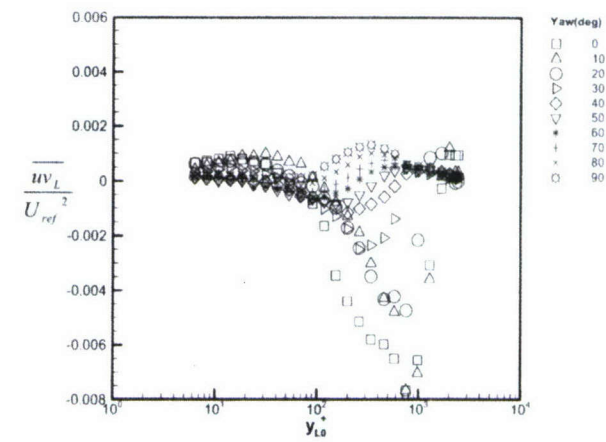


Figure 5.17 Contours of normalized $\overline{w^2}$ in tunnel coordinates.

(a) $r/H = 0.644$ (b) $r/H = 0.91$ (c) $r/H = 1.386$ (d) $r/H = 1.615$ Figure 5.18 Normalized $-\overline{uv_L}$ in local coordinates.

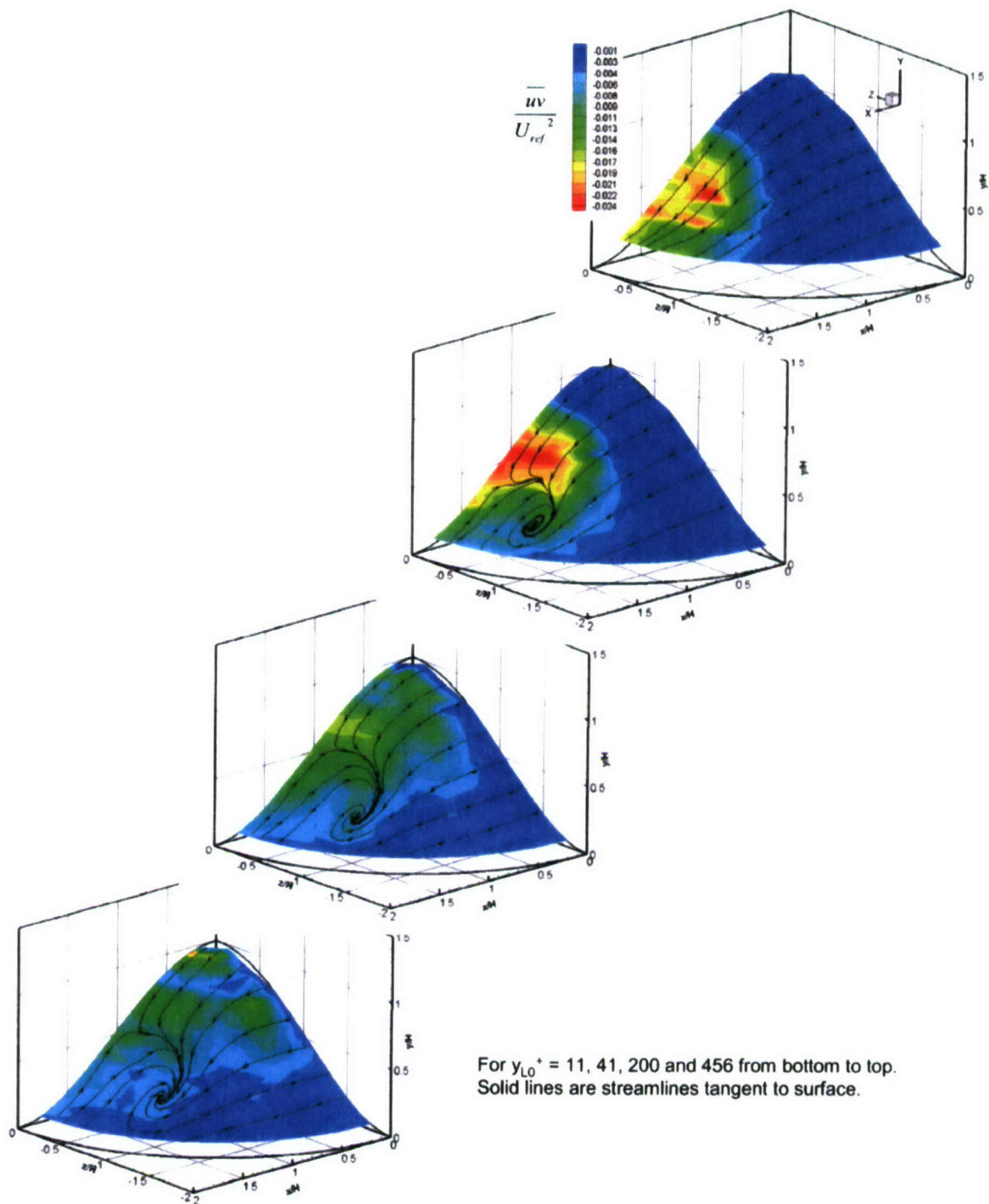
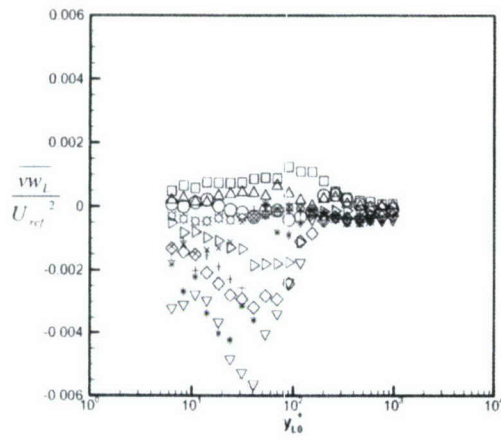
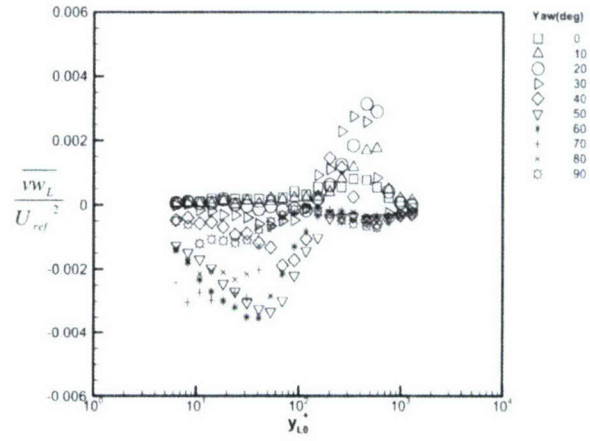
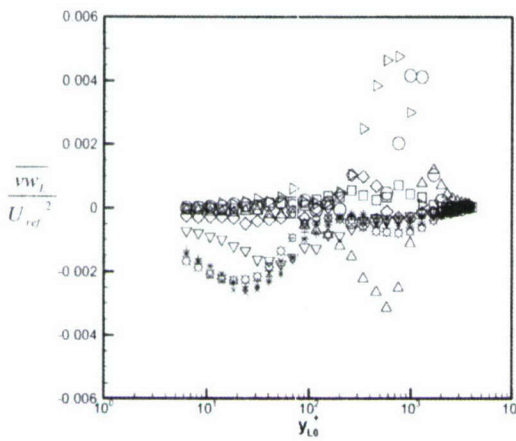
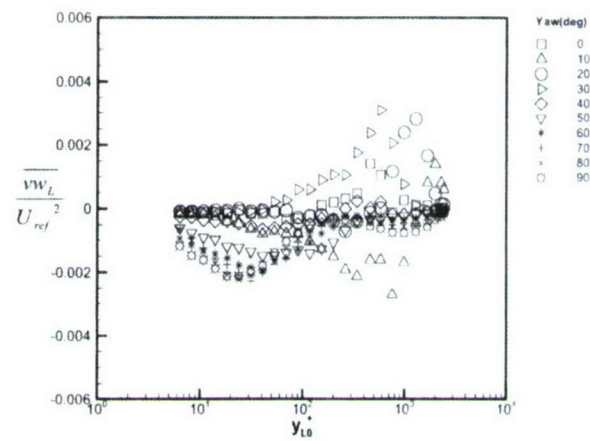


Figure 5.19 Contours of normalized $-\frac{uv}{U_{ref}^2}$ in tunnel coordinates.

(a) $r/H = 0.644$ (b) $r/H = 0.91$ (c) $r/H = 1.386$ (d) $r/H = 1.615$ Figure 5.20 Normalized $-vw_L$ in local coordinates.

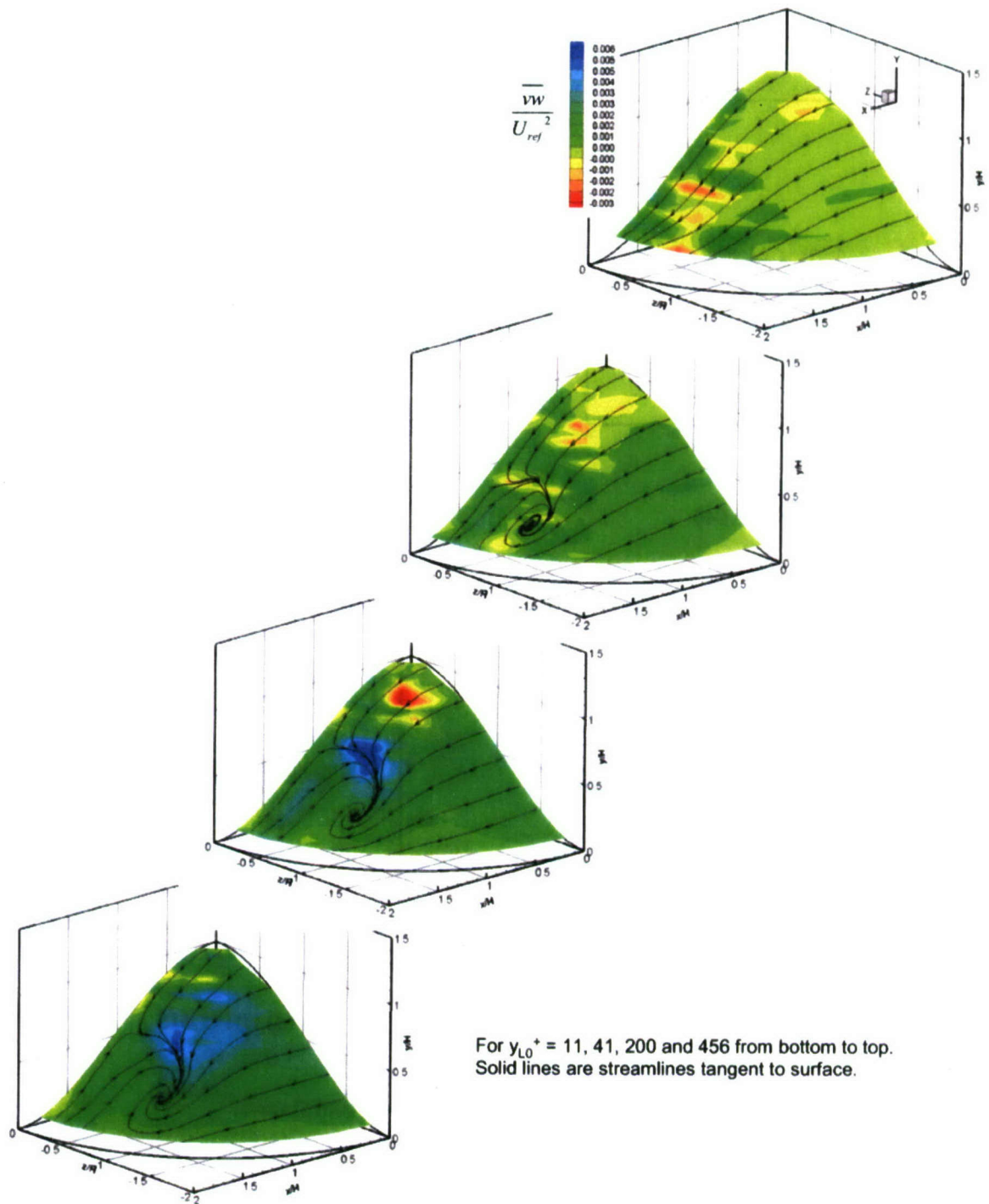


Figure 5.21 Contours of normalized \overline{vw} in tunnel coordinates.

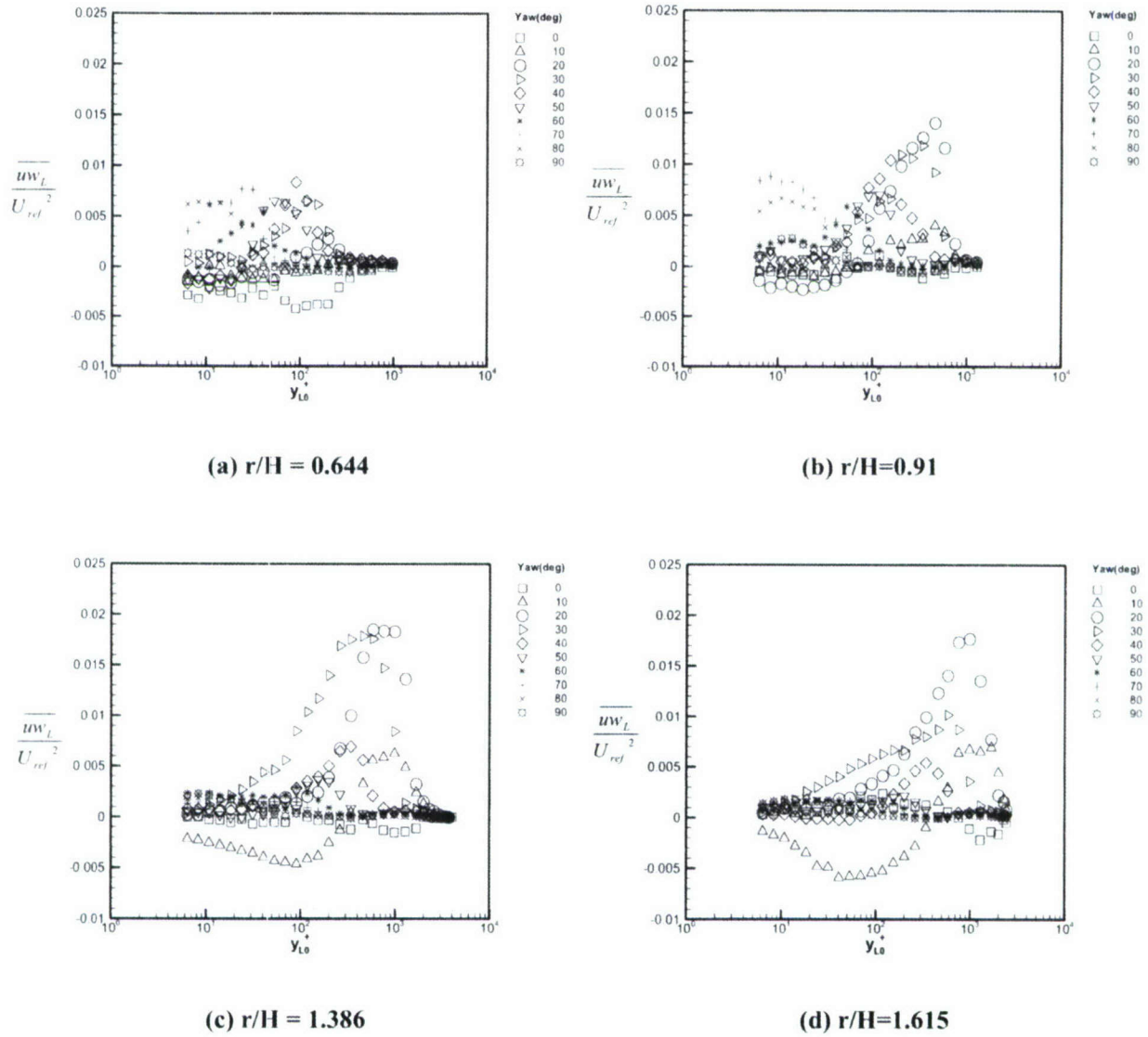


Figure 5.22 Normalized $-\overline{uw_L}$ in local coordinates.

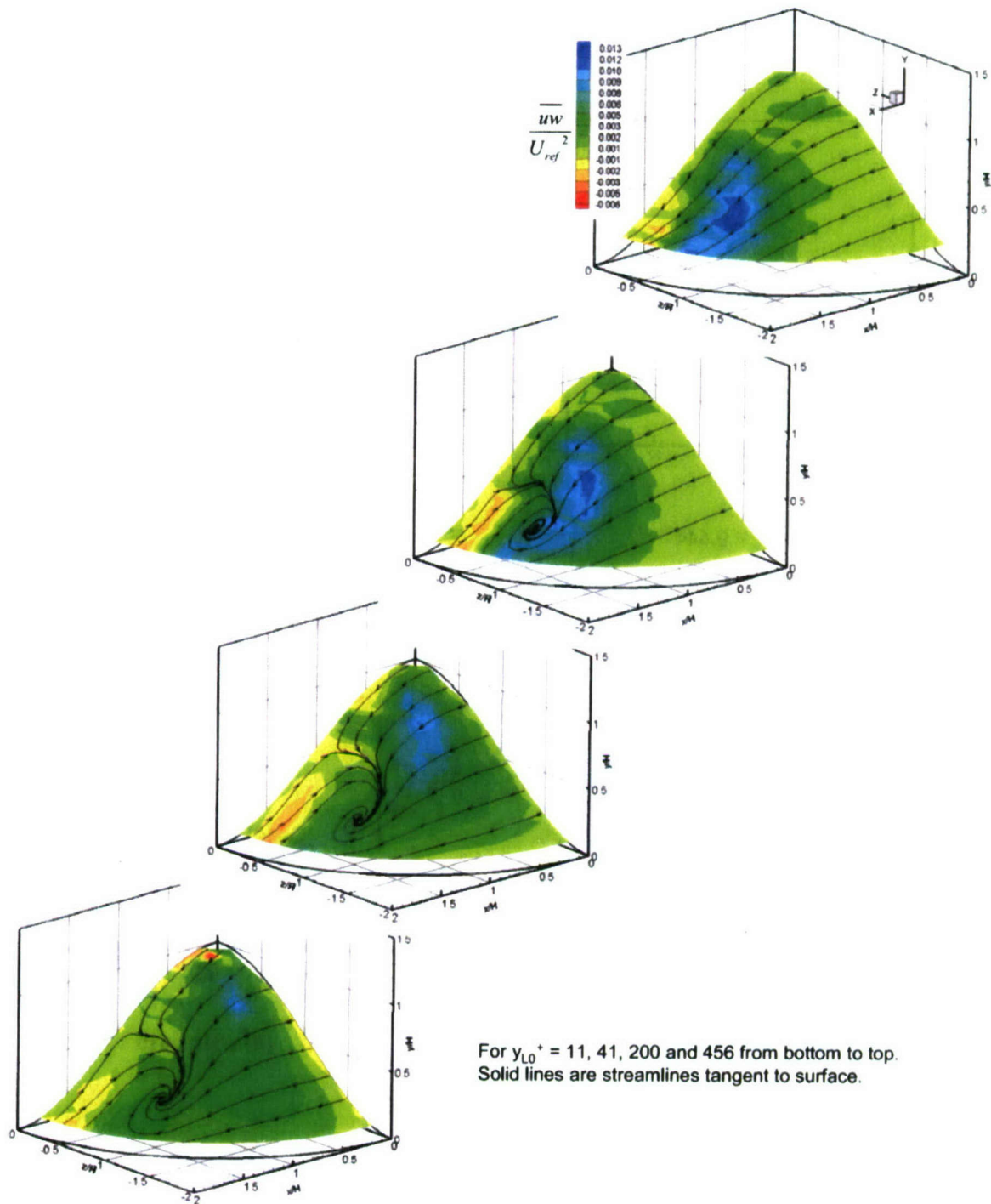
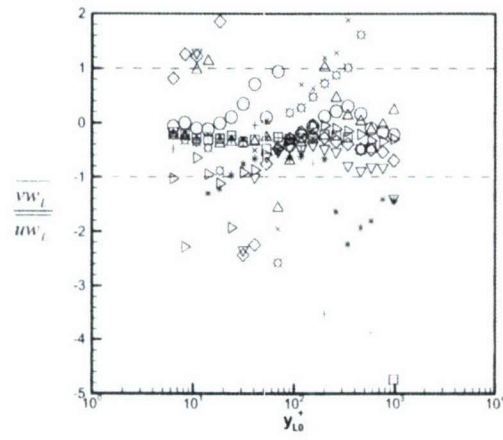
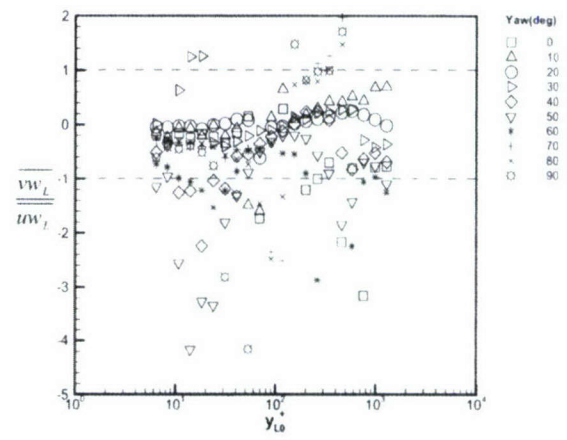
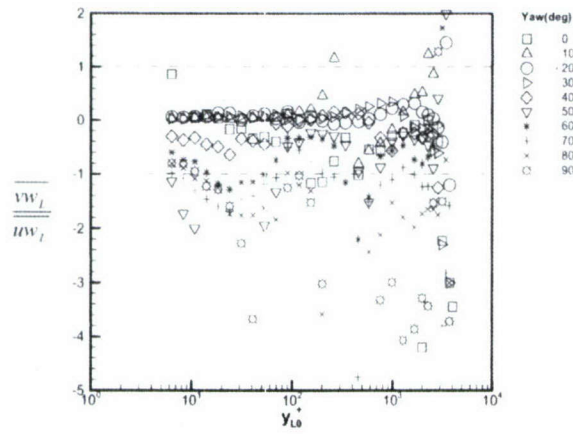
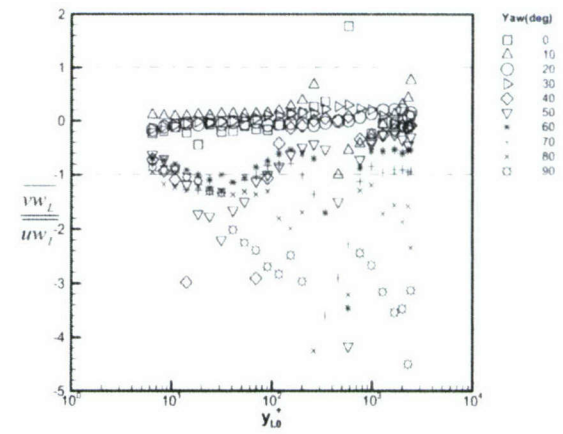


Figure 5.23 Contours of normalized $-\overline{uw}$ in tunnel coordinates.

(a) $r/H = 0.644$ (b) $r/H = 0.91$ (c) $r/H = 1.386$ (d) $r/H = 1.615$ Figure 5.24 The ratio of $-vw_L$ to $-uw_L$ in local coordinates.

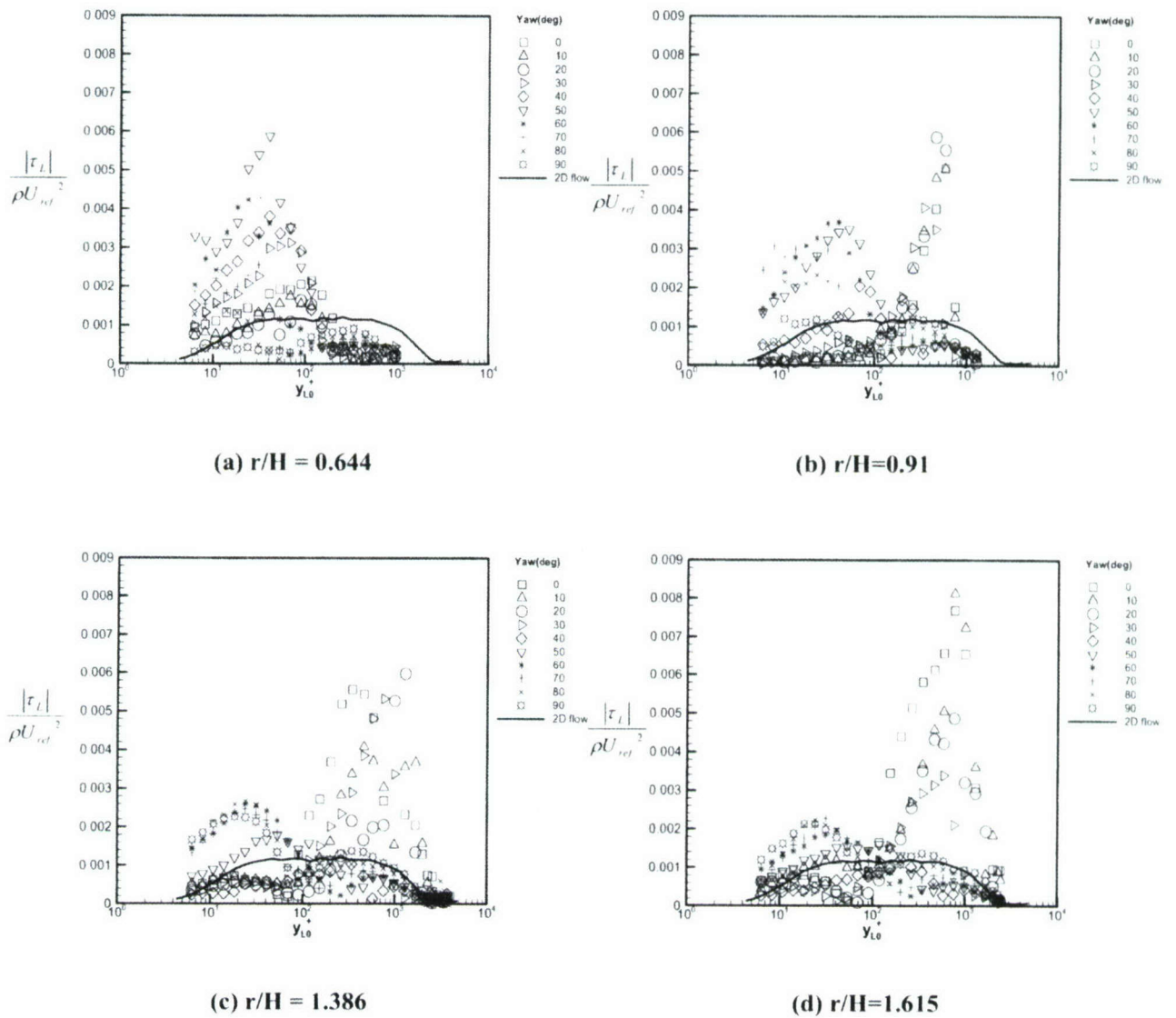
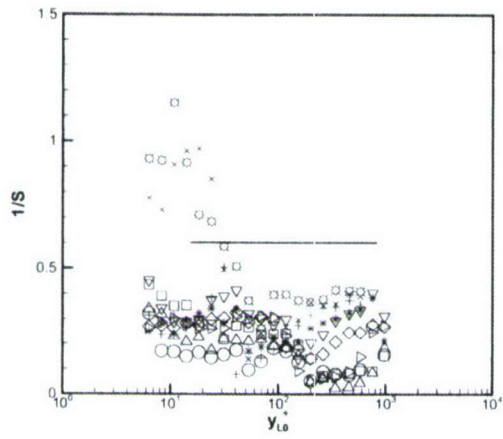
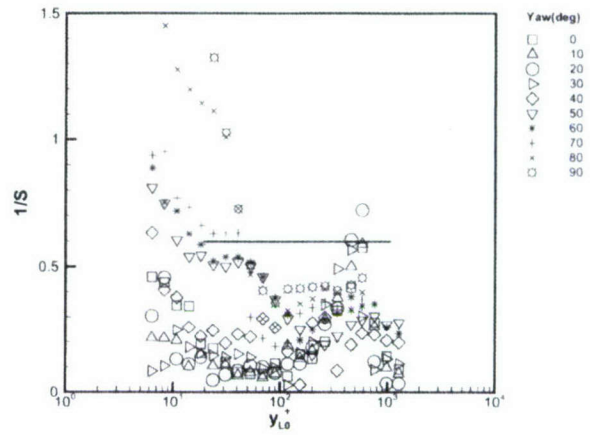
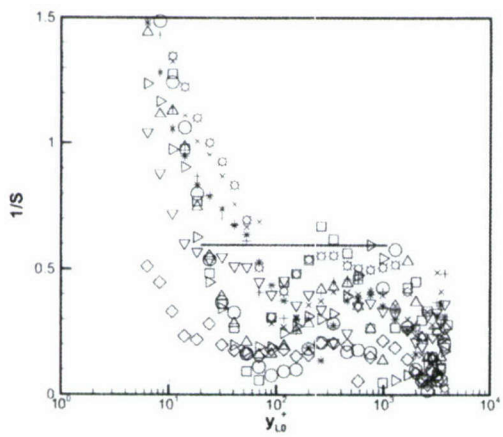
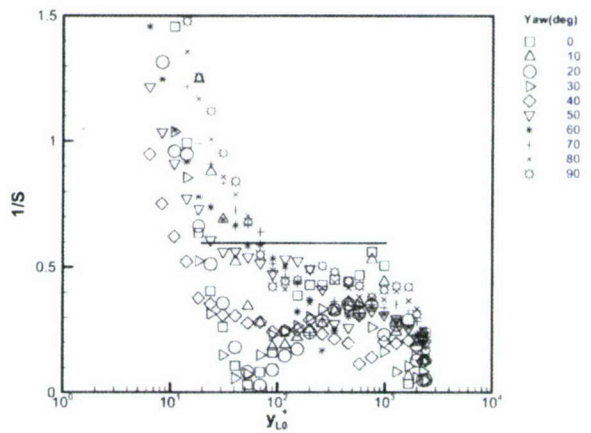
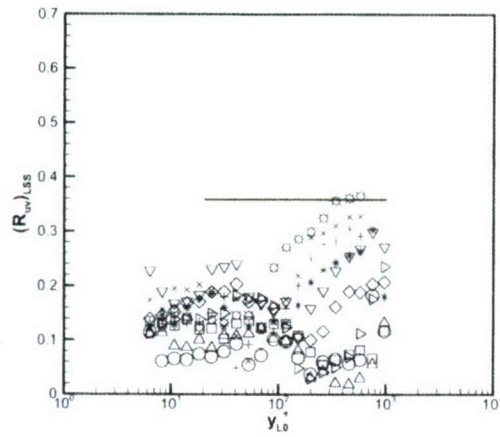
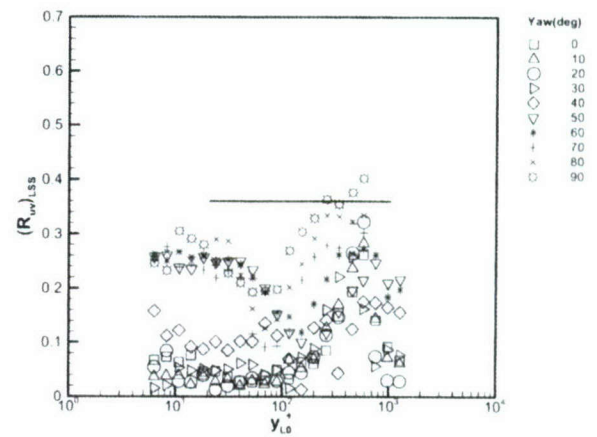
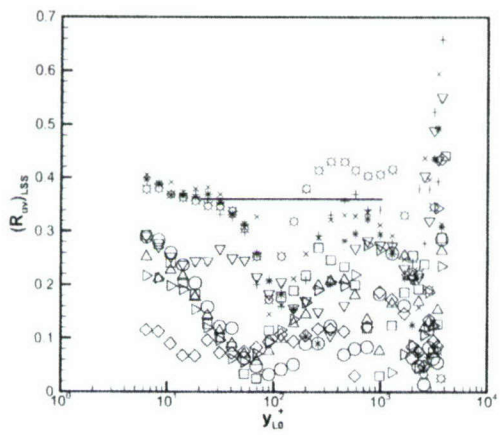
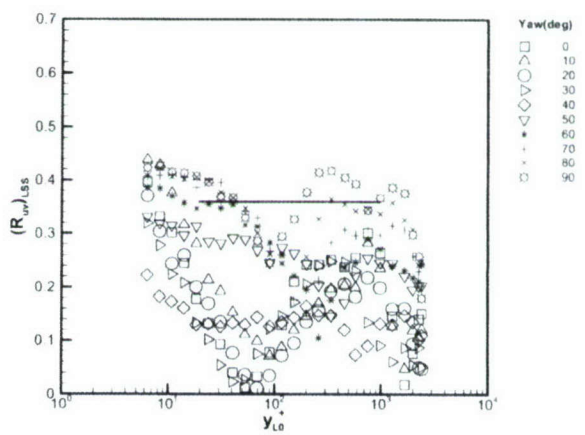


Figure 5.25 The magnitude of Reynolds shear stresses in local coordinates.

(a) $r/H = 0.644$ (b) $r/H = 0.91$ (c) $r/H = 1.386$ (d) $r/H = 1.615$

Horizontal lines show 2-DTBL level over middle region.

Figure 5.26 $1/S$ parameter in local coordinates.

(a) $r/H = 0.644$ (b) $r/H = 0.91$ (c) $r/H = 1.386$ (d) $r/H = 1.615$ Figure 5.27 R_{uv} in local shear stress coordinates.

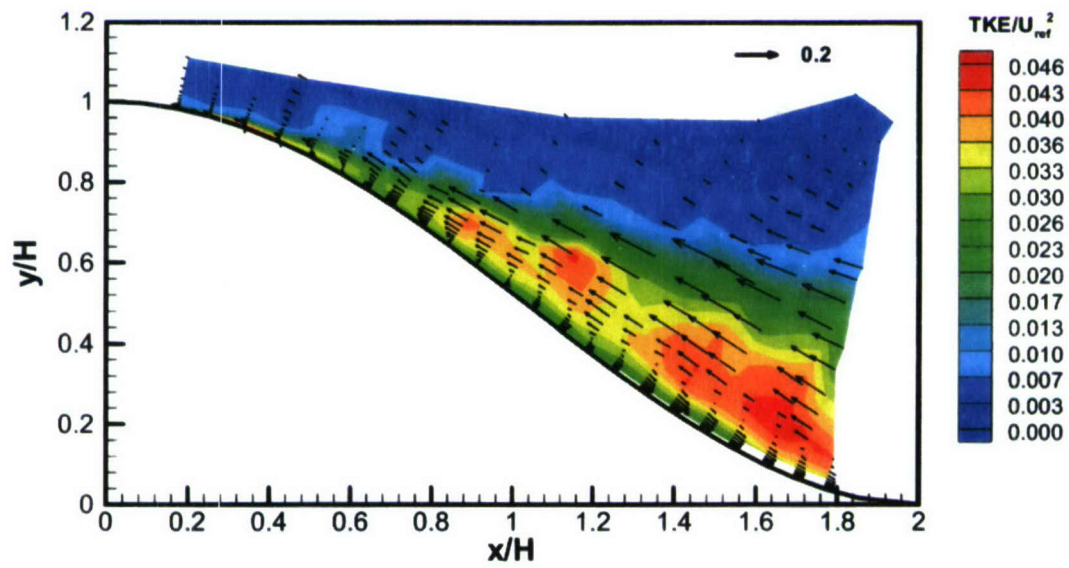
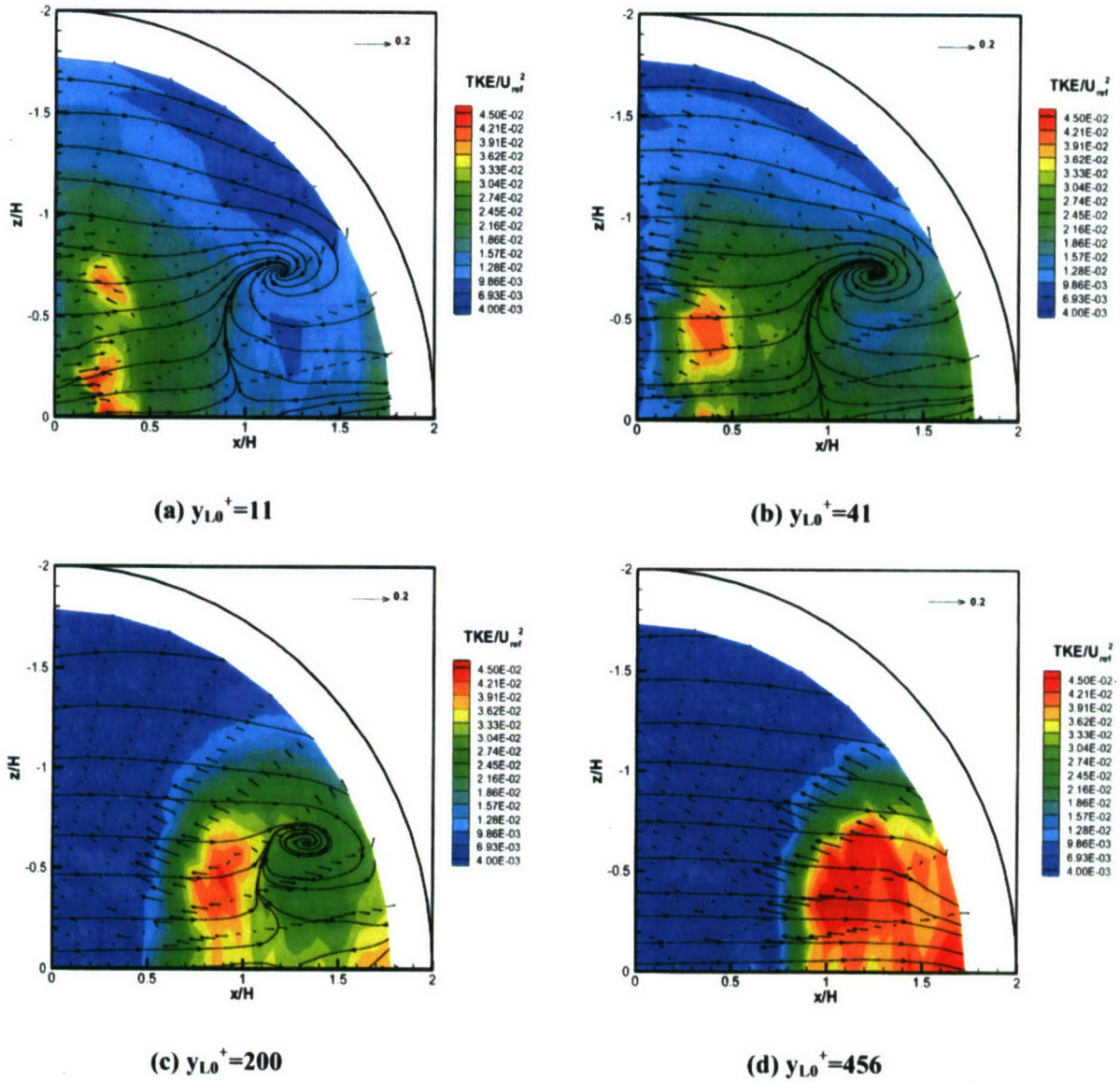


Figure 5.28 TKE contour and its normalized transport vectors $V_{qu}\vec{i} + V_{qv}\vec{j}$ in the center plane.



Lines from Fig. 5.7 for visual aid of locally tangential mean velocity directions.

Figure 5.29 TKE contours and its normalized transport vectors $V_{qu} \vec{i}_L + V_{qn} \vec{k}_L$ locally tangent to surface at different $y_{L,0}^+$.

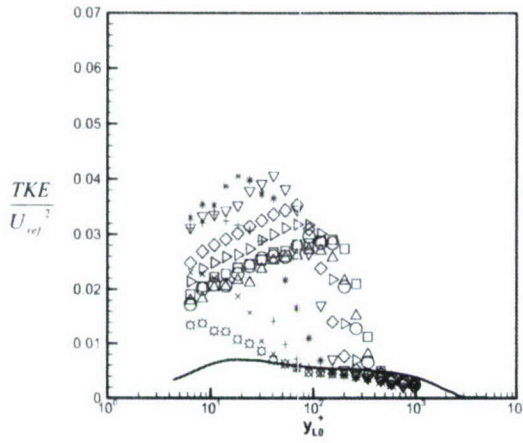
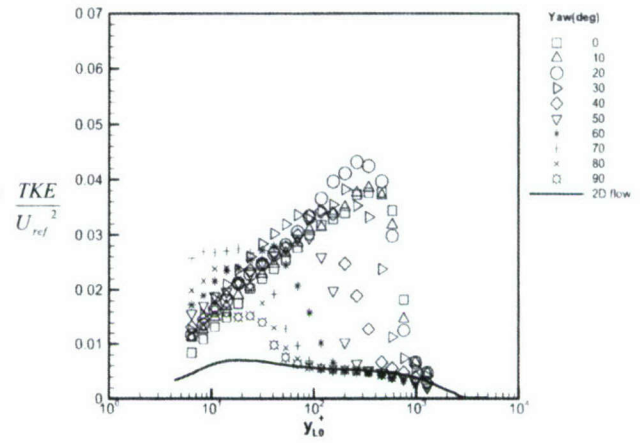
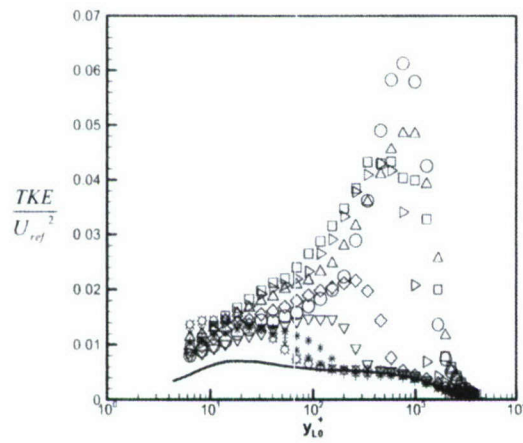
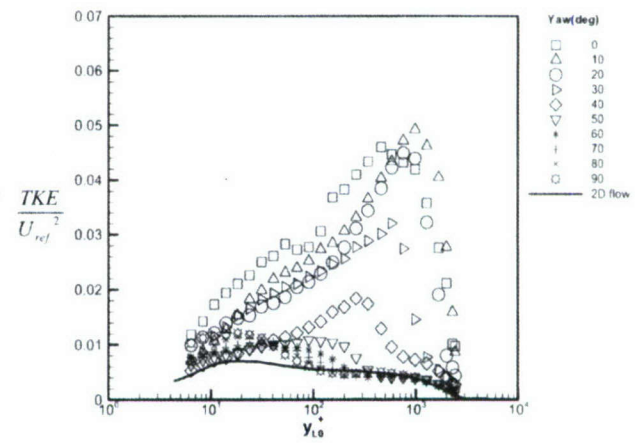
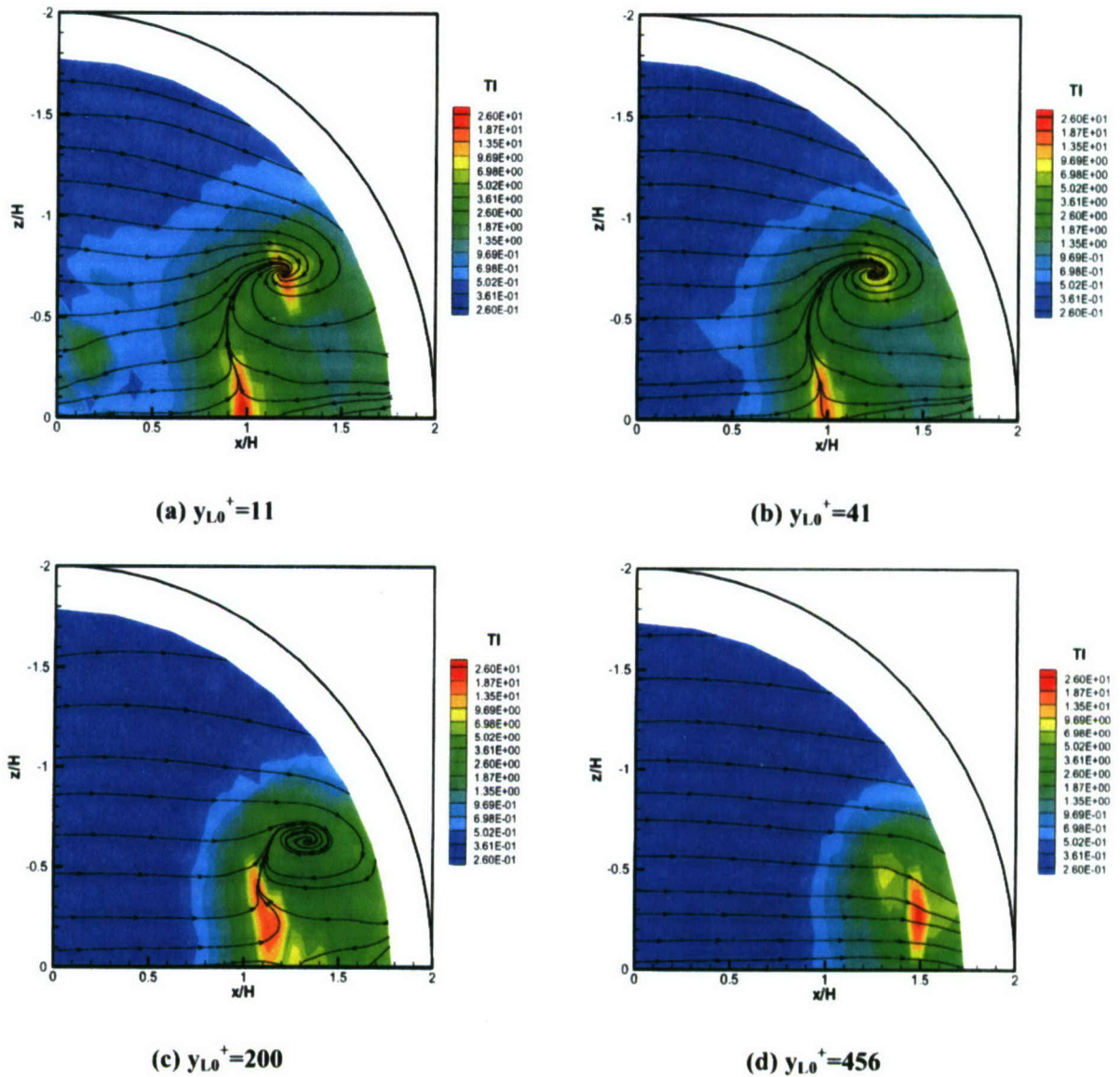
(a) $r/H = 0.644$ (b) $r/H = 0.91$ (c) $r/H = 1.386$ (d) $r/H = 1.615$

Figure 5.30 Normalized TKE in local coordinates.



Lines from Fig. 5.7 for visual aid of locally tangential mean velocity directions.

Figure 5.31 Turbulence Intensity contours at different $y_{L,0}^+$.

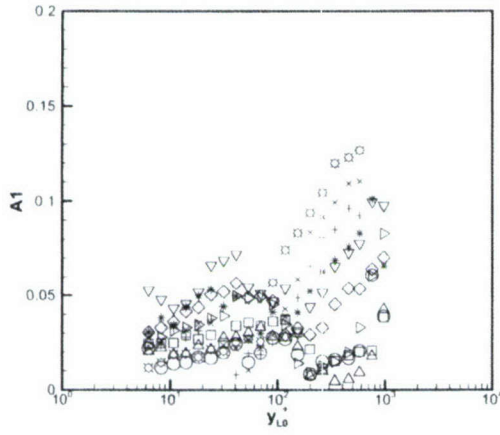
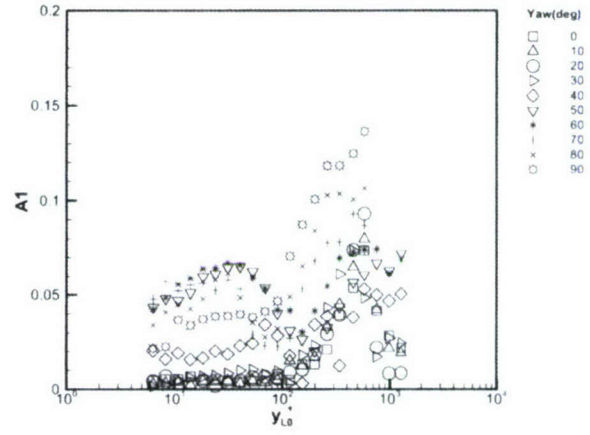
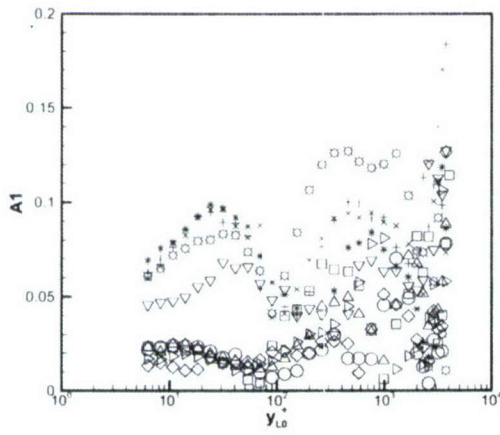
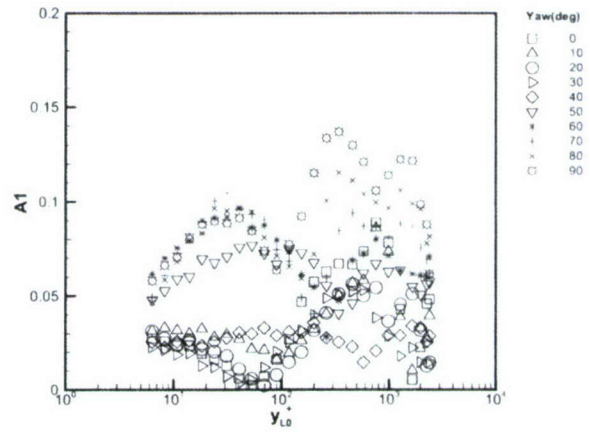
(a) $r/H = 0.644$ (b) $r/H=0.91$ (c) $r/H = 1.386$ (d) $r/H=1.615$

Figure 5.32 A1 parameter in local coordinates.

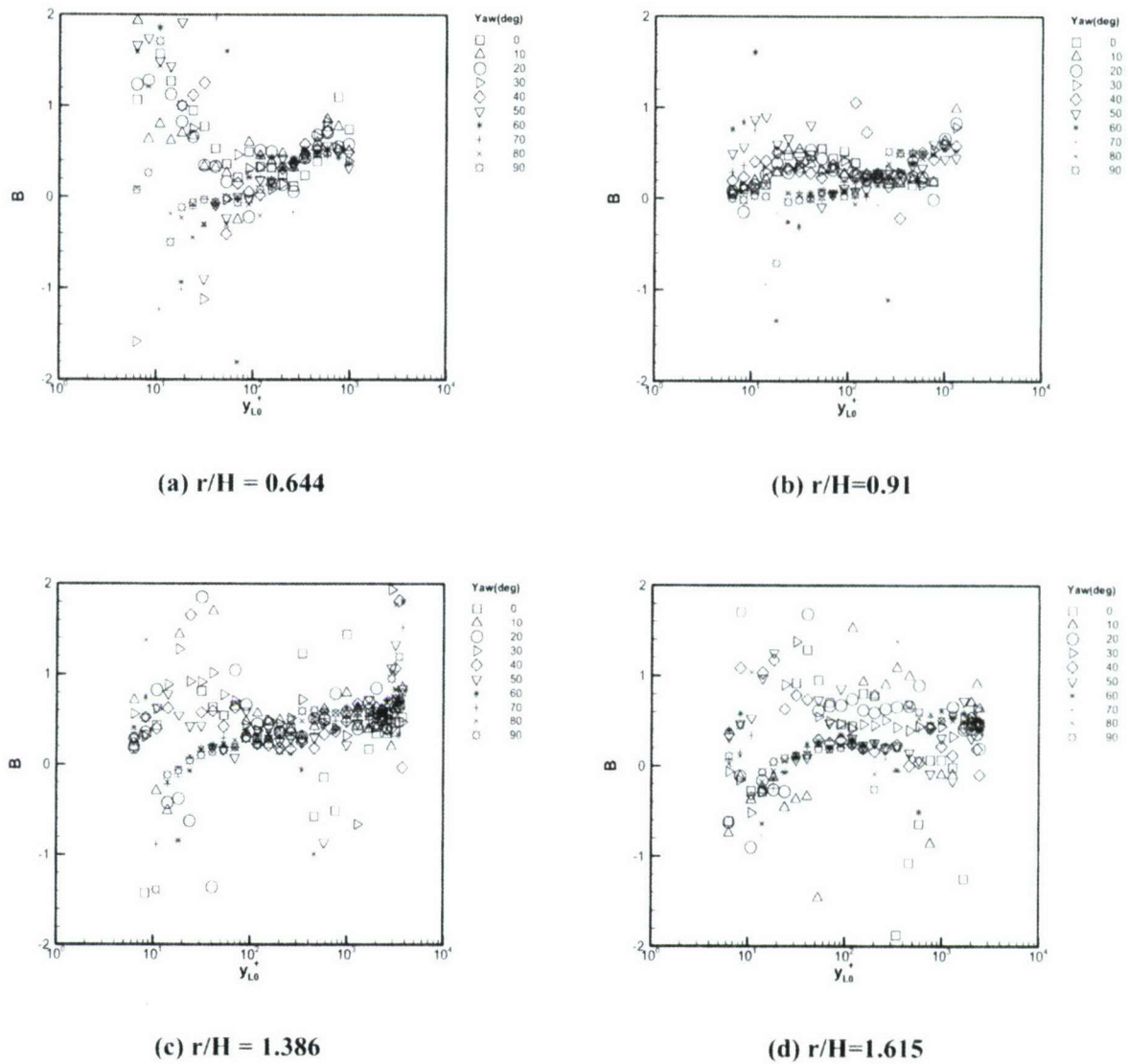


Figure 5.33 B parameter in local coordinates.

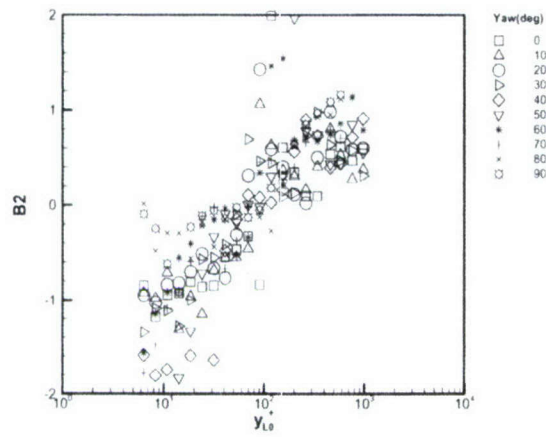
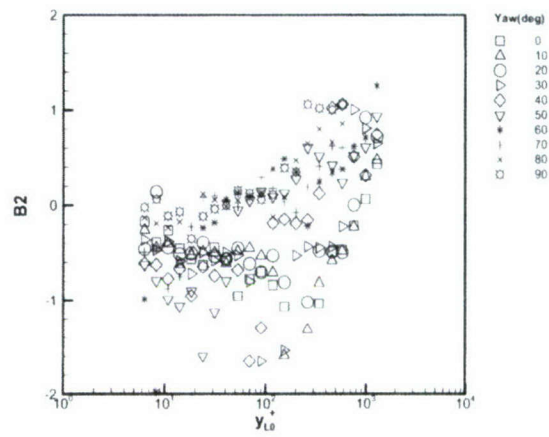
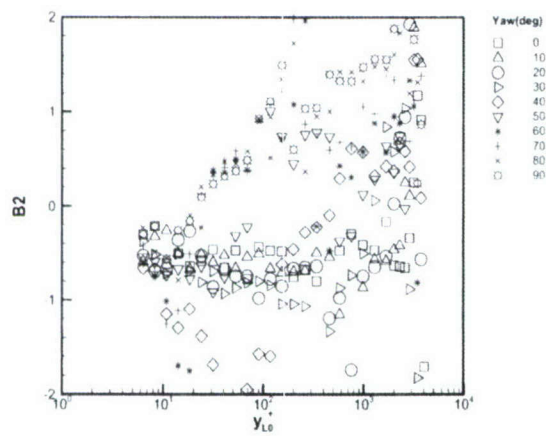
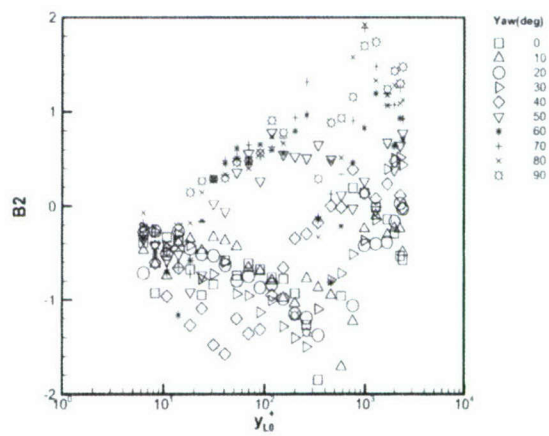
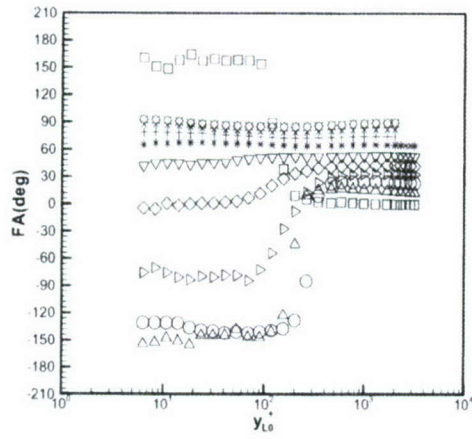
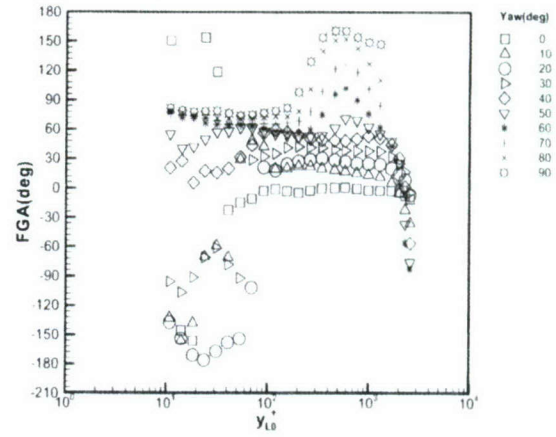
(a) $r/H = 0.644$ (b) $r/H = 0.91$ (c) $r/H = 1.386$ (d) $r/H = 1.615$

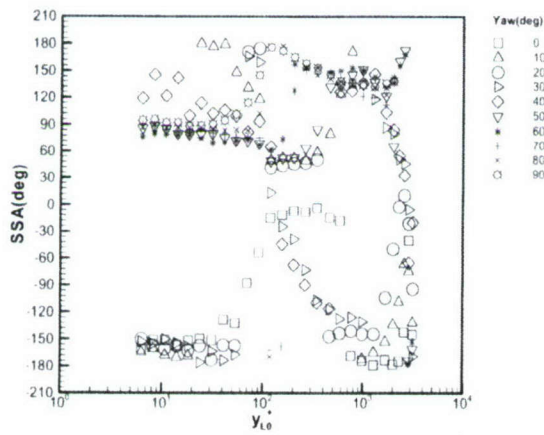
Figure 5.34 B2 parameter in local coordinates.



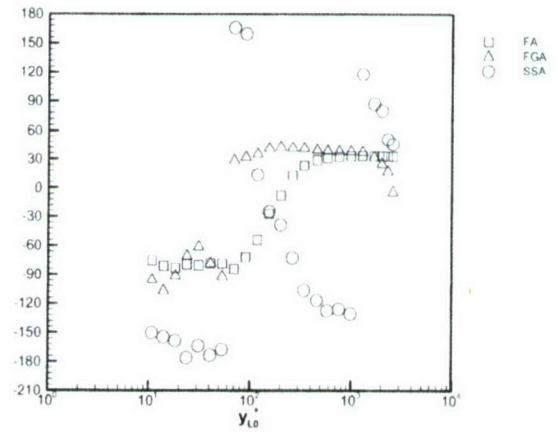
(a) Flow angle

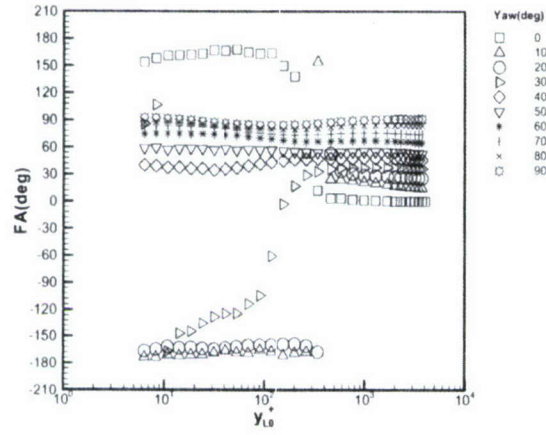


(b) Flow gradient angle

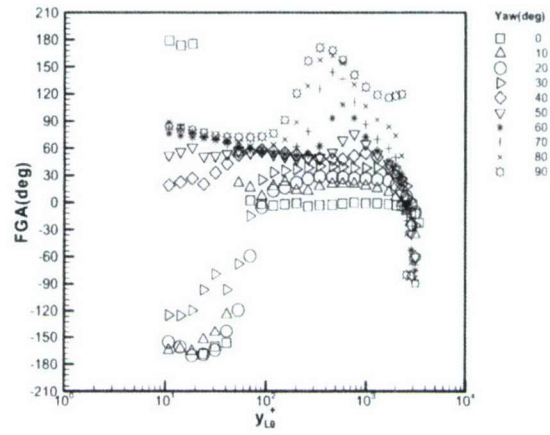


(c) Shear stress angle

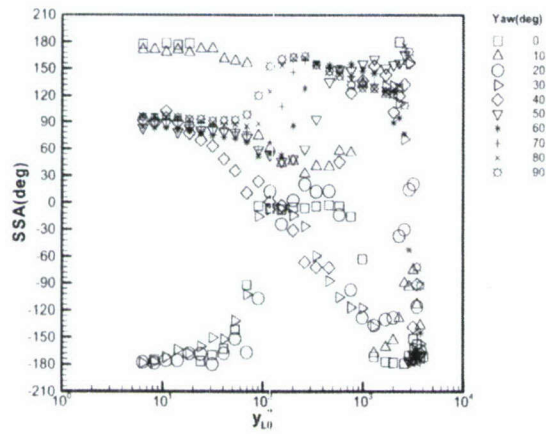
(d) Three angles at $\psi = 30^\circ$ Figure 5.35 FA, FGA and SSA in local coordinates along $r/H = 1.179$.



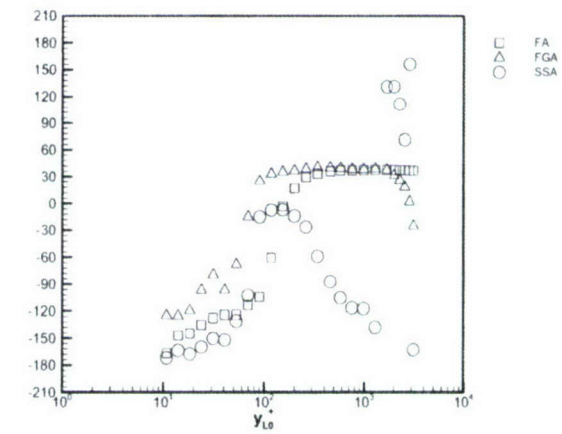
(a) Flow angle

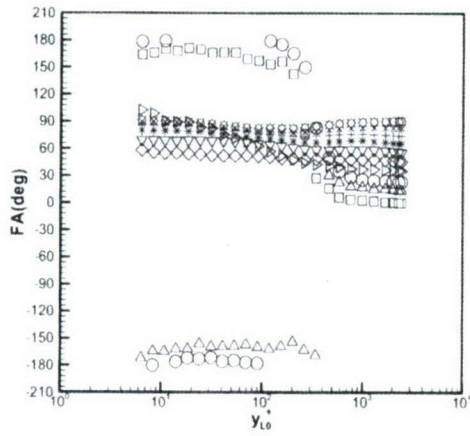


(b) Flow gradient angle

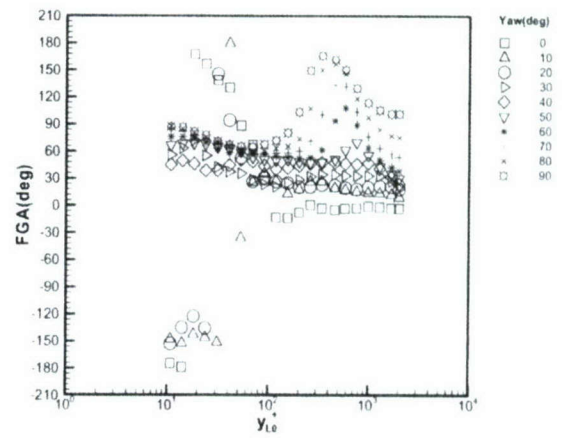


(c) Shear stress angle

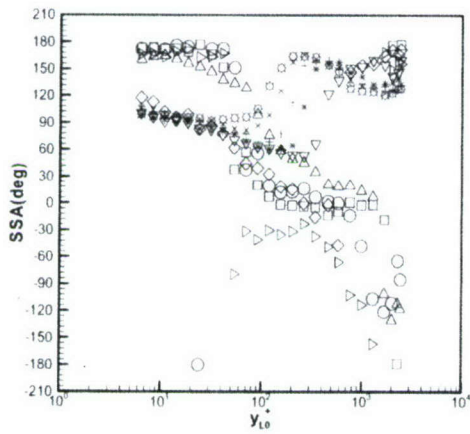
(d) Three angles at $\psi = 30^\circ$ Figure 5.36 FA, FGA and SSA in local coordinates along $r/H = 1.386$.



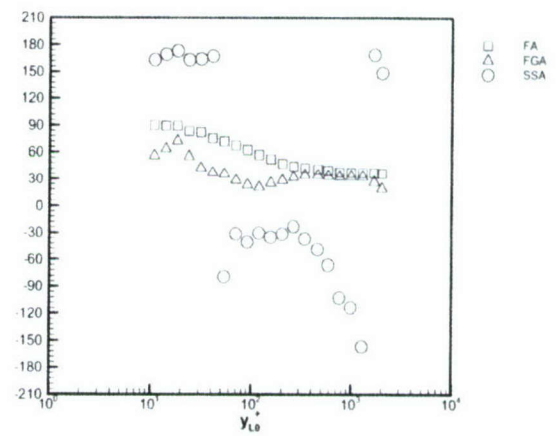
(a) Flow angle

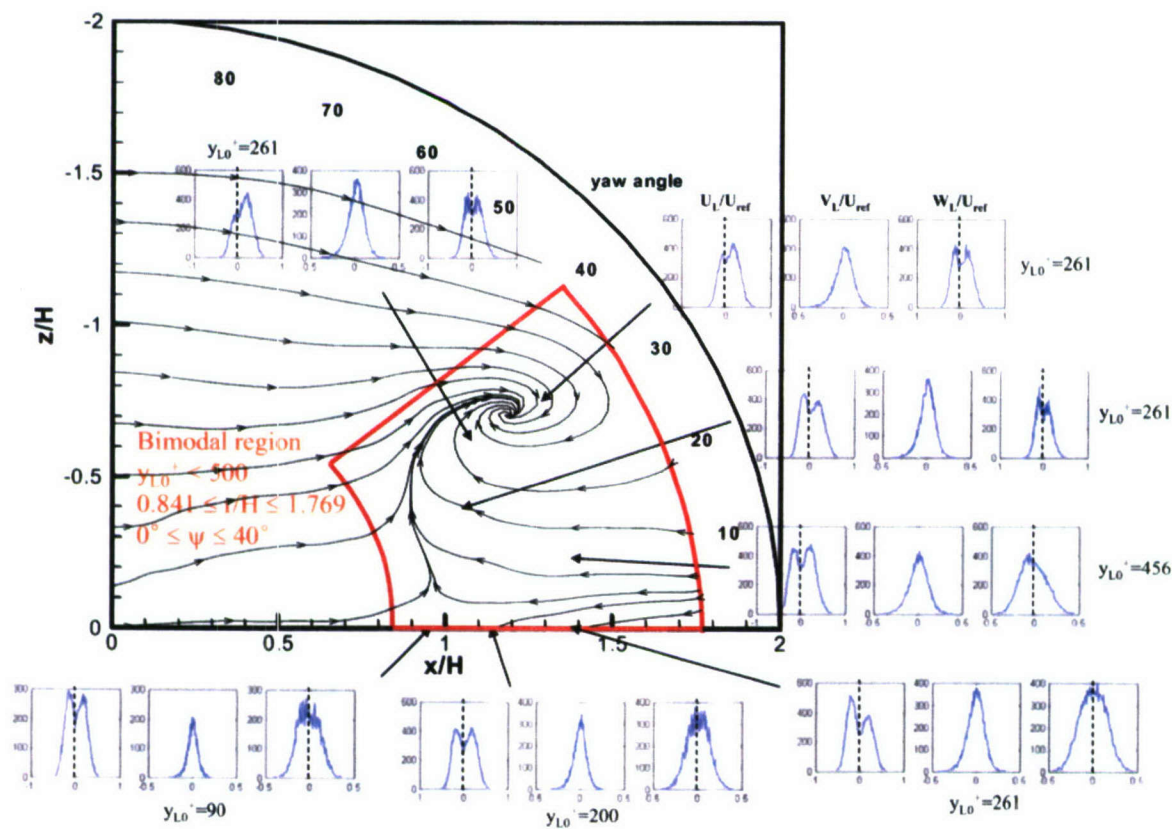


(b) Flow gradient angle



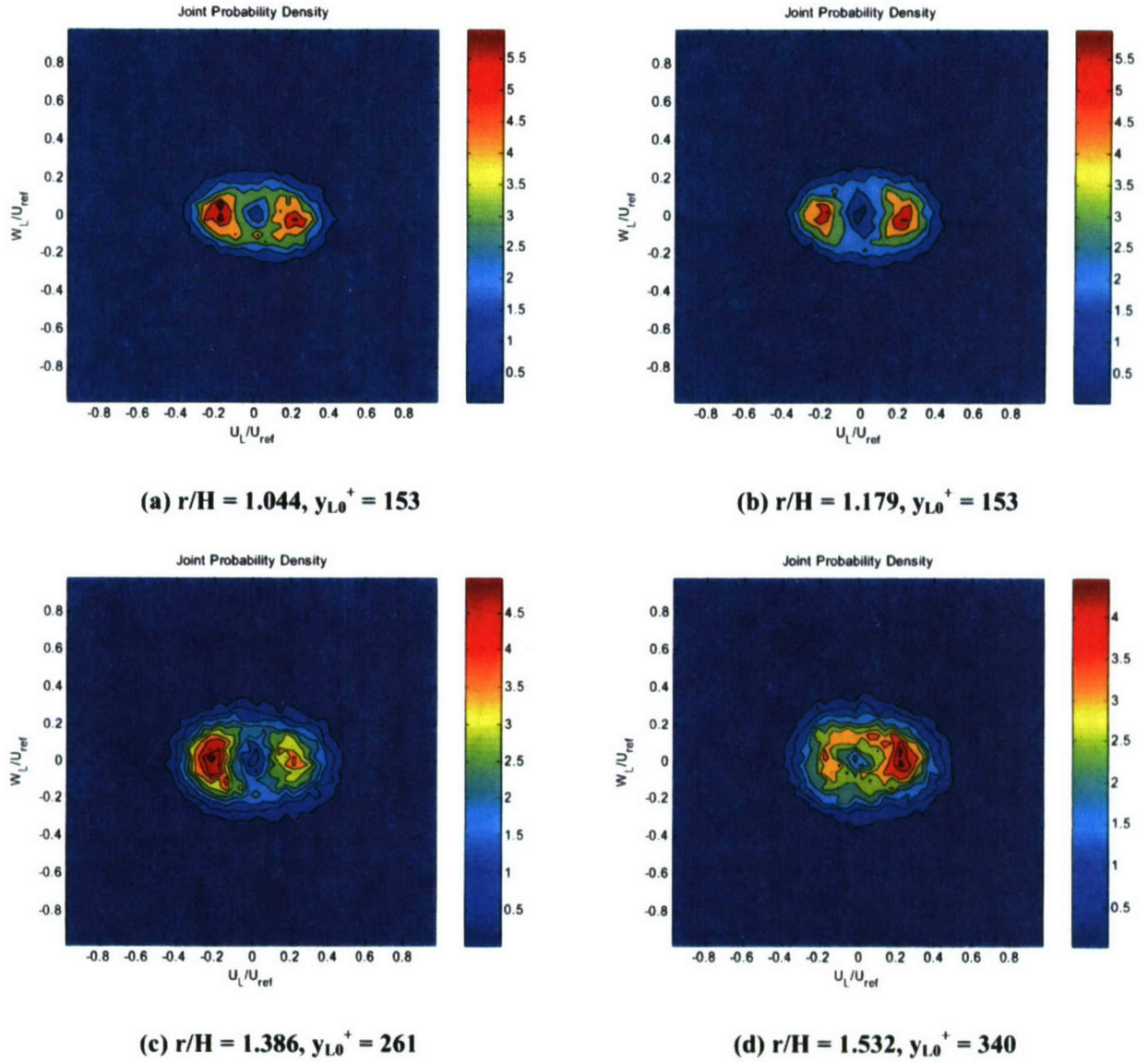
(c) Shear stress angle

(d) Three angles at $\psi = 30^\circ$ Figure 5.37 FA, FGA and SSA in local coordinates along $r/H = 1.615$.



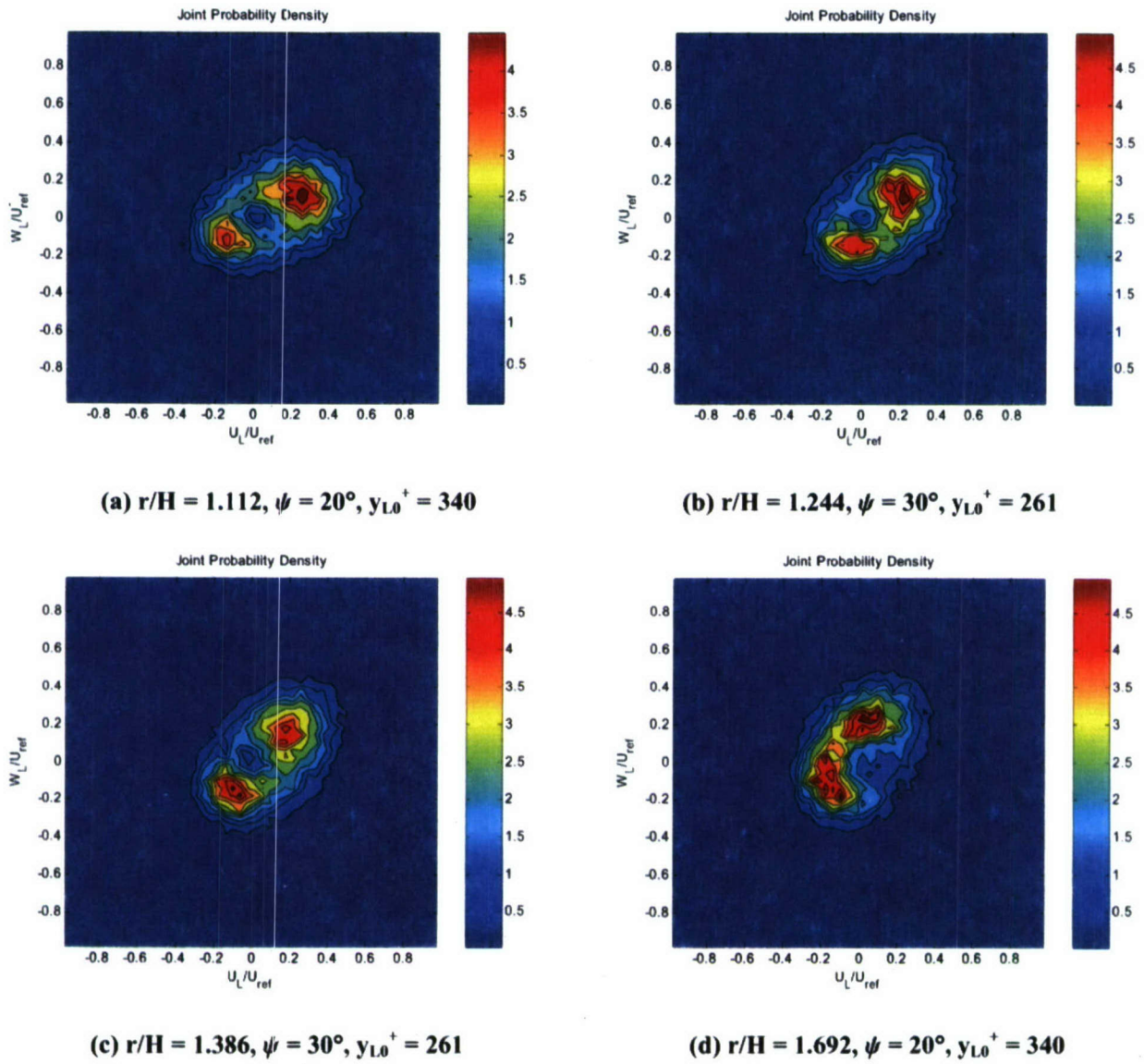
Dashed lines at $U_L = 0$ and $W_L = 0$ in histograms.

Figure 5.38 Bimodal histograms of U_L and W_L in local coordinates.



$$\int_{-\infty}^{\infty} \int_{-\infty}^{\infty} P(U_L, W_L) dU_L dW_L = 1$$

Figure 5.39 Joint probability density function of U_L and W_L along the centerline in local coordinates.



$$\int_{-\infty}^{\infty} \int_{-\infty}^{\infty} P(U_L, W_L) dU_L dW_L = 1$$

Figure 5.40 Joint probability density function of U_L and W_L in local coordinates.

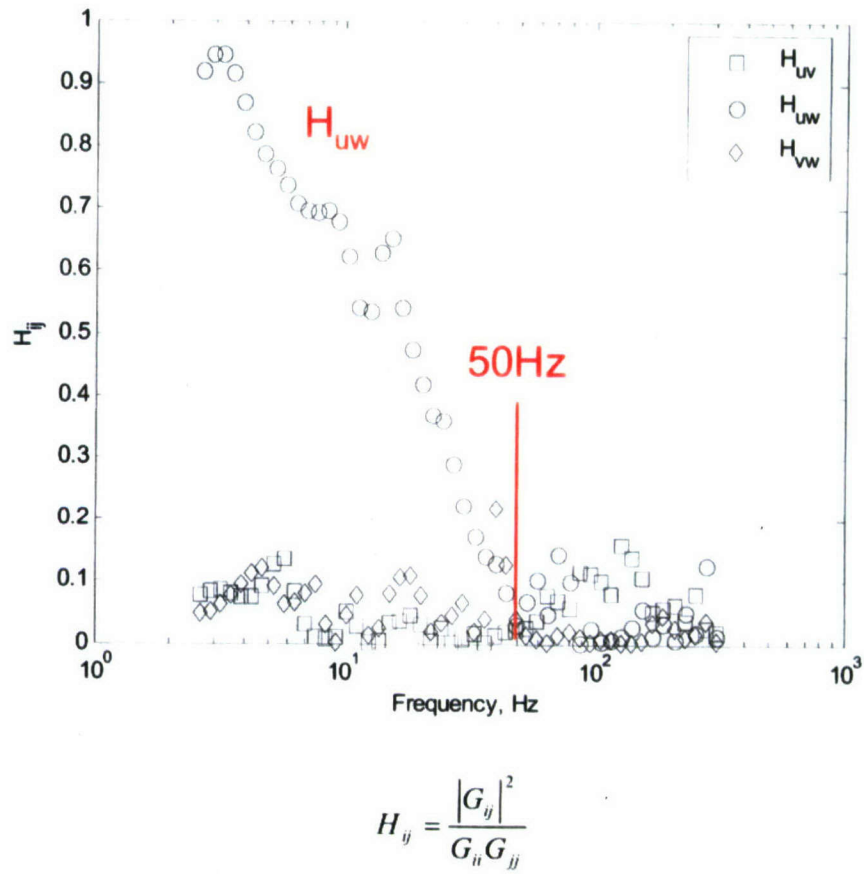
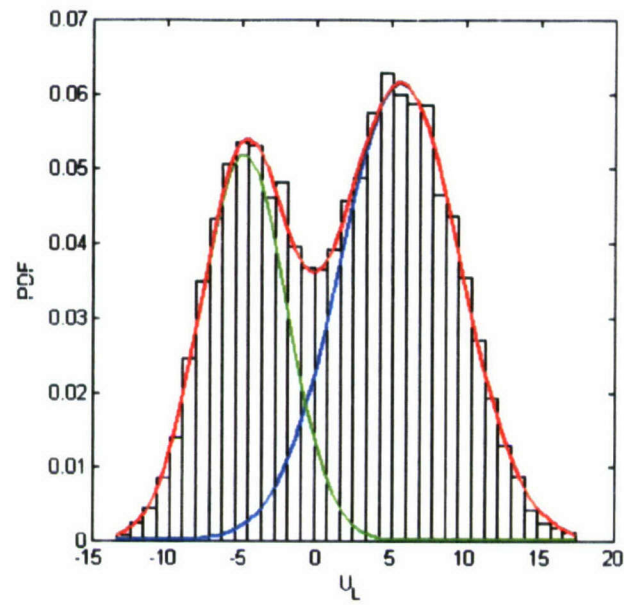
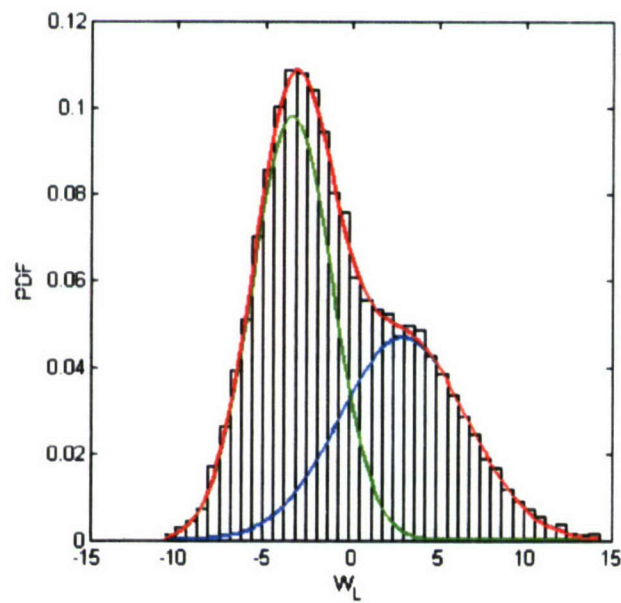


Figure 5.41 Coherency functions at $r/H = 1.386$, $\psi = 30^\circ$, $y_{1.0}^+ = 261$



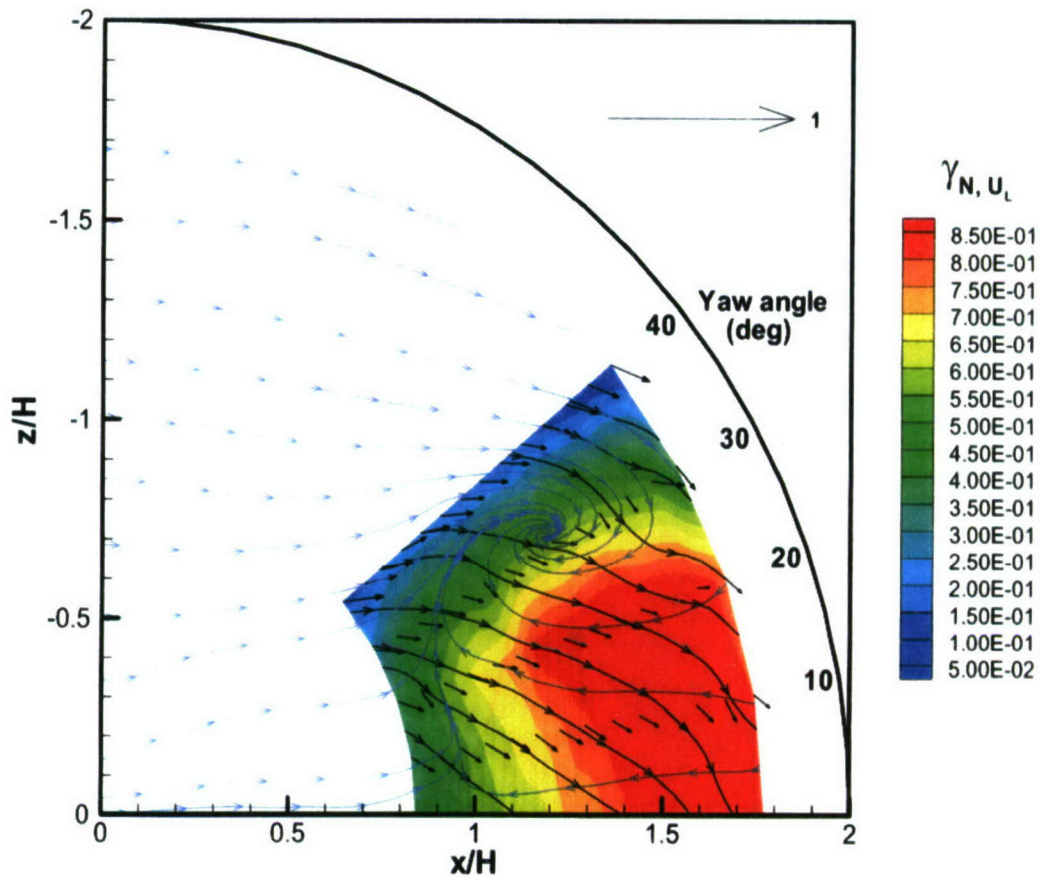
(a) $r/H = 1.179$, $\psi = 10^\circ$, $y_{L0}^+ = 261$



(b) $r/H = 1.179$, $\psi = 20^\circ$, $y_{L0}^+ = 261$

Green line for backward mode, blue line for forward mode and red line for the summation of backward and forward modes.

Figure 5.42 Least square fit of bimodal PDF.

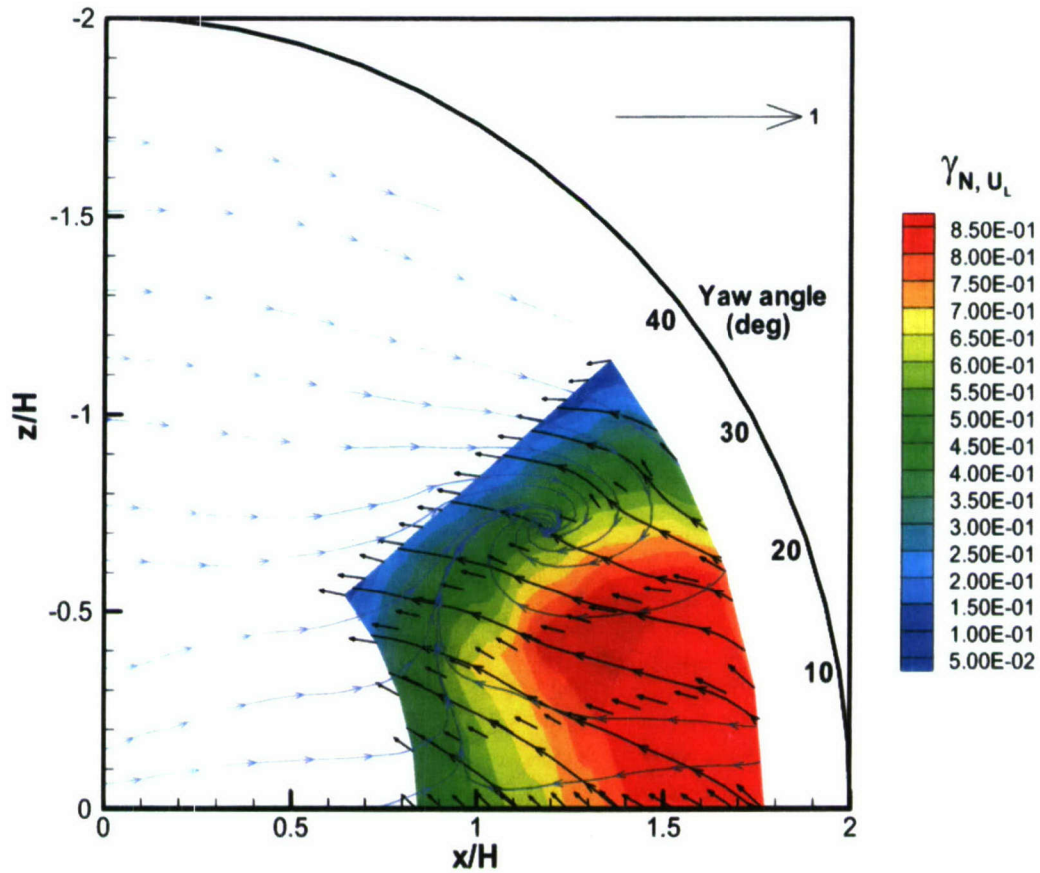


Vectors for velocity components locally tangent to surface in bimodal region and contours for the time fraction of negative U_L in local coordinates.

Lines connecting locally tangential velocity vectors are only for visual aid.

Blue lines for time-averaging original histograms and black lines only for bimodal region.

Figure 5.43 The forward mode at $y_{L0}^+ = 11$.

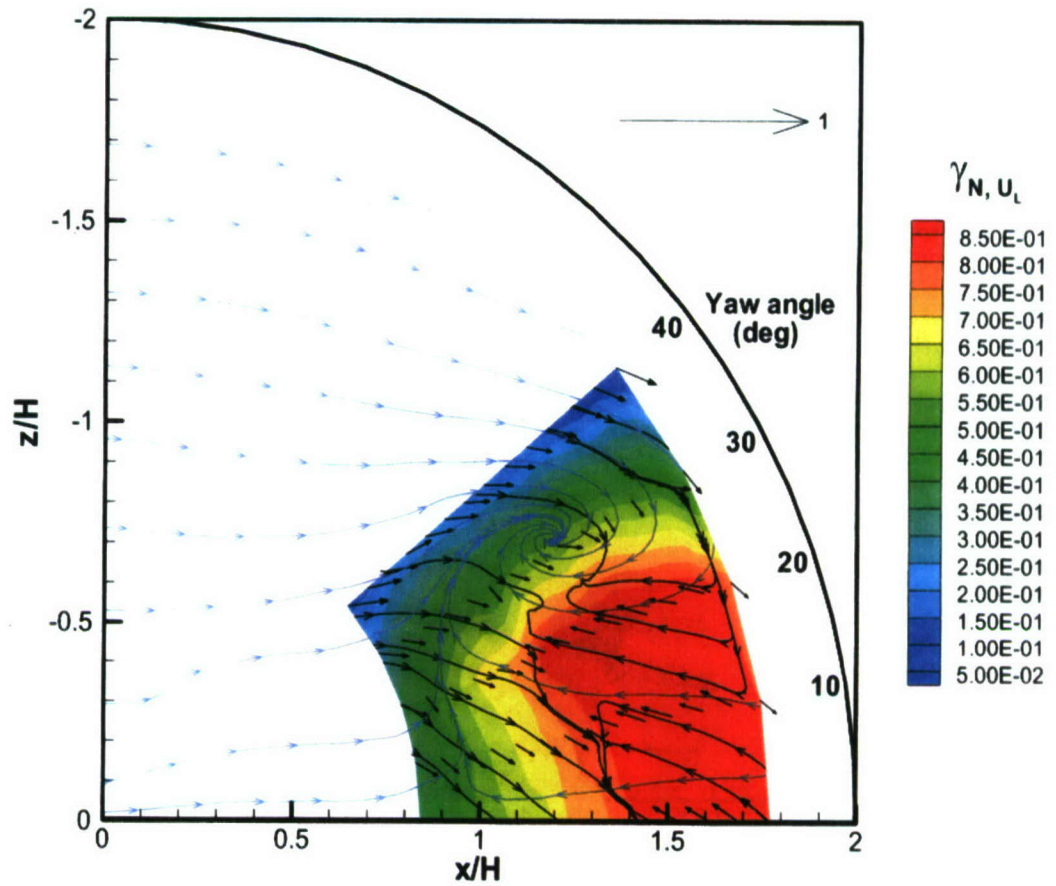


Vectors for velocity components locally tangent to surface in bimodal region and contours for the time fraction of negative U_L in local coordinates.

Lines connecting locally tangential velocity vectors are only for visual aid.

Blue lines for time-averaging original histograms and black lines only for bimodal region.

Figure 5.44 The backward mode at $y_{L0}^+ = 11$.

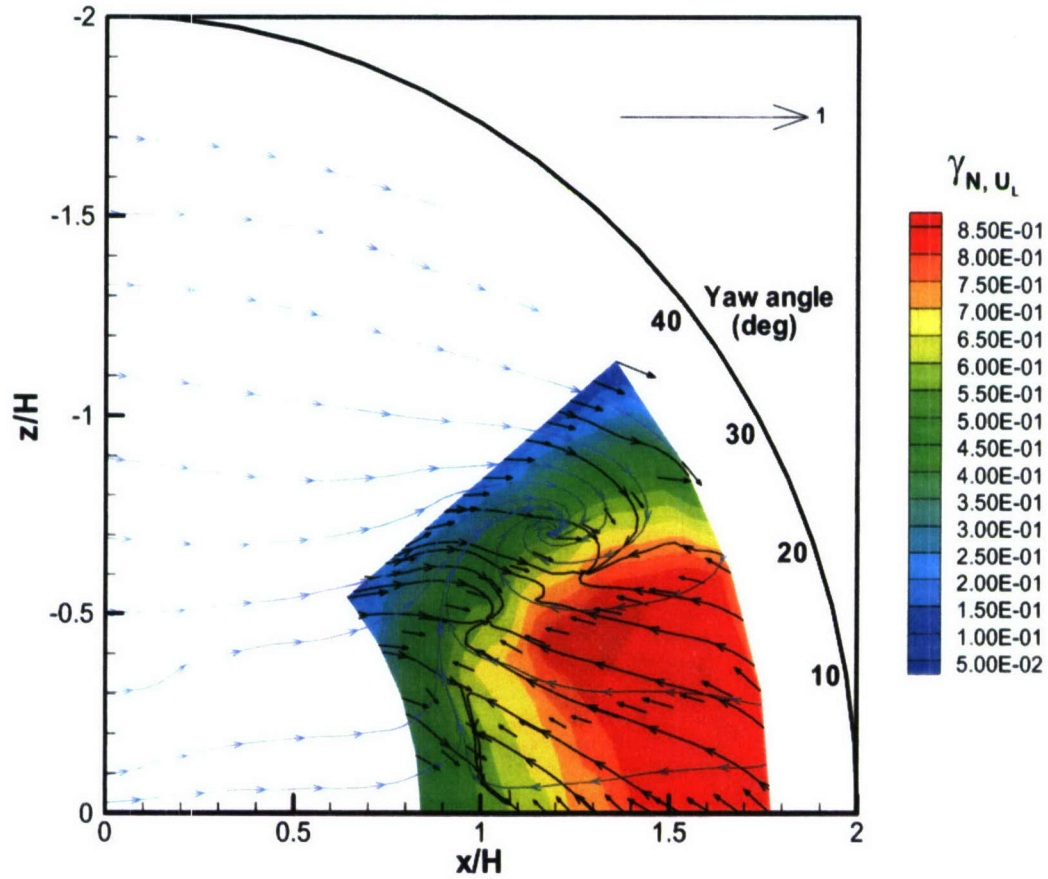


Vectors for velocity components locally tangent to surface in bimodal region and contours for the time fraction of negative U_L in local coordinates.

Lines connecting locally tangential velocity vectors are only for visual aid.

Blue lines for time-averaging original histograms and black lines only for bimodal region.

Figure 5.45 The combination of forward and backward modes at $y_{L0}^+ = 11$ for $\gamma_{N,U_L} = 0.8$.

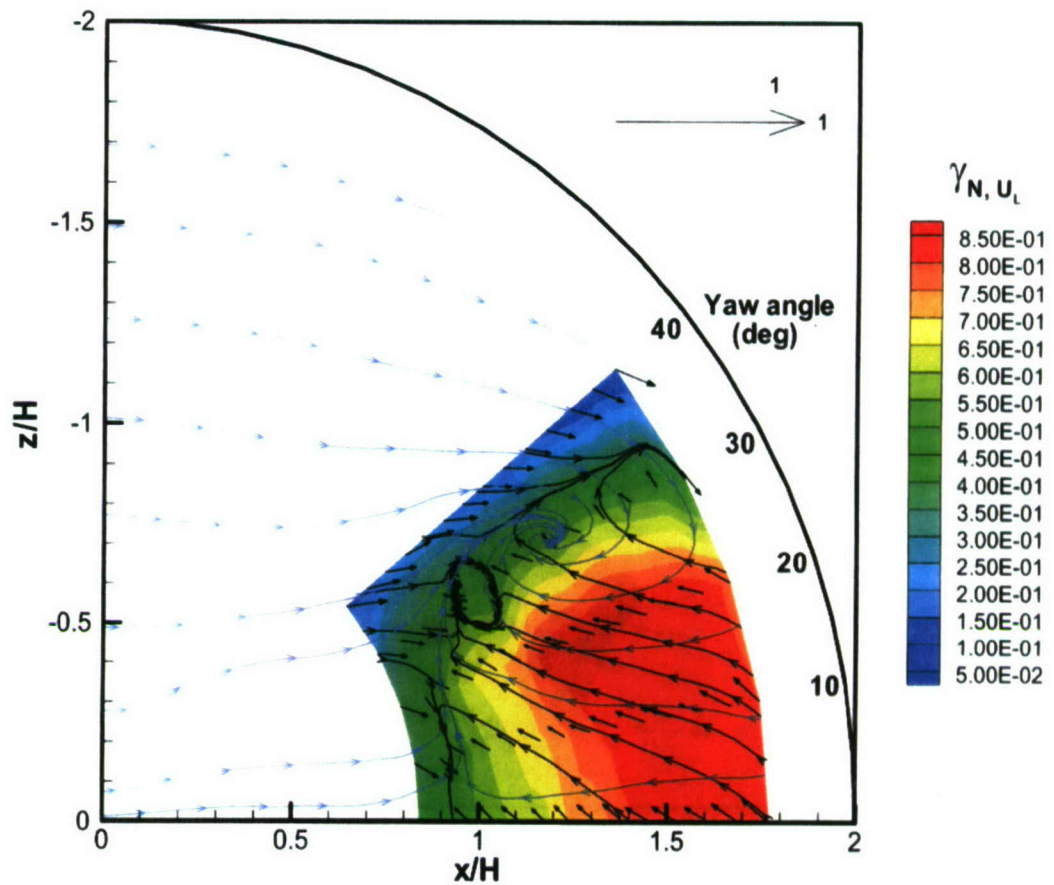


Vectors for velocity components locally tangent to surface in bimodal region and contours for the time fraction of negative U_L in local coordinates.

Lines connecting locally tangential velocity vectors are only for visual aid.

Blue lines for time-averaging original histograms and black lines only for bimodal region.

Figure 5.46 The combination of forward and backward modes at $y_{L0}^+ = 11$ for $\gamma_{N,U_L} = 0.6$.

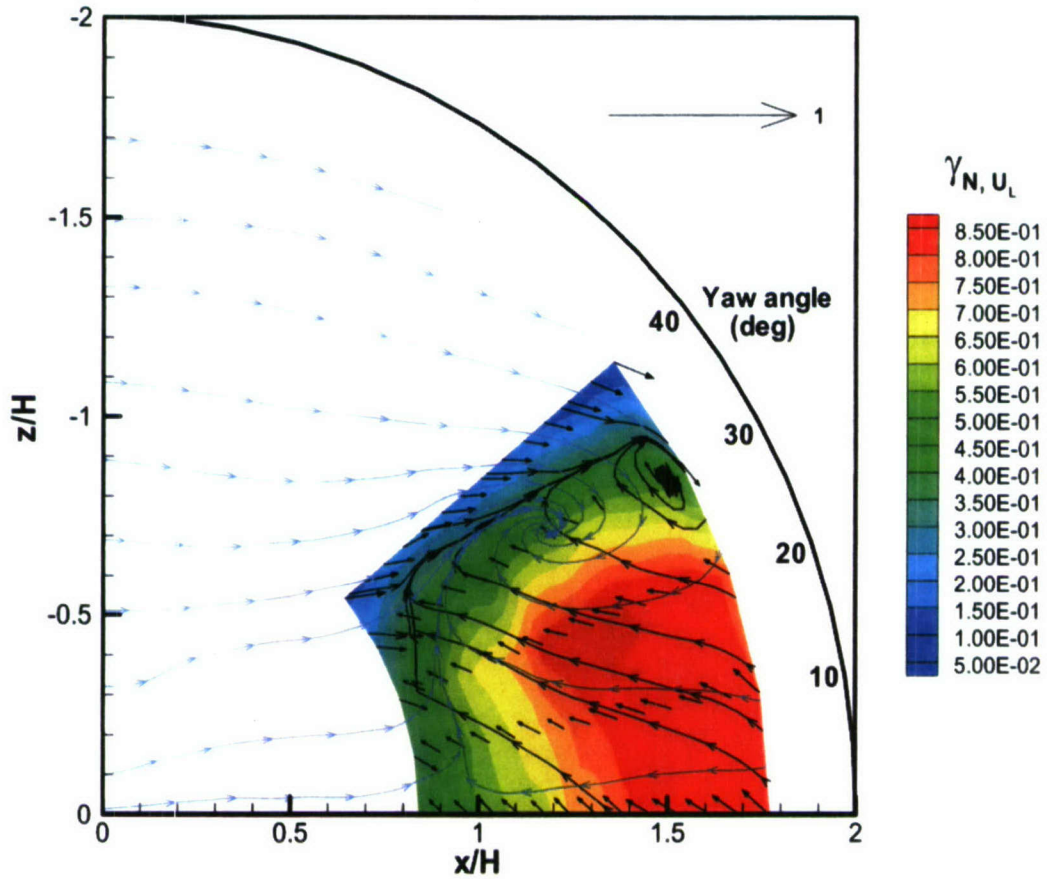


Vectors for velocity components locally tangent to surface in bimodal region and contours for the time fraction of negative U_L in local coordinates.

Lines connecting locally tangential velocity vectors are only for visual aid.

Blue lines for time-averaging original histograms and black lines only for bimodal region.

Figure 5.47 The combination of forward and backward modes at $y_{L0}^+ = 11$ for $\gamma_{N,U_L} = 0.5$.

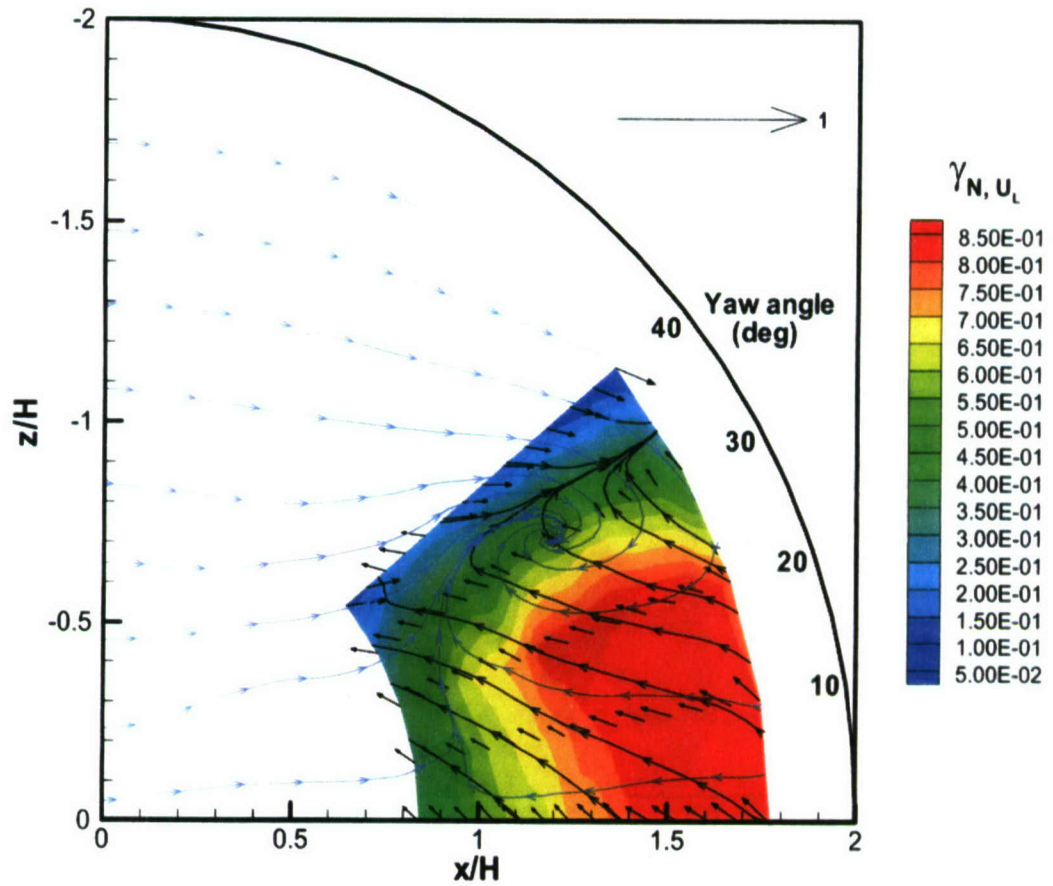


Vectors for velocity components locally tangent to surface in bimodal region and contours for the time fraction of negative U_L in local coordinates.

Lines connecting locally tangential velocity vectors are only for visual aid.

Blue lines for time-averaging original histograms and black lines only for bimodal region.

Figure 5.48 The combination of forward and backward modes at $y_{L0}^+ = 11$ for $\gamma_{N,U_L} = 0.4$.

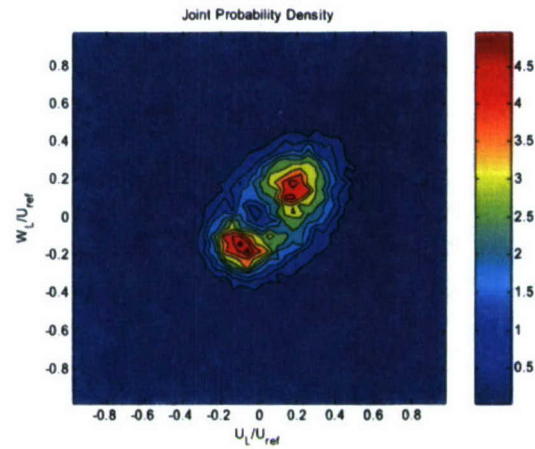
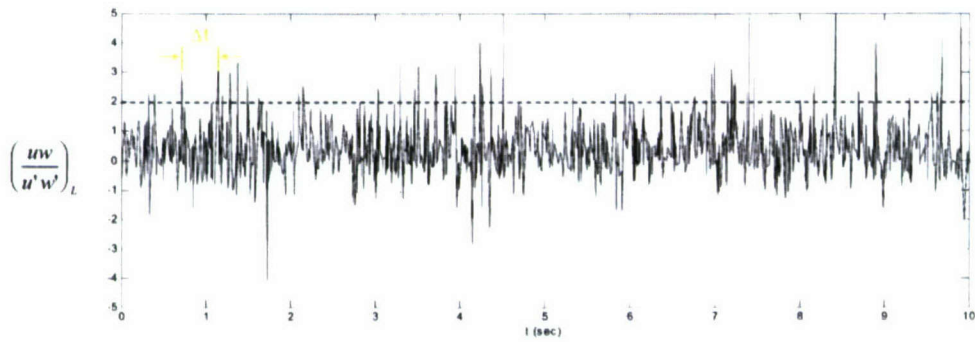
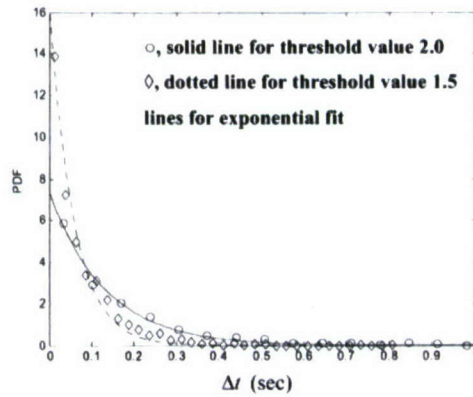


Vectors for velocity components locally tangent to surface in bimodal region and contours for the time fraction of negative U_L in local coordinates.

Lines connecting locally tangential velocity vectors are only for visual aid.

Blue lines for time-averaging original histograms and black lines only for bimodal region.

Figure 5.49 The combination of forward and backward modes at $y_{1,0}^+ = 11$ for $\gamma_{N,U_L} = 0.2$.

(a) JPDF of U_L and W_L (b) Time series of $(uw/u'w')_L$. Dashed line for the threshold value(c) Distribution of the times between threshold value excess in the time series of $(uw/u'w')_L$ **Figure. 5.50** Time dependence of bimodal U_L and W_L

at $r/H = 1.386$, $\psi = 30^\circ$ and $y_{L,0}^+ = 261$ in local coordinates.

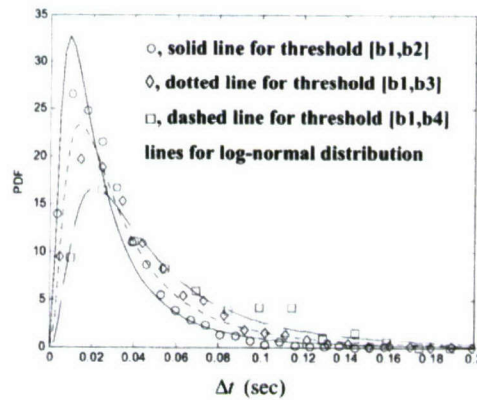
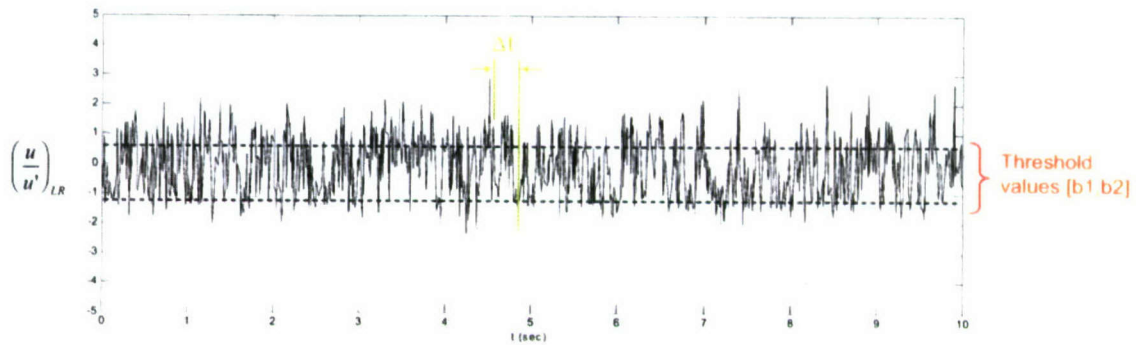
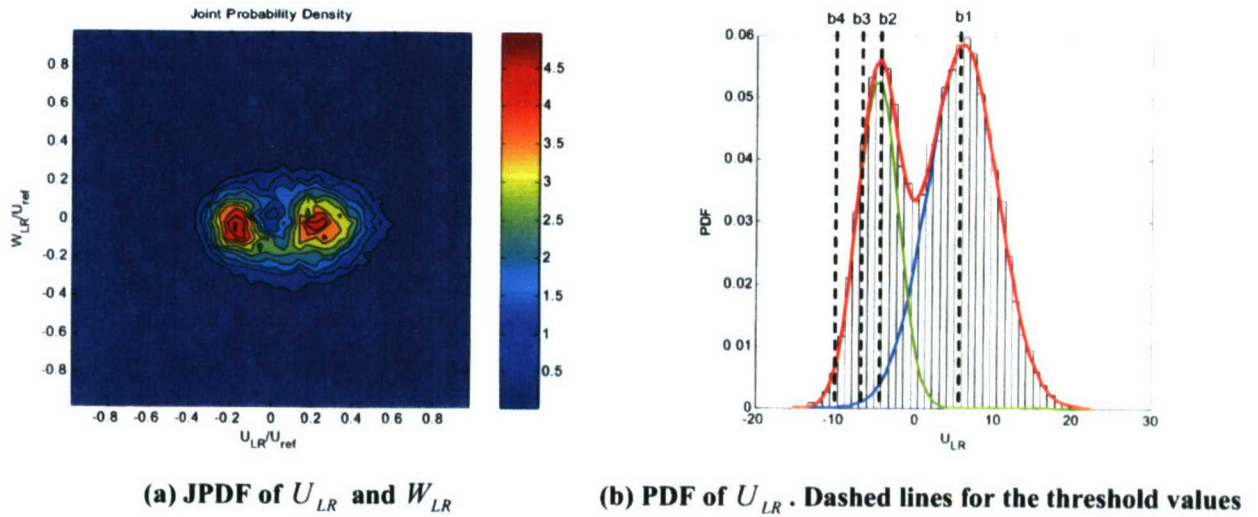
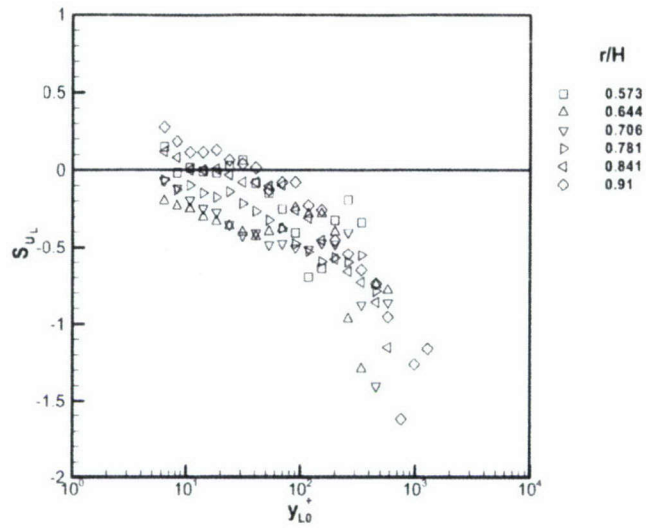
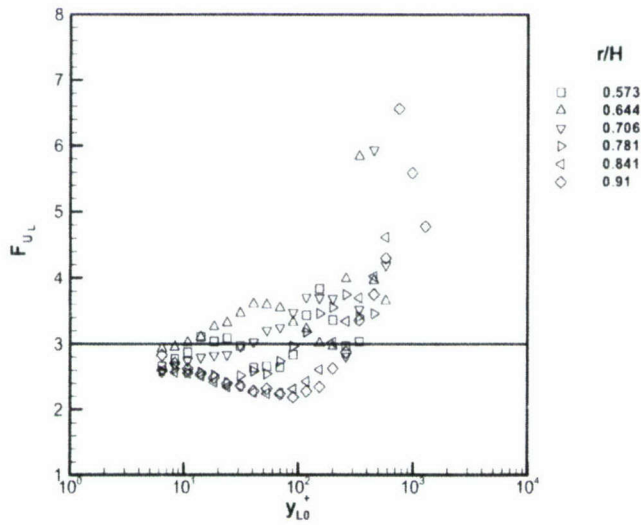


Figure. 5.51 Time dependence of bimodal U_{LR}

at $r/H = 1.386$, $\psi = 30^\circ$ and $y_{L0}^+ = 261$ in locally rotated coordinates.



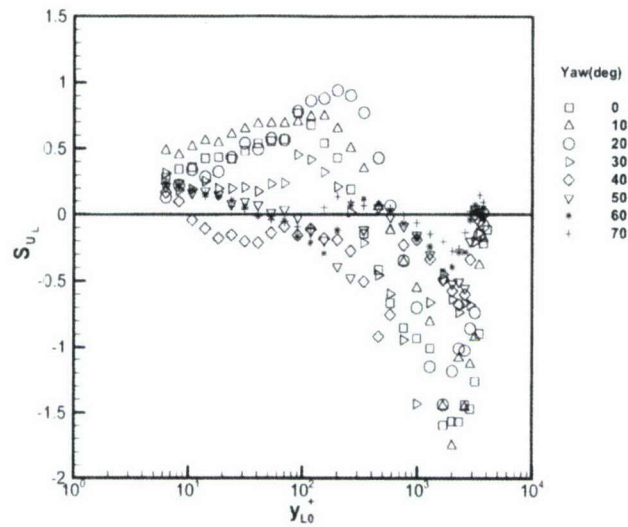
(a) Skewness factor



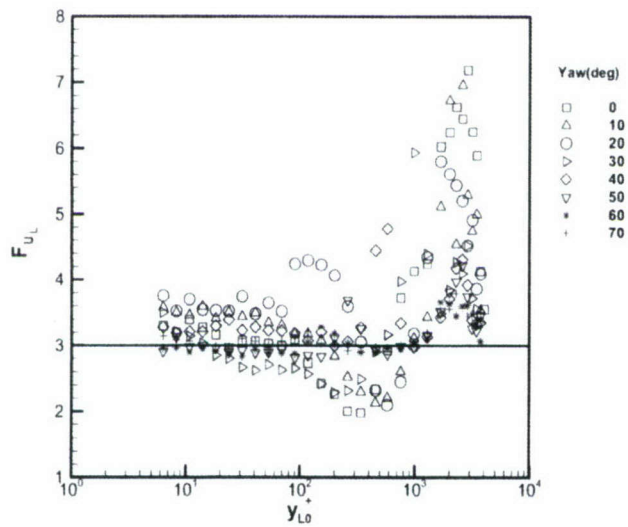
(b) Flatness factor

Horizontal lines show Gaussian distribution factors.

Figure 5.52 Skewness and flatness factor of U_L upstream from separation along the centerline in local coordinates.



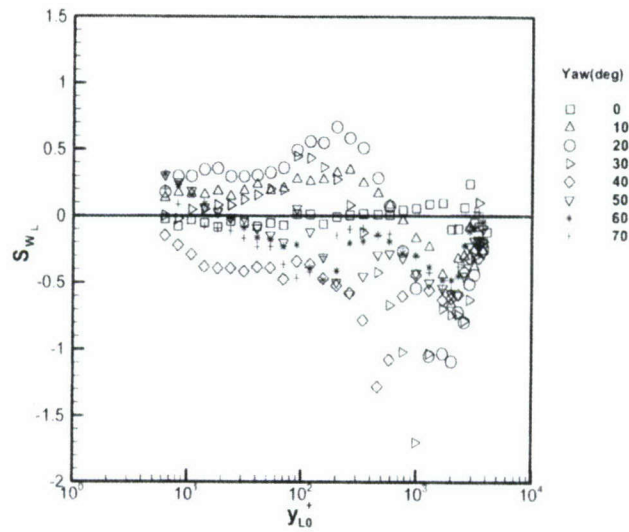
(a) Skewness factor



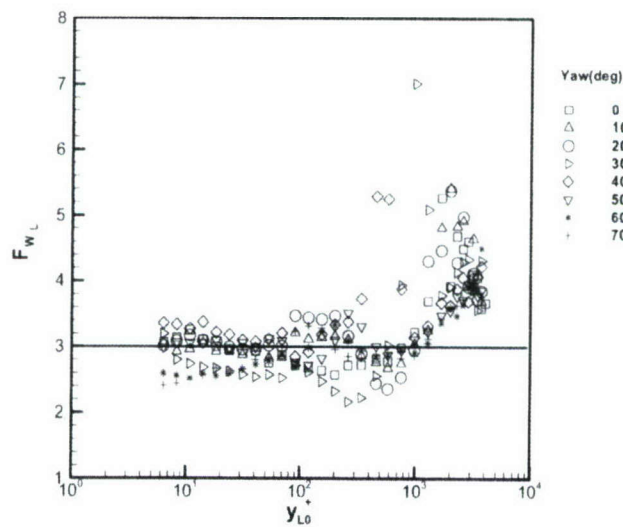
(b) Flatness factor

Horizontal lines show Gaussian distribution factors.

Figure 5.54 Skewness and flatness factor of U_L along $r/H = 1.386$ in local coordinates.



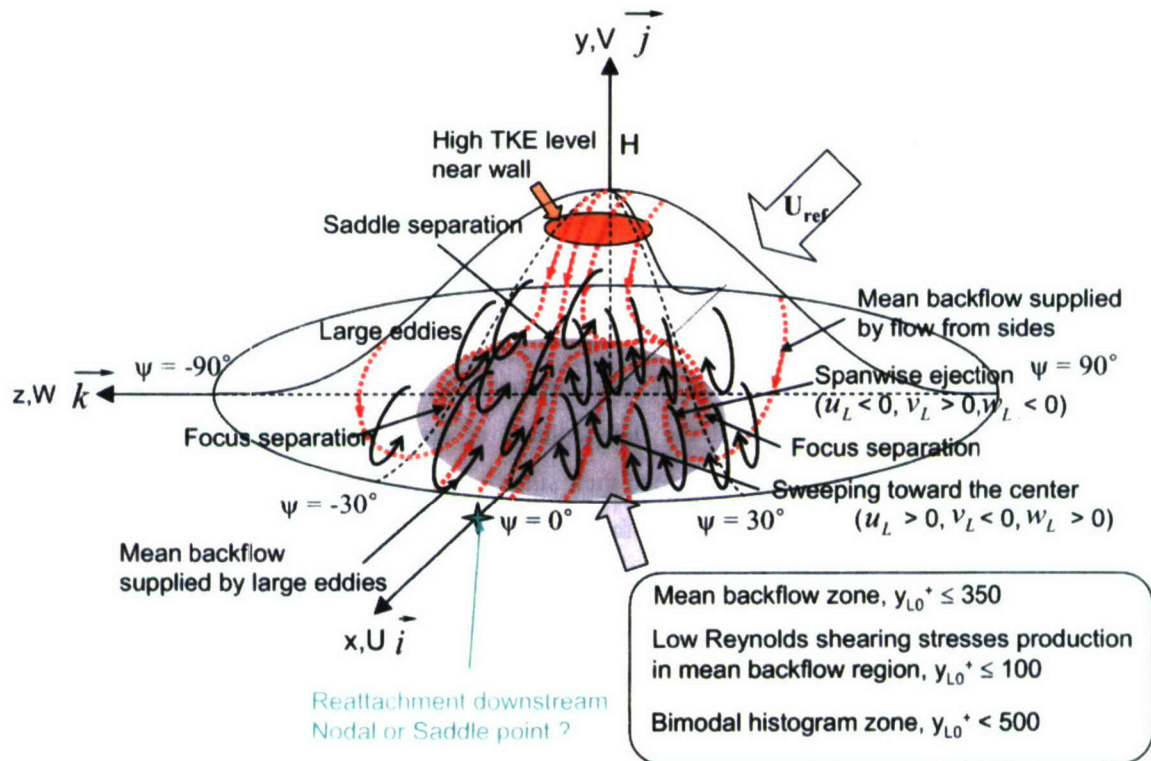
(a) Skewness factor



(b) Flatness factor

Horizontal lines show Gaussian distribution factors.

Figure 5.55 Skewness and flatness factor of W_L along $r/H = 1.386$ in local coordinates.



large eddies shown in black; near surface flow patterns in dashed; mean backflow zone in gray.

Figure 5.56 Illustration of flow structures on leeward side of bump.

6

Large Bump#3 CFD Calculations

6.1 Introduction

CFD has been a very useful method to calculate the flow fields around solid bodies due to the improvement of its modeling and the development of computational technology. Many CFD researchers have been challenged to extend their simulations to more complex 3D flow fields from 2D cases. The turbulent flow separation from a 3D body might be a major challenge for CFD researchers because its flow structure is not completely understood so that it seems difficult to model the flow field properly. Even though one can calculate a 2D turbulent boundary layer, 3D turbulent flow has totally different flow characteristics. Therefore, their efforts have been limited to well-documented test cases in order to verify their modeling and methods.

This bump flow measured and presented here has provided CFD researchers a reliable test case for high Reynolds number turbulent flow separation from 3D curved surfaces. There are three different research groups, Prof. Menon in Georgia Tech (Menon, Kemenov, and Patel, 2004; Patel, Stone and Menon, 2003), Prof. Leschziner in Imperial College London (Temmerman, Wang and Leschziner, 2004; Wang, Jang and Leschziner, 2004) and Prof. Davidson in Chalmers University of Technology (Davidson and Dahlström, 2004) which have calculated this bump flow field using different simulation methods and have published their results. In this chapter, their significant results are discussed and compared with the present measured data to show the improvement and limitation of their models and schemes. Table 6.1 summarizes features of their schemes.

6.2 Prof. Menon Group

Patel et al. (2003) and Menon et al. (2004) have used Large eddy simulation (LES) with an isotropy eddy viscosity model. The subgrid kinetic energy and the local grid size are used for the characteristic velocity and the length scale, respectively. The subgrid kinetic energy is obtained by solving a transport equation. So, this is a one-equation model. There are two coefficients in the viscosity term and the dissipation term in their model. They determined these two coefficients locally as a function of space and time using Localized dynamic K-equation model (LDKM).

Figure 6.1 shows the computational domain for the LES. The no-slip condition at the lower wall and slip condition at other walls are applied, which result $256 \times 128 \times 128$ grid resolution, $56\mu\text{m}$ near wall minimum grid spacing in the wall normal direction and minimum (Δx^+ , Δy^+ , Δz^+) as (12,4,100). The computational domain is $20H \times 3.2H \times 6H$ (H is the bump height). They consider the effect of no-slip condition at the upper wall, which results $1926 \times 184 \times 144$ grid resolution and $12H \times 3.2H \times 10H$ computational domain. Reynolds number based on bump height is same as a experimental case.

They reported mean velocities, Reynolds stresses, skin friction velocity, turbulent kinetic energy (TKE) and velocity spectra at $x/H = 3.63$ wake plane and pressure distributions and mean streamlines on the bump surface. They got good agreement with presented experimental data qualitatively having the same trends. Figure 6.2 shows C_p distributions on the bump surface. It shows very good agreement with experimental data. Figure 6.3 shows mean streamline patterns at $y^+ = 8.63$ over the bump surface. It shows multiple saddles and foci separations on the leeside. However, they are more than experiment. In Fig. 6.4, skin friction velocities at $z/H = 3.63$ show the same trend as the experiment, but they are quantitatively lower than experiment. \overline{U}^+ and \overline{W}^+ at $x/H = 3.63$ in Fig. 6.5 and 6.6, respectively also show qualitative agreements. Menon et al. explained that these differences might be due to lower simulated skin friction velocities. The \overline{uv}^+ in Fig. 6.7 shows a poor agreement especially in outer regions. However, secondary flow vectors in y - z plane at $x/H = 3.63$ in Fig. 6.8 are consistent with experiment showing only one pair of stream-wise vortices generating the downwash near the center.

6.3 Prof. Leschziner Group

Prof. Leschziner's group is one of the most intense research groups modeling 3-D turbulent separated flow around a 3-D bump. His group has published many papers reporting the simulations around the 3-D large bump#3 with LES, RANS and zonal LES/RANS modelings.

Temmerman et al. (2004) have used LES with a classic Smagorinsky subgrid scale model which is an isotropy eddy viscosity model. They did not mention the characteristic velocity and the length scale. However, the characteristic velocity and the length scale might be assumed the filter width and the filtered rate of strain multiplied by the filter width, respectively. So, this might be a zero-equation model. The no-slip condition at the lower and upper wall and slip condition at side walls are applied, which result in $192 \times 96 \times 192$ grid resolution. The computational domain is $26H \times 3.2H \times 11.67H$. Reynolds number based on bump height is 10 times less than the experimental case.

They reported mean velocities, TKE at the center plane and several wake planes and the skin friction line on the bump surface. In general, they show poor agreement with experimental data at a different Reynolds number. The skin friction lines on the bump surface show the saddle separation along the centerline and only one focus separation on each side which is consistent with experiment. However, there is the attachment line between two separation lines. In the calculation of the stream-wise velocity contours across the center plane ($z/H = 0$), the huge mean backflow region appears downstream and it is up to about $x/H \approx 3$. For the streamlines of secondary vectors at wake planes, only one pair of stream-wise vortices appears but its rotating direction is opposite to experiment, upwashing near the center.

The other interesting reference is the Reynolds-averaged Navier-Stokes (RANS) method using five different non-linear anisotropy eddy viscosity and second-moment closure models (Wang et al., 2004). The turbulent kinetic energy (TKE) and the dissipation rate (ε) or the specific dissipation ($\omega = \varepsilon/\text{TKE}$) are used for the characteristic velocity and the length scale, respectively. The turbulent kinetic energy and the dissipation are obtained by solving two transport equations. So, this is a two-equation model.

For the RANS calculation, no-slip condition at the lower and upper wall and slip condition at side walls are applied, which result in $110 \times 105 \times 80$ grid resolution with the wall nearest nodes

lying within $y^+ < 1$. The computational domain is about $11.5H \times 3.4H \times 11H$. The Reynolds number based on bump height is same as an experimental case.

They reported mean velocities, $1/S$ parameter, skin friction velocity, TKE at $x/H = 3.63$ wake plane and pressure distributions and skin friction lines on the bump surface. They got good agreement with experimental data qualitatively on the bump surface but poor agreement at the wake plane. For the mean stream-wise velocity \bar{U} and TKE normalized by U_{ref} at $x/H = 3.63$, the \bar{U} has a poor agreement with experiment especially near the centerline and TKE seems worse. Furthermore, in the secondary flow streamlines at $x/H = 3.63$ plane, there are two counter-rotating stream-wise vortices at one side. Near the centerline, the upwashing vortex appears like the LES calculation done by Temmerman et al. (2004). This makes skin friction velocities near the center much lower than experimental values. However, it is very interesting that the prediction of skin friction lines on the bump leeside is one of the most consistent with experimental data having one saddle separation along the centerline and one strong focus separation on each side although the saddle separation appears farther upstream than experimental data. Unfortunately, they did not report any flow patterns above the leeside bump surface. They predict C_p well along the centerline.

Tessicini et al. (2005) reported their latest effort to apply the combined LES and RANS as well as LES schemes for the separated flow around a 3-D bump. For the combined LES-RANS, they used the zonal two-layer approach in order to reduce the requirement of finer grid for high Reynolds number LES scheme. As shown in Fig. 6.9, for a very near the wall layer, an algebraic law of the wall model or the solution of TBL differential equations provide the wall shear stress to the outer LES region. The eddy viscosity is calculated by a mixing length model with a wall damping function. The computational domain is $16H \times 3.205H \times 11.67H$ under the almost same Reynolds number as experiments. The LES computation uses $448 \times 112 \times 192$ grid with classical and dynamic Smagorinsky models. This grid is not sufficient for a near wall region and the closest node to the wall is located at $y^+ \approx 5 \sim 10$. For the combined computation, the $192 \times 96 \times 192$ grid is used with a dynamic Smagorinsky model for LES region. The closest node to the wall in LES region is located at $y^+ \approx 20 \sim 40$. Therefore, the CPU time is saved about 80 %.

Their C_p prediction along the bump centerline agrees well with the measurement. The most interesting and surprising results are the mean velocity vectors across the centerline and the streamline patterns on the leeside near wall plane as shown in Fig. 6.10 and 6.11, respectively. The LES with dynamic Smagorinsky model and the combined computations capture the thin mean

backflow layer downstream of separation along the centerline and the saddle-focus structure on the leeside. Although the two-layer zonal approach shows a little thicker backflow layer and the separation farther upstream along the centerline than experimental data, these are much improved from their previous studies. These predictions might be the best for the leeside surface of bump among the published works so far.

6.4 Prof. Davidson Group

The last reference is a hybrid LES-RANS method with an isotropy eddy viscosity model by Davidson and Dahlström (2004). The turbulent kinetic energy is used for the characteristic velocity in both LES and unsteady RANS (URANS) region. The turbulent kinetic energy is obtained by solving a transport equation. So, this is a one-equation model. The characteristic lengths are taken as being proportional to the distance from the nearest wall in URANS region and as the filter width in the LES region, respectively. Channel flow DNS fluctuations ($Re_\tau = 500$) are taken as momentum sources in the cell in the LES region adjacent to URANS region. The boundary or matching plane between LES and URANS is located in the inner log-region.

Figure 6.12 shows the computational domain for the hybrid LES-RANS calculation. The no-slip condition at the lower and upper wall and slip condition at side walls are applied, which result $162 \times 82 \times 130$ grid resolution. The computational domain is $19.8H \times 3.2H \times 11.7H$. Reynolds number based on bump height is same as a experimental case.

They reported mean velocities, TKE at $x/H = 3.63$ wake plane and pressure distributions and velocity vectors on the bump surface. This simulation seems very good because they got good agreement with experimental data qualitatively on the bump surface, as well as at the wake plane. Figure 6.13 and 6.14 show the mean velocity \bar{U} and \bar{W} normalized by U_{in} which is the velocity at channel inlet at $x/H = 3.63$ plane, respectively. They show excellent agreement with experimental data. Figure 6.15 shows secondary flow vectors at the same wake plane. It is consistent with the experimental results too. They also show the mean velocity vector field at the center plane in Fig. 6.16. The flow separated at $x/H \approx 1$ and reattached at $x/H \approx 2$ generating the mean backflow regions. Figure 6.17 shows the direction of the flow at the leeside bump surface. Although it is not clear, a saddle separation appears at $x/H \approx 1$ and a nodal reattachment at $x/H \approx 2$ along the centerline. There

are two more saddle separation at $x/H \approx 2$ and $z/H \approx \pm 0.5$ where the measurement was not possible. To satisfy the kinematical rule, there must be two foci separations at $x/H \approx 1$ and $z/H \approx \pm 0.5$ even though they are weaker than measured focus. The TKE normalized by U_{in} in Fig. 6.18 and C_p along the centerline in Fig. 6.19 agree well with measured quantities.

6.5 Summary

Although all CFD results mentioned above show some agreement with measured data, their models still seem to need to be improved. There are no models which can predict the entire flow field from around the bump and the wake region properly. For example, Prof. Leschziner et al. RANS calculation shows good agreement of the skin friction lines on the bump surface. It shows, however, totally different flow structures at the wake plane from experimental data even though this model is a complicated, anisotropy non-linear eddy viscosity, second-moment closure and two-equation model. The RANS models are not proper to discover the flow physics and dynamics related to large scale turbulent motions which are dominant on the leeside of bump.

In spite of their simplicity and contributions to the simulation of practical flows, zero- and one-equation model are not complete due to the deficiency of the turbulent length scale. An isotropy eddy viscosity model generally seems to be not proper for curvature effects and non-local and history effects on Reynolds stresses anisotropies. Basically, this incompleteness comes from the Reynolds stress tensor and eddy viscosity hypothesis, which is the linear relation of velocity gradients. Therefore, higher moment closure anisotropy turbulence models might be necessary. All models and schemes discussed here seem to fail to calculate Reynolds shear stresses even though they can fairly capture the mean flow features around a 3-D bump.

In order to improve the LES calculation, the integral time scale may be longer enough to represent the large scale low frequency turbulent motion. Even though it increases directly the computational cost, this motion is one of the key features of the flow dynamics of bump leeside which is presented in LDV and hot-wire anemometer (Ma and Simpson, 2005) measurements. Ma and Simpson (2005) suggested that the contribution of low frequency less than 34 Hz are dominant.

However, all CFD efforts to calculate the separated flow on the curved surface have progressed. The hybrid LES-RANS and zonal LES/RANS models show very good possibility to get

rid of the requirement of finer mesh near the wall for LES, even though there are some arguments about the schemes to match RANS and LES region because it plays a very important roles to final results.

Finally, the LES seems to be able to capture mean velocity fields better downstream where large scale eddies detaching from the bump are dominant. However, RANS with properly defined wall functions near the wall seems to work well very near surface regions, although RANS results farther from the surface are questionable. That might be why the hybrid LES-URANS and zonal modeling schemes are appropriate and should be further developed.

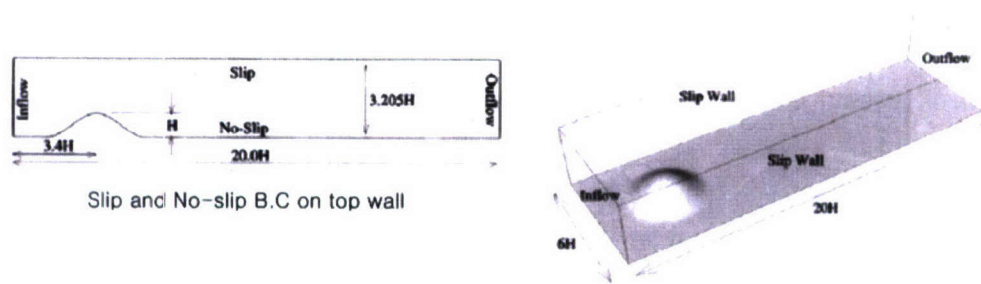
Table 6.1 Simulation methods.

	Prof. Menon	Prof. Davidson
	LES	Hybrid LES-RANS
	Patel et al. (2003) and Menon et al. (2005)	Davidson and Dahlström (2004)
Reynolds Number based on H	Same as experiment	Same as experiment
Closure	Eddy viscosity TKE transport equation (LDKM)	Eddy viscosity TKE transport Equation
Grid Resolution	Slip-ceiling $256 \times 128 \times 128$ Non-slip ceiling $1926 \times 184 \times 144$ Min. $y^+ \approx 4$	$162 \times 82 \times 130$ Min. y^+ for LES ≈ 4
Other Applications	Turbulent plane couette flows Turbulent recirculating flows Weakly separated 2DTBL	Channel flows Asymmetric plane diffuser
Good Results	C_p on bump surface One pair of mean stream-wise vortices at wake plane	C_p on bump surface Mean velocity vectors near bump surface One pair of mean stream-wise vortices at wake plane

LDKM : Localized Dynamic K-equation Model(Menon et al., 2004)

Table 6.1 Continued.

Prof. Leschziner				
	LES Temmerman et al. (2004)	LES Tessicini et al. (2005)	RANS Wang et al. (2004)	Combined LES-RANS Tessicini et al. (2005)
Reynolds Number based on H	10 times less than experiment	Same as experiment	Same as experiment	Same as experiment
Closure	Classical Smagorinsky model	Classical and Dynamic Smagorinsky model	Nonlinear eddy viscosity k- ω or k- ϵ Transport equations	Eddy viscosity TBL equation Log-law wall function Two-layer zonal
Grid Resolution	192 \times 96 \times 192	448 \times 112 \times 192 Min. $y^+ \approx 5 \sim 10$	110 \times 105 \times 80 Min. $y^+ \approx 1$	192 \times 96 \times 192 Min. y^+ for LES $\approx 20 \sim 40$
Other Applications		Hydrofoil	2D periodic hills	Hydrofoil
Good Results		C_p on bump surface Mean velocity vectors near bump surface and across the center plane	C_p on bump surface Skin friction lines on bump surface	C_p on bump surface Mean velocity vectors near bump surface and across the center plane



Slip top wall : $20H \times 3.205H \times 6H$
 Non-slip top wall : $12H \times 3.205H \times 10H$

Figure 6.1 Computational domain for Patel et al. (2003) LES.^{§§}

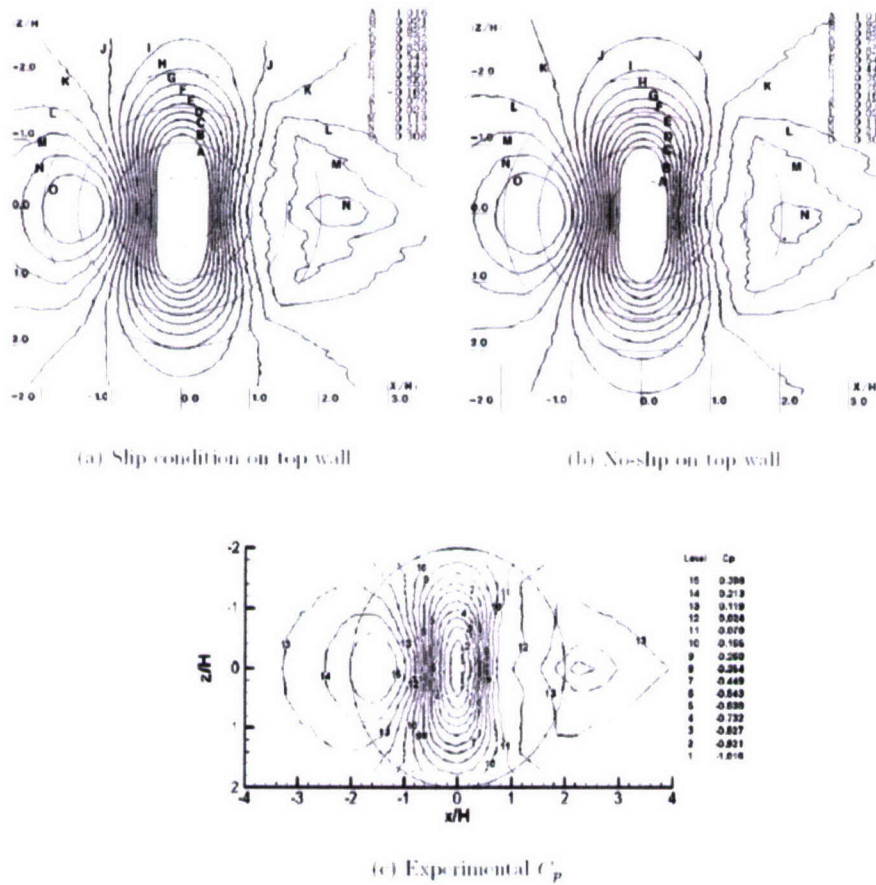


Figure 6.2 C_p on bump surface from Patel et al. (2003) LES.

^{§§} All plots in this chapter are reprinted with permission of original authors.

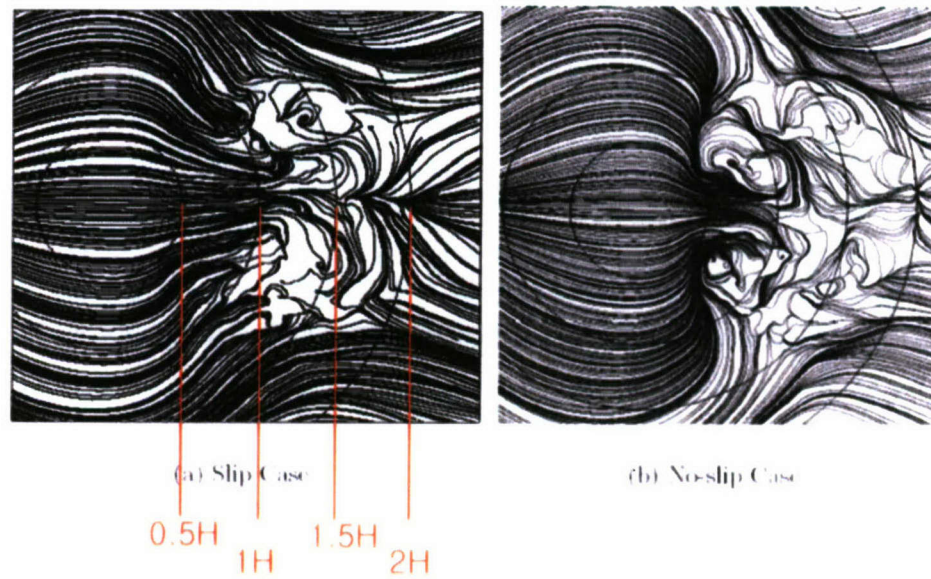


Figure 6.3 Mean streamline patterns at $y^+ = 8.63$ over the bump surface from Patel et al. (2003) LES.

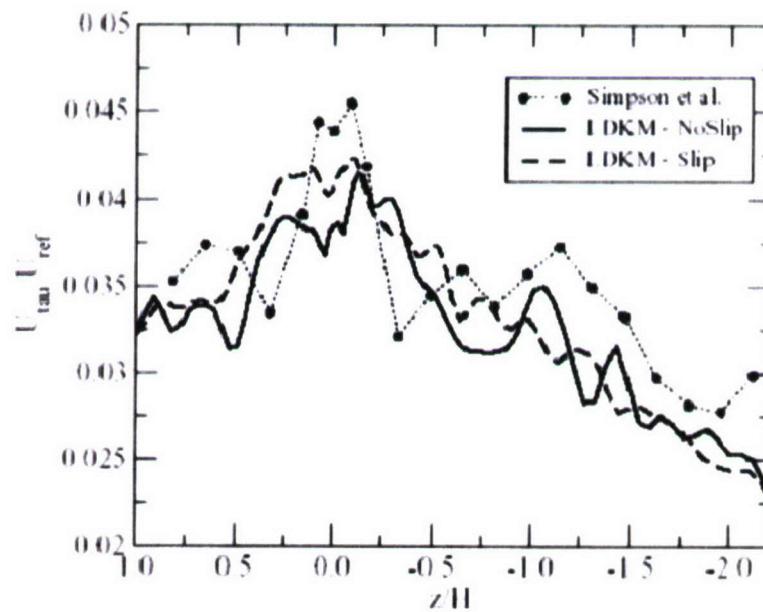
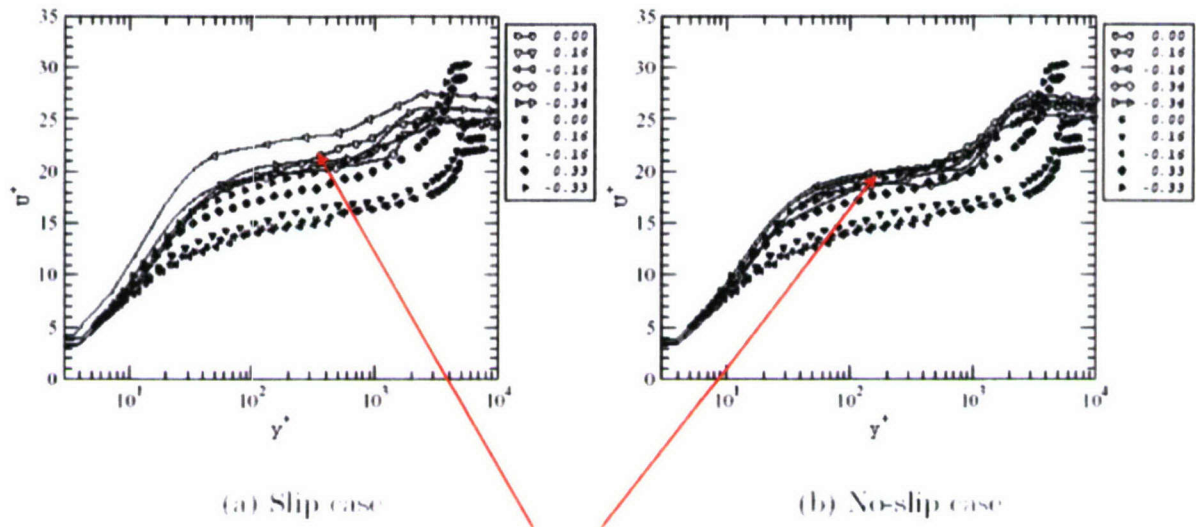


Figure 6.4 Skin friction velocity at $x/H=3.63$ from Patel et al. (2003) LES.



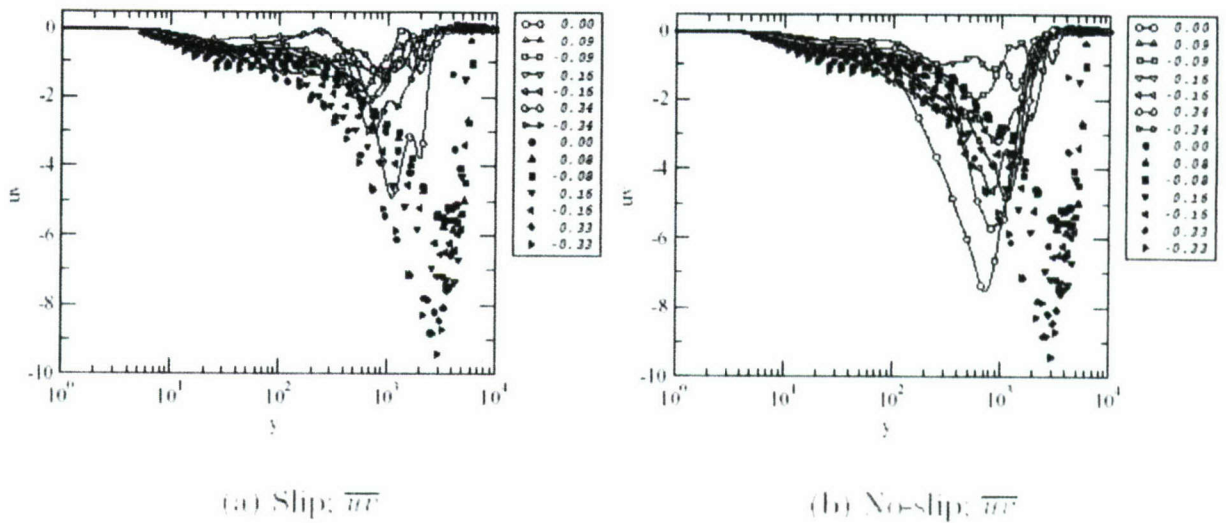


Figure 6.7 \overline{uv}^+ at $x/H=3.63$ from Patel et al. (2003) LES.

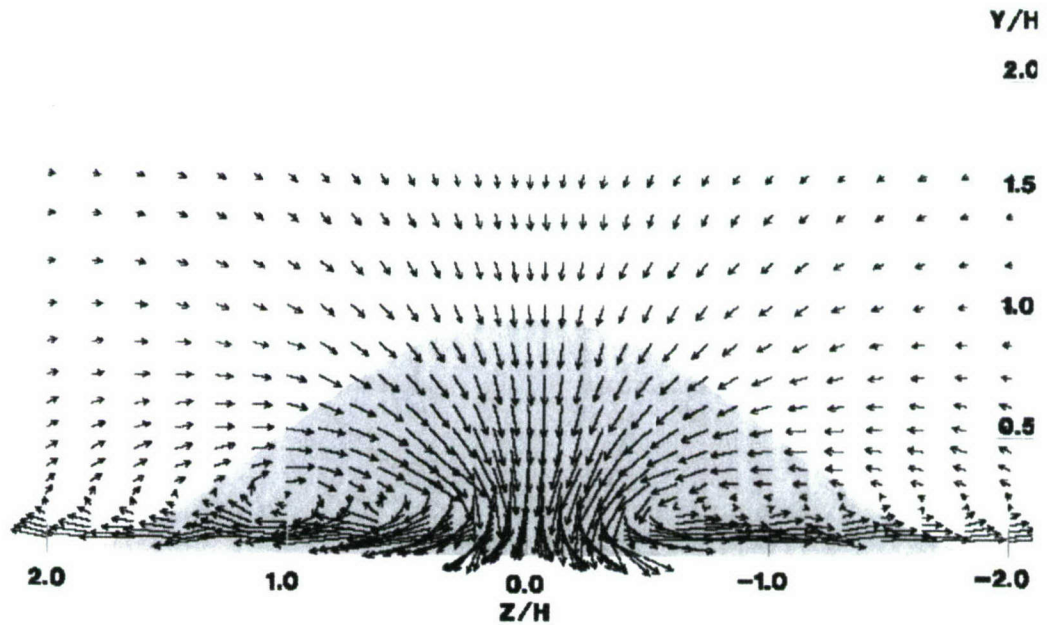


Figure 6.8 Secondary flow vectors at $x/H=3.63$ from Menon et al. (2004) LES.

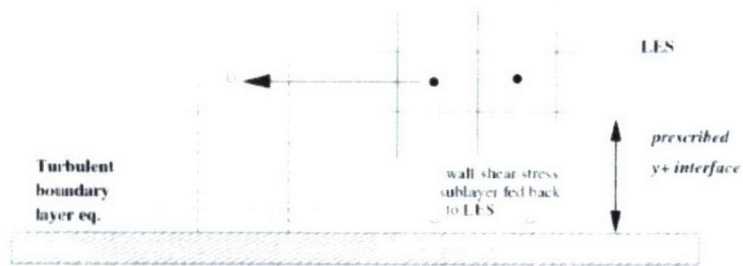
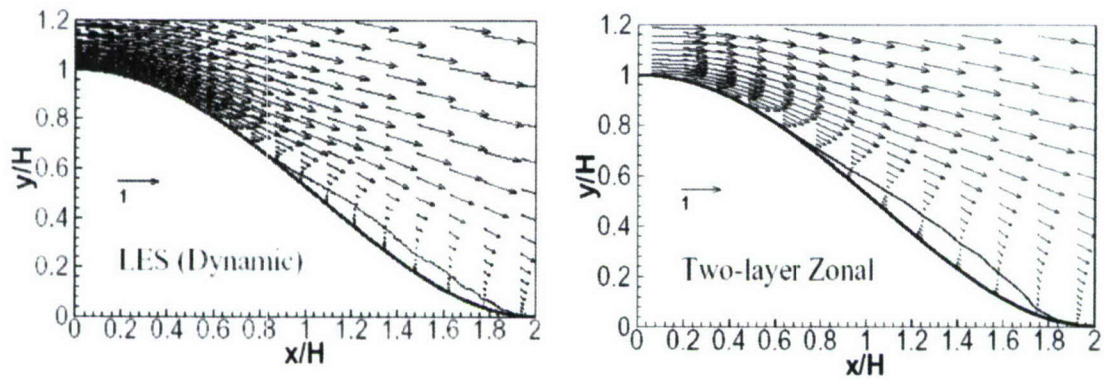


Figure 6.9 Two-layer zonal model of Tessicini et al. (2005).



Lines for $\bar{U} = 0$. Refer to Fig. 5.2(b) for another combined LES-RANS computation.

Figure 6.10 Mean velocity vectors across the center plane from Tessicini et al. (2005).

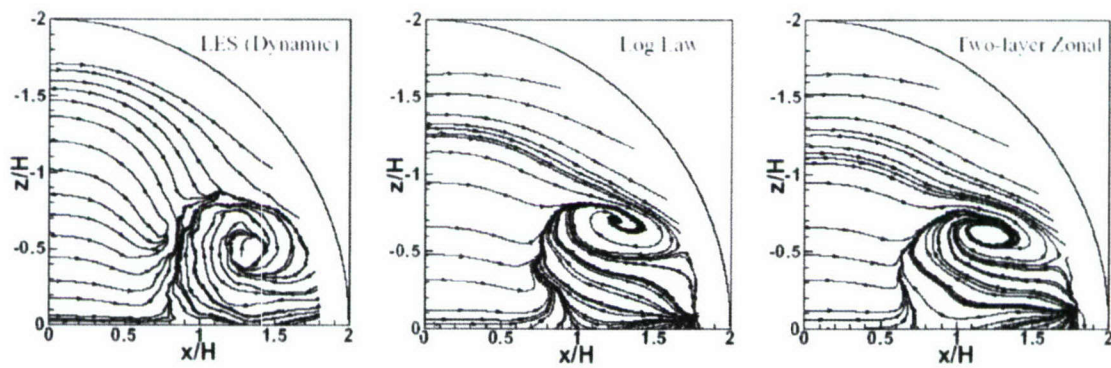


Figure 6.11 Streamline patterns of the closest wall plane from Tessicini et al. (2005).

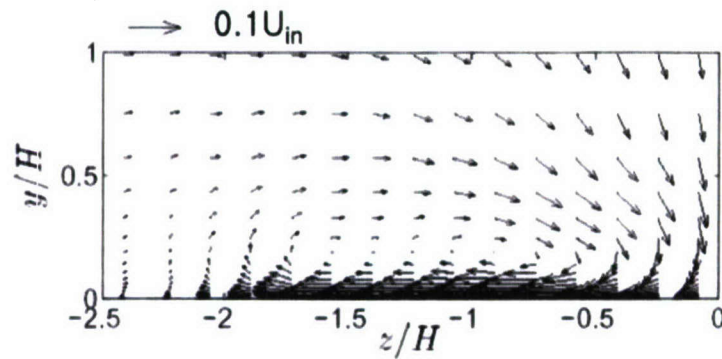


Figure 6.15 Secondary flow vectors at $x/H=3.63$ from Davidson's Hybrid LES-RANS (2005).

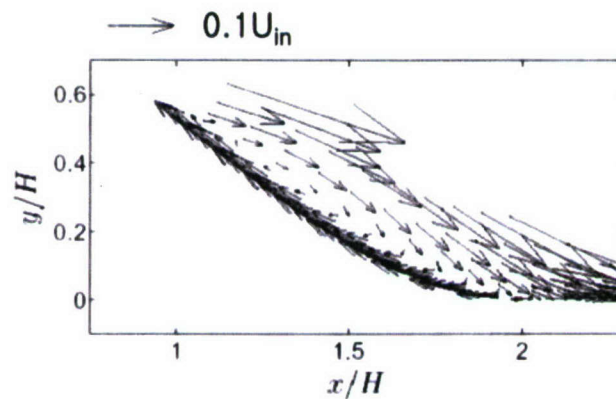


Figure 6.16 Vector fields in the center plane from Davidson's Hybrid LES-RANS (2005).

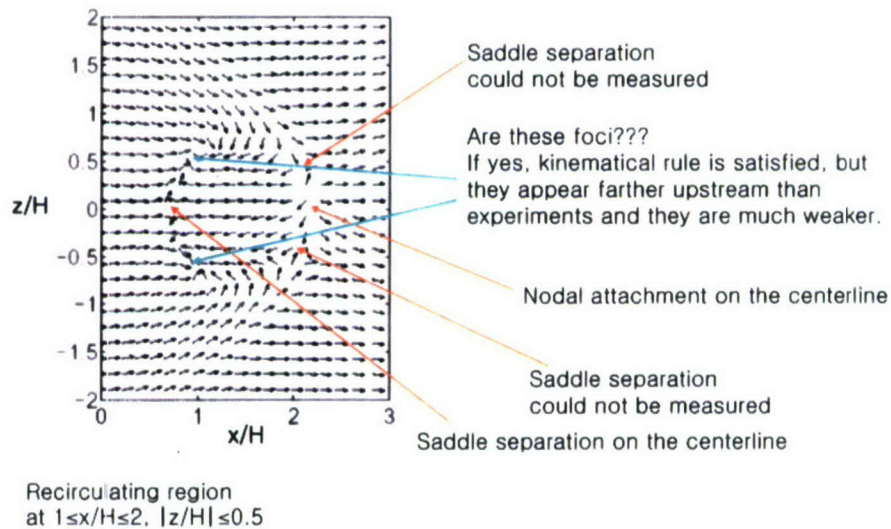


Figure 6.17 The direction of the flow at the wall from Davidson's Hybrid LES-RANS(2005).

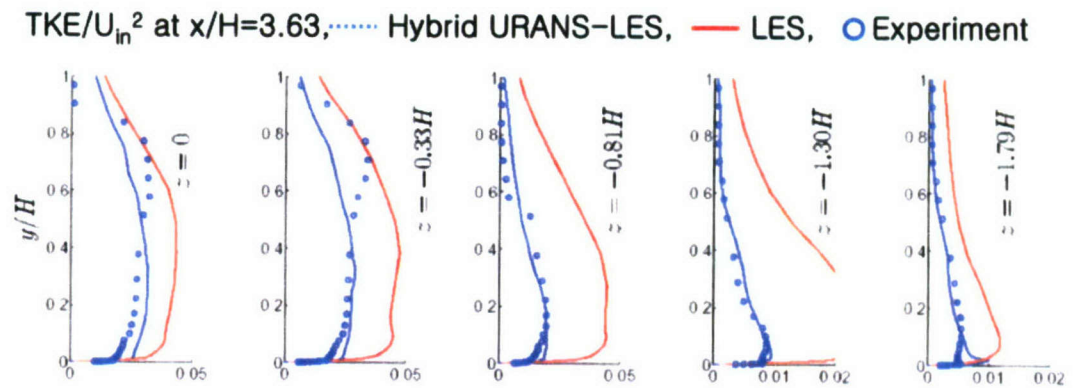


Figure 6.18 TKE/ U_{in}^2 at $x/H=3.63$ from Davidson's Hybrid LES-RANS (2005).

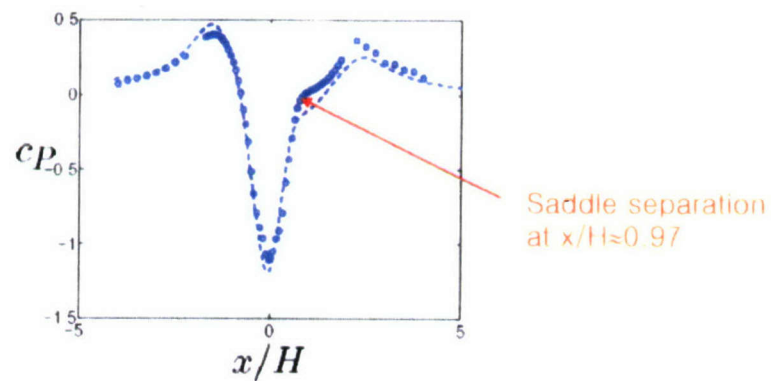


Figure 6.19 C_p along the centerline from Davidson's Hybrid LES-RANS (2005).

7

Conclusions

This research program was motivated in order to understand the flow structure and associated physics of separated flow around a 3-D curved body which is of interest in practical engineering applications and to provide a benchmark for researchers who have been challenged to model this complicated flow field.

To accomplish these objectives, surface mean pressures, oil flow visualizations, and 3-velocity-component laser-Doppler velocimeter measurements were presented for turbulent boundary layers over three bumps, two axisymmetric bumps of height $H = \delta$ and 2δ and one symmetric bump of $H = 2\delta$. The mean flow appears to be closely symmetric about the centerline for each case. Vortical separations occur on the leeside and merge into two large stream-wise vortices downstream.

For the bumps #3, at the downstream measurement plane, the near-wall flow is dominated by the wall, while the vortices in the outer region produce large turbulence levels near the centerline and appear to have low frequency motions that contribute to turbulent diffusion. Bump#1, which has a different flow separation pattern showing a relatively sharper separation on the surface from the bumps #3, creates a stronger stream-wise vortex with low turbulence levels and more steadiness. Bump#1 is a much more effective vortex generator than bumps #3 for producing higher mean velocity flow near the wall.

The LDV and oilflow results of downstream of the bump are clearly consistent with one another. For each bump, the flow along the stream-wise centerline is a downwashing reattachment flow with only one mean vortex on each side of the centerline away from the wall.

For large bump#3, the secondary flows are almost the same as the measurement results reported by Willits and Boger (1999), Pisterman (2004) and Ma and Simpson (2005) for the same shape bump with the same $\delta/H=1/2$. These independent sets of results do not support the computational results for this geometry and flow from several different research groups using several 1 or 2-equation turbulence models in steady Reynolds-averaged Navier-Stokes (RANS) codes. The $k-\omega$ model has been observed to improve calculations for mean 2-D separating flows (Simpson, 1996). When used to compute this bump flow, however, a separation is calculated along the centerline and 2 stream-wise mean vortices are produced on each side of the centerline. These current LDV results indicate that this $k-\omega$ turbulence model in a steady RANS code does not capture the important physics of this separating vortical 3-D flow. The diffusion and merger of the leeside separations into the observed downstream structure needs to be better modeled. The low frequency chaotic meandering of the shed vortex structure for the bumps #3 probably needs to be included since this would increase the time-averaged diffusion. Perhaps an unsteady RANS code or LES will capture this unsteadiness. Therefore, more detailed 3-velocity-component LDV measurements closer to the wall and around the locations of the separations are needed to understand the dynamics and physical processes associated with 3-D separations on the leeside.

For greater understanding the flow physics and dynamics associated with 3-D separations on a 3-D curved surface, LDV measurements were obtained on half of the leeside of an axisymmetric bump, large bump#3, in a turbulent boundary layer. The ratio of bump height, H and boundary layer thickness, δ is $H/\delta = 2$. Three-dimensional (3-D) separations occur on the leeside with one saddle separation on the centerline that is connected with a separation line to one focus separation on each side. Downstream of the saddle point the mean backflow converges to the focal separation points in a thin region confined within about 0.15δ from the local bump surface. The mean backflow zone is supplied by the intermittent large eddies as well as by the near surface flow from the side of the bump. The separated flow has a higher turbulent kinetic energy and shows bimodal histograms in local U_L and W_L , which appear to be due to highly unsteady motions. By the mode averaged analysis of bimodal histograms, highly unsteady flow structures are estimated and unsteady 3-D separations seem to be occurring in wide range on the bump leeside. The process of these separations has very complex dynamics having intermittent large portions of attached and detached flow varying in time. These bimodal features with highly correlated u_L and w_L fluctuating motions

are the major source of large Reynolds stresses $\overline{u_l^2}$, $\overline{w_l^2}$ and $-\overline{uw_l}$. Because of the variation of the mean flow angle in the separation zones, the turbulent flow from different directions is decorrelated, resulting in lower shearing stresses. Farther from the wall, large stream-wise vortices form from flow around the sides of the bump.

Beside presented LDV data, the flow structures around 3-D bumps have been investigated intensely by Pisterman (2004), Long (2005) and Ma and Simpson (2005). All these experimental results and data sets from upstream inflow to downstream of bump have been provided to CFD researchers who have been trying to model and simulate a separated flow around a 3-D curved surface. This is one of the major contributions of this research program. Even though several simulations have been able to predict the key features of mean flow patterns in the leeside, they have to include the effect of low frequency turbulent motions on the turbulent quantities.

As mentioned earlier, the LDV measurements show only one saddle and two foci mean separation points on the bump surface. It is expected that there is an attachment point on the centerline downstream. If this attachment point is nodal, as suggested by the oilflow visualizations, then 2 saddle separation points must be present downstream in order to satisfy the kinematical rules. However, if there is a saddle reattachment point along the centerline, as suggested by the CFD calculations, then no additional separation points are needed to satisfy the kinematics. Therefore, to get complete flow features over this bump, measurements are needed for this attachment and separation region downstream. The spectra measurements with an advanced LDV technique (Lowe and Simpson, 2005) and the wall pressure fluctuation measurements on the leeside of bump also might give further understand for the unsteady behaviors of attached and detached flows and the bimodal flow structure such as coherency length scales and time scales which are very important for LES computations.

References

- Ahn, S., 1986, "Unsteady Features of Turbulent Boundary Layers", MS thesis, Dept. Aerospace and Ocean Engineering, Virginia Polytechnic Inst. and State Univ., Blacksburg, VA.
- Albrecht, H.-E., Borys, M., Damaschke, N. and Tropea, C., 2003, "*Laser Doppler and Phase Doppler Measurement Techniques*", Springer, pp.396-401.
- Arya, S.P.S. and Gadiyaram, P.S., 1985, "An Experimental Study of Flow and Dispersion in the Wakes of Three-Dimensional Low Hills", *Atmospheric Environment*, Vol. 20, pp.729-740.
- Azad, R.S. and Kassab, S.Z., 1989, "New Method of Obtaining Dissipation", *Experiments in Fluids*, Vol. 7, pp.81-87.
- Bates, C.J. and Hughes, T.D., 1976, "Real-Time Statistical LDV System for the Study of a High Reynolds Number, Low Turbulence Intensity Flow", *Journal of Physics E*, Vol. 9, pp.955-958.
- Berton E., Favier D., Nsi Mba M., Maresca C. and Allain C., 2001, "Embedded LDV Measurement Methods Applied to Unsteady Flow Investigation", *Exp. Fluids*, 30, pp.102-110.
- Bradshaw, P., 1969, "Conditions for the Existence of an Inertial Subrange in Turbulent Flow", Aeronautical Research Council Report and Memoranda No. 3603.
- Bradshaw, P., Ferriss, D.H. and Atwell, N.P., 1967, "Calculation of Boundary Layer Development Using the Energy Equation", *J. Fluid Mech.*, Vol. 28, pp. 593-616.
- Byun, G., Simpson, R.L. and Long, C.H., 2003, "Study of Vortical Separation from Three-Dimensional Symmetric Bumps", AIAA-2003-0641.
- Byun, G., Simpson, R.L. and Long, C.H., 2004, "Study of Vortical Separation from Three-Dimensional Symmetric Bumps", *AIAA Journal*, Vol. 42, No. 4, pp. 754-765

-
- Byun, G. and Simpson, R.L., 2005, "Structure of Three-Dimensional Separated Flow on an Axisymmetric Bump", AIAA-2005-0113.
- Castro, I.P. and Snyder, W.H., 1982, "A Wind Tunnel Study of Dispersion from Sources Downwind of Three-Dimensional Hills", *Atmospheric Environment*, Vol. 16, pp.1869-1887.
- Cebeci, T., 1984, "Problems and Opportunities with Three-Dimensional Boundary Layers", AGARD-Rept. 719, Neuilly sur Seine, France, pp.6-35.
- Chen, H.C. and Patel, V.C., 1988, "Near-Wall Turbulence Models for Complex Flows Including Separation", *AIAA J.*, Vol. 26, No. 6, pp.641-648.
- Chesnakas C.J. and Simpson R.L., 1994, "Full Three-Dimensional Measurements of the Cross-Flow Separation Region of a 6:1 Prolate Spheroid", *Exp. Fluids*, 17, pp.68-74.
- Czarske, J., 2001, "A Miniaturized Dual-Fibre Laser-Doppler Sensor", *Meas. Sci. Technol.*, Vol. 12, pp.1191-1198.
- Davidson, L. and Dahlström, S., 2004, "Hybrid LES-RANS : An Approach to Make LES Applicable at High Reynolds Number", CHT-04-K1, Proceedings of CHT-04.
- Davidson, L. and Dahlström, S., 2005, "Hybrid LES-RANS : Computation of the Flow around a Three-Dimensional Hill", Submitted for publication, International Symposium on Engineering Turbulence Modeling and Measurements, Italy, May.
- DeGraaff, D.B and Eaton, J.K., 2000. "Reynolds-Number Scaling of the Flat-Plate Turbulent Boundary Layer", *J. Fluid Mech.*, Vol. 422, pp. 319-346.
- Delery, J.M., 1992, "Physics of Vortical Flows", *AIAA Journal*, Vol. 29, No. 5, pp. 856-876.
- Derksen, R.W. and Azad, R.S., 1983, "An Examination of Hot-Wire Length Corrections", *Physics of Fluids*, Vol. 26, No. 7, pp.1751-1754.
- Devenport, W.J. and Simpson, R.L., 1990, "Time-Dependent and Time-Averaged Turbulence Structure Near the Nose of a Wing-Body Junction", *J. Fluid Mech.*, Vol. 210, pp. 23-55.
- Eaton, J.K., 1995, "Effects of Mean Flow Three Dimensionality on Turbulent Boundary-Layer Structure", *AIAA Journal*, Vol. 33, No. 11, pp.2020-2025.

- Echols, W.H. and Young, J.W., 1963, "Studies of Portable Air-Operated Aerosol Generators", *NRL Rep. 5929*.
- Elsner, J.W., Domagala, P. and Elsner, W., 1993, "Effect of Finite Spatial Resolution of Hot-Wire Anemometry on Measurements of Turbulence Energy Dissipation", *Meas. Sci. Tech.*, Vol. 4, pp.517-523.
- Fernholz, H.H. and Finley, P.J., 1996. "Incompressible Zero-Pressure-Gradient Turbulent Boundary Layers: an Assessment of the Data", *Progress in Aerospace Science*, Vol. 32, pp.245-311.
- Fischer, M., Jovanovic, J. and Durst, F., 2000. "Near-Wall Behavior of Statistical Properties in Turbulent Flows", *International Journal of Heat and Fluid Flow*, 21, pp.471~479.
- Fraden, J., 1993, "*AIP Handbook of Modern Sensors: Physics, Designs and Applications*", American Institute of Physics, pp.37-43.
- Fureby, C., Alin, N., Wikström, N., Menon, S., Svanstedt, N. and Perrson, L., 2004, "Large-Eddy Simulation of High-Reynolds-Number Wall-Bounded Flows", *AIAA Journal*, Vol. 42, No. 3, pp. 457-468.
- George, J., Simpson, R.L., 2000, "Some Effects of Sparsely Distributed Three-Dimensional Roughness Elements on Two-Dimensional Turbulent Boundary Layers". *AIAA-2000-0915*, 38th Aerospace and Sciences Meeting and Exhibit, 14-17 Jan., Reno, NV.
- Gong, W. and Ibbetson, A., 1989, "A Wind Tunnel Study of Turbulent Flow over Model Hills", *Boundary-Layer Meteorology*, 49, pp.113-148.
- Hanson, S., 1973, "Broadening of the Measured Frequency Spectrum in a Differential Laser Anemometer due to Interference Plane Gradients", *J. Phys. D: Appl. Phys.*, Vol. 6, pp.164-171.
- Hinze, J.O., 1975, "*Turbulence*", 2nd Edition, McGraw-Hill, pp.119-123.
- Hunt, J.C.R., Abell, C.J., Peterka, J. A., Woo, H., 1978, "Kinematical Studies of the Flows around Free or Surface-Mounted Obstacles; Applying Topology to Flow Visualization", *J. Fluid Mech*, Vol. 86, No. 1, pp.179- 200.
- Hunt, J.C.R. and Snyder, W.H., 1980, "Experiments on Stable and Neutrally Stratified Flow over a Model Three-Dimensional Hill", *J. Fluid Mechanics*, Vol. 96, pp.671-704.

- Ishihara, T., Hibi, K., Oikawa, S., 1999, "A Wind Tunnel Study of Turbulent Flow over a Three-Dimensional Steep Hill", *J. Wind Eng. Ind. Aerodyn.* Vol. 83, pp.95-107.
- Jang, Y.J., Leschziner, M.A., Abe, K and Temmerman, L., 2002, "Investigation of Anisotropy-Resolving Turbulence Models by Reference to Highly-Resolved LES Data for Separated Flow", *Flow, Turbulence and Combustion*, 69, pp.161-203.
- Johnson, D.A. and King, L.S., 1985, "A New Turbulence Closure Model for Boundary Layer Flows with Strong Adverse Pressure Gradient and Separation", *AIAA J.*, Vol. 23, No. 11, pp.1684-1692.
- Kim J., Moin P. and Moser R., 1987. "Turbulence Statistics in Fully Developed Channel Flow at Low Reynolds Number". *J. Fluid Mech.* Vol. 177, pp.133-166.
- Larousse, A., Martinuzzi, R. and Tropea, C., 1991, "Flow around Surface-Mounted, Three-Dimensional Obstacle", 8th Symposium on Turbulent Shear Flows, Sept. 9-11.
- Larssen, J.V., 2005, "Large Scale Homogeneous Turbulence and Interactions with a Flat-Plate Cascade", Ph.D. dissertation, Aerospace and Ocean Engineering, Virginia Polytechnic Inst. and State Univ., Blacksburg, VA.
- Lowe K.T. and Simpson R.L., 2005, "Measurements of Velocity-Acceleration Statistics in Turbulent Boundary Layers", 4th International Symposium on Turbulence and Shear Flow Phenomena, 27-29 June, Williamsburg, VA., pp.1043-1048.
- Larousse, A., Martinuzzi, R. and Tropea, C., 1991, "Flow around Surface-Mounted, Three-Dimensional Obstacles", 8th Symposium on Turbulent Shear Flows, Sept. 9-11, Technical University of Munich.
- Long, C. H., 2005, "A Study of Vortical Separation from Symmetric Bumps", M.S. Thesis, Aerospace and Ocean Engineering, Virginia Polytechnic Inst. and State Univ., Blacksburg, VA (in progress).
- Lugt, H. J., 1996, "Introduction to Vortex Theory", Vortex flow press, pp.101-107.
- Ma, R., 2003, "Unsteady Turbulence Interaction in a Tip Leakage Flow Downstream of a Simulated Axial Compressor Rotor", Ph.D. dissertation, Aerospace and Ocean Engineering, Virginia Polytechnic Inst. and State Univ., Blacksburg, VA.

- Ma, R. and Simpson, R.L., 2005, "Characterization of Turbulent Flow Downstream of a Three-Dimensional Axisymmetric Bump", 4th International Symposium on Turbulence and Shear Flow Phenomena, 27-29 June, Williamsburg, VA., pp.1171-1176.
- Martinuzzi, R., Melling, A. and Tropea, C., 1993, "Reynolds Stress Field for the Turbulent Flow around a Surface-Mounted Cube Placed in a Channel", 9th Symposium on Turbulent Shear Flows, Aug. 16-18, Kyoto, Japan.
- Martinuzzi, R., Melling, A. and Tropea, C., 1992, "Der Wandgebundene Würfel Im Flachkanal: Zeitaufgelöste Betrachtung Der Nachlaufströmung", AG STAB Symposium, Nov. 10-12.
- McLean, C. and Camci, C., 1995, "Analysis and Quantification of a Solid-state Laser Doppler Anemometer", *AIAA Journal*, Vol. 33, No. 10, pp. 1880-1887.
- Menon, S., Kemenov, K. and Patel, N., 2004, "Two-Level Simulations of High-Reynolds Number Wall Bounded Shear Flows", CCL Report 2004-021, Georgia Tech.
- Mouaze D. and Belorgey P.M., 2001, "Internally Mounted Laser-Doppler-Anemometry System for Boundary Layer Measurement", *Exp. Fluids*, 30, pp.111-114.
- Nobach, H., 2002, "Local Time Estimation for the Slotted Correlation Function of Randomly Sampled LDA Data", *Exp. Fluids*, 32, pp. 337-345.
- Ölçmen, M.S. and Simpson, R.L., 1995a, "A 5-Velocity-Component Laser-Doppler Velocimeter for Measurements of a Three-Dimensional Turbulent Boundary Layer", *Meas. Sci. Tech.*, Vol. 6, pp.702-716.
- Ölçmen, M. S. and Simpson, R.L., 1995b, "An Experimental Study of a Three-Dimensional Pressure-Driven Turbulent Boundary Layer", *J. Fluid Mech.*, Vol. 290, pp.225-262.
- Ölçmen, M. S., Simpson, R.L., George, J., 2001, "Some Reynolds Number Effects on Two- and Three-Dimensional Turbulent Boundary Layers", *Exp. Fluids*, Vol. 31, pp.219-228.
- Pao, Y., 1965, "Structure of Turbulent Velocity and Scalar Fields at Large Wavenumbers", *Physics of Fluids*, Vol. 8, pp.1063-1073.

- Patel, N., Stone, C. and Menon, S., 2003, "Large-Eddy Simulation of Turbulent Flow Over an Axisymmetric Hill", *AIAA-2003-0967*, AIAA 41st Aerospace Science Meeting and Exhibit, 6-9, Jan., Reno, NV.
- Pearse, J.R., 1982, "Wind Flow over Conical Hills in a Simulated Atmospheric Boundary Layer", *J. Wind Eng. Ind. Aerodyn.*, 10, pp.303-313.
- Pisterman, K., 2004, "Use of a Seven-Hole Pressure Probe in Highly Turbulent Flow-Field", M.S. Thesis, Aerospace and Ocean Engineering, Virginia Polytechnic Inst. and State Univ., Blacksburg, VA.
- Pope, S.B., 2000, "*Turbulent flows*", Cambridge University Press, pp.182-263.
- Roberts, J.B. and Ajmani, D.B.S., 1986, "Spectral Analysis of Randomly Sampled Signals Using a Correlation-Based Slotting Technique", *IEEE Proceedings*, Vol. 133, pp.153-162.
- Rotta, J.C., 1962, "Turbulent Boundary Layers in Incompressible Flow", *Progress in Aeronautical Sciences*, Vol. 2, pp.70-72.
- Rotta, J.C., 1980, "On the Effect of the Pressure Strain Correlations on the Three-Dimensional Turbulent Boundary Layers", *Turbulent Shear Flows 2*, edited by F. Durst et al., Springer-Verlag, Berlin, pp.17-24.
- Saddoughi, S.G. and Veeravalli, S.V., 1994, "Local Isotropy in Turbulent Boundary Layers at High Reynolds Number", *J. Fluid Mech.* Vol. 268, pp.333-372.
- Savory, E. and Toy, N., 1986a, "The Flow Regime in the Turbulent Near Wake of a Hemisphere", *Experiments in Fluid*, 4, pp.181-188.
- Savory, E. and Toy, N., 1986b, "Hemisphere and Hemisphere-Cylinders in Turbulent Boundary Layers", *J. Wind Eng. Ind. Aerodyn.*, 23, pp.345-364.
- Savory, E. and Toy, N., 1988, "The Separated Shear Layer Associated with Hemispherical Bodies in Turbulent Boundary Layers", *J. Wind Eng. Ind. Aerodyn.*, 28, pp.291-300.
- Schetz, A.J., 1993, "*Boundary Layer Analysis*", Prentice Hall, p.249.
- Schumann, U., 1977, "Realizability of Reynolds Stress Turbulent Model", *Physics of Fluids*, Vol. 20, pp.721-725.

- Scott, D., 1979, "On Optimal and Data-Based Histograms", *Biometrika*, 66, pp.605-610.
- Shinpaugh, K.A., Simpson, R.L., Wicks, A.L., Ha, S.M. and Fleming, J.L., 1992, "Signal-Processing Techniques for Low Signal-to-Noise Ratio Laser Doppler Velocimetry Signals", *Experiments in Fluids*, 12, pp.319-328.
- Simpson, R.L., 1983, "A Model for the Backflow Mean Velocity Profile", *AIAA Journal*, Vol. 21, No. 1, pp.142-143.
- Simpson, R.L., 1989, "Turbulent Boundary Layer Separation", *Annual Review of Fluid Mechanics*, 21, pp. 205-234.
- Simpson, R.L., 1996, "Aspects of Turbulent Boundary-Layer Separation", *Prog. Aerospace Sci.* Vol. 32, pp.457-521.
- Simpson, R.L., Long, C.H. and Byun, G., 2002, "Study of Vortical Separation from an Axisymmetric Hill", *International Journal of Heat and Fluid Flow*, 23, pp. 582-591.
- Simpson, R.L., Strickland, J.H. and Barr, P.W., 1977, "Features of a Separating Turbulent Boundary Layer in the Vicinity of Separation", *J. Fluid Mech.*, Vol. 79, pp.553-594.
- Spalart P.R., 1988. "Direct Simulation of a Turbulent Boundary Layer up to $Re_\theta = 1410$ ". *J. Fluid Mech.* Vol. 187, pp.61-98.
- Speziale, C.G., 1991, "Analytical Methods for the Development of Reynolds-Stress Closures in Turbulence", *Annual Review of Fluid Mechanics*, 23, pp.107-157.
- Temmerman, L., Wang, C. and Leschziner, M.A., 2004, "A Comparative Study of Separation from a Three-Dimensional Hill Using LES and Second-Moment-Closure RANS Modeling", European Congress on Computational Methods in Applied Sciences and Engineering, July.
- Tessicini, F., Li N. and Leschziner M.A., 2005, "Zonal LES/RANS Modeling of Separated Flow around a Three-Dimensional Hill", Proc. Direct and Large Eddy Simulation 6, Poitiers, Sept.
- Tian, Q., 2003, "Some Features of Tip Gap Flow Fields of a Linear Compressor Cascade", M.S. Thesis, Aerospace and Ocean Engineering, Virginia Polytechnic Inst. and State Univ., Blacksburg, VA.

-
- Tian, Q., Simpson, R.L. and Tang, G., 2004, "Flow Visualization on the Linear Compressor Cascade Endwall Using Oilflows and Laser Doppler Anemometry", *Meas. Sci. Tech.*, Vol. 15, pp.1910-1916.
- Tobak, M. and Peake, D.J., 1982, "Topology of Three-Dimensional Separated Flows", *Annual Review of Fluid Mechanics*, 14, pp. 61-85.
- Wang, C., Jang, Y.J. and Leschziner, M.A., 2004, "Modelling Two- and Three-Dimensional Separation from Curved Surfaces with Anisotropy-Resolving Turbulence Closures", *International Journal of Heat and Fluid Flow*, 25, pp. 499-512.
- Webster, D.R., DeGraaff, D.B. and Eaton, J.K., 1996, "Turbulence Characteristics of a Boundary Layer over a Swept Bump", *J. Fluid Mech.*, Vol. 323, pp.1-22.
- Willits, S.M. and Boger, D.A., 1999, "Measured and predicted flows behind a protuberance mounted on a flat plate", Applied Research Laboratory Report, Penn State Univ., State College, PA.
- Wyngaard, J.C., 1968, "Measurement of Small-Scale Turbulence Structure with Hot-Wires", *J. Scientific Instruments*, Vol. 1, pp.1105-1108.
- Wyngaard, J.C. and Clifford, S.F., 1977, "Taylor's Hypothesis and High-Frequency Turbulence Spectra", *J. Atmospheric Sciences*, Vol. 34, No. 6, pp.922-929.

Appendix A

Uncertainties of LDV Measurements

A.1 Standard Uncertainty Analysis

Basically, an individual velocity C measured from LDV is calculated using Eq.(A.1):

$$C = \frac{f_D \lambda}{2 \sin(\theta / 2)} \quad (\text{A.1})$$

The velocity calculation is a function of Doppler frequency f_D , laser wavelength λ and beam crossing angle θ , which affect the uncertainty of a measured velocity. Therefore, the overall uncertainty in an instantaneous velocity measurement is able to be given by

$$S_C = \sqrt{\left(\frac{\partial C}{\partial f_D} S_{f_D} \right)^2 + \left(\frac{\partial C}{\partial \lambda} S_{\lambda} \right)^2 + \left(\frac{\partial C}{\partial (\theta / 2)} S_{\theta / 2} \right)^2} \quad (\text{A.2})$$

$$B_C = \sqrt{\left(\frac{\partial C}{\partial f_D} B_{f_D} \right)^2 + \left(\frac{\partial C}{\partial \lambda} B_{\lambda} \right)^2 + \left(\frac{\partial C}{\partial (\theta / 2)} B_{\theta / 2} \right)^2} \quad (\text{A.3})$$

where, S_C in Eq.(A.2) and B_C in Eq.(A.3) denote the precision and bias errors, respectively. The final uncertainty is a combination of the precision and bias errors.

$$\delta C = \sqrt{S_C^2 + B_C^2} \quad (A.4)$$

The possible uncertainty error sources (McLean and Camci, 1995) for velocity measurements are discussed in the following sections.

A.1.1 Cross Angle Measurement

The angle between two laser beams was calculated by using the dot product between the two spatial vectors. The bias error came from the measurement of beam vectors. The present measurement allowed a bias error $B_{\theta/2} \approx 1.873 \times 10^{-4}$ rad for the half angle measurement.

A.1.2 Laser Wavelength

The variation of laser wavelength might occur during the measurements even though the lasers used for the present study generate highly coherent laser beams. However, it was not able to measure this variation during the measurement. Therefore, it was assumed that the wavelength was constant during the measurement of each location, which results in a bias error B_λ of 8.83×10^{-3} nm.^{***}

A.1.3 Fringe Spacing Gradient due to Misalignment

The fringe spacing may not be uniform in the measurement probe volume because of misalignments of the beam waist. It causes a precision error of detected Doppler frequency. The fringe spacing is diverging under this situation. Hanson (1973) described the uncertainty of Doppler frequency due to misalignments. For a small crossing angle θ , the precision error S_{fD1} is

$$S_{fD1} \approx \frac{D}{R} \quad (A.5)$$

^{***} INNOVA 90 laser manual.

where, D is the measurement volume diameter and R is the wavefront curvature, respectively. The $S_{\mu 1}$ was computed to be about 1.5×10^{-3} for the present experiment.

A.1.4 Signal Processor Resolution

Another possible source of a precision error of detected Doppler frequency is due to the finite resolution of a signal processor using the fast Fourier transform algorithm. Shinsaugh et al. (1992) suggested that this error was dependent on the sampling frequency f_s and the record length N , given by Eq.(A.6).

$$S_{\mu 2} \approx 0.1 \frac{f_s}{N} \quad (\text{A.6})$$

It was calculated to be about 1.95×10^{-4} for the present experiment. Therefore, the total S_{μ} is given by $\sqrt{(S_{\mu 1})^2 + (S_{\mu 2})^2}$.

Now, the uncertainty of an instantaneous velocity measurement δC is able to be estimated by using all precision and bias errors in Eqs.(A.2), (A.3) and (A.4). It should be noted that high velocity bias, finite transit-time and instrument broadenings are negligible as mentioned in section 2.4.3. The velocity gradient broadening across the finite probe volume also is negligible as mentioned in section 4.1.1.

The C , however, is a velocity component which is normal to the fringe set. Therefore, it is necessary to transform to an orthogonal coordinate system such as tunnel coordinates or local coordinates. The three-velocity component (C_1, C_2, C_3) is transformed by Eq.(A.7):

$$\begin{bmatrix} U_1 \\ U_2 \\ U_3 \end{bmatrix} = A \begin{bmatrix} C_1 \\ C_2 \\ C_3 \end{bmatrix} = \begin{bmatrix} a_{11} & a_{12} & a_{13} \\ a_{21} & a_{22} & a_{23} \\ a_{31} & a_{32} & a_{33} \end{bmatrix} \begin{bmatrix} C_1 \\ C_2 \\ C_3 \end{bmatrix} \quad (\text{A.7})$$

where, (U_1, U_2, U_3) is the transformed three-velocity component in an orthogonal coordinate system and A is the transformation matrix. Therefore, the errors in the measured velocity components δC_i will be propagated by using the transformation matrix A . Albrecht et al. (2003) described the propagation of errors given by Eqs.(A.8) ~ (A.10) assuming the stochastic errors on different velocity components are not correlated with one another.

$$\delta \overline{U}_i \Big|_{S,B} = \frac{\partial \overline{U}_i}{\partial C_j} \delta C_j = a_{ij} \delta C_j \quad (\text{A.8})$$

$$\delta \overline{u_i u_j} \Big|_{S,B} = \overline{\delta u_i \delta u_j} = a_{ij} a_{jk} (\delta C_k)^2 \quad (\text{A.9})$$

$$\delta \overline{u_i u_j u_k} \Big|_{S,B} = \overline{\delta u_i \delta u_j \delta u_k} = a_{ij} a_{jk} a_{kl} (\delta C_l)^3 \quad (\text{A.10})$$

where, i, j, k and l are tensor indices of 1, 2, 3. The uncertainties of mean velocities, Reynolds stresses and triple products due to system and bias errors are able to be estimated by using Eqs. (A.8) ~ (A.10).

The additional uncertainty source for mean values is considered. It is due to the velocity fluctuation of turbulent flow over a significant number of integral length and time scales. It's 20 to 1 odds uncertainty, similar to that given by (Ma, 2003) is given as:

$$\delta \overline{U}_i \Big|_T = \sqrt{\frac{3.84 \overline{u_i^2}}{N_{turb}}} \quad (\text{A.11})$$

$$\delta \overline{u_i u_j} \Big|_T = \sqrt{\frac{7.68 \overline{u_i^2} \overline{u_j^2}}{N_{turb}}} \quad (\text{A.12})$$

$$\delta \overline{u_i^3} \Big|_T = \sqrt{\frac{34.56 (\overline{u_i^2})^3}{N_{turb}}} \quad (\text{A.13})$$

where, $N_{turb} = N / f_S \tau_E$ is the ratio of measuring time to integral time scale τ_E . For example, τ_E is about 1.4 ms and N_{turb} is about 50000 for a reference 2-DTBL measurement and the number of samples of 15000 ~ 30000 was taken in several minutes for most locations of wake plane and leeside measurements, which means that the measuring time over a large number of integral length and time scales is long enough to get statistically ergodic mean quantities as suggested by Bates and Hughes (1976). Therefore, the final uncertainty is taken to be a root mean square combination.

$$\delta \bar{U}_i = \sqrt{\left(\delta \bar{U}_i \Big|_{S,B} \right)^2 + \left(\delta \bar{U}_i \Big|_T \right)^2} \quad (\text{A.14})$$

A.2 Uncertainty Estimation using Measured Quantities

The other overall uncertainty was estimated using two acquired data sets and Chauvenet's criterion (Fraden, 1993) to estimate the standard deviation, σ from:

$$\frac{d_{\max}}{\sigma} = 1.15 \quad (\text{A.15})$$

where, d_{\max} is the average of the half of the differences between two data values for each quantity. The 20 to 1 odds uncertainties were calculated as $\pm 1.96 \sigma$. While this is a measure of repeatability of data, it is also related to the statistical uncertainty since all biases have been eliminated by calibration or corrections as shown in Fig. 4.1. Finally, comparing uncertainties from independent two methods, standard uncertainty analysis and uncertainty estimation using measured quantities, the larger uncertainties estimated from measured quantities are selected and shown in Table A.1 ~ A.3.

Table A.1 Uncertainties of 2-DTBL MiniLDV measurement in 20:1 odds.

\overline{U}/u_τ	± 0.27	$\overline{u^2 v}/u_\tau^3$	± 0.083
\overline{V}/u_τ	± 0.019	$\overline{u^2 w}/u_\tau^3$	± 0.063
\overline{W}/u_τ	± 0.02	$\overline{v^2 w}/u_\tau^3$	± 0.022
$\overline{u^2}/u_\tau^2$	± 0.18	$\overline{uv^2}/u_\tau^3$	± 0.046
$\overline{v^2}/u_\tau^2$	± 0.027	$\overline{uw^2}/u_\tau^3$	± 0.097
$\overline{w^2}/u_\tau^2$	± 0.072	$\overline{vw^2}/u_\tau^3$	± 0.018
\overline{uv}/u_τ^2	± 0.035	\overline{uvw}/u_τ^3	± 0.023
\overline{uw}/u_τ^2	± 0.022	$\overline{u^3}/u_\tau^3$	± 0.54
\overline{vw}/u_τ^2	± 0.013	$\overline{v^3}/u_\tau^3$	± 0.034
		$\overline{w^3}/u_\tau^3$	± 0.098

Table A.2 Uncertainties of wake plane Short and Long LDV measurements in 20:1 odds.

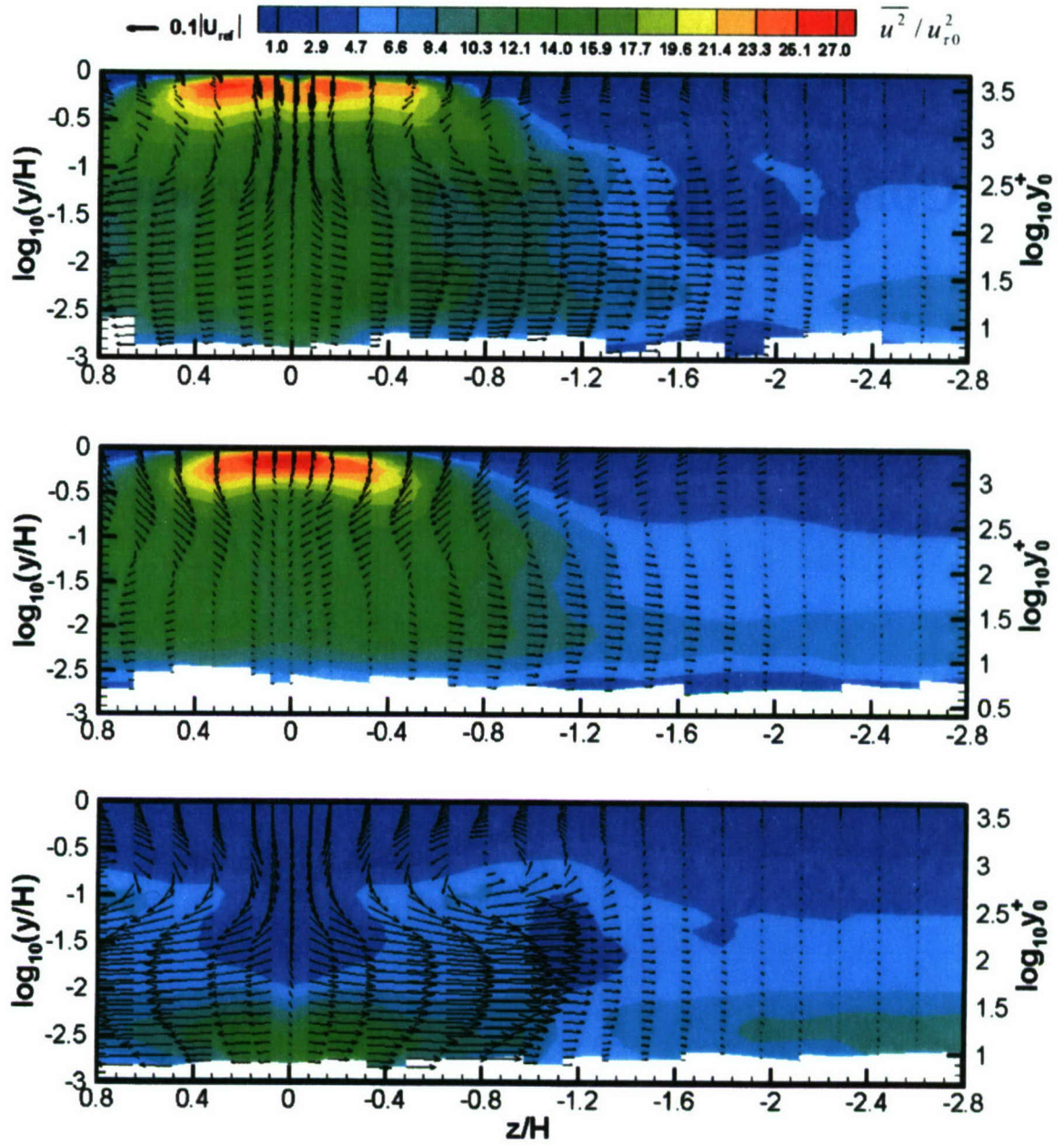
\overline{U}/u_τ	± 0.16	$\overline{u^2 v}/u_\tau^3$	± 1.15
\overline{V}/u_τ	± 0.09	$\overline{u^2 w}/u_\tau^3$	± 1.32
\overline{W}/u_τ	± 0.16	$\overline{v^2 w}/u_\tau^3$	± 1.76
$\overline{u^2}/u_\tau^2$	± 0.5	$\overline{uv^2}/u_\tau^3$	± 0.97
$\overline{v^2}/u_\tau^2$	± 0.22	$\overline{uw^2}/u_\tau^3$	± 1.44
$\overline{w^2}/u_\tau^2$	± 0.45	$\overline{vw^2}/u_\tau^3$	± 0.9
\overline{uv}/u_τ^2	± 0.17	\overline{uvw}/u_τ^3	± 0.84
\overline{uw}/u_τ^2	± 0.27	$\overline{u^3}/u_\tau^3$	± 4.35
\overline{vw}/u_τ^2	± 0.32	$\overline{v^3}/u_\tau^3$	± 1.68
		$\overline{w^3}/u_\tau^3$	± 3.28

Table A.3 Uncertainties of large bump#3 leeside MiniLDV measurements in 20:1 odds.

\overline{U} / U_{ref}	± 0.0096	$\overline{u^2 v} / U_{ref}^3$	± 0.000066
\overline{V} / U_{ref}	± 0.0046	$\overline{u^2 w} / U_{ref}^3$	± 0.000051
\overline{W} / U_{ref}	± 0.0037	$\overline{v^2 w} / U_{ref}^3$	± 0.000022
$\overline{u^2} / U_{ref}^2$	± 0.00098	$\overline{uv^2} / U_{ref}^3$	± 0.000043
$\overline{v^2} / U_{ref}^2$	± 0.00034	$\overline{uw^2} / U_{ref}^3$	± 0.00004
$\overline{w^2} / U_{ref}^2$	± 0.00069	$\overline{vw^2} / U_{ref}^3$	± 0.000024
$\overline{uv} / U_{ref}^2$	± 0.00038	$\overline{uvw} / U_{ref}^3$	± 0.000023
$\overline{uw} / U_{ref}^2$	± 0.00052	$\overline{u^3} / U_{ref}^3$	± 0.00013
$\overline{vw} / U_{ref}^2$	± 0.00024	$\overline{v^3} / U_{ref}^3$	± 0.000038
		$\overline{w^3} / U_{ref}^3$	± 0.000043

Appendix B

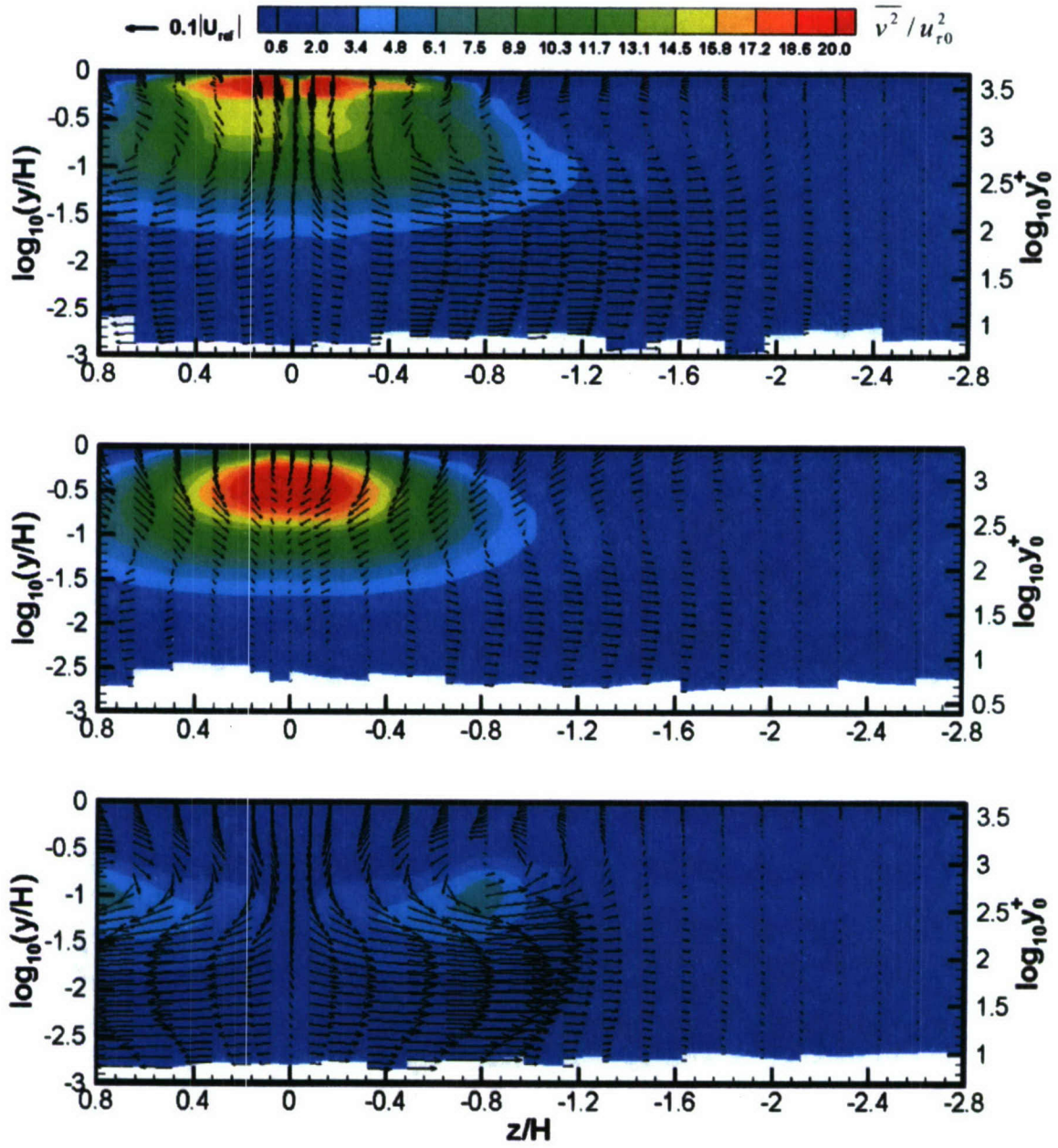
Contour Plots of Reynolds Stresses at the Wake Plane

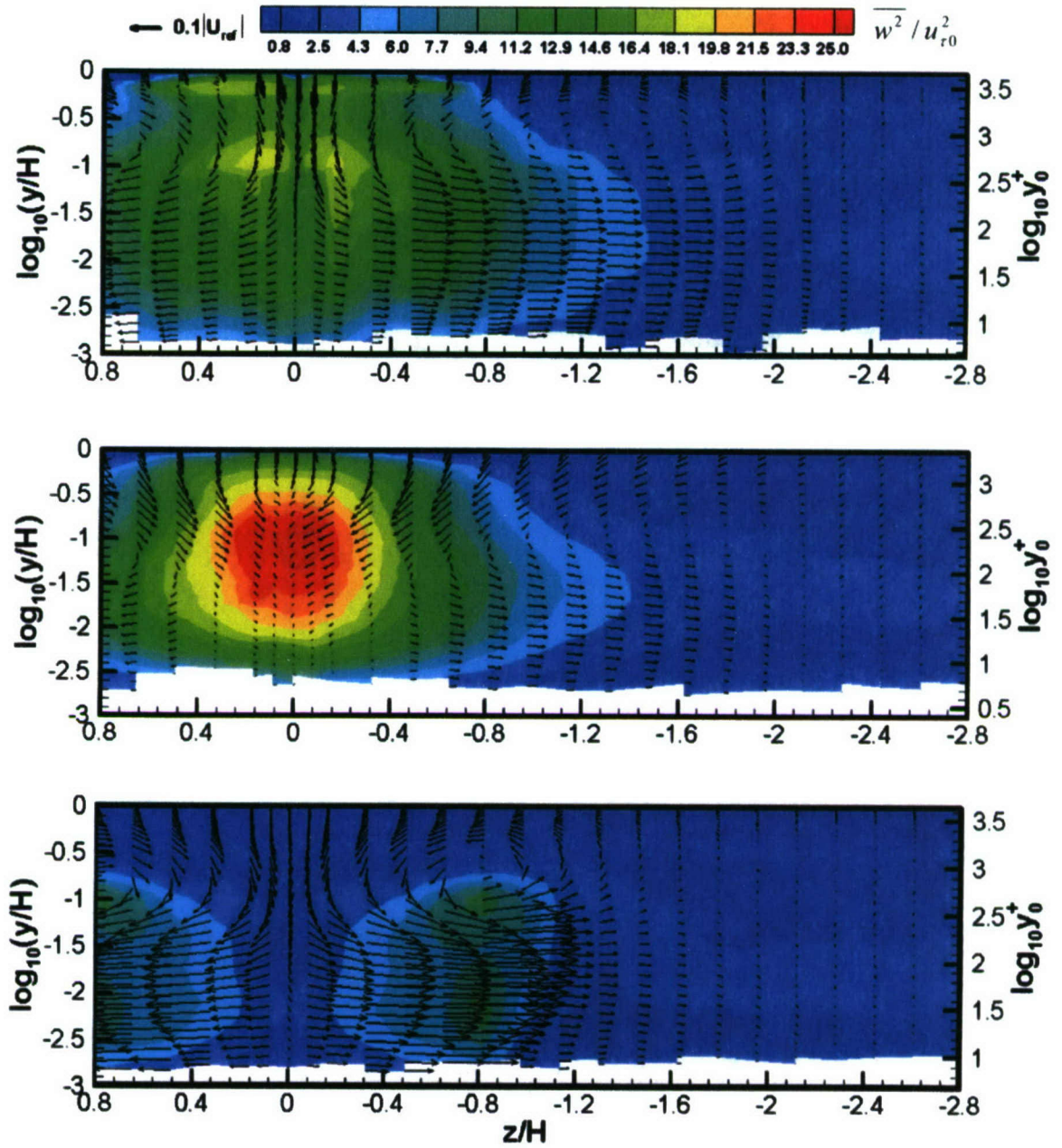


Top to bottom : large bump#3 ($x/H = 3.63$), small bump#3 ($x/H = 3.26$) and bump#1 ($x/H = 3.46$).

Vectors for \bar{V} and \bar{W} .

Figure B.1 Contour of normalized $\overline{u^2}$ at wake planes.

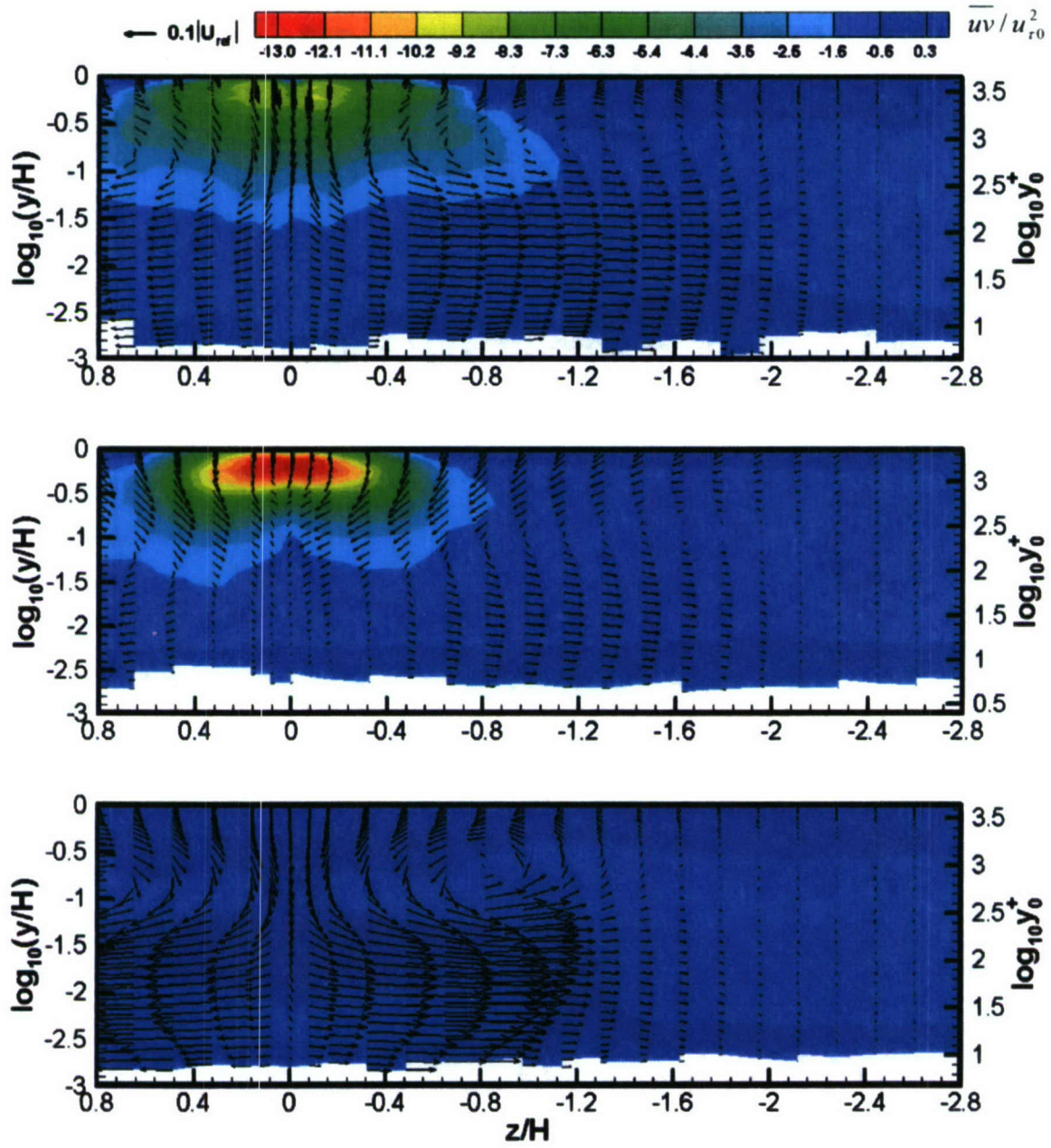
Figure B.2 Contour of normalized $\overline{v^2}$ at wake planes.



Top to bottom : large bump#3 ($x/H = 3.63$), small bump#3 ($x/H = 3.26$) and bump#1 ($x/H = 3.46$).

Vectors for \overline{V} and \overline{W} .

Figure B.3 Contour of normalized $\overline{w^2}$ at wake planes.



Top to bottom : large bump#3 ($x/H = 3.63$), small bump#3 ($x/H = 3.26$) and bump#1 ($x/H = 3.46$).

Vectors for \vec{V} and \vec{W} .

Figure B.4 Contour of normalized \overline{uv} at wake planes.

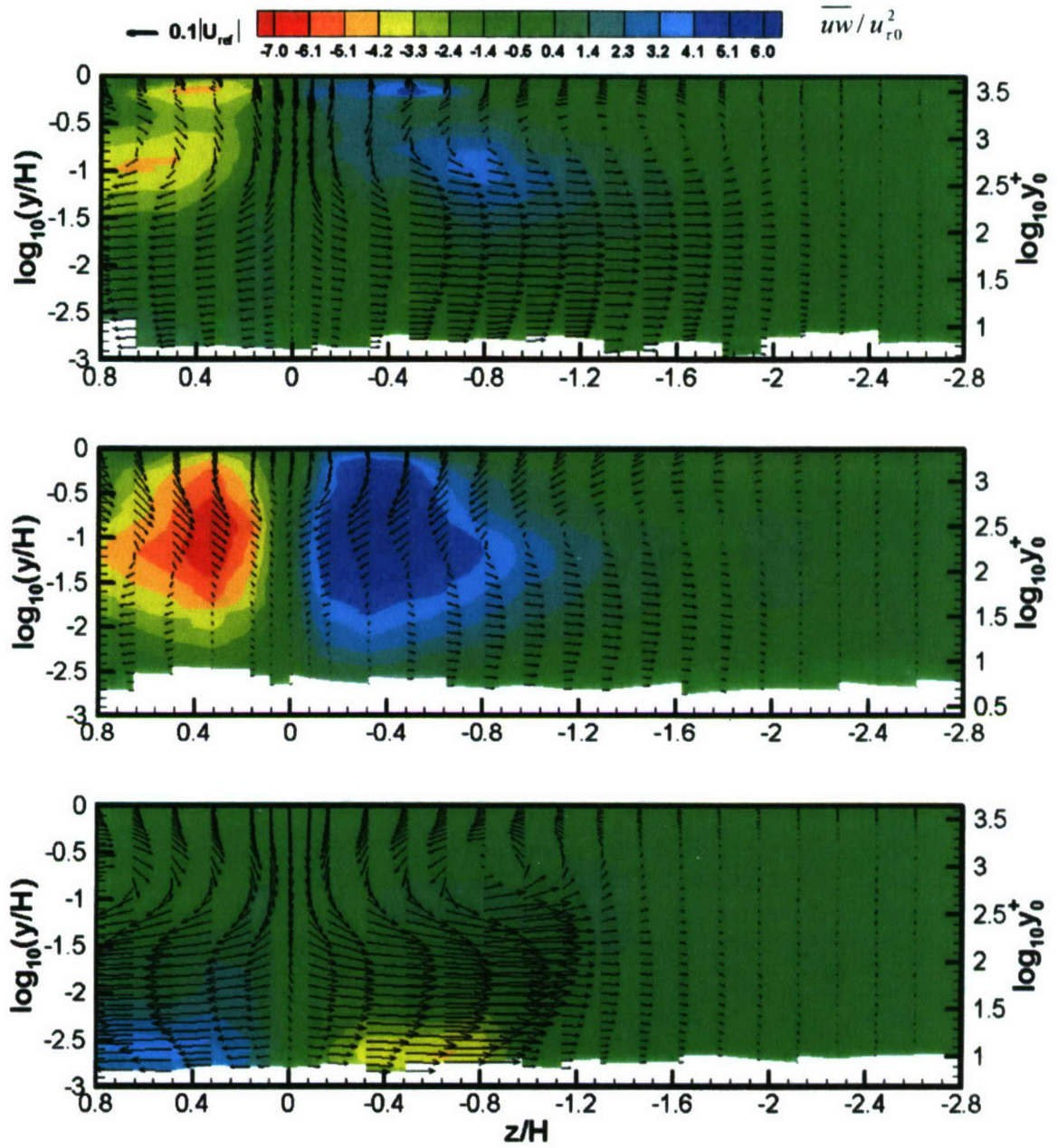
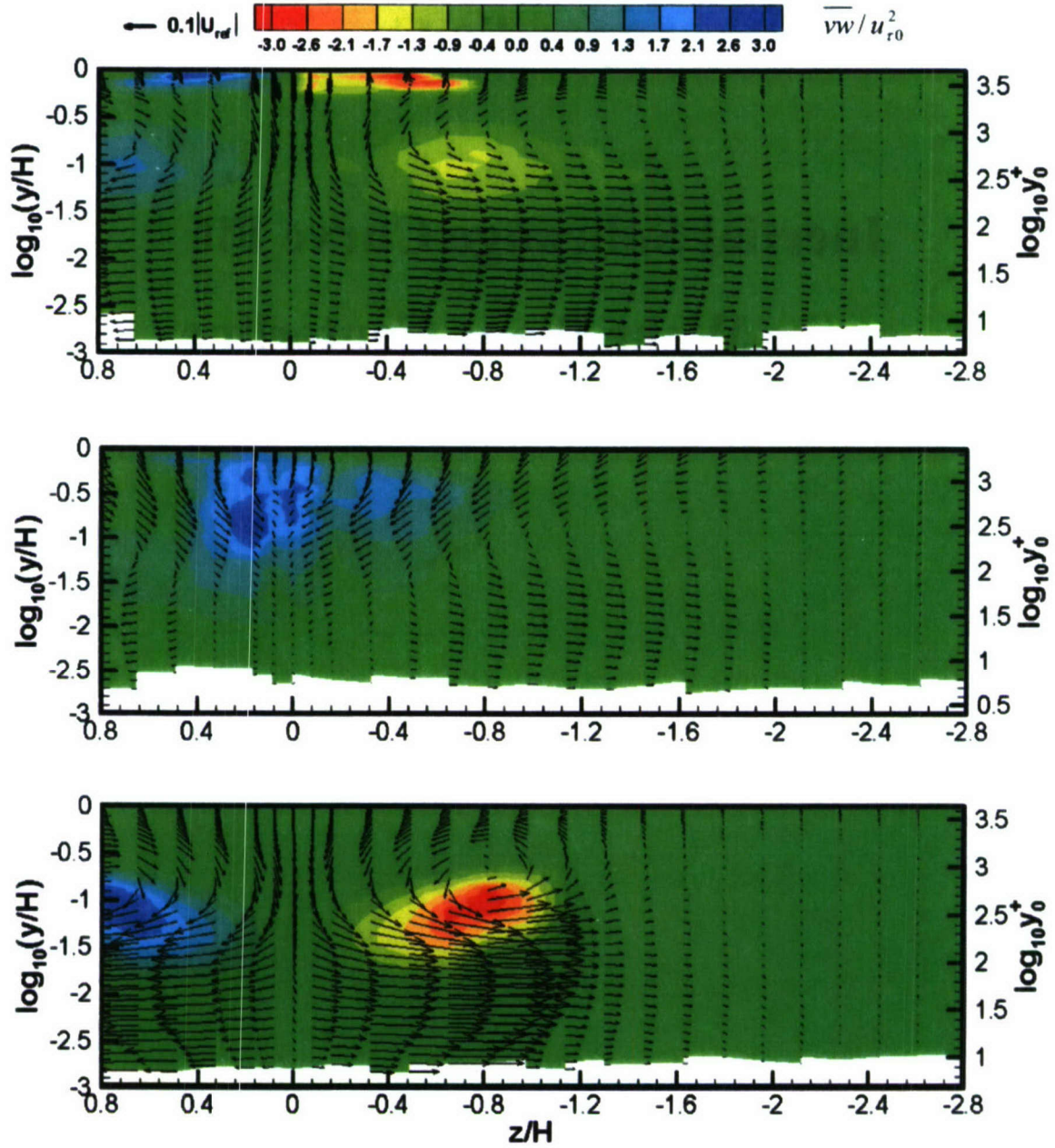
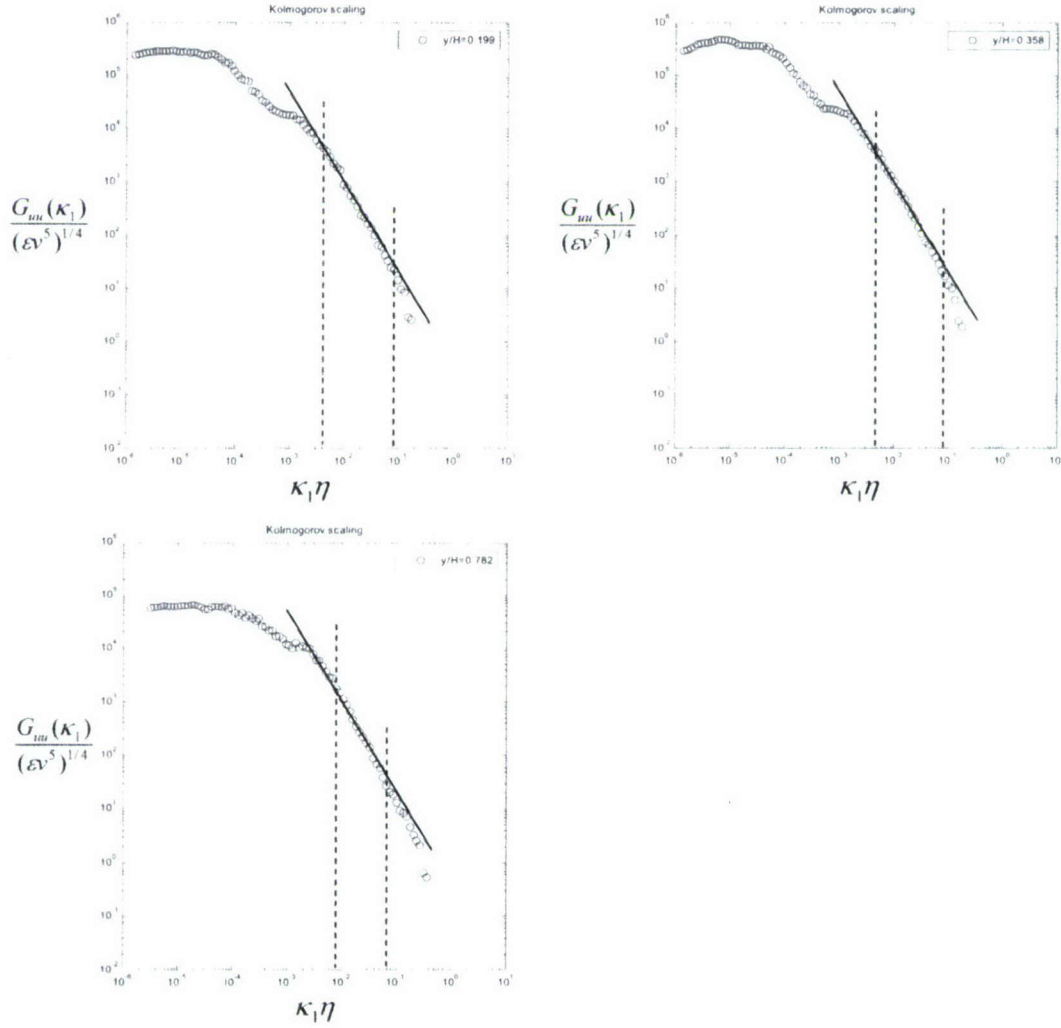


Figure B.5 Contour of normalized \overline{uw} at wake planes.

Figure B.6 Contour of normalized \overline{vw} at wake planes.

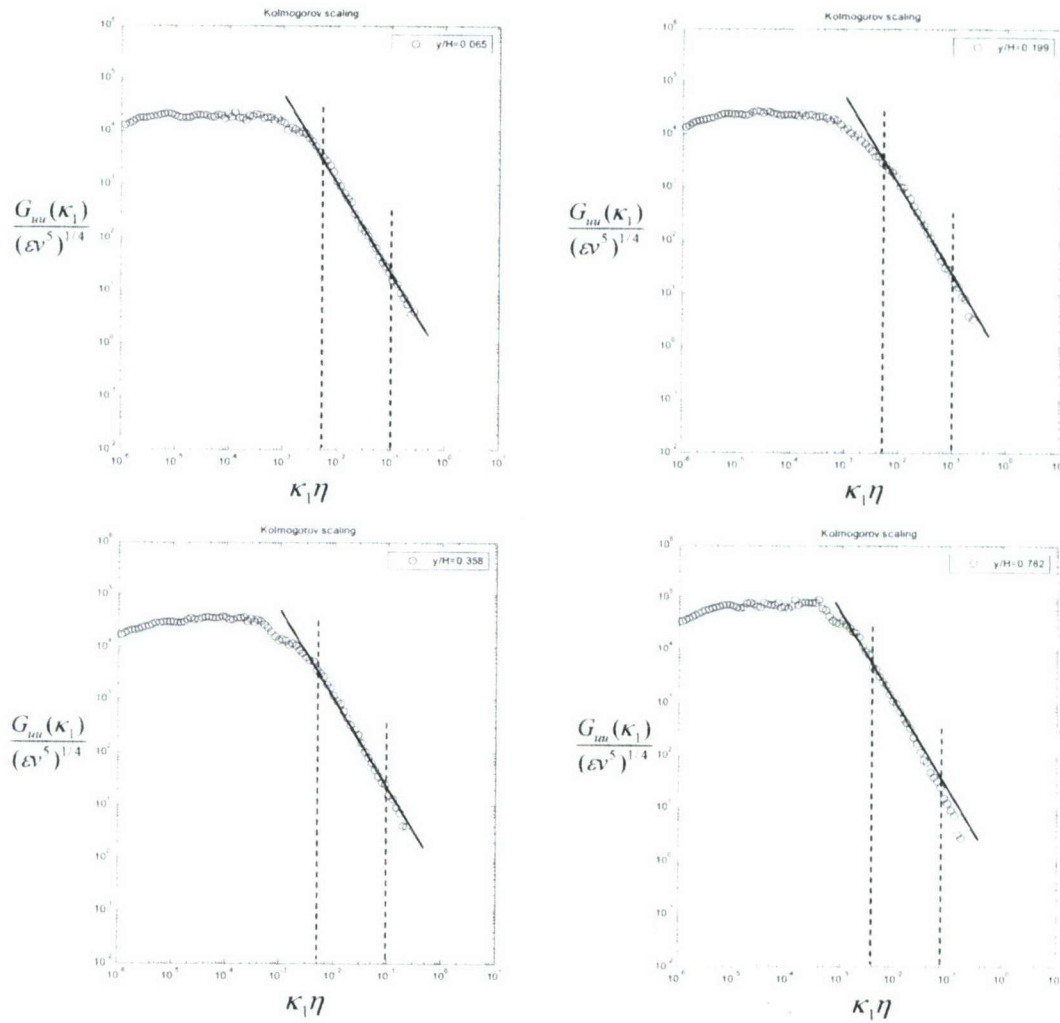
Appendix C

Inertial Subrange Curve Fit at the Wake Plane Centerline



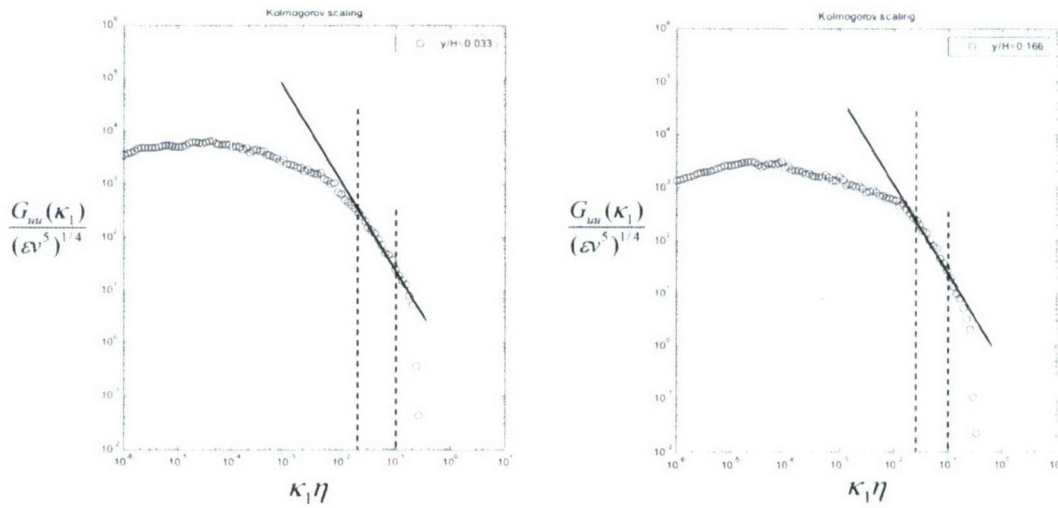
Solid line for Eq.(4.20). Dashed lines show fitting range.

Figure C.1 Curve fitting of $G_{III}(\kappa_1)$ at the wake plane centerline of large bump#3, $x/H = 3.63$.



Solid line for Eq.(4.20). Dashed lines show fitting range.

Figure C.2 Curve fitting of $G_{uu}(\kappa_1)$ at the wake plane centerline of small bump#3, $x/H = 3.26$.

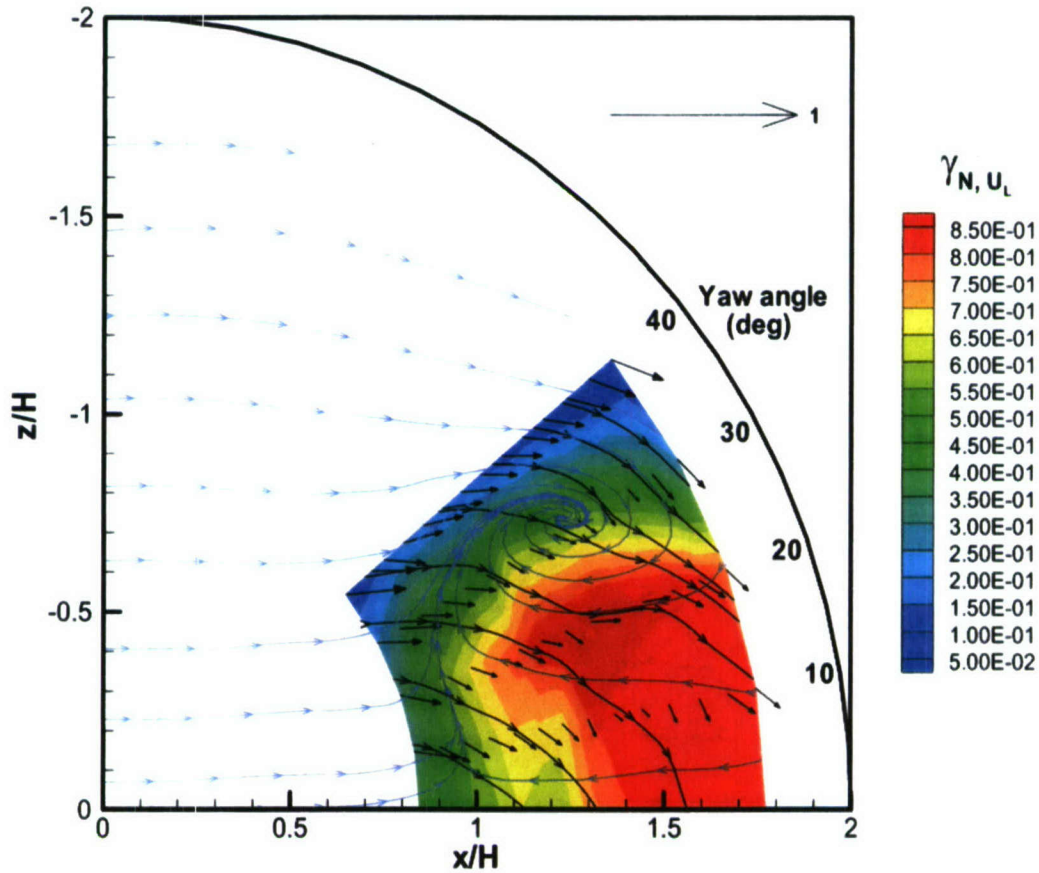


Solid line for Eq.(4.20). Dashed lines show fitting range.

Figure C.3 Curve fitting of $G_{uu}(\kappa_1)$ at the wake plane centerline of bump#1, $x/H = 3.46$.

Appendix D

Combination of Forward and Backward Modes on the Leeseide

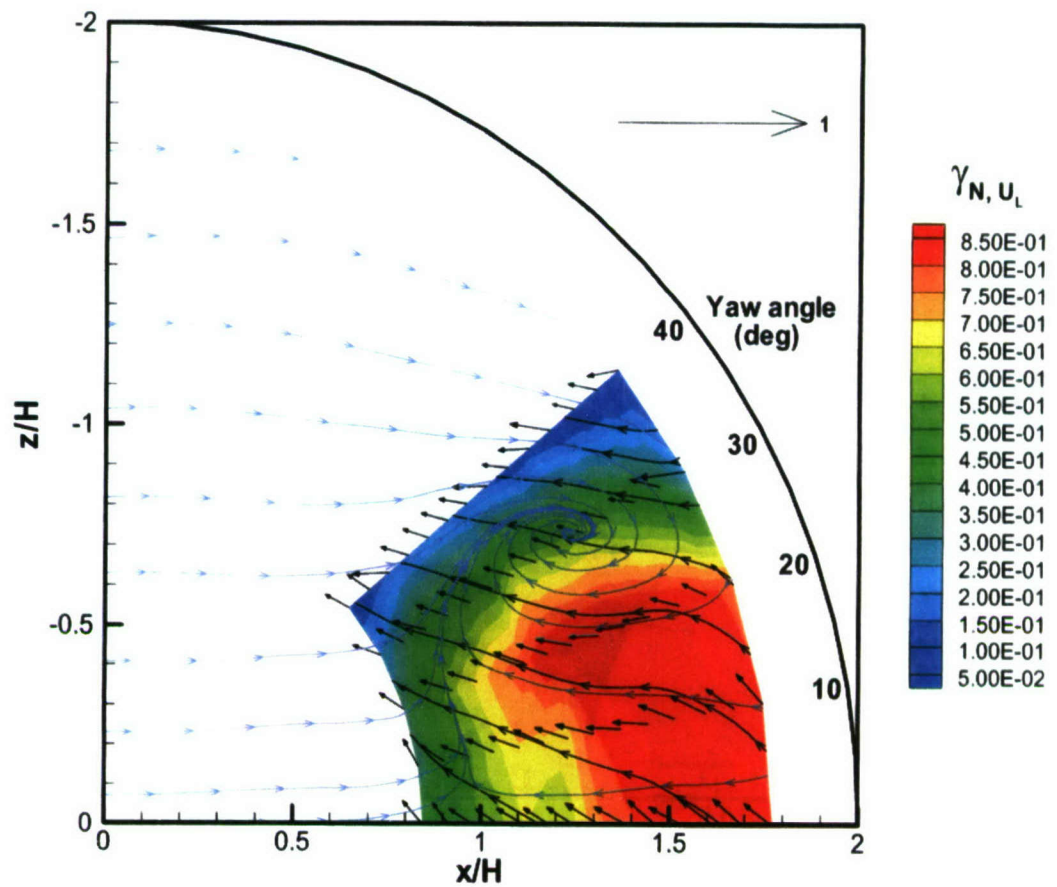


Vectors for velocity components locally tangent to surface in bimodal region and contours for the time fraction of negative U_L in local coordinates.

Lines connecting locally tangential velocity vectors are only for visual aid.

Blue lines for time-averaging original histograms and black lines only for bimodal region.

Figure D.1 The forward mode at $y_{L0}^+ = 41$.

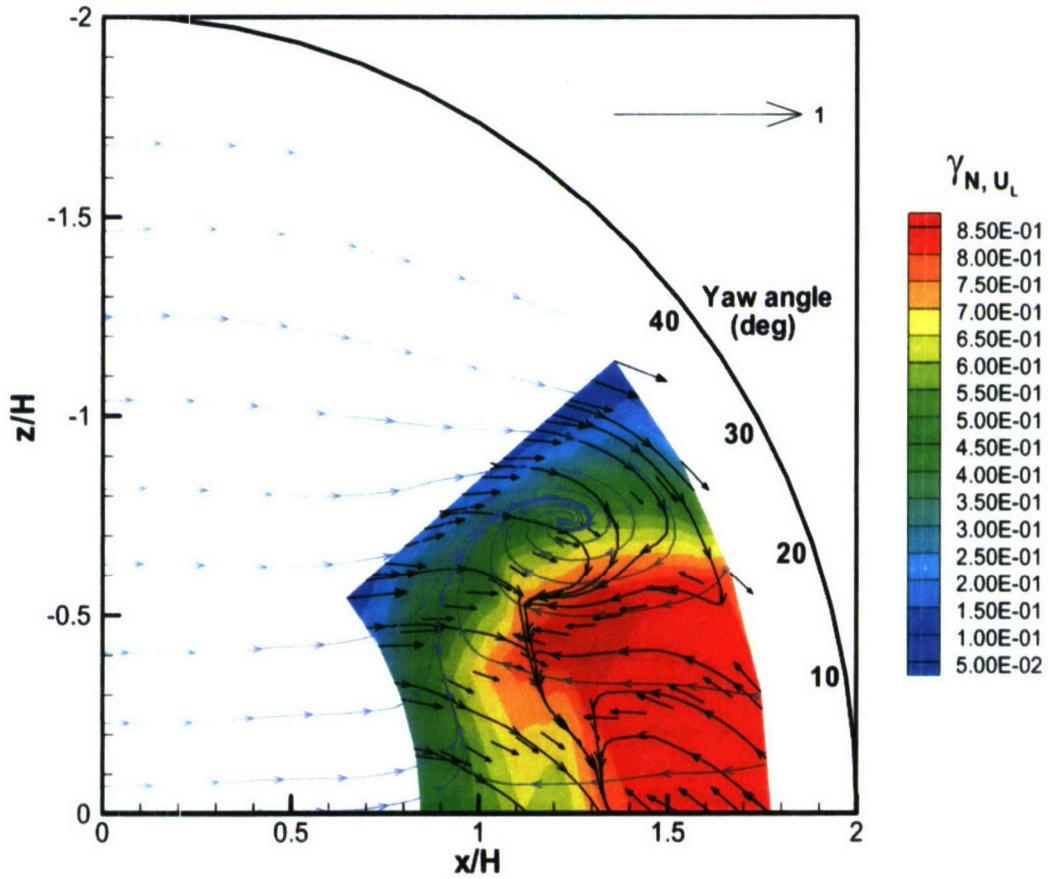


Vectors for velocity components locally tangent to surface in bimodal region and contours for the time fraction of negative U_L in local coordinates.

Lines connecting locally tangential velocity vectors are only for visual aid.

Blue lines for time-averaging original histograms and black lines only for bimodal region.

Figure D.2 The backward mode at $y_{L0}^+ = 41$.

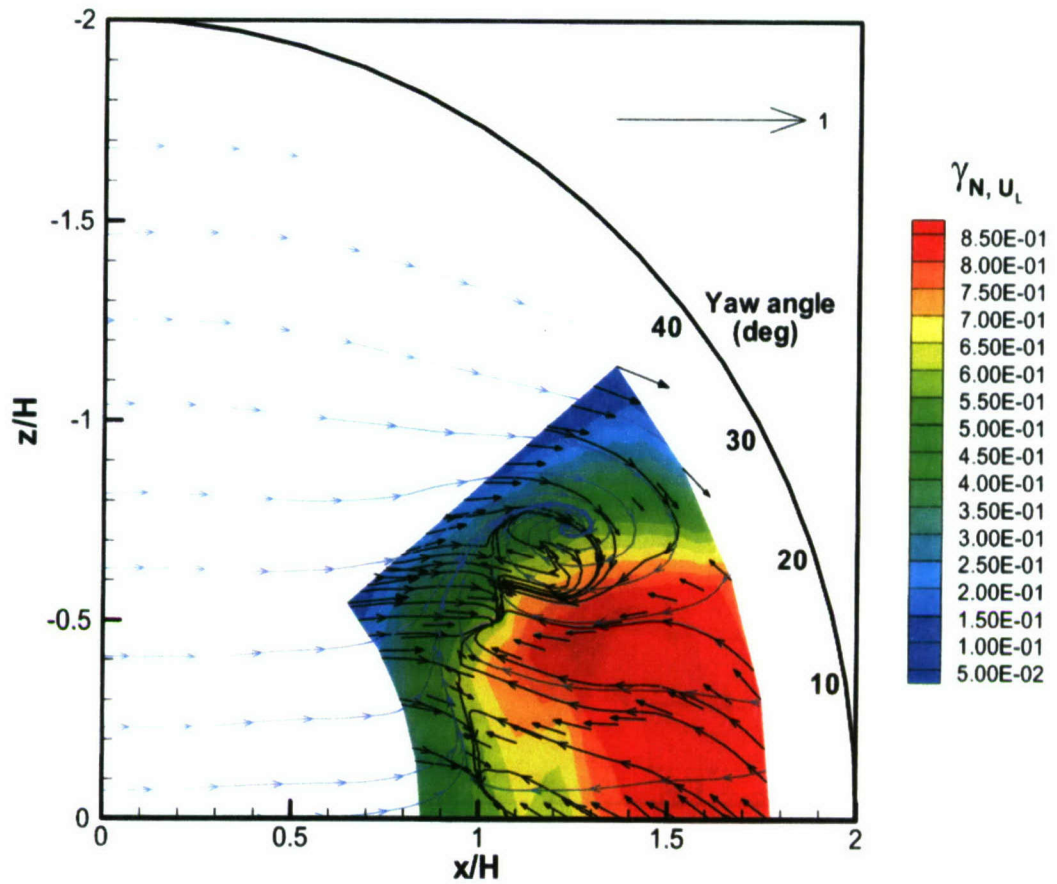


Vectors for velocity components locally tangent to surface in bimodal region and contours for the time fraction of negative U_L in local coordinates.

Lines connecting locally tangential velocity vectors are only for visual aid.

Blue lines for time-averaging original histograms and black lines only for bimodal region.

Figure D.3 The combination of forward and backward modes at $y_{L0}^+ = 41$ for $\gamma_{N,U_L} = 0.8$.

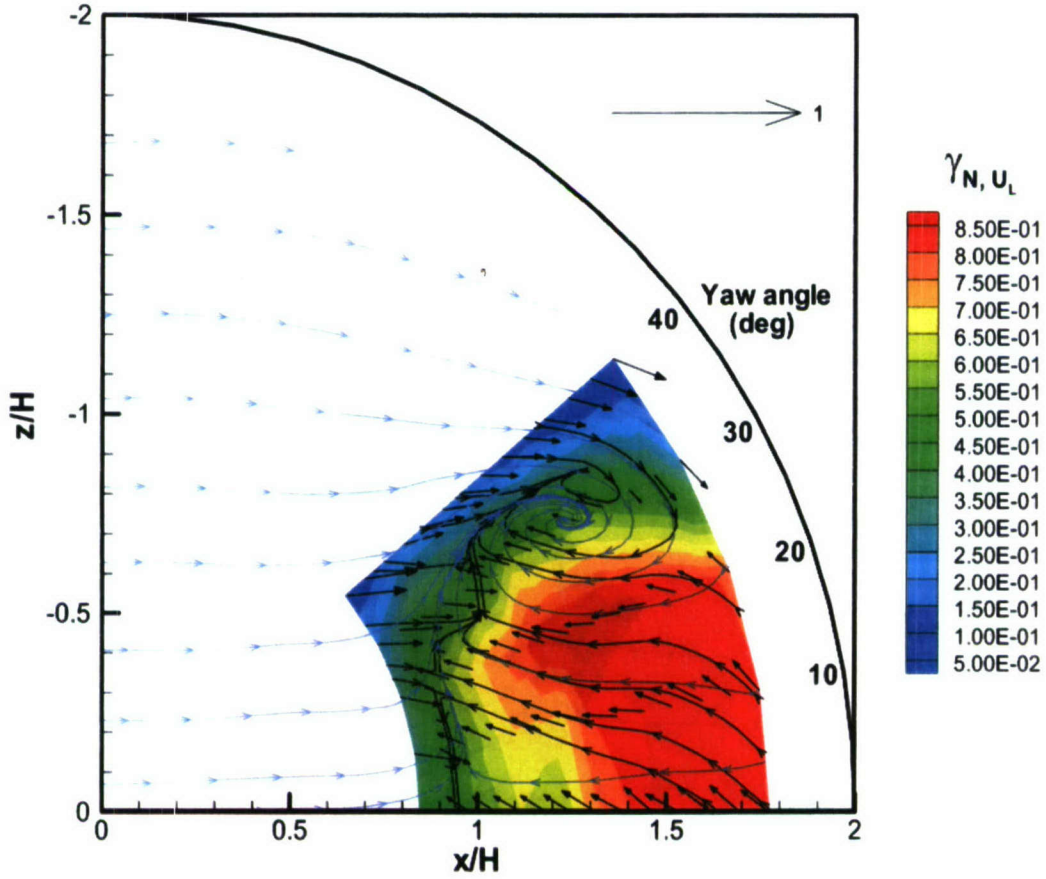


Vectors for velocity components locally tangent to surface in bimodal region and contours for the time fraction of negative U_L in local coordinates.

Lines connecting locally tangential velocity vectors are only for visual aid.

Blue lines for time-averaging original histograms and black lines only for bimodal region.

Figure D.4 The combination of forward and backward modes at $y_{L0}^+ = 41$ for $\gamma_{N,U_L} = 0.6$.



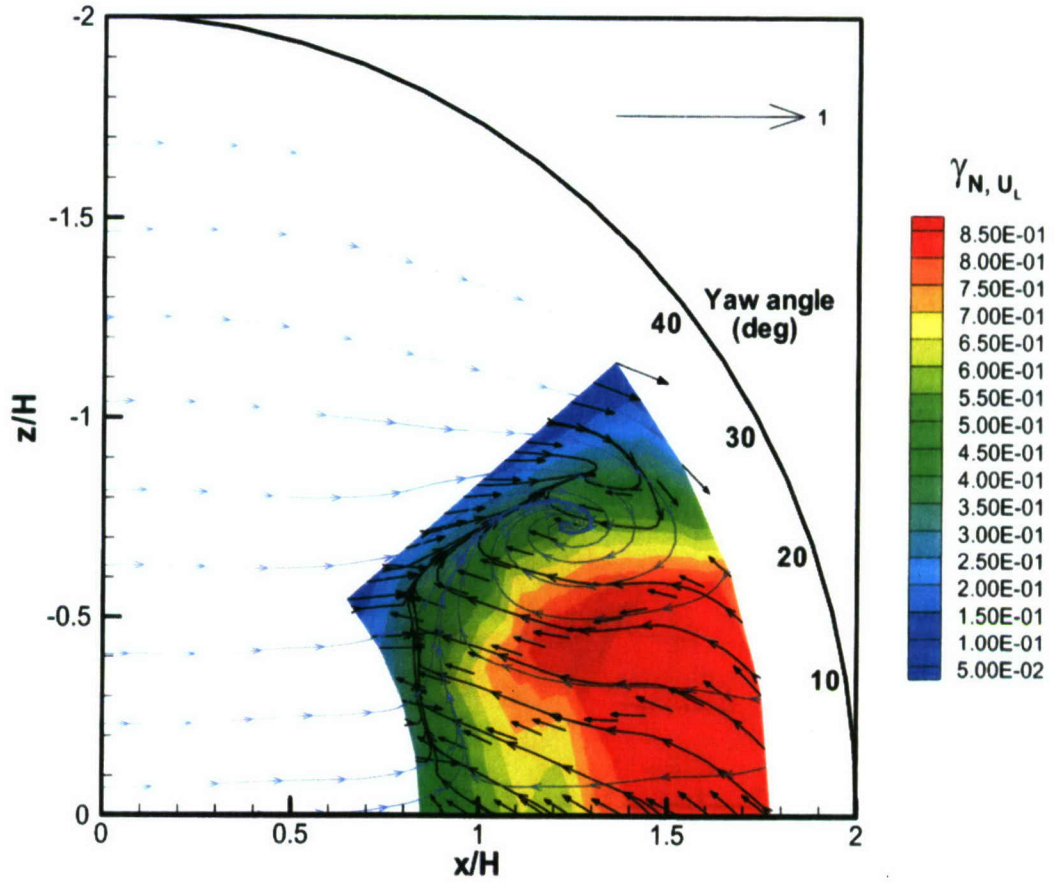
Vectors for velocity components locally tangent to surface in bimodal region and

contours for the time fraction of negative U_L in local coordinates.

Lines connecting locally tangential velocity vectors are only for visual aid.

Blue lines for time-averaging original histograms and black lines only for bimodal region.

Figure D.5 The combination of forward and backward modes at $y_{L0}^+ = 41$ for $\gamma_{N,U_L} = 0.5$.

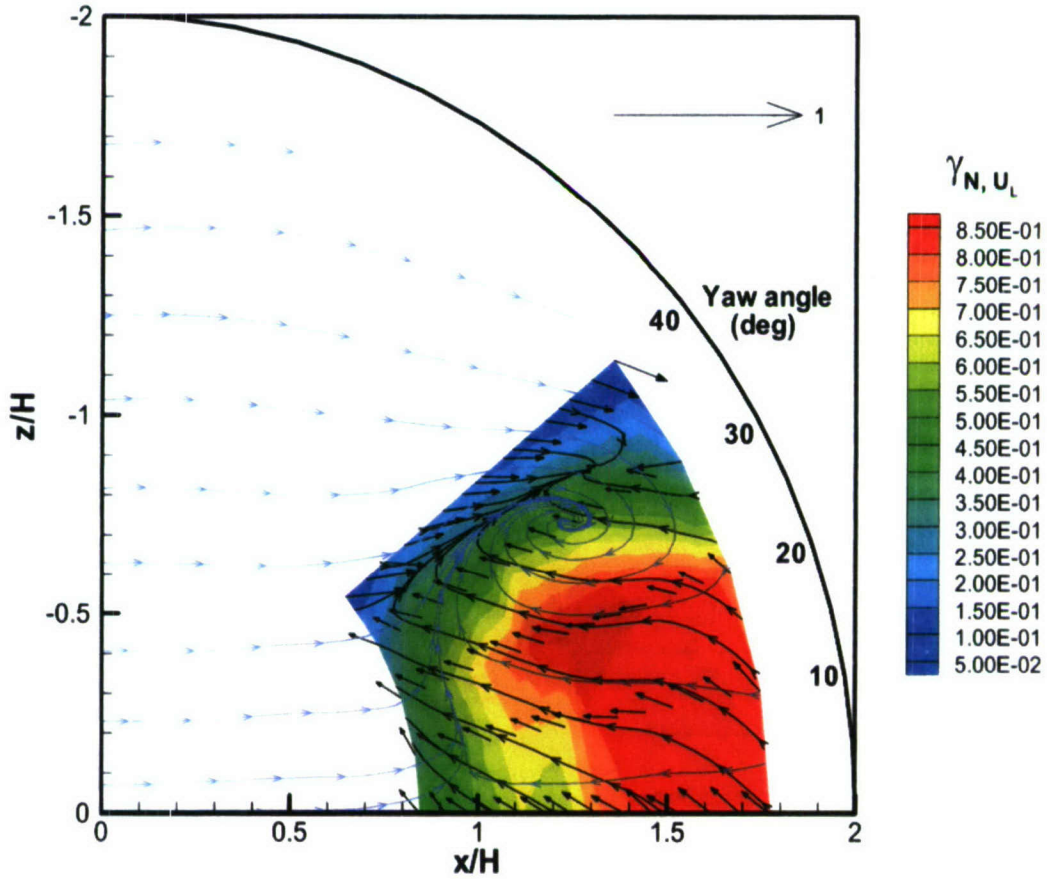


Vectors for velocity components locally tangent to surface in bimodal region and contours for the time fraction of negative U_L in local coordinates.

Lines connecting locally tangential velocity vectors are only for visual aid.

Blue lines for time-averaging original histograms and black lines only for bimodal region.

Figure D.6 The combination of forward and backward modes at $y_{L0}^+ = 41$ for $\gamma_{N,U_L} = 0.4$.

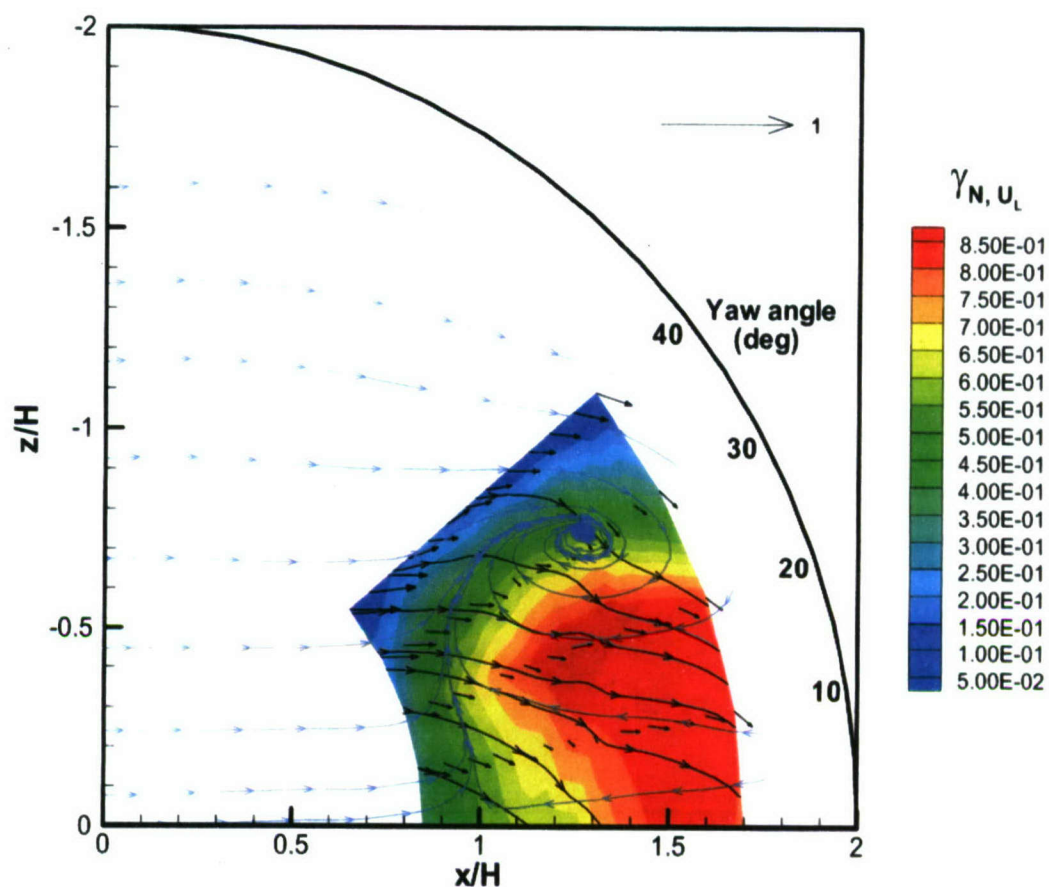


Vectors for velocity components locally tangent to surface in bimodal region and contours for the time fraction of negative U_L in local coordinates.

Lines connecting locally tangential velocity vectors are only for visual aid.

Blue lines for time-averaging original histograms and black lines only for bimodal region.

Figure D.7 The combination of forward and backward modes at $y_{L,0}^+ = 41$ for $\gamma_{N,U_L} = 0.2$.

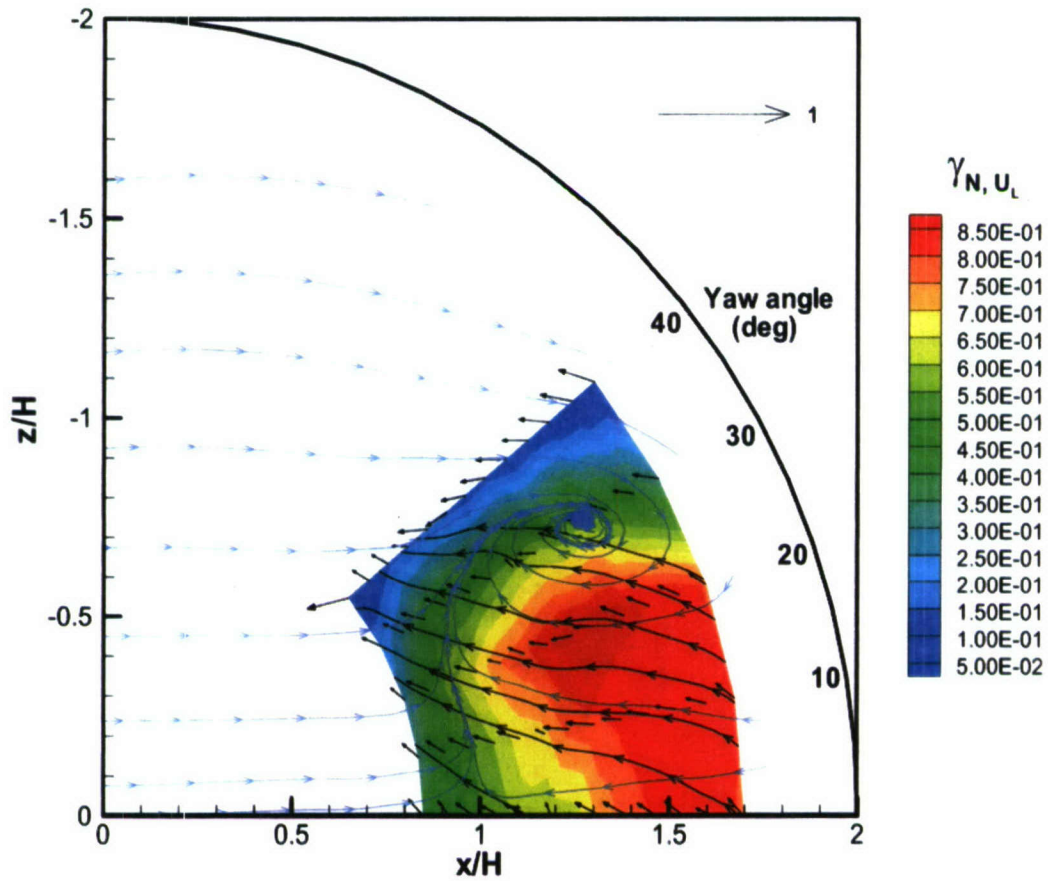


Vectors for velocity components locally tangent to surface in bimodal region and contours for the time fraction of negative U_L in local coordinates.

Lines connecting locally tangential velocity vectors are only for visual aid.

Blue lines for time-averaging original histograms and black lines only for bimodal region.

Figure D.8 The forward mode at $y_{1,0}^+ = 69$.



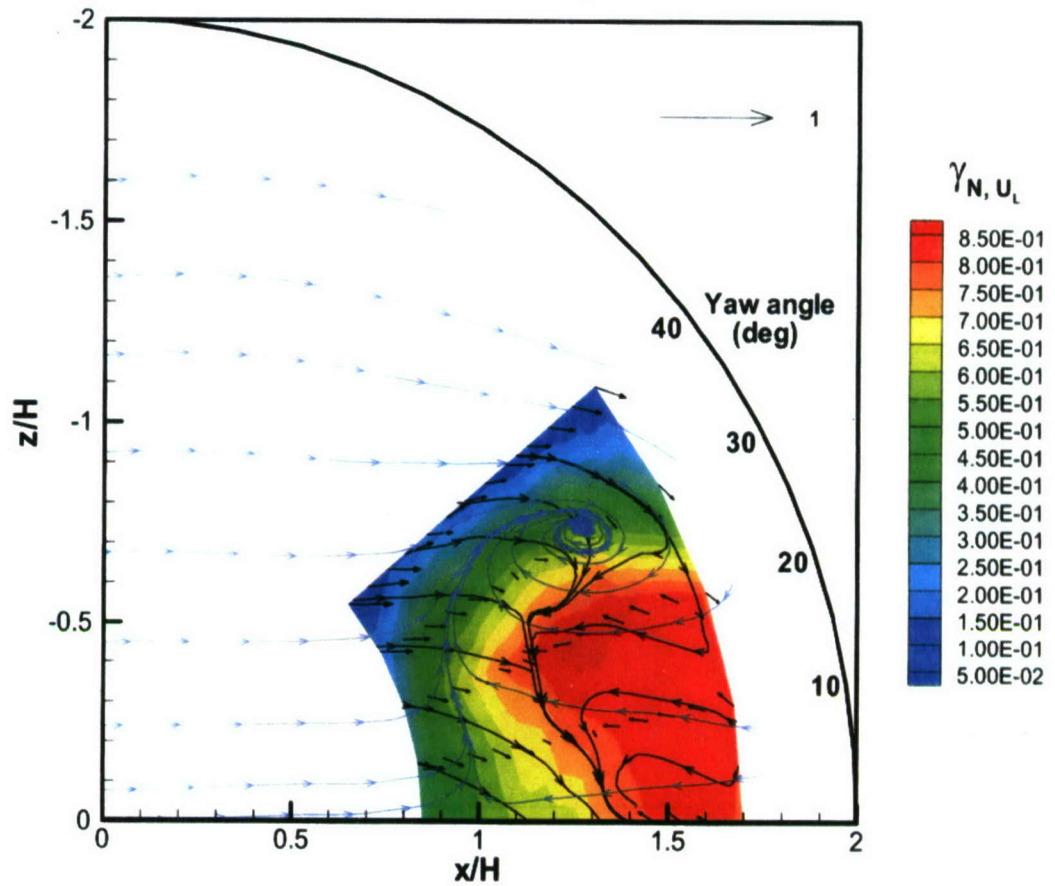
Vectors for velocity components locally tangent to surface in bimodal region and

contours for the time fraction of negative U_L in local coordinates.

Lines connecting locally tangential velocity vectors are only for visual aid.

Blue lines for time-averaging original histograms and black lines only for bimodal region.

Figure D.9 The backward mode at $y_{L0}^+ = 69$.

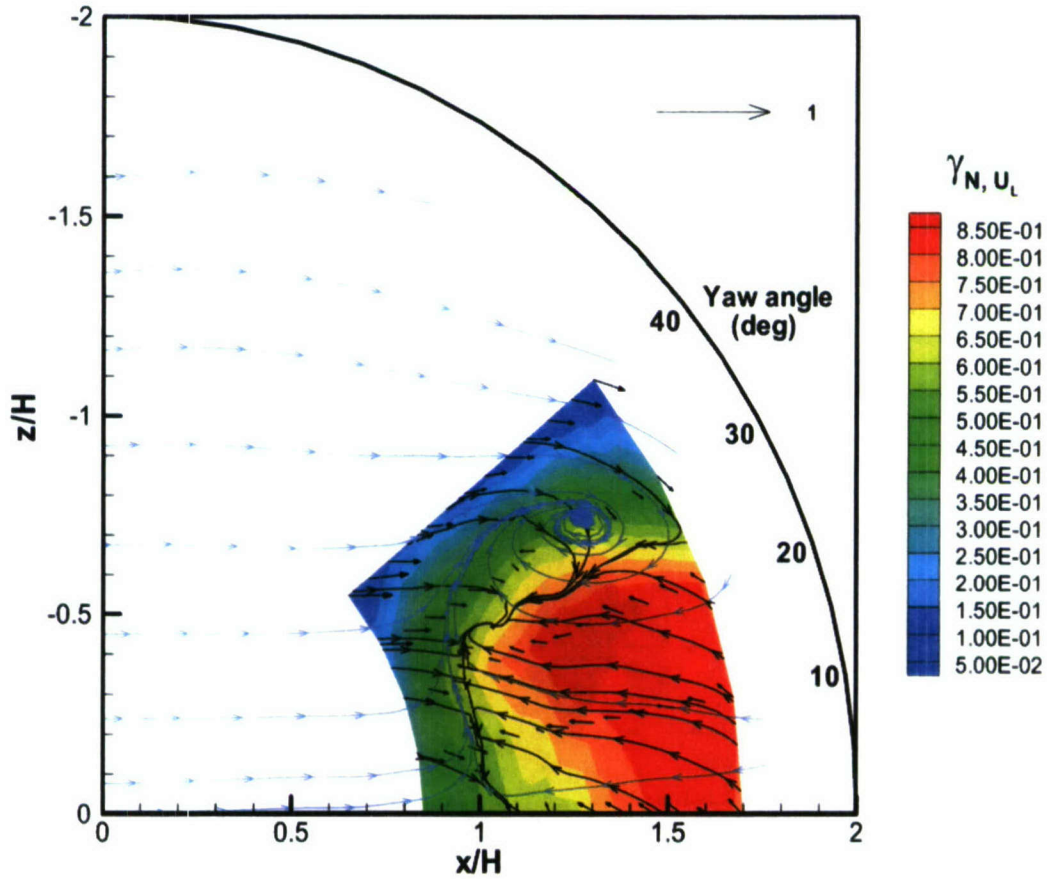


Vectors for velocity components locally tangent to surface in bimodal region and contours for the time fraction of negative U_L in local coordinates.

Lines connecting locally tangential velocity vectors are only for visual aid.

Blue lines for time-averaging original histograms and black lines only for bimodal region.

Figure D.10 The combination of forward and backward modes at $y_{L0}^+ = 69$ for $\gamma_{N,U_L} = 0.8$.



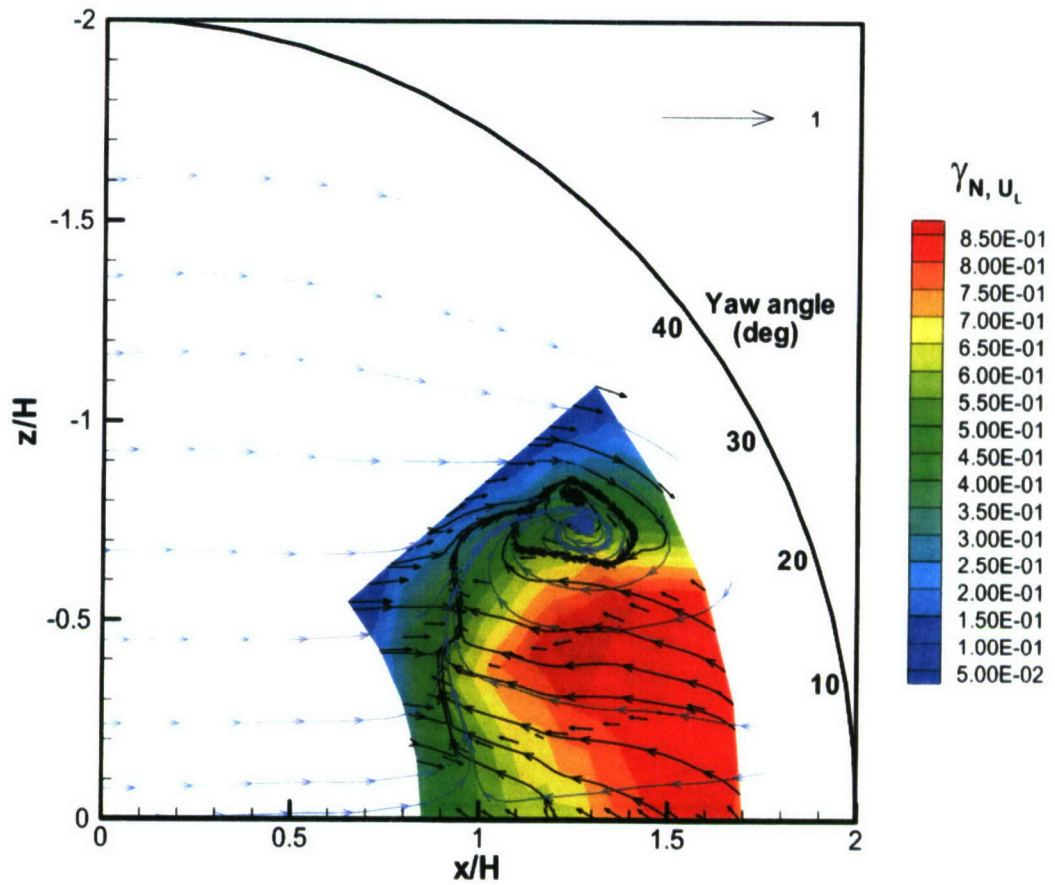
Vectors for velocity components locally tangent to surface in bimodal region and

contours for the time fraction of negative U_L in local coordinates.

Lines connecting locally tangential velocity vectors are only for visual aid.

Blue lines for time-averaging original histograms and black lines only for bimodal region.

Figure D.11 The combination of forward and backward modes at $y_{L0}^+ = 69$ for $\gamma_{N,U_L} = 0.6$.

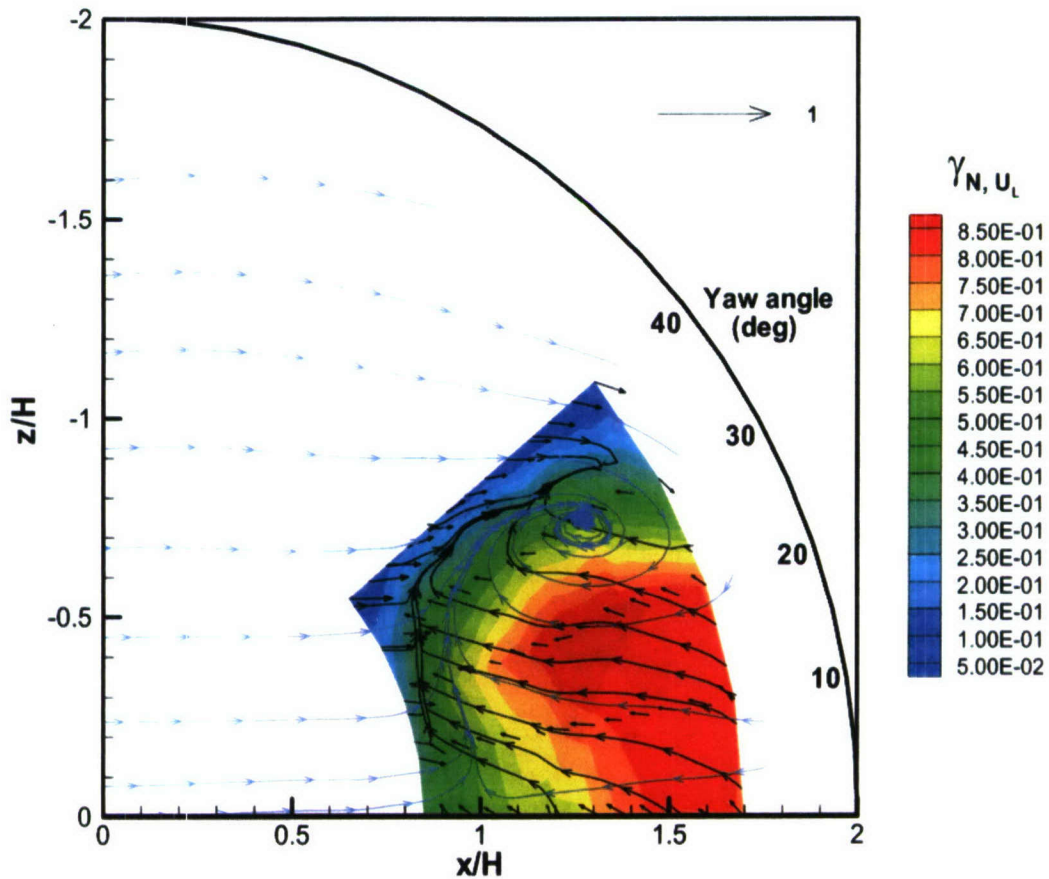


Vectors for velocity components locally tangent to surface in bimodal region and contours for the time fraction of negative U_L in local coordinates.

Lines connecting locally tangential velocity vectors are only for visual aid.

Blue lines for time-averaging original histograms and black lines only for bimodal region.

Figure D.12 The combination of forward and backward modes at $y_{L0}^+ = 69$ for $\gamma_{N,U_L} = 0.5$.

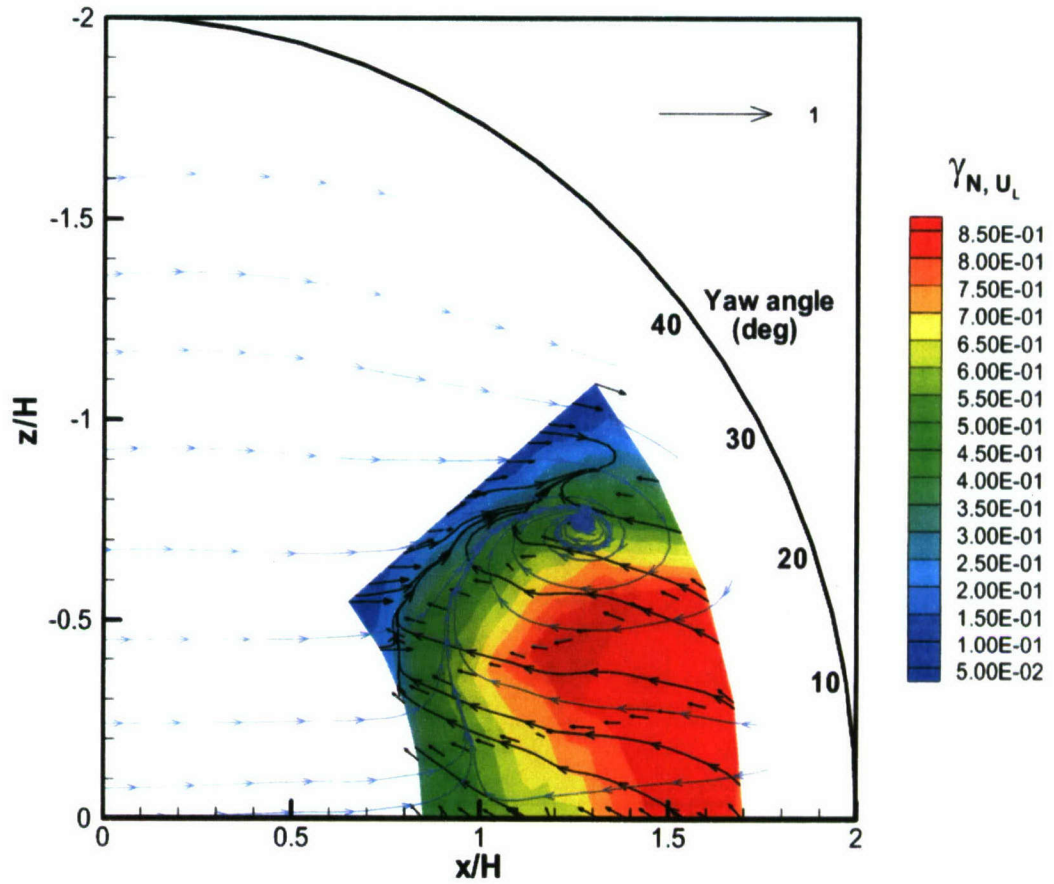


Vectors for velocity components locally tangent to surface in bimodal region and contours for the time fraction of negative U_L in local coordinates.

Lines connecting locally tangential velocity vectors are only for visual aid.

Blue lines for time-averaging original histograms and black lines only for bimodal region.

Figure D.13 The combination of forward and backward modes at $y_{L0}^+ = 69$ for $\gamma_{N,U_L} = 0.4$.



Vectors for velocity components locally tangent to surface in bimodal region and contours for the time fraction of negative U_L in local coordinates.

Lines connecting locally tangential velocity vectors are only for visual aid.

Blue lines for time-averaging original histograms and black lines only for bimodal region.

Figure D.14 The combination of forward and backward modes at $y_{L0}^+ = 69$ for $\gamma_{N,U_L} = 0.2$.